Deciphering the Solar Wind Interaction with the Terrestrial and Saturnian Magnetospheres

Wayne (Stewart) Gould, MPhys (Hons)

Space and Planetary Physics Group

Physics Department

Lancaster University

A thesis submitted for the degree of

Doctor of Philosophy

November 10, 2024

Declaration

I declare that the work presented in this thesis is, to the best of my knowledge and belief, original and my own work. The material has not been submitted, either in whole or in part, for a degree at this, or any other university. This thesis does not exceed the maximum permitted word length of 80,000 words including appendices and footnotes, but excluding the bibliography.

Wayne (Stewart) Gould

Deciphering the Solar Wind

Wayne (Stewart) Gould, MPhys (Hons).

Space and Planetary Physics Group

Physics Department

Lancaster University

A thesis submitted for the degree of *Doctor of Philosophy.* November 10, 2024

Abstract

Due to a lack of upstream monitors, the effects of the solar wind on Saturn's magnetosphere are not well understood. Consequently, previous investigations of this relationship have been restricted to time limited case studies. However, it is known that the solar wind plays an important role in magnetosphere dynamics. With the conclusion of the Cassini mission in 2017, continuous data, spanning 13 years is available to conduct an investigation.

In this thesis, we present three studies. The first exploring the relationship of directly measured solar wind and IMF data to the magnetic field perturbations detected via the geomagnetic indices, AL and SYM/H. The second then continues this work with a comparative study between coupling functions and their utility versus individual solar wind and IMF parameters to detection of the geomagnetic indices, AL and SYM/H. This research then culminates in a large-scale statistical study of Saturn kilometric radiation as a proxy for the solar wind. Due to the lack of direct solar wind monitoring at Saturn, we use a solar wind propagation model to explore several solar wind and IMF parameters and their relationship with Saturn kilometric

radiation.

To assess the strength of the relationships between the solar wind parameters and both the geomagnetic indices, AL and SYM/H, and Saturn kilometric radiation, we use mutual information (chapter 5). Mutual information is a measurement of how strong the relationship is between two variables, and by extension, how much we can infer from one about the other. In the latter study, that is how confident we can be of Saturn kilometric radiation's strength when measuring a given solar wind and IMF parameter value from the propagation model. It has significant advantages over traditional metrics such as correlation, which can only consider linear relationships. Mutual information is able to explore and reveal non-linear relationships in addition. This thesis first outlines the theory behind and a means of applying mutual information to the data considered (chapter 6). Additionally, a means of calculating uncertainties for singular data sets is adapted and tested on predictable Gaussian data to ascertain the utility of this technique.

In our first study (chapter 7) we analyse geomagnetic indices with directly measured solar wind data. Known relationships are drawn out in expectations with previous studies, confirming the application of the methods in this thesis. Our second study (chapter 8) investigates the utility of coupling functions as a means of describing the solar wind and IMF coupling with the terrestrial magnetosphere, relating them to the enhancement of geomagnetic indices. We find that even under general conditions, coupling functions are a much stronger indicator of the solar wind and IMF relationship to geomagnetic indices.

Finally, we apply the methods of this thesis to propagated solar wind and IMF data with Saturnian kilometric radiation (chapter 9). We find the IMF parameter, B_y, to

present a statistically significant relationship with Saturn kilometric radiation, acting as a proxy for the IMF strength and rate of magnetic reconnection. Unlike previous case studies that predict the dynamic pressure, p_{dyn}, as the strongest relationship, this is found to be the weakest relationship of all the parameters considered. However, this is related to the uncertainty in propagation arrival times associated with the Sun-Earth-Saturn angle and therefore conclude that mutual information values for this chapter should be considered a lower limit. Further work is then suggested to improve upon these results by relating the Sun-Earth-Saturn angle to the time offset described in section 6.4.

Acknowledgements

Undertaking a PhD thesis is a daunting task; it is a long journey filled with highs and lows. The challenge is then exponentially increased when a global pandemic occurs just as you get going with it. Nevertheless, the end result has been a rewarding journey, one began 14 years ago when I first decided to undertake a degree in Physics and Astrophysics, following the release of Brian Cox's series: *Wonders of the Solar System* and *Wonders of the Universe*. Why I decided to devote the next 14 years of my life to the pursuit of a doctorate, based upon a decision made as quickly as the idea came to me, is a question for philosophers long after I have passed. Regardless, I leave the reader with a quote that might encapsulate what I would say to my younger self if I could speak to that bright eyed young man before he believed in himself and what he could do. It is of course a quote from Captain Jean-Luc Picard of Star Trek: The Next Generation, one of the earliest influences on my love of all things related to space and the cosmos.

> "Buried deep within you, beneath all the years of pain and anger there is something that has never been nurtured. The potential to make yourself a better man—and that is what it is, to be human. To make yourself more than you are. Oh, yes, I know you. There was a time you looked at the stars and dreamed of what might be" - Jean Luc Picard

Regardless of why I began this journey, I could not have made it with the support of those around me. Therefore, I would like to acknowledge those who have been instrumental in helping me achieve this herculean task. To all those I have not named, who helped in their own small ways, I also say thank you.

Licia C Ray - My PhD Supervisor. Thank you for continued support and patience. The circumstances of supervising a PhD through a pandemic have presented challenges to us both, yet you have been there to offer your support and guidance always.

Chris Arridge - My Secondary PhD Supervisor. Thank you for all the times you lent me an extra set of eyes and ears when I was running into walls.

Andrew Walsh - My ESAC Supervisor. I'm grateful for all the Friday afternoons we came together and you offered your advice. Not only did you help to validate my work but provided me with the experience I needed to take my career forward. That we met for our Friday catch up each week in a taberna may have also helped.

Joe Kinrade, Josh Wiggs, Chris Lorch, Maria Walach, and George Xystouris - My Friends at Lancaster University. Thank you for all the nights at the pub, the cups of tea in the corridors, and the shared ramblings as we vented on the bad days. I am forever grateful for your support when I needed to sound out a problem and your advice when I need your subject matter expertise.

My DnD group - Lockdowns during the pandemic were an isolating experience. The friendships we forged and the stories we created quickly became the highlights of my week, they helped me keep going through the worst of moments. That our group still gathers every week, 4 years strong and continuing, is testament to the support we found in one another and the joy of an adventure shared with friends.

Josh Aldred, Josh Tilley, and Arron Coe - My Oldest and Closest Friends. It's almost impossible to describe the meaning of our friendship and the support it has offered. You've held me up through all of life's highs and lows. For the drinks you bought, the days you were there, and the endless mockery you offered without cause,

may it never end.

Maiki - My Partner. You moved half way across the world to build your own life. When you met me, you decided to move a little bit further to build a life together. No sooner had you come than I had to write my thesis. My love and thanks for all the nights and weekends you supported me through the stress, brought me cups of tea, and showed endless patience as I sat hunched over my laptop night after night. I look forward to a future shared, with free weekends.

Sandra Waller - My mother. My love and thanks for never putting my ambitions down, questioning my dreams, and for always being there when I needed you.

Above all I wish to dedicate this Thesis to my grandparents: Joan and Peter Cook.

Joan Cook - My Grandmother. Through all the turbulence of my life, you've stood by with unwavering love, support, and belief in me. You have always given me the encouragement to make the most of myself, done your best to show me the world, and ensured I always knew I had somewhere to go, no matter my circumstances. I can never thank you enough for making sure I believed I could be more than life expected of me.

Peter Cook - My Grandfather. Thank you for showing me all those black and white sci-fi films before I was old enough to understand them. Thank you for sharing your love of science and science-fiction, and for all those walks to the Millfield where you would point out the constellations and tell me everything you knew about space. I wouldn't have found the path I'm on without you.

Contents

List of Figures

List of Tables

Chapter 1

Introduction

Due to a lack of upstream monitors, the effects of the solar wind on magnetospheres other than the Earth's are not well understood. At Saturn, previous investigations of this relationship have been restricted to time limited case studies.(Desch (1982); Desch and Rucker (1983); Taubenschuss et al. (2006); Badman et al. (2008); Clarke et al. (2009); Jackman et al. (2010)). Existing studies into Saturn's magnetosphere have made clear that the solar wind plays an important role in magnetospheric dynamics. What is unclear, is the extent to which the solar wind drives the magnetospheric dynamics where other mechanisms contribute, such as internal plasma sources from Enceladus. As such, the need for a general method to investigate the relationship between the solar wind and planetary magnetospheres is much needed.

With the conclusion of the Cassini mission in 2017, 13 years of continuous data is available to conduct an investigation connecting the solar wind to driving of the Saturnian magnetosphere. In this thesis we present a large-scale statistical study of Saturn Kilometric Radiation (SKR) as a proxy for the solar wind, building a method of comparison being generally applicable to other celestial objects and data sets. Due

to the lack of upstream monitors at Saturn, we use a propagation model to explore several solar wind parameters and their relationship with SKR. The structure of this thesis and a brief description of its contents are outlined here.

chapter 2: We begin by first exploring the physics required to understand and interpret the results presented in this thesis. This begins with the fundamentals; defining what a plasma is, how it behaves in the presence of magnetic fields, and the frozen-in relationship that binds plasmas and magnetic fields together. We follow these basics by explaining the behaviours of the solar wind, from the violent expulsion of plasma from the solar environment, to its varied behaviours in the interplanetary medium (IPM).

chapter 3: Following the path of the solar wind as it moves through the IPM, this chapter explores what happens when the solar wind reaches a planetary magnetosphere within the Solar System. The relationship between the solar wind and magnetospheric systems are understood, outlining the Dungey cycle and magnetic reconnection. Finally, we close our exploration of the fundamental physics by outlining the various phenomena to be investigated: geomagnetic indices, coupling functions, and SKR, defining their properties and the mechanisms that generate them.

chapter 4: Before relationships with the solar wind can be explored, the origins, caveats, and limitations of the data must be accounted for. In particular, when exploring the solar wind relationship with SKR, due to the absence of upstream monitors, solar wind conditions must be propagated to Saturn. This is achieved using direct measurements of the solar wind at Earth and the L1 Lagrange point. Thus, the solar wind, one-dimensional, magnetohydrodynamic propagation model of Tao et al. (2005) is outlined to achieve this. The limitations of the model and the constraints it

puts upon the use of Cassini mission data are the largest limitation on data availability for this investigation, primarily in uncertainties of the arrival time of propagated data and the constraints placed by the Sun-Earth-Saturn angle, Φ_S.

chapter 5: To characterise the strength of the relationship between various solar wind parameters and SKR, we use Mutual Information (MI). MI is a measurement of the strength of a relationship between two variables, and by extension, how much we can infer from one about the other. Unlike traditional statistical comparisons, such as correlation, which can only reveal linear relationships, MI can explore all relationships, including non-linear ones. As the means by which we can interpret the relationship between the solar wind and Saturn, this chapter is devoted to understanding the derivation of MI and the value of its measurements.

chapter 6: A limitation of space studies is the expense of developing, manufacturing, and deploying instrumentation to measure the phenomena crucial to our understanding of the universe. It is unfortunate then that only one data set for the solar wind and SKR exists. There are no multiples of the data sets recorded, from which we can calculate repeated values of MI, in order to derive the uncertainties of the results presented here. Thus, this chapter is devoted to adapting the methods of Holmes et al. (2019), to solve the MI uncertainties of our results. We test these methods extensively, using Gaussian data with known MI values to verify the adaptation.

chapter 7: With a means of exploring relationships between the solar wind and planetary magnetospheres formed, the remaining question stands, *Will it work?*. Assessing the relationship between the solar wind and SKR lends the challenge to any results that this is a new exploration, using propagated, in the absence of directly

measured, solar wind data. Thus, any unexpected relationships found, particularly if they are in contradiction to the present understanding of the relationship between the solar wind and SKR, will raise questions around confidence in the method. This chapter then conducts our first investigation in the terrestrial system, exploring the relationship between the geomagnetic indices, AL and SYM/H, to the solar wind. Geomagnetic indices are measures of magnetic field enhancement in the terrestrial magnetosphere, in response to the solar wind. Results confirm the relationship, and crucially draw out the response time of the magnetosphere, the time taken for solar wind plasma to travel through the magnetospheric system, confirming the methods of this thesis to draw out relationships from real data using MI.

chapter 8: Following verification of this thesis' ability to draw out known relationships, remaining time during a placement at the European Space Agency was used to conduct an investigation on the utility of coupling functions. Coupling functions measure the coupling of the solar wind to the magnetosphere by fitting equations, with empirically derived constants and powers, to measured data. As geomagnetic indices are strongly related to the solar wind, we compare the coupling functions to the AL and SYM/H indices. Compared to the north-south aligned interplanetary magnetic field (IMF), B_z, coupling functions are found to be more powerful measures of the solar wind-magnetosphere coupling. They also reveal the response time of the magnetosphere more clearly and consistently across multiple solar wind parameters. Thus, this chapter reinforces those of chapter 7 in confirming the methods of this thesis using MI.

chapter 9: Finally, with the application of MI verified, we explore the use of SKR as a proxy for the solar wind. Using propagated solar wind data in the absence of direct

measurements, the relationship between the solar wind and SKR can be assessed. Results reveal a clear relationship between the tangential magnetic field, B_y, acting as a proxy for the IMF strength and rate of magnetic reconnection, with the generation of SKR emissions. Some limitations of the approach due to the propagation uncertainty associated with Φ_s are addressed and suggestions for remediation in future work is suggested.

Chapter 2

The Origins of the Solar Wind

The solar wind, central to the questions of this thesis, is an energetic plasma present throughout the solar system. Originating within the Sun, the solar wind is violently expelled into the Interplanetary Medium (IPM), the vast space that surrounds the bodies of the solar system and stretches out to the limits of the heliosphere. Along its journey through the IPM, the solar wind will encounter the major planets, where numerous phenomena occur as it interacts with the planetary magnetospheres. In order to understand the consequences of these interactions one must first understand the fundamental physics relating to the solar wind, its journey, and the magnetospheric interactions that occur as a consequence. Throughout this chapter and the following chapter 3, the fundamental principles and concepts relevant to this work are presented, following this journey from star to magnetosphere.

In this chapter, we set the foundations of this thesis by first defining a plasma and its criterion. We then delve into the underlying physics that governs the behaviour of particles within a plasma and in the presence of magnetic fields. Next, we outline the equations that govern a plasma as a magnetohydrodynamic (MHD) fluid,

building the foundational knowledge needed to understand the behaviour of the solar wind propagation model presented in section 4.3. Finally, we explore the dynamic environment that is the solar wind, it's properties, and the mechanisms that cause this dynamism.

By no means is this an exhaustive exploration into the physics that govern the solar wind. This chapter is presented to aid the readers understanding of the work in this thesis and inform the results outlined in the final chapters. Except where other sources are listed, this chapter uses the works of "Space Physics An Introduction" by Russell et al. (2016) and "Basic Space Plasma Physics" by Baumjohann et al. (2012).

2.1 Plasma Definition

Local to the Earth, few examples of a plasma can be found naturally occurring (examples include flames and lightning strikes). However, move away and one will quickly find that more than 99% of all known matter is in the form of a plasma, i.e. a gas composed of electrically conducting charged particles, which differentiate it from a general gas. Plasmas environments are dynamic, composed of fast moving interacting electrons and ions.

The fast moving electrons within a plasma are referred to as free electrons, unbound to any parent atoms. Ions are atoms possessing a net positive or negative charge. Ionisation can occur from photo-ionisation, charge exchange, and collisions. Photo-ionisation is a process whereby energetic photons interact with an atom, providing enough energy exchange to overcome the potential energy that binds an electron to an atom, causing the release of the electron and leaving behind positively

charged ions. Collisions cause ionisation when particles collide, transferring sufficient energy to release an electron and create a positively charged ion, or bind a free electron to an atom, creating a negatively charged ion. Charge exchange occurs when one atom transfers an electron to another atom, resulting in no net gain or loss of ionisation.

Ions are also a type of free particle, defined as a particle whose motion is free of the influence of other nearby charged particles. In MHD models, such as that of Tao et al. (2005), free particles (and plasmas) exist in a collisionless regime and is what will be assumed in this thesis. To be a free particle, the particle must have a kinetic (thermal) energy that greatly exceeds the potential energy from its nearest neighbour, to prevent particle coupling. These energies, in order to overcome the neighbourhood potential energies, must therefore be in excess of a few electronvolts.

Plasmas exist in a quasi-neutral state at scale; when the net balance of positive and negative charge carriers within a volume is roughly equal. In order to more rigorously define when an ionised gas is in a plasma state, we define the following criterion.

2.1.1 Debye Shielding

A quasi-neutral state will appear electrically neutral, due to the positive and negative charge carriers shielding one another at a macroscopic level (cancelling out one another). In order to appear electrically neutral, the Coulomb potential field of each charge, q, and hence the electric field, is shielded by other charges according to the Debye potential

$$\phi_D = \frac{q}{4\pi\epsilon_0 r} \exp\left(-\frac{r}{\lambda_D}\right) \tag{2.1}$$

where ϵ_0 is the free space permittivity, r is the distance, and λ_D is the Debye length.

The Debye length is the distance at which the kinetic (thermal) particle energy and electrostatic potential energy, resulting from charge separation, shield one another. The Debye length is a function of both the electron and ion temperatures, T_e and T_i, and plasma densities, n_e and n_i, where it is assumed that $T_e \simeq T_i$ and $n_e \simeq n_i$. It is defined as

$$\lambda_D = \left(\frac{\epsilon_0 k_B T_e}{n_e e^2} \right)^{\frac{1}{2}} \tag{2.2}$$

where k_B is the Boltzmann constant and e the electron charge.

In order to be quasi-neutral, sufficient space must exist for collective shielding to occur. As such, the following condition must be satisfied, called the first plasma criterion,

$$\lambda_D << L \tag{2.3}$$

where L is the volume of the system containing the plasma.

2.1.2 Plasma Parameter

Debye shielding occurs within a sphere of radius λ_D within which is a sufficient number of particles to create the collective shielding behaviour. By definition, the number of particles within the sphere, N_D, is therefore

$$N_D = \frac{4\pi}{3} n_e \lambda_D^3 \tag{2.4}$$

where $n_e \lambda_D^3$ is referred to as the Plasma parameter. Equation 2.1 assumes a sufficient number density of particles exist for the potential of an isolated charge to

be shielded. This therefore leads to the definition of the second plasma criterion from the Plasma parameter:

$$n_e \lambda_D^3 >> 1 \tag{2.5}$$

2.1.3 Plasma Frequency

When the quasi-neutral state of a plasma is disturbed by an external force, free electrons within a plasma, being of a much smaller mass and inertia than ions, are accelerated to restore charge neutrality. This field of electrons will oscillate rapidly about the equilibrium position with a characteristic frequency. This frequency, referred to as the plasma frequency, is defined as

$$\omega_{pe} = \left(\frac{n_e e^2}{m_e \epsilon_0} \right)^{\frac{1}{2}} \tag{2.6}$$

where m_e is the electron mass and ω_{pe} is the electron plasma frequency. ω_{pe} comes from the system plasma frequency definition, $\omega_p = (\omega_{pe}^2 + \omega_{pi}^2)^{1/2}$, where ω_{pi} is the ion plasma frequency. Due to the heavier mass of the ions compared to the electrons, $\omega_p \simeq \omega_{pe}$.

Not all plasmas exist in fully ionised spaces. For example, the plasma in the ionosphere is deeply embedded within the Earth's neutral thermosphere. In environments such as these, should the charged particles collide with neutrals too frequently, then the plasma will cease to behave as one and instead behave as a neutral gas. In order for the plasma to avoid behaving as a neutral gas, the time between collisions, τ_n, must be much greater that the reciprocal of the plasma frequency. This defines the third plasma criterion:

$$\omega_p \tau_n >> 1 \tag{2.7}$$

Collectively, these criterion, Equation 2.3 for the Debye Length, Equation 2.5 for the Plasma Parameter, and Equation 2.7 for the Plasma frequency, characterize the plasma state of an ionized gas.

2.2 Single Particle Motion

Plasmas are ionized gases made up of electrically charged particles that each generate electric and magnetic fields. These fields will affect the motion of surrounding charged particles, who will couple with the electromagnetic field of the charged particle. In turn, these affected charged particles will affect others particle's motion through their own generated electric and magnetic fields. However, whilst these charged particles are interacting with one another, it can be advantageous to begin our understanding by considering the motion of a single charged particle to understand its behaviour in the presence of electric and magnetic fields.

A charged particle is surrounded by an electric field, $\mathbf{E}$, which exerts an electrostatic force, $\mathbf{F}_C$, on other particles. This force is given by Coulomb's Law

$$F_C = -k_e \frac{q_1 q_2}{r^2} \tag{2.8}$$

where q is the particle charge, r is the separation between the two charges, and k_e is Coulomb's constant ($\simeq 8.987$ N·m^2·C^{-2}). The length scale over which a charged particle can interact with the surrounding plasma is then given by the Debye length, defined in Equation 2.2.

For a charged particle in motion, the force acting upon it is

$$m\frac{dv}{dt} = q(\mathbf{E} + \mathbf{v} \times \mathbf{B}) + \mathbf{F}_g + m\frac{dv}{dt}\bigg|_c \tag{2.9}$$

where m is the particle mass, $\mathbf{B}$ is the magnetic field, $\mathbf{v}$ is the velocity, $\mathbf{F}_g$ represents non-electromagnetic forces (e.g gravity), and $m\frac{dv}{dt}|_c$ represents the momentum change from collisions. In the case of the solar wind, the collisionless mean free path is of the order of 10^8 km. At such a scale, the frequency of collisions is low ($\sim 10^{-4}$Hz) compared to the plasma frequency given by Equation 2.6 ($\sim 10^4$Hz) and as such the solar wind plasma can be treated as collisionless going forward. Non-electromagnetic forces can also be neglected, whereby Equation 2.9 reduces to the Lorentz Force

$$\mathbf{F}_L = m\frac{dv}{dt} = q(\mathbf{E} + \mathbf{v} \times \mathbf{B}) \tag{2.10}$$

Magnetic fields, $\mathbf{B}$, are vector fields that arise from charged particles in motion, which produce electric currents and/or the intrinsic magnetic moments of fundamental particles. Together, the magnetic and electric fields form the components of the electromagnetic force, described by Maxwell's equations

$$\nabla \times \mathbf{E} = -\frac{\partial \mathbf{B}}{\partial t} \tag{2.11}$$

$$\nabla \times \mathbf{B} = \mu_0 \left(\mathbf{j} + \xi_0 \frac{\partial \mathbf{E}}{\partial t}\right) \tag{2.12}$$

$$\nabla \cdot \mathbf{E} = \frac{\rho_q}{\xi_0} \tag{2.13}$$

$$\nabla \cdot \mathbf{B} = 0 \tag{2.14}$$

where t is time, μ_0 is the permeability of space, ξ_0 is the permittivity of free space, ρ_p is the charge density, and $\mathbf{j}$ is the current density. Equation 2.11 is Faraday's Law, which describes how an electromotive force is produced by the interaction of a magnetic field with an electric current. Equation 2.12 is Ampere's Law, which relates the net magnetic field along a closed loop to the electric current passing through the loop. Equation 2.13 is Gauss's Law, which states that the electric flux across a closed surface is proportional to the net electric charge enclosed by the surface. Finally, Equation 2.14 states that there are no magnetic monopoles.

2.3 Particle Gyration

From Equation 2.10, the motion of a charged particle can be determined by first considering the case where there is no electric field ($\mathbf{E} = 0$) and a uniform magnetic field in the z direction ($\mathbf{B} = B_z\ \hat{\mathbf{z}}$). In this case Equation 2.10 gives the resultant components

$$m\frac{\partial v_x}{\partial t} = qB_z v_y \tag{2.15}$$

$$m\frac{\partial v_y}{\partial t} = -qB_z v_x \tag{2.16}$$

$$m\frac{\partial v_z}{\partial t} = 0 \tag{2.17}$$

where for Equation 2.17, the velocity component parallel to the magnetic field, $v_{\parallel}$ = v_z, is a constant. Taking the second derivative gives

$$m\frac{\partial^2 v_x}{\partial t^2} = qB_z\frac{\partial v_y}{\partial t} \tag{2.18}$$

$$m\frac{\partial^2 v_y}{\partial t^2} = -qB_z\frac{\partial v_x}{\partial t} \tag{2.19}$$

Substituting Equation 2.16 into Equation 2.18 and Equation 2.15 into Equation 2.19 both then result in the equation for a simple harmonic oscillator

$$\frac{\partial^2 v_x}{\partial t^2} = -\left(\frac{qB_z}{m}\right)^2 v_x \tag{2.20}$$

$$\frac{\partial^2 v_x}{\partial t^2} = -\left(\frac{qB_z}{m}\right)^2 v_y \tag{2.21}$$

which shows that a particle, under a magnetic field, will gyrate about the field with an angular frequency, ω_g, at a radius, r_g

$$\omega_g = \left(\frac{qB_z}{m}\right) \tag{2.22}$$

$$r_g = \frac{v_\perp}{\omega_g} \tag{2.23}$$

where $v_\perp = (v_x^2 + v_y^2)^{1/2}$. The angular frequency, ω_g, is referred to as the gyro-frequency or cyclotron frequency, and the radius, r_g, is referred to as the gyro-radius. Equation 2.20 and Equation 2.21 are harmonic oscillator equations with solutions

$$x - x_0 = r_g \sin\omega_g t \tag{2.24}$$

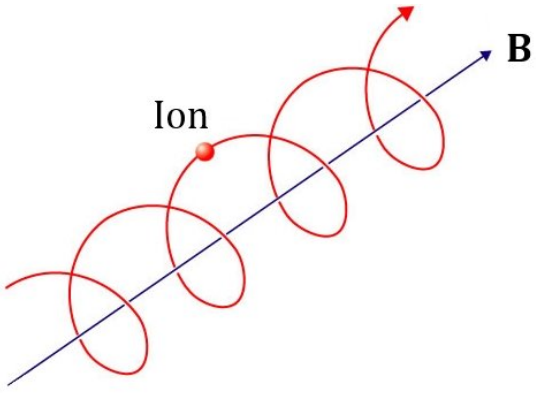

Figure 2.1: Helicoidal motion of a charged particle about a magnetic field. Image credit: EUROfusion (2023)

$$y - y_0 = r_g \cos \omega_g t \tag{2.25}$$

Equations 2.24 and 2.25 show that a particle will move in a circular path perpendicular to the magnetic field. In this case moving along the x-y plane perpendicular to the z plane aligned magnetic field. The orientation of the rotation is then dependent on the particle charge. The orbital centre is referred to as the guiding centre and in a uniform field, rests along the magnetic field line. However, as stated for Equation 2.17, the parallel velocity component is a constant. This circular path is then helicoidal, travelling parallel to the field line (Figure 2.1) at a pitch angle, α, dependent on the parallel and perpendicular velocity components given by Equation 2.26:

$$\alpha = \tan^{-1}\left(\frac{v_\perp}{v_\parallel}\right) \tag{2.26}$$

2.4 Particle Drift

This idealised scenario we have just explored assumes no electric field and a homogenous magnetic field. By definition, an electric field must exist from an electrically charged particle. The presence of an electric field can influence the motion of a particle along the magnetic field line inducing a drift. Magnetic fields, generally, are inhomogeneous and so can also induce drifts. We now describe these drift mechanisms as a fundamental part of single particle motion to reinforce the readers understanding.

2.4.1 E × B Drift

Now, assuming the presence of an electric field and that in the perpendicular direction the electric field component is parallel to the x plane ($\mathbf{E}_\perp = E_x\ \hat{\mathbf{x}}$), Equation 2.10 separates into the following components

$$m\frac{\partial v_x}{\partial t} = \omega_g v_y + \frac{q}{m}E_x \tag{2.27}$$

$$m\frac{\partial v_y}{\partial t} = -\omega_g v_x \tag{2.28}$$

$$m\frac{\partial v_z}{\partial t} = qE_z \tag{2.29}$$

In the z direction, Equation 2.29 describes acceleration along the magnetic field. Though parallel fields do exist they typically vanish, as the parallel component will accelerate electrons and ions along the magnetic field line in opposing directions, thus cancelling one another out.

Taking the second derivative of the components then gives

$$m\frac{\partial^2 v_x}{\partial t^2} = -\omega_g^2 v_x \tag{2.30}$$

$$m\frac{\partial^2 v_y}{\partial t^2} = -\omega_g^2 \left(v_y + \frac{E_x}{B}\right) \tag{2.31}$$

Substituting $v_y^{'} = v_y + E_x/B$ into equation Equation 2.31 results in Equation 2.21, describing a particle gyration about its guiding centre. Thus, under the influence of the electric field, a particle will gyrate about its guiding centre with a drift in the $\mathbf{E}\times\mathbf{B}$ direction. $\mathbf{E}\times\mathbf{B}$ is independent of charge and so all charged particles drift with this velocity, given by Equation 2.32. The consequence of this is that over the course of a single orbit, a particle will accelerate in $v_\perp$ through the first half its orbit, increasing r_g, and for the other half of its orbit will decelerate in $v_\perp$, decreasing r_g, resulting in an orbit deformed from that in Figure 2.1.

$$v_E = \frac{\mathbf{E}\times\mathbf{B}}{B^2} \tag{2.32}$$

2.4.2 Grad-B Drift

In the case where the magnetic field is inhomogeneous, a gyrating particle would now experience a varying gyro-frequency and gyro-radius. Consequently, the particle will experience a gradient drift perpendicular both to the magnetic field and the magnetic field gradient. This drift is thus termed grad-B drift, defined as

$$v_\nabla = \frac{m v_\perp^2}{2qB^3}\left(\mathbf{B}\times\nabla B\right) \tag{2.33}$$

which shows that ions and electrons will drift in opposite directions and particles will experience a gradient drift proportional to the perpendicular energy of the particle, $W_\perp = \frac{1}{2}mv_\perp^2$.

2.4.3 Curvature Drift

When the magnetic field line is curved with radius R_c, the particles experience a centrifugal force parallel to the curvature of the field, resulting in a curvature drift. This force causes electrons and ions to drift perpendicular to the field line. Over the course of a gyration they will undergo acceleration and deceleration, altering the gyro-radius much like grad-B drift, whilst following the path of curvature. The curvature drift is defined as:

$$v_R = \frac{mv_\parallel^2}{q}\frac{\mathbf{R}_c \times \mathbf{B}}{R_c^2 B^2} \tag{2.34}$$

In the case of both grad-B and curvature drift, the opposing motion of the electrons and ions leads to the production of transverse currents. In a magnetospheric environment, both forms of magnetic drift will be present and thus the total magnetic drift can be given by the summation of the two as:

$$v_B = v_R + v_\nabla = \left(v_\parallel^2 + \frac{v_\perp^2}{2}\right)\frac{\mathbf{B} \times \nabla B}{\omega_g B^2} \tag{2.35}$$

At the Earth, electrons move in an easterly direction whilst ions move in a westerly direction. The transverse current associated with full magnetic drift is then responsible for creating the ring current.

2.5 Magnetohydrodynamics

So far we have explored the behaviour of single charged particle motion acting in a plasma environment. However, this does not describe the bulk behaviour of a plasma. For this, we must turn to the ideal MHD equations which seeks to describe the fluid behaviour of electrically charged fluids (bulk plasma) in the presence of external and internal magnetic fields. For complete derivations of the MHD equations, the reader is directed to chapter 7 of Russell et al. (2016) and chapter 3 of Baumjohann et al. (2012).

In ideal MHD a number of reasonable assumptions are made. We first assume that the plasma exists in a collisionless environment and is in a quasi-neutral state. We further assume that gravity is negligible, pressure is isotropic, and that heat flux and Joule dissipation ($\nabla \cdot q = 0$) can be ignored. Under these assumptions the fluid equations of MHD are

$$\frac{\partial \rho}{\partial t} + \nabla \cdot (\rho \mathbf{v}) = 0 \tag{2.36}$$

$$\rho \left(\frac{\partial}{\partial t} + \mathbf{v} \cdot \nabla \right) \mathbf{v} + \nabla \cdot \mathbf{P} - \mathbf{j} \times \mathbf{B} = 0 \tag{2.37}$$

$$\frac{d}{dt} \left(\frac{P}{\rho^{\gamma}} \right) = 0 \tag{2.38}$$

where ρ is the mass density defined as $\rho = \sum_s n_s m_s$, where s represents the particle species; $\mathbf{P}$ is a total pressure tensor; P is the thermodynamic pressure, defined as $P = \sum_s n_s KT$; and γ is the specific heats ratio.

Equation 2.36 is the continuity equation and states that, in the absence of any

process that adds or removes particles from the environment, the particle number density and mass of the environment is conserved. Equation 2.37 is the momentum equation and relates the rate of change of momentum to the various forces acting upon particles within a plasma environment. Equation 2.38 is the energy equation for an adiabatic process.

2.5.1 Frozen-in Theorem

There is a fourth MHD equation, the induction equation, which relates the magnetic field and velocity of a plasma. The induction equation leads to frozen-in theorem, which is crucial for understanding the behaviour of the solar wind. Hence, we briefly describe its origin.

Take the generalized Ohm's law

$$\mathbf{j} = \sigma_0(\mathbf{E} + \mathbf{v} \times \mathbf{B}) \tag{2.39}$$

where $\mathbf{j}$ is the electric current density and σ_0 is the plasma conductivity, defined as

$$\sigma_0 = \frac{n_e e^2}{m_e v_c} \tag{2.40}$$

where v_c is the frequency of collisions in the plasma. Using generalised Ohm's law, one can eliminate the electric field in Faraday's law, Equation 2.11. Then, with Ampere's law, Equation 2.12 and the absence of magnetic monopoles, Equation 2.14, one reaches the general induction equation for magnetic fields[1]

[1] $\nabla^2\mathbf{A} = \nabla(\nabla \cdot \mathbf{A}) - \nabla \times (\nabla \times \mathbf{A})$

$$\frac{\partial \mathbf{B}}{\partial t} = \nabla \times (\mathbf{v} \times \mathbf{B}) + \frac{\nabla^2 \mathbf{B}}{\mu_0 \sigma_0} \tag{2.41}$$

The first term on the RHS of Equation 2.41 is the convective term that governs the freezing in of the magnetic field into a plasma, showing that a magnetic field is changed by the motion of the plasma. The second term on the RHS is the diffusive element that determines how the magnetic field diffuses throughout the plasma.

To define which term dominates mathematically, the ratio of the two terms in the induction equation can be expressed in dimensional form as

$$\frac{B}{\tau} = \frac{VB}{L_B} + \frac{B}{\tau_d} \tag{2.42}$$

where B is the average magnetic field strength, V the average plasma velocity perpendicular to the field, τ is the characteristic time of magnetic field variations, τ_d is the characteristic time of magnetic field variations due to diffusion, and L_B is the characteristic length over which the field varies. The first and second terms on the RHS represent the convective and diffusive terms, respectively. The ratio of the terms on the RHS gives the magnetic Reynolds number

$$R_m = \mu_0 \sigma_0 L_B V \tag{2.43}$$

The Reynolds number can be used to determine whether a medium is dominated by plasma convection or magnetic diffusion. Where $R_m >> 1$, plasma flow dominates and the diffusion term can be neglected, thus Equation 2.41 reduces to

$$\frac{\partial \mathbf{B}}{\partial t} = \nabla \times (\mathbf{v} \times \mathbf{B}) \tag{2.44}$$

Equation 2.44 is widely referred to as the frozen-in theorem, whereby the magnetic field can be treated as if it were frozen to the MHD fluid and moves with it. Frozen-in theorem states that the magnetic flux through an enclosed area remains constant as the area is transported with a moving plasma. Also, that any magnetic field line that connects two fluid elements remains connected.

Furthermore, the reverse is also true. In sufficiently strong magnetic fields, magnetic field strength dominates over the plasma pressure; the plasma will move with the magnetic field, rather than the field with the plasma. Determination of which will dominate can be expressed by a beta parameter under ideal assumptions

$$\beta = \frac{2\mu_0 P}{B^2} \tag{2.45}$$

The plasma is referred to as a low-beta plasma for $\beta << 1$, where the magnetic field leads, and a high-beta plasma for $\beta > 1$, where the plasma leads.

The frozen-in theorem is a potent tool, as it allows one to understand the evolution of a magnetic field based solely on the motion of the solar wind and is responsible for the convection of structures in the Interplanetary Magnetic Field (IMF) by the solar wind. In turn, the violation of the frozen-in theorem allows the solar wind to drive magnetospheric convection by magnetic reconnection.

2.6 The Solar Wind

Sitting at the centre of our solar system is the Sun, a massive ball of hot gas continuously converting hydrogen into helium deep within its core, through the process of nuclear fusion. The by-product of this process is vast amounts of radiating energy

that photo-ionise surrounding matter into a plasma state and generates convection to carry the hot plasma to the Sun's uppermost layer, the corona. There, a percentage of the coronal plasma will become so energetic it is able to undergo supersonic expansion and breakout into the IPM. However, such is the strength of the solar magnetic field in combination with the highly ionised corona that both the subsonic and supersonic plasma is not uniformly distributed.

The electrically charged plasma of the corona is in constant motion, creating powerful local magnetic fields called coronal loops, rooted in the base of the Sun's atmosphere. Coronal loops are characteristically seen via sun spots, dark patches on the observable solar surface where the powerful local magnetic field obstructs convection and cools the surrounding corona. The plasma flows along the coronal loops due to frozen-in theorem, described in subsection 2.5.1. However, these loops cannot contain the plasma entirely, coronal loops pushed out to several solar radii can be pushed onwards by enhanced plasma pressure gradients, until they effectively burst into open field lines called coronal holes. High velocity plasma continues along the open field lines creating a continuous stream of highly conducting plasma consisting mainly of electrons, protons, and a small amount of heavier elements, into the IPM. This plasma is called the solar wind.

The solar wind is responsible for a range of phenomena. Interactions between the solar wind and terrestrial magnetosphere produce auroras, geomagnetic storms, and space weather. With other objects in our solar system similar effects occur. It extends beyond the planets in our solar system to its outer boundary, the heliopause, where the solar wind dynamic pressure balances against the dynamic pressure of the interstellar wind, a highly variable boundary of ~ 100 AU. The solar wind is a natural

consequence of stellar evolution and a solar wind is understood to be present in all solar systems.

The present day understanding of the solar wind has been achieved over decades of unravelling observations and measurements. In 1943, C. Hoffmeister observed a comet's tail and saw that its orientation was several degrees from the anti-sunward direction, indicting a medium carrying the ions at a finite speed. In 1951, L. Biermann concluded the lag was due to interactions with a solar wind. In 1957, Hannes Alfvén realised the solar wind is magnetised and that the magnetic field was draped over the comet by the solar wind, resulting in a long downstream tail. By 1958, E. W. Parker recognised that the fluid-like pressure-driven behaviour of the solar wind, whereby plasma thermal pressure gradients were able to overcome solar gravity, to produce supersonic outflows. To date much of the research into the solar wind has used MHD fluid descriptions of the solar wind, like those in section 2.5, though kinematic descriptions still play a role.

There exists a point, referred to as the Alfvén critical point, where the thermal pressure of the coronal plasma equals the solar gravitational and magnetic field forces. This critical point defines the boundary where the coronal plasma becomes the solar wind ($\sim$ 10 - 20 R_s, where R_s is the solar radius). The coronal environment and its tapestry of closed magnetic loops and coronal holes is in a continuous state of evolution throughout the solar activity cycle. This complex, ever shifting system, is what makes the solar wind such a dynamic medium.

2.6.1 The Parker Spiral

Within the distance to the critical point, the coronal plasma is a low-beta plasma, led by the coronal field lines which corotate with the Sun's 27 day period. Beyond, the now solar wind becomes a high-beta plasma, transitioning the plasma from field-dominated to flow-dominated. In the high-beta environment, due to the high conductivity of the solar wind, it is now the solar wind that leads the open field lines. The open magnetic field lines, now moving into the IPM, becomes know as the Interplanetary Magnetic Field, the IMF. Beyond this point the information carried in the solar wind flows outward, carrying the imprint of the plasma and magnetic field characteristics from the source regions in the corona.

With a single foot-point anchored to the rotating Sun and flowing outward with a constant velocity, the IMF lines bend to form an Archimedean spiral. This spiralling occurs much in the same way as happens with a garden sprinkler. As parcels of solar wind plasma are expelled they travel radially outwards from the source at a continuous velocity, as illustrated in Figure 2.2. As radial distance increases, the stream of plasma parcels must cover greater azimuthal distances. With no acceleration mechanism, the parcels maintain their azimuthal velocity and so lose their co-rotation positions with the Sun. Thus, like a jet of water from a sprinkler, the parcels take on the shape of a spiral, as illustrated in Figure 2.3, commonly termed the Parker Spiral (Parker, 1958). It is important to note that it is the IMF lines that create the distinctive Parker spiral arms, as it is pulled out by *sequential* solar wind parcels, as seen in Figure 2.2.

The Parker Spiral of Figure 2.3 can be defined mathematically. According to flux conservation, following polar coordinates (r, θ, φ), the radial magnetic field is given by Equation 2.46

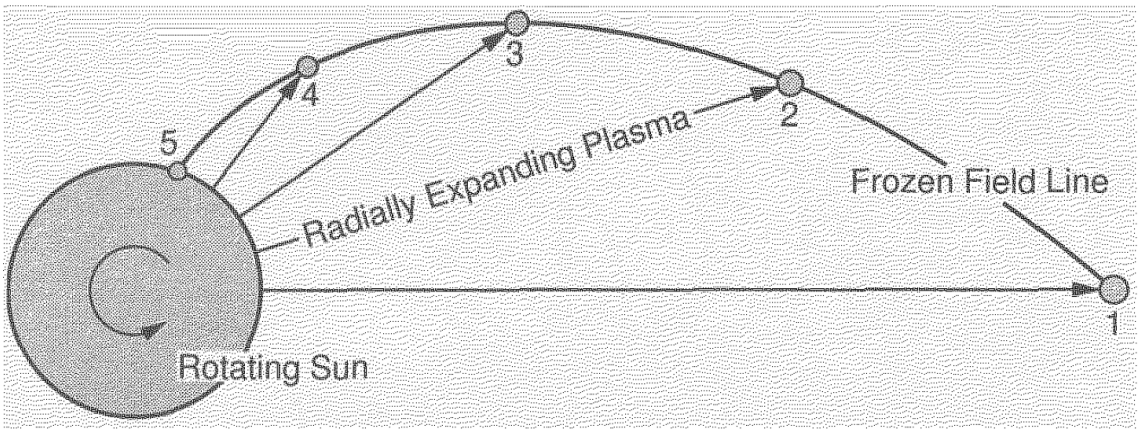

Figure 2.2: As the sun rotates, parcels of solar wind plasma are emitted with a roughly constant radial velocity. Due to frozen-in theorem, these parcels drage the IMF lines with them, creating distinctive spiral arms. Image credit: Baumjohann et al. (2012)

$$B_r = \pm B_0 \left(\frac{r_0}{r}\right)^2 \tag{2.46}$$

Assuming flux is in the ecliptic plane the latitude component of the magnetic field is given by

$$B_\theta = 0 \tag{2.47}$$

and solar rotation adds the longitudinal component

$$B_\varphi = -\frac{\omega r_0 B_r}{v_x}\left(\frac{r}{r_0}\right)\sin\theta \tag{2.48}$$

where 0 refers to the solar wind source surface, ω is the solar rotation rate, and v_x is the radial velocity. Magnetic field lines then take the form of Archimedean spirals:

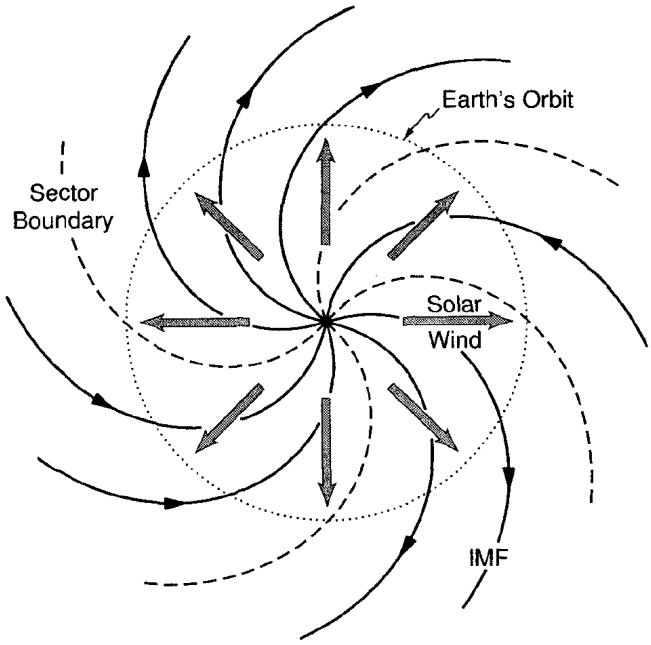

Figure 2.3: The Parker Spiral field in the ecliptic plane showing IMF lines under a solar wind velocity of $\sim$ 400 km·s^{-1}. At Earth's orbit, the angle of the IMF is $\sim 45°$ to the radial direction. At lower/higher solar wind velocities, the spiral arms will tighten/loosen. Sector boundaries represent the meeting points of opposing polarity regions of the IMF and hence net-zero magnetic field strength. Image credit: Baumjohann et al. (2012)

$$r - R = -\frac{v}{\omega \sin\theta}(\varphi - \varphi_0) \tag{2.49}$$

As illustrated in Figure 2.3, the spiral form does not take shape immediately as the plasma becomes high-beta. Beginning with emission from the solar corona, the IMF field lines are entirely radial, as they moves further into the IPM the radial component of the IMF continues to dominate at Mercury's orbit ($\sim$ 0.3 AU), upon arriving at

the Earth's orbit ($\sim$ 1 AU) the radial and azimuthal IMF components become equal, with the IMF line bending $\sim 45°$ from the radial direction, by the time the solar wind reaches Saturn's orbit ($\sim$ 10 AU) the IMF becomes almost entirely dominated by the azimuthal IMF component.

2.6.2 Properties of the Solar Wind

However, this picture is simplistic, assumes the solar wind has constant velocity ($\sim$ 400 km·s^{-1}) and lies entirely in the ecliptic. The configuration of the Parker spiral at any moment is dependent not only on radial distance but also latitude and solar wind velocity. At low helioaltitudes, the IMF is almost parallel to the ecliptic but this picture evolves the higher the emission. Solar wind speed affects a range of factors, the Earth's azimuthal velocity is approximately 30 km·s^{-1} and hence, the solar wind at typical speeds meets the Earth's magnetosphere at an angle of approximately 5° from the radial direction. However, at higher solar wind velocities this angle will become smaller, until it is almost entirely radial at speeds in excess of 1,000 km·s^{-1}.

Solar wind values vary across a range of time scales, showing variation across minutes, the solar rotation period ($\sim$ 27 days), and the solar cycle ($\sim$ 11 years). The solar cycle describes the evolution of the magnetic field as it changes polarity, roughly tracked by the number of sunspots on the solar surface. The magnetic field moves through an active (solar maxima) and slow (solar minima) phase which respectively relate to high/low quantities of coronal holes and plasma emission as illustrated in Figure 2.4. Magnetic polarities of active regions reverse from Northern to Southern hemispheres and vice versa during each cycle (Hathaway, 2015). Solar wind velocity and pressure, geomagnetic activity, solar flares, and coronal mass ejections all vary in

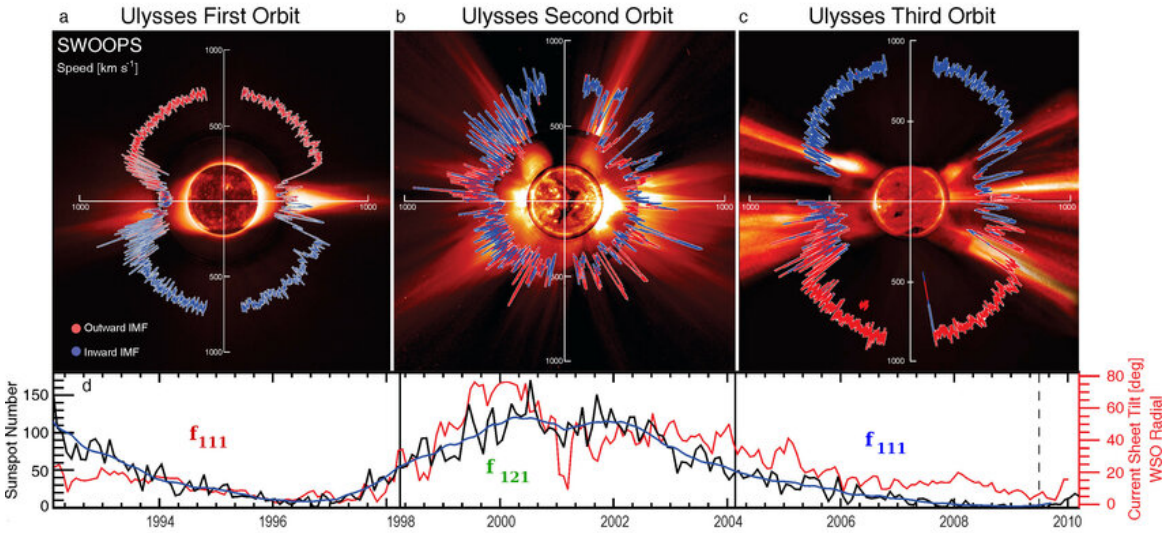

Figure 2.4: (a) - (c): Solar wind and IMF plots from Ulysses polar orbits in 1996, 2000, and 2006, during one solar cycle. The flybys clearly show the variability of the solar wind as the Sun's polarisation flips through the solar cycle. IMF is coloured blue and red to denote inward and outward IMF polarity respectively. (d) Evolution of the smoothed sunspot number (black) and current sheet tilt (red). The number of sunspots correlates with the evolution of the solar cycle through periods of solar maxima (b) and solar minima ((a), and (c)) Image credit: McComas et al. (2008).

line with the solar cycle.

The solar wind velocity, as measured at Earth, typically ranges from 300 - 800 km·s^{-1}, reaching maximum speeds in particularly active moments of up to 1,400 km·s^{-1}. Where solar wind velocities fall below 400 km·s^{-1}, they are deemed low-speed solar wind streams originating from the coronal hole boundaries where magnetic field polarity changes, whilst velocities exceeding 600 km·s^{-1} are deemed high-speed solar wind streams originating from the coronal hole centres. Sources for the fast and slow

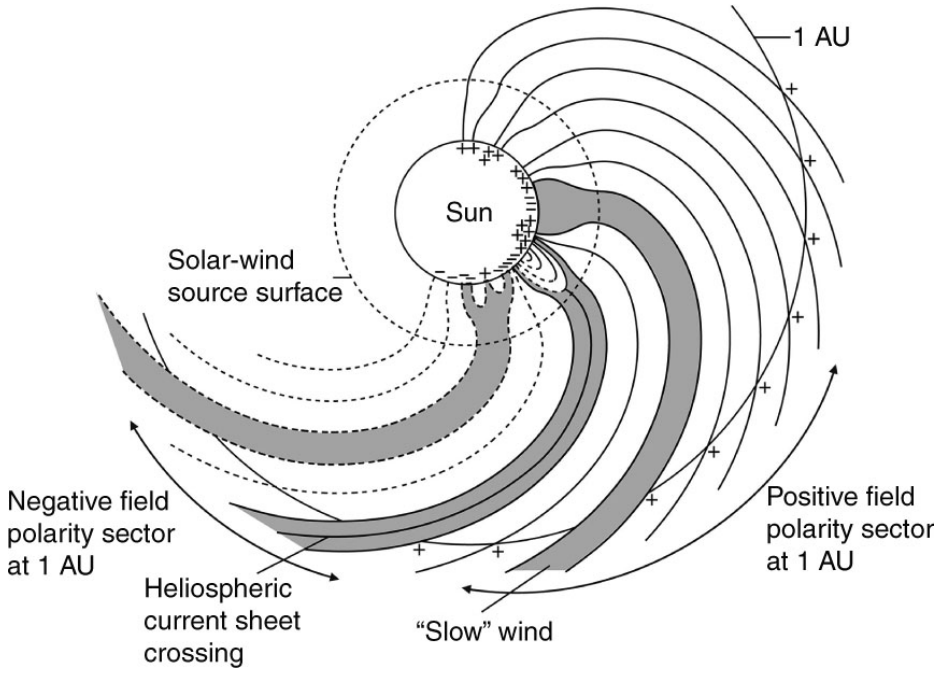

Figure 2.5: High-speed solar wind sources originate in coronal holes along open magnetic field lines. Slow-speed solar wind originates at the boundaries of coronal holes, where they push up against closed field lines and changing polarity of the magnetic field. + signs indicate positive (outward) magnetic field sources and - signs indicate negative (inward) field sources. Image credit: Russell et al. (2016).

solar winds are illustrated in Figure 2.5.

Near Earth, the solar wind has a typical solar wind density, $n_e \approx 5$ cm^{-3}, and a temperature, $T_e \approx 10^5$ K (1eV = 11600 K). The typical IMF strength is of the order of 5 nT. Solar wind velocity is well correlated with both the solar wind proton-temperature and proton-density. The relationship with temperature is fairly linear, with higher temperatures resulting from higher velocities. The relationship between velocity and density means the solar wind flux is near constant ($n_e v$). Therefore, when solar wind speeds are slow, they are generally dense, and when solar wind

speeds are fast, density typically rarefies. Throughout the IPM, with increasing radial distance the solar wind density decreases as $n(r) \propto r^{-2}$. Thus, as the velocity-temperature/density relationships indicate, as density decreases with radial distance, solar wind will gradually cool, as without an external mechanism of acceleration, the velocity cannot increase.

2.6.3 Corotating Interaction Regions

It is now understood that both high-speed and low-speed regions are present in the solar wind. Observation of Figure 2.6 shows the effects of a high-speed solar wind interaction with the ambient solar wind, known as a corotating interaction region (CIR) or stream interaction region if the fast stream is not corotating with the solar period. High-speed solar wind collides with the slower region ahead of it, causing a compression of the solar wind. This results in an intensification of the solar wind observations as illustrated in the Figure 2.6 . These interactions act to redistribute momentum, speeding up slow solar wind and slowing down fast solar wind. Naturally, these fast regions leave behind lower density, rarefied regions of solar wind. The effect of the compression is to homogenise the velocity distribution with increasing radial distance, though at 1 AU these regions are still observable. However, this effect of homogenisation will be relevant out to 10 AU (R_{Saturn}) when interpreting the use of solar wind propagation models in chapter 9.

2.6.4 Coronal Mass Ejections

Finally, we note the existence of Coronal Mass Ejections (CME). CMEs are unique, though not infrequent, events whereby volumes of plasma far larger than is typical for

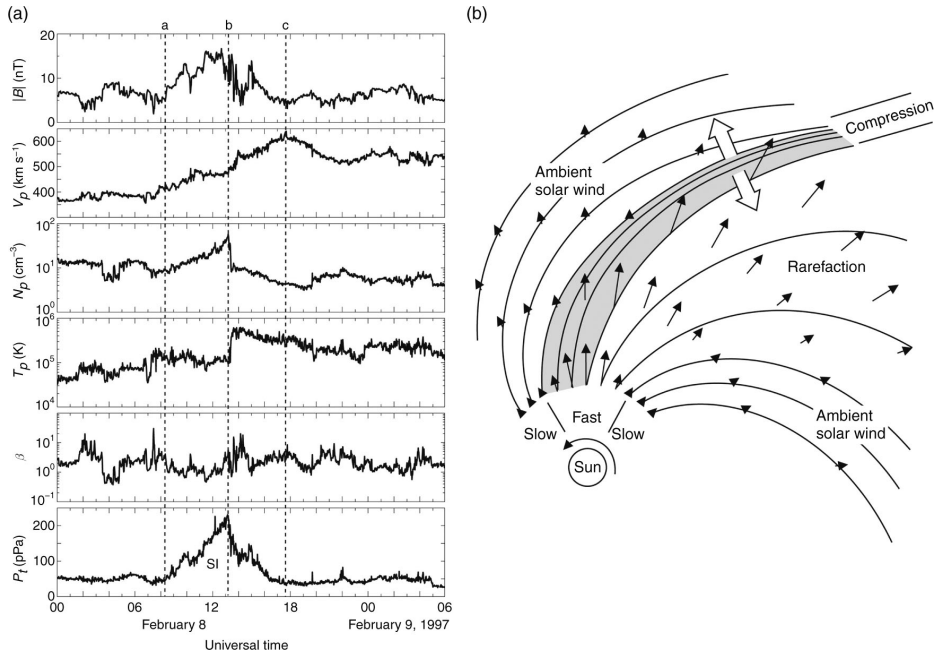

Figure 2.6: (a) Solar wind parameter observations, taken by the WIND spacecraft. The time-series data shows the presence of a compression region, where a fast solar wind stream interacts with the slow solar wind. The dotted lines *a*, *b*, and, *c* mark the beginning, peak, and end moments of the stream interaction, respectively. (b) An illustration of a CIR where a fast solar wind stream collides with the preceding slower wind stream. This interaction acts to produce a denser local region, whilst having the net long-term effect of homogenising the solar wind at large radial distances (several AU). Image credit: Russell et al. (2016).

the solar wind explode out into the IPM, where they are termed Interplanetary CME (ICME). The frequency of CME emission roughly follows the solar cycle. There are a variety of mechanisms that may cause CMEs but they possess the same structure: huge volumes of plasma with powerful magnetic fields free from the magnetic field of the Sun. Though CMEs can be emitted at up to 3,000 km$\cdot s^{-1}$, ICMEs typically

have velocities comparable to fast-solar wind streams. These powerful structures are known for causing intense interactions with planetary magnetospheres, responsible for increases in aurora, geomagnetic storms, and other space weather events.

2.7 Closing Remarks

Whilst there is an understanding of the processes at play, the complex dynamics of the corona and solar magnetic field mean the characteristics of the solar wind and IMF can take on a broad range of values. Without direct measurement of the solar wind via satellites or the measurements of its effects at the Earth's surface, one cannot know characteristics such as solar wind velocity and IMF orientation with a significant degree of accuracy.

In this opening chapter we have explored the necessary theory to understand the physical principles that underpin the behaviours of the solar wind and IMF relevant to this thesis. As has been made clear, this is by no means a comprehensive explanation of all things solar wind. Nevertheless, the reader should now have sufficient understanding of the behaviour of plasmas and magnetic fields: single particle motion, fluid behaviour, frozen-in theorem, and the origins and properties of the solar wind. We are now well equipped to move into the next chapter, exploring the magnetospheres of Earth and Saturn, and the interactions the solar wind and IMF have with them.

Chapter 3

Solar Wind: First Contact

Understanding the journey of the solar wind is only half the picture, the other half is to understand the interactions that occur once it reaches the planetary magnetospheres. Magnetospheres are powerful magnetic fields, generated by the internal dynamos of a planets core. In the case of the Earth, it is well understood that our planetary core is in a liquid state and composed of significant amounts of iron. This convection of conducting fluid (liquid iron) creates electrical currents which induce magnetic fields.

In this chapter, we continue to lay the foundations of this thesis, defining Earth's magnetosphere, its interactions with the solar wind, and the mechanisms that transport solar wind plasma throughout the magnetosphere, driving the magnetosphere dynamics responsible for a range of phenomena. A subset of these phenomena are then explained in depth: the Geomagnetic Indices, AL and SYM/H. We conclude our exploration of the terrestrial magnetosphere by investigating a range of coupling functions, empirically derived attempts to explain the solar wind-magnetosphere coupling mathematically, for given conditions.

Finally, we delve into the second magnetospheric system of interest to this thesis,

Saturn's. Focussing on what differentiates it from the terrestrial magnetosphere, its unique properties, and the phenomena caused by the solar wind-magnetosphere interactions. In depth, we explore Saturn Kilometric Radiation (SKR), a phenomena central to the questions behind the work of this thesis.

Except where other sources are listed, this chapter uses the works of "Space Physics An Introduction" by Russell et al. (2016) and "Basic Space Plasma Physics" by Baumjohann et al. (2012).

3.1 The Terrestrial Magnetosphere

When the solar wind reaches a body in the solar system, be this a comet, asteroid, moon or planet, it interacts with it. These interactions are particularly strong when the body is magnetised, like in the case of the Earth. The cavity carved out within the heliosphere in which the Earth's own magnetic field dominates over that of the surrounding IPM is termed the terrestrial magnetosphere. The size of the magnetosphere is in constant flux, determined by the opposing forces of its internal magnetic pressure against the sum of the IMF pressure and solar wind dynamic (which dominates) and thermal (kinetic) pressures.

As the solar wind, travelling at supersonic speeds impacts the Earth's dipolar magnetic field, a bow shock forms. This bow shock comes about because the solar wind cannot simply penetrate the magnetic field of the object; solar wind plasma particles are locked into the IMF lines which themselves cannot easily merge with the Earth's magnetic field due to frozen-in theorem (subsection 2.5.1). Consequently, the solar wind is slowed and the majority is deflected around the magnetosphere as

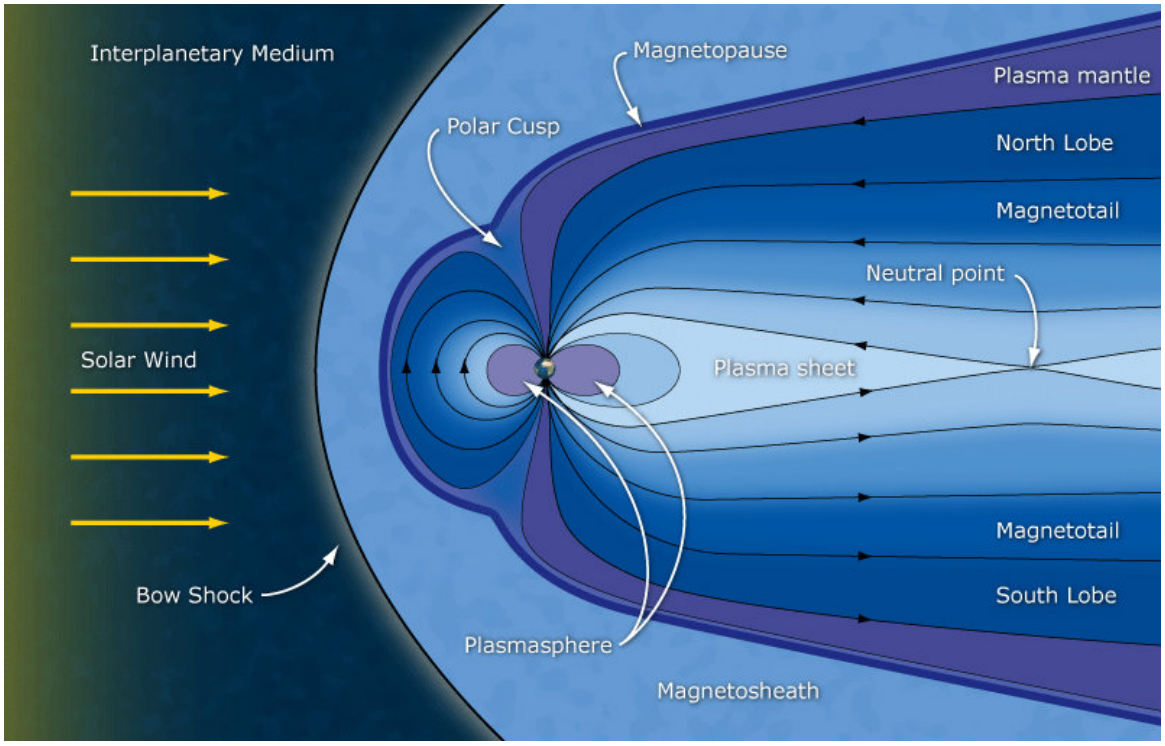

Figure 3.1: Topography of the solar-terrestrial Magnetosphere environment. Image credit: ESA (Updated)/Russell et al. (2016)

illustrated in Figure 3.1.

A large proportion of the solar wind particles, when the plasma is slowed down by the bow shock, have their kinetic energy converted into thermal energy. This region behind the bow shock is referred to as the magnetosheath and the sub-sonic solar wind here is denser and hotter, with a much stronger magnetic field strength. Further in is the magnetopause, a thin layer that defines the transition point between the objects magnetosphere and the magnetosheath (transition layers such as these are referred to as discontinuities). At the nose of the magnetopause (facing sunward) the solar wind dynamic pressure acts perpendicular to the magnetospheric field. Here the solar

wind dynamic pressure ($P_{dyn} = \rho v^2$) is at equilibrium with the magnetospheric field pressure ($P_B = B^2/2\mu_0$). Assuming the magnetic field is dipolar, it falls off at a rate of $B(r) = B_0/r^3$, then the stand-off distance, the distance of the magnetopause from the planets surface, r_{mp}, can be given as

$$r_{mp} = \left(\frac{2B_0^2}{\mu_0 \rho v^2} \right)^{\frac{1}{6}} \tag{3.1}$$

where B_0 is the magnetic field strength of the Earth at its surface, μ_0 is the permittivity of free space, ρ is the solar wind density, and v is the solar wind velocity.

The increase in pressure at the bow shock from the solar wind compresses the dayside (sunward) magnetosphere, limiting its expansion to a stand-off distance of $r_{mp} \approx 10$ R_E ahead of the Earth for average solar wind conditions. As the majority of the solar wind plasma is deflected around the magnetosphere, the nightside (anti-sunward) of the Earth's magnetosphere is elongated into the magnetotail.

The dayside magnetosphere consists of closed magnetic fields lines with both foot-points rooted in the magnetic poles. On the nightside, open magnetic field lines with one foot-point rooted in the Earth's magnetic poles form northern and southern lobes at the North pole and South pole, respectively. Separating these two regions is the plasma sheet, a region of warm dense plasma. These open magnetic field lines come together downtail, at the neutral point, where they can reconnect with one another. This neutral point can be as close as 10 R_E and as far as 60 R_E (the Lunar orbital radius).

At high latitudes from the equatorial magnetopause, as seen in Figure 3.1, there exists a transition point between the last dayside facing to the first tail ward facing magnetic field lines. A transition point exists in both the Northern and Southern

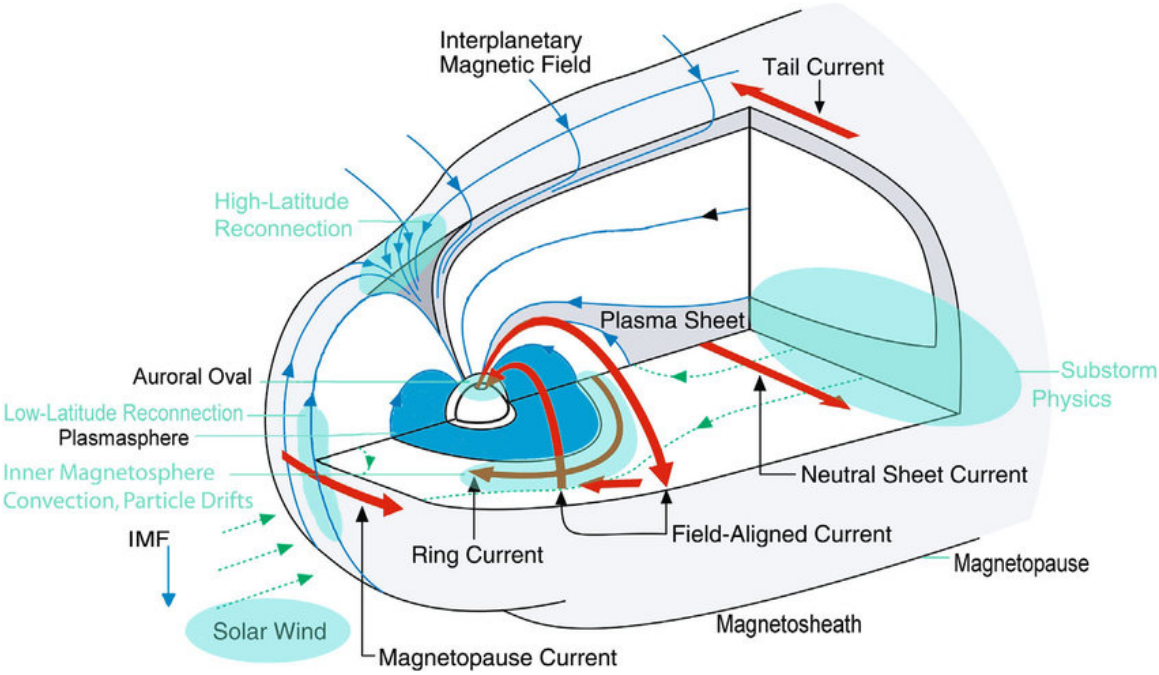

Figure 3.2: Topological diagram of the Earth's magnetosphere showing the major current systems (red), plasma regions (blue and grey) and physical processes (green). The Earth's magnetosphere dynamics move electrons and ions in opposing directions, generating the terrestrial current systems that drive plasma dynamics. Image credit: Kuijpers et al. (2016).

hemispheres and is referred to as the polar cusps. Their location is highly dependant on the solar wind conditions, sitting between 77° and 90° invariant latitude (Russell, 2000).

The polar cusps are one of the main points in which magnetosheath and magnetospheric plasma are able to directly access the ionosphere in addition to magnetic reconnection.

The dynamic magnetospheric system transports plasma around the magnetosphere

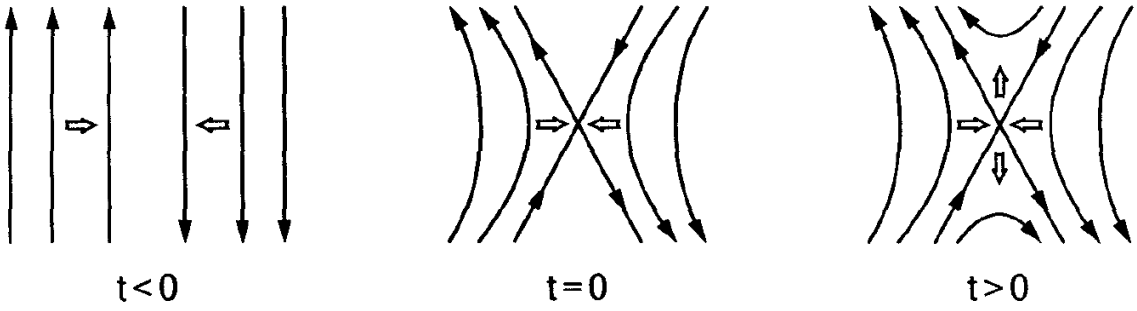

Figure 3.3: Magnetic Reconnection. Opposing field lines connect with one another in a distinct X shape. Image credit: Baumjohann et al. (2012).

and within. The motion of these electrically charged fluids then generates currents, which are defined in several distinct regions as illustrated in Figure 3.2.

3.1.1 Magnetic Reconnection

In the simplest description of a magnetosphere the solar wind struggles to penetrate the magnetosphere, due to the IMF lines being unable to connect with the field lines of the magnetosphere (Axford et al., 1961). However, this description of solar wind-magnetosphere recoupling is highly dependent on the direction of the IMF. Where the IMF line is anti-parallel to the Earth's magnetic field line orientation (southward vs northward pointing), magnetic reconnection can occur, whereby oppositely directed magnetic field lines within a plasma *break* and reconnect. When reconnection occurs at the magnetopause, momentum flux is transferred from the solar wind to the magnetosphere. In these conditions the magnetospheric plasma can then carry the added solar wind magnetic flux and plasma through the system.

Although the physics that allows magnetic reconnection are still poorly under-

stood, the process is illustrated Figure 3.3. Consider then anti-parallel magnetic field lines, frozen into moving plasma, as shown at time t<0. Such topologies exist around thin current sheets like the magnetopause and the tail neutral sheet. In the Earth's case this is a southward pointing IMF line meeting a northward pointing local magnetic field line from the Earth's magnetosphere.

At t=0, when the magnetic Reynolds number is greater than or equal to 1 (the solar wind magnetic Reynolds number is $\sim 7 \times 10^6$), the magnetic field may *vanish* due to diffusion at a particular point. Consequently, an X-type configuration occurs, with the magnetic field being zero at its centre, referred to as the magnetic neutral point.

Finally, at t>0, the field lines from the IMF and magnetosphere reconnect, composed of the respective upper and lower elements of the field lines prior to the point of reconnection and move in a perpendicular direction to their original path of motion. At this moment of reconnection, due to violation of the frozen-in theorem, plasma is able to move from the IMF to the magnetosphere. It should be understood that magnetic reconnection does not occur at a single point but along a line approximately perpendicular to the Earth's Dipoles.

3.1.1.1 Dungey Cycle

This principle of reconnection forms an integral part of the Dungey cycle, first proposed by James Dungey in 1961 (Dungey, 1961). Observing Figure 3.4, the southward pointing IMF line undergoes magnetic reconnection with a northward directed terrestrial field line on the dayside of the magnetosphere, creating two open field lines. Each of these field lines has a foot-point in the Earth, with the other

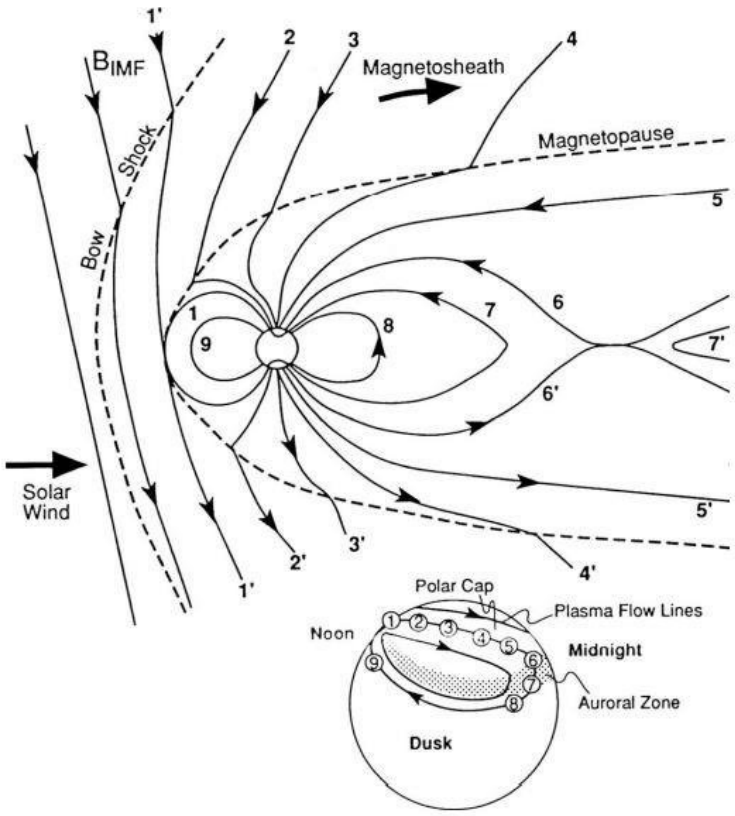

Figure 3.4: The Dungey Cycle. (1',1) Southward IMF lines connect with northward terrestrial field lines (2) producing two open field lines. (2 - 5) Open fields lines are dragged poleward, to the magnetotail, carrying solar wind plasma with them. (6) Where magnetic reconnection occurs in the plasma sheet (centre of the magnetotail), plasma continues to flow along the field lines which travel in opposing directions. (7') The open IMF lines carry plasma away from the Earth and into the heliosphere, (7) whilst the closed terrestrial field line carries plasma into the Earth. (8-9) Where able, the field lines travel around to the dayside, where the cycle can reoccur. Image bottom: Illustration of the anti-sunward flow of plasma across the polar cap and sunward return at lower latitudes. Image credit: Russell et al. (2016).

ends extending into the IMF. These open field lines travel tailward, with the IMF component pulled by the solar wind and the magnetospheric component pulled by magnetic tension. These field lines travel across the hemispheres to the nightside of the planet where they are stretched by the pull of the solar wind to form the magnetotail. During this period of travel, solar wind plasma can travel freely along the open IMF lines into Earth's magnetosphere at the polar cusp. At the magnetotail neutral point, these two field lines reconnect to form both an open solar wind field line that will continue to move down-tail of the magnetosphere, and a closed field line that will draw itself back into the Earth, due to magnetic tension. The latter closed field line will, under equilibrium conditions, move back to the dayside of the magnetosphere, all the while allowing the transport of plasma further into the Earth's magnetospheric environment. Returning to the dayside, the process of magnetic reconnection can reoccur whilst conditions allow.

Due to the violation of the frozen-in theorem, magnetic reconnection acts as point of entry for plasma to within the magnetosphere, which can flow along the new field lines. Whether these be the open field lines formed at the magnetopause, each with foot-points in the Earth, or the now closed terrestrial field line that draws itself back in towards the Earth at the magnetotail. Whilst the descriptions given above describe reconnection at the dayside magnetopause for a southward directed IMF, reconnection can occur in other ways. For example, reconnection can occur at any point where the magnetic field lines are anti-parallel; at higher latitudes than the polar cusp, a northward pointing IMF line can reconnect, which can lead to displacements of the cusp's location.

It is these moments of magnetic reconnection that allow plasma to enter and

populate regions of the magnetosphere; feeding energy into the magnetosphere and driving its dynamics, like auroras and magnetospheric substorms. A more complete image of this system is illustrated in Figure 3.2.

The plasma within the Earth's magnetosphere is not evenly distributed, different regions have significant variations in temperature and density between one another. These include regions such as the radiation belt, a region within a few Earth radii where electrons and ions oscillate between hemispheres along dipolar magnetic field lines, the plasmasphere, and the plasma sheet (see Figure 3.1). Magnetotail plasma is primarily concentrated in the tail mid-plane, where the plasma sheet has a thickness of approximately 10 R_E. Along field lines this plasma can reach the high-latitude auroral ionosphere, an important region for this study, producing auroral electrojets.

3.1.2 Magnetospheric Currents

As is now self-evident, plasmas are not stationery gases but are dynamic, evolving environments under the presence of external forces. Subsequently, when ions and electrons move in opposing directions, electric currents are created. The Dungey cycle, driving the dynamic magnetospheric environment and pressing solar plasma into the Earth's magnetosphere, via reconnection, results in such an opposition of charged particles, creating electric currents (see Figure 3.2). These current systems are the drivers of the plasma environment within the Earth's magnetosphere, they carry charge, mass, momentum, and energy.

One such system is the *ring current*, flowing westward at a distance of several Earth radii. This system is generated by energetic particles, trapped on circularly closed magnetic field lines, forming the radiation belts. These radiation belt particles slowly

drift around the Earth in addition to oscillating between hemispheres. Crucially, where there are currents magnetic fields are created, which will subsequently interact with and distort the local magnetic field.

3.2 Geomagnetic Indices

Solar activity intensity is variable and affects the dynamics of the Earth's magnetospheric system. This activity can have a broad range of effects, from the captivating production of auroras through to catastrophic disruption of a range of technologies. For example, variations in the perturbation fields generated by magnetospheric currents can affect navigation systems, or create a build up of geomagnetically induced currents that can lead to the malfunctioning of power transformers and telegraph lines. It is therefore self-evident why having a clear indicator of solar activity is crucial.

Fortunately, geomagnetic indices are well known as proxies for the solar wind and IMF conditions. Using ground-based magnetometers, geomagnetic indices quantify disturbed states of the Earth's plasma environment. They are measures of the effects of fluctuations in the geomagnetic field caused by changes in the upstream solar wind and IMF observed through effects such as the modification of ionospheric, ring, and magnetospheric currents, and production of auroral particles. These fluctuations are triggered by two primary methods, substorms and geomagnetic storms.

Substorms are global reconfiguration events caused by rapid plasma loading due to magnetic tail reconnection. When dayside reconnection is enhanced, due to a southward turning of the IMF, the plasma flux increases due to enhanced reconnection. Plasma is transported to the tail, where some is carried back to the dayside following

reconnection and convection. However, the rate of magnetotail reconnection is often unequal to the dayside reconnection rate, it only required that they are equal as an average over time. Thus, when magnetotail reconnection is less frequent, field lines and plasma build up in the northern and southern lobes, referred to as the *substorm growth phase*. When the magnetic flux density becomes sufficiently high, tail reconnection occurs rapidly, releasing the stored magnetic energy and injecting equally large volumes of energetic plasma into the near-Earth environment. The sudden magnetic convection is focused primarily in the polar regions, generating aurora and enhancement of the ionospheric and magnetospheric currents, this is referred to as the *substorm onset and expansion phase*. After sufficient release of the stored up magnetic energy, reconnection decreases and substorm activity lowers, referred to as the *substorm recovery phase*.

Geomagnetic storms occur when fast moving solar wind from two primary sources, ICMEs and the shocked and compressed regions of the solar wind due to CIRs, intensifies solar wind-magnetosphere coupling. Large numbers of particles are injected from the magnetotail into the ring current, primarily caused by strong dawn-dusk electric fields when the southward directed IMF passes the Earth for sufficient time. Particle injection induces strong intensification of the magnetic disturbance fields at low-mid latitudes and also generates aurora at high-latitudes.

In this thesis, we will focus on two geomagnetic indices, the AL and SYM/H indices. Figure 3.5 illustrates the solar-interplanetary-magnetosphere coupling with the main magnetospheric dissipation mechanisms, substorms and geomagnetic storms, along with the basic role of the magnetosphere dynamo in magnetospheric energization. In region 1, auroral dissipation occurs at high latitudes (Davis et al.,

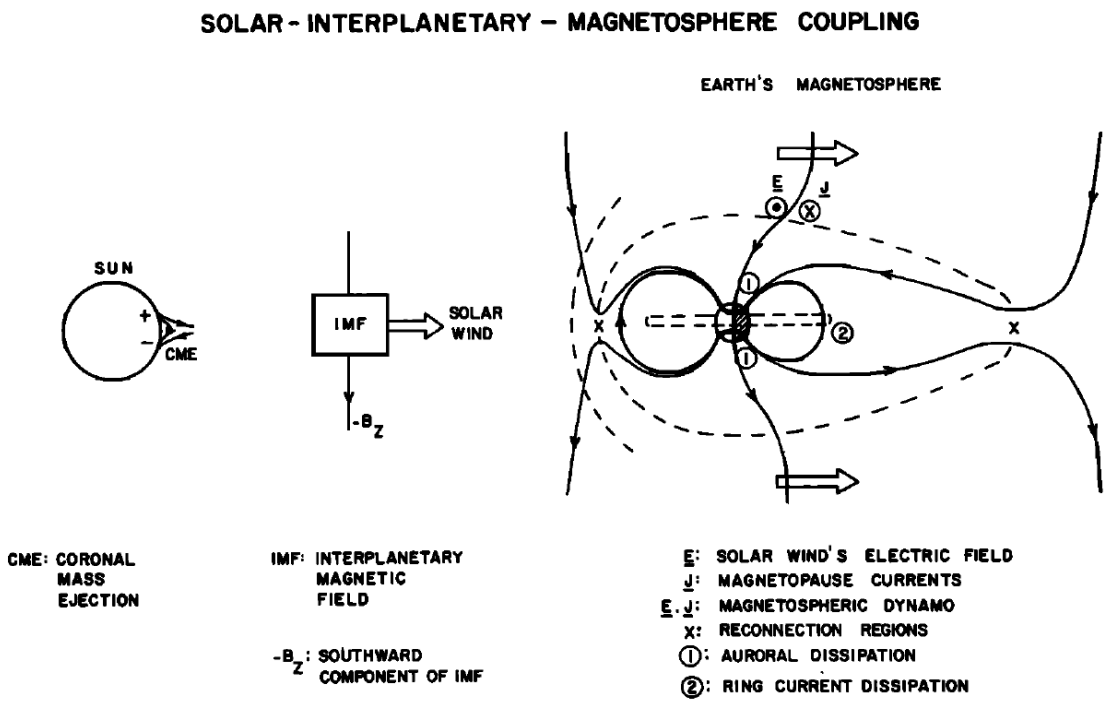

Figure 3.5: A CME releases energetic plasma carrying frozen-in IMF lines, which travel radially outward through the IPM. Through the Dungey cycle, plasma is drawn into the Earth's magnetosphere where plasma can be introduced to (1) the auroral oval and (2) the ring current. Image Credit: Gonzalez et al. (1994).

1966) and is where the AL index is observed, whilst region 2, ring current dissipation at mid-low latitudes (Iyemori, 1990), is where the SYM/H index is observed. Continuing through subsection 3.2.1 and subsection 3.2.2 the reader should refer back to Figure 3.6, displaying the onset of a geomagnetic storm and the associated effect of the strengths of the IMF and solar wind parameters, alongside the consequent AL and SYM/H indices, representing the high latitude auroral disturbance and low-mid latitude magnetic field intensification/disturbance.

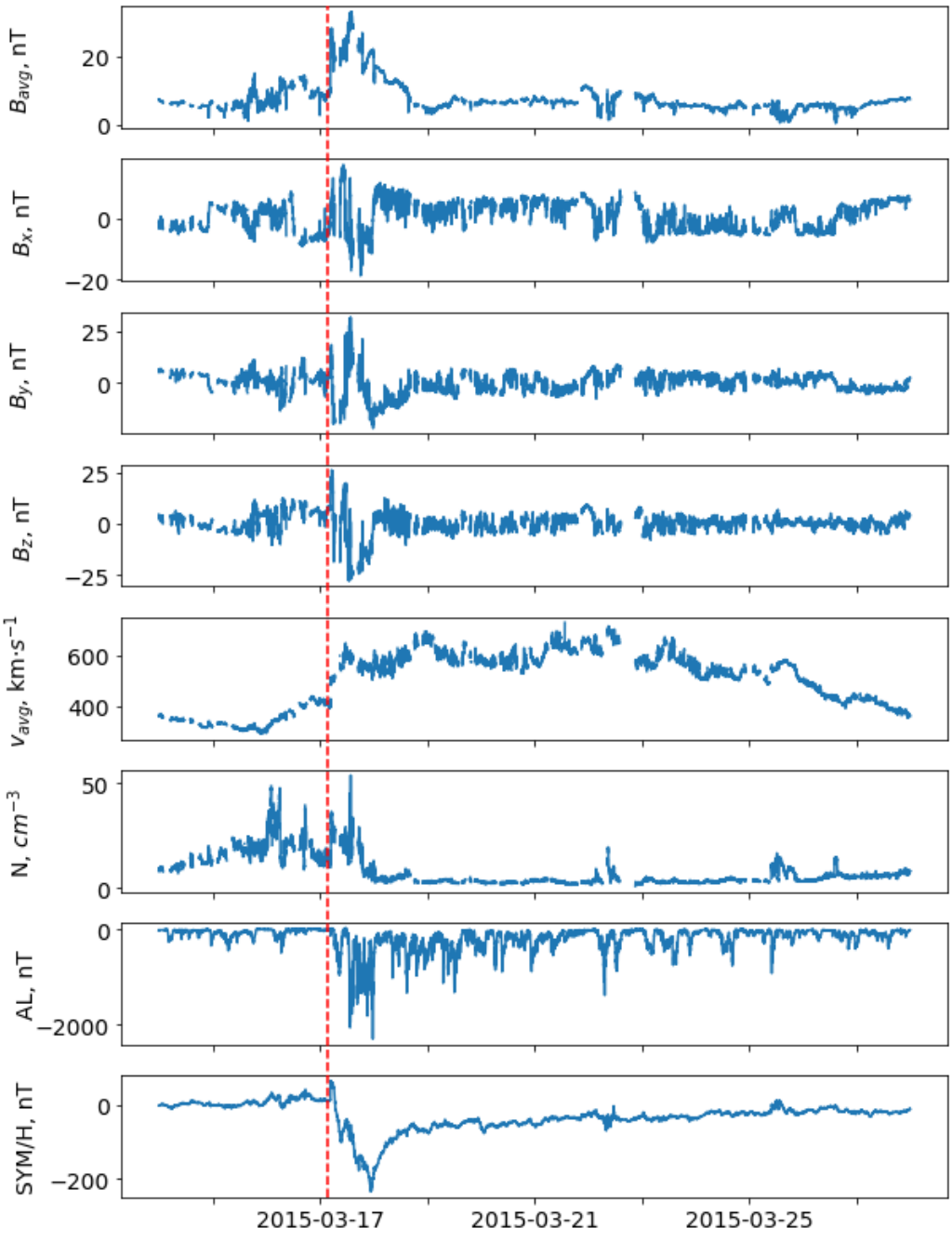

Figure 3.6: Geomagnetic storm event occurring on 17th March 2015. Caption continues on the following page.

Figure 3.6: Red dashed line indicates the onset of the geomagnetic storm. Variables in descending order are solar wind average magnetic field, B_{avg}, in GSE/GSM coordinates; the solar wind magnetic field components, B_x, B_y, and B_z, in GSE coordinates; average solar wind velocity, v_{avg}; proton density, N; AL Index, AL; and SYM/H Index, SYM/H. The onset of the geomagnetic storm triggers the intensification of the low-mid latitude magnetic field intensification, seen in the SYM/H index, as well as an increase in auroral disturbances as particles are carried into the high latitude regions, seen in the AL index. Data taken from the OMNI database for the period of March 14th to March 28th (Papitashvili et al., 2020).

3.2.1 AL Index

Along the terrestrial magnetic field lines, plasma sheet electrons are able to precipitate down into the ionosphere. There, they are able to interact with and ionise the neutral atoms which release energetic photons. These photons produce the distinct light and colours seen in the auroras encircling the magnetic poles, where colours correspond to the binding energy of the atomic element.

First introduced in 1966 by Davis et al. (1966), auroral electrojets are the most prominent high-latitude current flows, concentrated within the auroral oval and are widely used as indicators of auroral activity. The auroral oval, with a centre approximately 5° off-centre from the geomagnetic pole and a varying radius dependent on ring current intensification during geomagnetic storms (Milan, Hutchinson, et al., 2009), contains foot-points of terrestrial field lines that pass through the plasma sheet, Figure 3.7a. Electrons and ions, precipitating from along the magnetic field into the atmosphere, ionise neutral atoms and molecules, which in turn enhances ionospheric

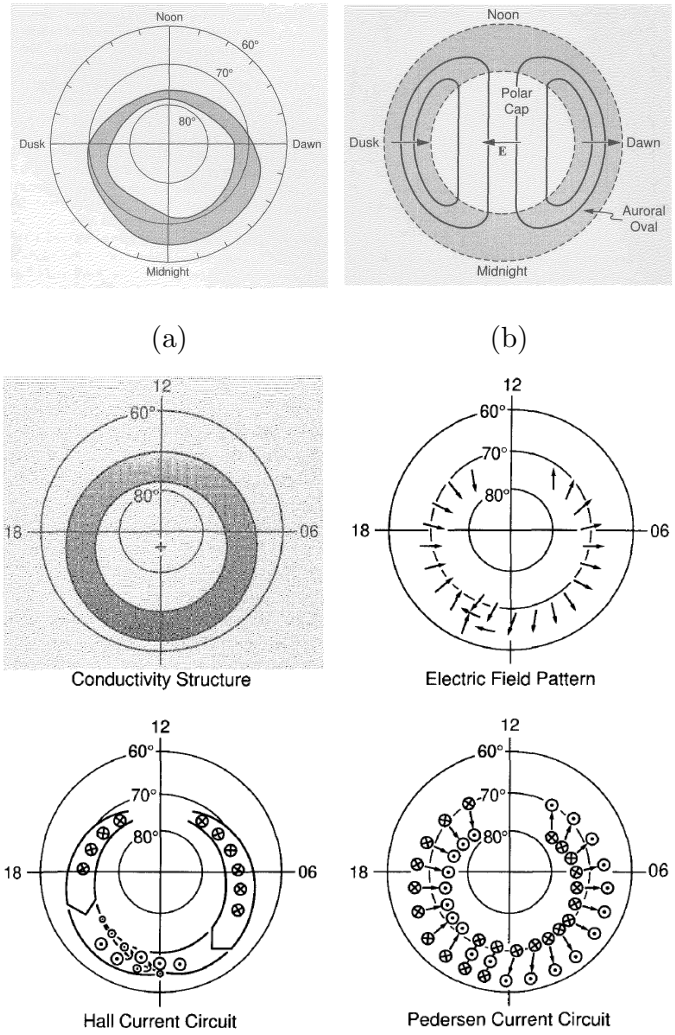

Figure 3.7: (a) Auroral oval (b) Equipotential contours of the high-latitude electric field. (c) Auroral Electrojet components. Image credits: Baumjohann et al. (2012)

conductivity. The time-sectors the particles precipitate to are a function of their energy and pitch-angle. As discussed in section 2.2, the energy (velocity) and pitch angle determine the rate and path of particle motion about a magnetic field line.

Significant plasma loading from magnetic tail reconnection and substorms allows the plasma to dominate in the nightside of the auroral oval. In addition, a small amount of plasma will be able to travel via the polar cusp during transit from dayside to nightside (and back around). This distribution is then reflected in the conductivity structure that arises from ionisation, Figure 3.7c.

Within the auroral oval, large-scale magnetospheric plasma convection is reflected in the electric field pattern, Figure 3.7c. This convection pattern has two distinct cells, caused by the transport of open and closed flux tubes, a simplified version of which is illustrated in Figure 3.7b. This auroral zone electric field, reflecting the two zone plasma convection, is poleward directed in the afternoon and early evening sectors and points anti-poleward towards the equator in post-midnight and morning sectors. The electric field rotates westward, moving from poleward (North) to anti-poleward (South) in the pre-midnight sector (Davis et al. (1966); Baumjohann et al. (2012)).

Auroral electrojets have Universal Time (UT) dependence and feature seasonal, annual, and solar cycle variations (Davis et al. (1966); Li et al. (2007); Luo et al. (2013)). With a total current of 10^6 A, they are of an equivalent order of magnitude as the ring current. However, these electrojets are much closer at 100 km above the Earth's surface, thus creating the largest ground magnetic disturbances of all current systems in the Earth's environment, with magnitudes of 100 - 1,000 nT and up to 3,000 nT during intense magnetic storms (Baumjohann et al., 2012). Models from Li et al. (2007) show that not only is it the IMF direction that controls the magnetospheric activity that produces the AL index but that solar wind velocity plays a role too.

Westward (and eastward) electrojets are primarily Hall currents but are also composed of Pedersen currents. They originate at the dayside and are fed by

downward field aligned currents. Westward electrojets flow from the morning and midnight sectors, extending to the evening sector along the poleward border of the auroral oval and diverges as upward field aligned currents, see *Hall* and *Pedersen* Current Circuits, Figure 3.7c. The most intense electrojet currents are found on the midnight side of the dawn dusk boundary (Davis et al., 1966).

The AL and AU indices are measures of the strongest current intensities of the westward and eastward auroral electrojets, respectively. These indices are measured by a series of magnetometers in the auroral zone and are the Northward (H) component of the magnetic field, where AL and AU are measures of the negative and positive H component (Davis et al., 1966). For completeness of the indices, the AE auroral electrojet index is the difference of the AL and AU indices, $AE = AU - AL$, and represents the overall activity of the electrojets (Davis et al., 1966), derivation of the indices can be found at WDC for Geomagnetism (2005). Intensification of the AL index during a geomagnetic storm can be observed in the data of Figure 3.6.

Although both indices may be candidates, the AL index, as the westward electrojet current, has been chosen for this work. It is known to have little UT dependence, whereas the AU index has seasonal time variations. The AL index is also known to contain significant contributions from directly driven and substorm expansion phase activity. As discussed in chapter 7, Bargatze, Baker, et al. (1985) demonstrates two distinct peaks for the AL index relation with the solar wind. The first is a symmetrical response for the AL and AU indices as a result of enhanced convection. However, the second response (due to tail reconnection) is greater in the AL index due to the enhanced current of the westward electrojet. Furthermore, Li et al. (2007) states that the AL and AU indices should be considered separate time series for all scientific

studies. For these reasons we do not consider the AL and AU indices solely as two-sides of the same coin and that the AL index is more suited as a proxy to show the measure of the solar wind relationship than its counterpart. However, this is not to say that further work to investigate the AU index is without merit, as demonstrated in Petrukovich et al. (2005), the AU index is more sensitive to dynamic pressure enhancements of the solar wind, whereas the AL index finds this to be of secondary importance, more affected by the solar wind velocity.

3.2.2 SYM/H Index

As already discussed, charged particles undergo azimuthal drift within the magnetosphere and in the right conditions generate magnetospheric currents, section 2.4.

During geomagnetic storms, an initial, rapid increase in the horizontal (H) component of the magnetic field occurs due to a preceeding ICME or CIR shock front compressing the magnetosphere. This is then followed by the arrival of the ICME or CIR, which stimulates higher rates of reconnection, due to enhanced rates of southward pointing magnetic fields, feeding energetic plasma into the magnetosphere and thus inflating it. During this intensification, the solar wind conditions drive enhancements in the dusk-ward convection electric field, increasing particle injection from the magnetotail into the inner magnetosphere. As the particles enter the inner magnetosphere, electrons drift in an easterly direction whilst protons drift in a westerly direction. The opposing motion of the particles forms a current around the Earth referred to as the ring current. Consequently, the ring current strength and associated magnetic disturbance field increase which results in a decrease of the H component of the geomagnetic field. This increase in energy within the magnetosphere

will then gradually dissipate and the electric field returns to a normal strength, whereby charge exchange and pitch-angle scattering release electrons and ions from the ring current. Thus, the H component of the geomagnetic field returns to normal strength.

The mid/low latitude SYMmetric H (SYM/H) index represents changes of the H component of the equatorial magnetospheric ring current intensity during said storms (Wanliss et al. (2006); Cai et al. (2009), Bhaskar et al. (2019)). The cycle described, generating the SYM/H index, can be observed in the data of Figure 3.6, showing the onset of a geomagnetic storm.

3.3 Coupling Functions

The complexity of the magnetospheric system, with dynamic plasma environments, evolving magnetic fields, and multiple currents flows, operating on varying scales, makes it possible to characterise the system in multiple ways. Through magnetic reconnection, solar wind energy is input into the magnetosphere, which spreads into the many different environments, e.g. thorough auroral precipitation, ring current injection, and ionospheric heating. From first principles, these different energy systems are difficult to measure (Milan, Gosling, et al., 2012). Hence, for over a century, the default means of measuring magnetospheric activity has been thorough geomagnetic indices, such as AL and SYM/H, using ground based magnetometers. However, in the past few decades satellites have made available data sets of comparable continuity and longevity. Although they do not combine the high-resolution, global scope, and continuous daily coverage that magnetic indices do, they do help overcome

a number of uncertainties associated with the measurement of geomagnetic indices (Newell et al., 2007).

Historically, solar wind velocity, density, and pressure have been investigated as drivers for magnetosphere and ionosphere activity. However, after a multitude of studies, these were determined to be insufficient indicators on their own. After it had been determined that the IMF was continual and variable, Dungey (1961) put forward the B_z component of the IMF and magnetic reconnection as worthy of investigation, a cycle now well known to be the primary driver of terrestrial magnetosphere dynamics. Newell et al. (2007) and other investigations have determined that the B_z component is a much better indicator of magnetosphere dynamics than the aforementioned solar wind parameters but that this only accounted for a fraction of the variation in the magnetosphere dynamics.

As such, many attempts have been made to characterise the solar wind-magnetosphere coupling with the use of *coupling functions*, first proposed in 1974 by Perreault and Akasofu (1978). Combining parameters of the solar wind and IMF, coupling functions are used to try and better describe terrestrial space weather indices (Lockwood et al., 2021). A particular focus in the community has been on describing the solar wind electric field. The goal then, is to find a simple coupling function that best describes a range of indices, which could reveal much about the coupling of the solar wind with the magnetosphere (Newell et al., 2007).

Typically, coupling functions will combine solar wind and IMF parameters, such as: the magnetic field strength, B_z, the transverse magnetic field strength, B_{YZ}, solar wind speed, v, solar wind mass density, ρ, solar wind number density, N, and to allow for the orientation of the IMF, the clock angle, θ_c (Equation 3.7). Coupling function

equations are typically of the form

$$CF = \Lambda n^{\alpha} v_x^{\beta} B_{YZ}^{\gamma} \sin^{\delta} \frac{\theta_c}{2} \tag{3.2}$$

where Λ, α, β, γ, and δ are constants derived empirically by fitting the equation to the observed data considered.

3.3.1 Coordinate Systems

There are two coordinate systems used in this work when considering the IMF and solar wind data. The first is the Geocentric Solar Magnetospheric (GSM) frame of reference, which defines the x-axis pointing from the Earth to the Sun, and the z-axis is perpendicular to the x-axis and aligned with the Earth's northern magnetic dipole so that the x-z plane contains the dipole axis. The y-axis is then perpendicular to the x-z plane. This frame of reference is often used for defining the clock angle, θ_c, introduced in Equation 3.7, and the convention is followed in this work when solving coupling functions, see subsection 3.3.2.

Other data used in this thesis is given in the Geocentric Solar Ecliptic (GSE) frame of reference. The GSM frame of reference matches the coordinate reference frame of the solar wind MHD propagation model by Tao et al. (2005). GSE differs from GSM by a rotation about the x-axis. GSE defines the y-axis as perpendicular to the x-axis in the ecliptic plane, pointing dusk-ward. The z-axis is then defined as parallel to the ecliptic pole. Taking the magnetic field components (B_x, B_y, B_z) as an example, transformation between the GSM to GSE coordinate systems is of the form

$$\begin{bmatrix} 1 & 0 & 0 \\ 0 & \cos\theta & -\sin\theta \\ 0 & \sin\theta & \cos\theta \end{bmatrix} \times \begin{bmatrix} B_x \\ B_y \\ B_z \end{bmatrix}_{GSM} = \begin{bmatrix} B_x \\ B_y \\ B_z \end{bmatrix}_{GSE} \tag{3.3}$$

where θ is the angle between the GSE z-axis and projection of the magnetic dipole axis on the GSE yz-axis (GSM z-axis).

3.3.2 Coupling Functions Considered

Data used to calculate the coupling functions is taken from the OMNI database (Papitashvili et al., 2020), see subsection 4.1.2. Here, parameters are first defined that must be solved using the solar wind and IMF parameters taken from the OMNI database. Secondly, a selection of the most popular and commonly used coupling functions are included for investigation with the application of mutual information.

The solar wind speed, v, is defined as

$$v^2 = v_x^2 + v_y^2 + v_z^2 \tag{3.4}$$

where x, y, and z are the corresponding components of the GSE coordinate system. The IMF strength, B, is defined as

$$B^2 = B_x^2 + B_y^2 + B_z^2 \tag{3.5}$$

and the transverse component of the IMF, B_{YZ}, is defined as

$$B_{YZ}^2 = B_y^2 + B_z^2 \tag{3.6}$$

The clock angle, θ_c, the angle of the IMF vector projected into the Y-Z plane, is a parameter of the IMF with orientation perpendicular to the Sun-Earth line, and thus a factor that allows for the orientation of the IMF in the GSM frame of reference, Lockwood et al. (2021). It is composed of the azimuthal and polar components of the IMF (B_y and B_z). The clock angle is defined as

$$\theta_c = \arctan 2(B_y, B_z) \tag{3.7}$$

θ_c can be used to indicate the magnetosphere dynamics in a number of ways. During periods of geomagnetic activity, the altered distribution of field-aligned currents and the acceleration of particles can be related to θ_c. When the θ_c is large, it indicates explicit dawn-dusk asymmetry of the open-closed boundary at the polar cap. θ_c also affects dayside reconnection at the magnetopause and consequently magnetosphere-ionosphere system convection (Zhang et al., 2019).

The Akasofu Parameter, ϵ, is one of the earliest coupling functions and measures the variation of the Poynting flux (energy input) into the terrestrial magnetosphere. It is able to reasonably predict the growth and decay of substorms and geomagnetic storms by correlating with the Dst (low resolution SYM/H) and AE indices. Though originally defined in non-SI units, the Akasofu parameter of Perreault and Akasofu (1978) is defined in SI as

$$\epsilon = vB^2 \sin^4\left(\frac{\theta_c}{2}\right) \tag{3.8}$$

The Kan and Lee electric field, E_{KL}, is a measure of the power delivered by the solar wind dynamo to the open magnetosphere through field line reconnection. It is defined by Kan et al. (1979) as

$$E_{KL} = vB_{YZ} \sin^2 \left(\frac{\theta_c}{2} \right) \tag{3.9}$$

The calculated power is approximately proportional to ϵ (the Akasofu parameter given by Equation 3.8) correlation with AE, reinforcing the powering of geomagnetic activity by the solar wind dynamo.

Finally, the dayside magnetopause reconnection rate, Φ_D, measures the rate of coupling of the energy from the solar wind into the magnetosphere. It is defined by Milan, Gosling, et al. (2012) as

$$\Phi_D = \Lambda v_X^{4/3} B_{YZ} \sin^{9/2} \left(\frac{\theta_c}{2} \right) \tag{3.10}$$

where Λ is a constant of 3.3×10^5 $\mathrm{m}^{1/3}$ $\mathrm{s}^{1/3}$.

3.4 The Saturnian Magnetosphere

Except where other sources are listed, this section uses the works of "Saturn in the 21st Century" by Baines et al. (2018).

Saturn has the second largest magnetosphere in the solar system and whilst its configuration is broadly similar to that of the Earth's, it is far more complex. Unlike the Earth, Saturn's magnetosphere dipole axis uniquely aligns with its rotational axis.

Three distinct magnetospheric layers exist within the system, an inner, middle, and outer magnetosphere, as shown in Figure 3.8. The inner magnetosphere contains Enceladus, the radiation belts, and Saturn's rings. The middle magnetosphere contains the neutral torus, the inner plasma torus, where charged particles drift in opposite directions around Saturn, and the plasma sheet (magnetodisk), where

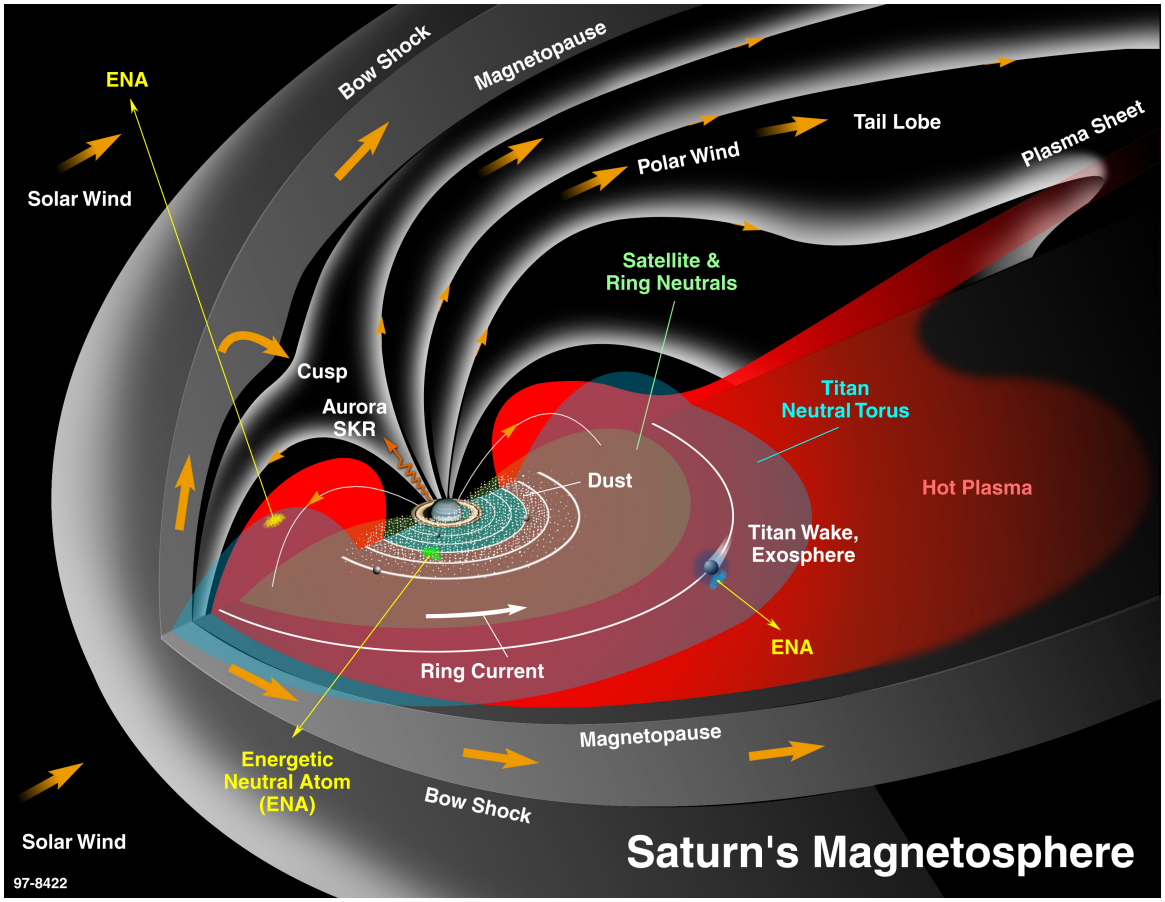

Figure 3.8: Detailed illustration of the Saturnian magnetosphere. Comparing with Figure 3.1, many similarities can be seen with the terrestrial magnetosphere. A bow shock and magnetopause exist due to solar wind interactions and a long stretching tail is present. However this tail is generated not only by magnetic tension but due to rotational driving. Differences are also present, such as energetic neutral atoms (ENA), generated by the moons inside the magnetosphere. The outer magnetosphere contains hot plasma (shown in red). Image Credit: Krimigis et al. (2004).

the magnetic field moves from a dipolar to disk like form. Finally, the outer magnetosphere, beyond the orbit of Titan, features highly stretched field lines,

especially in the generation of the magnetotail as a combination of the rotational driving of Saturn's rotation and magnetic tension (drag) of the solar wind.

Saturn's magnetosphere is rotationally dominated, with charged particles co-rotating out to the magnetopause. Internally sourced neutrals and plasma are driven out radially by the centrifugal force due to their fast rotation. This rotational driving is a significant source of plasma loss. As mass-loaded, frozen-in field lines are stretched, an equatorial plasma sheet forms in the middle magnetosphere. Continuous mass loading to the field lines further stretches the lines until downstream magnetic reconnection occurs, where the plasmas are released and flow tailward along the open, frozen-in, IMF lines. This process of plasma loss is termed the Vasyliunas cycle (Vasyliunas, 1983).

Saturn is also affected by the solar wind, with the magnetosphere experiencing driving in a process similar to that of the Dungey Cycle at Earth, which introduces plasma to the magnetosphere from the solar wind. However, like Io at Jupiter, Saturn features another major plasma source from its moon Enceladus, located within the inner magnetosphere. With more than 100 confirmed geysers continuously ejecting neutrals and ions into the magnetosphere, at a ratio of 100:1, Saturn's magnetospheric environment is dominated by neutrals. Other, less significant, sources of plasma include dissociation of Titan's N_2 molecules into fast atoms and ions; ionization of neutrals from the other moons, Mimas, Tethys, Dione, and Rhea; Saturn's main rings, from UV and cosmic ray interactions plus collisions; and interactions in Saturn's atmosphere.

3.5 Saturn Kilometric Radiation

Saturn Kilometric Radiation (SKR) is a radio wave signature of auroral activity understood to be generated by the Cyclotron Maser Instability (CMI). Discovered by the Voyager 1 planetary radio experiment in 1980, SKR is the most intense radio emission from Saturn with strong parallels to Earth's auroral kilometric radiation. SKR emission sources are located at high-latitudes within a radio oval matching the latitude of the UV auroral oval. SKR sources rotate with the planet, at a periodicity of $\sim$ 10h 39m (Gurnett, Persoon, et al., 2007), with power enhanced in the pre-morning to noon sector, matching UV auroral emissions.

SKR is also tied to the precipitation of electrons to the auroral zone and hence the generation of aurorae. Horseshoe (or shell-like) distributions of electron distributions have been observed within the auroral zone, which CMI is unstable to, coinciding with the emission of SKR (Baines et al., 2018).

As has been explored in chapter 2, energetic plasma particles orbit local magnetic field lines perpendicular to the magnetic field of the planet. These particles gyrate within the magnetic field with a characteristic gyro-frequency given by Equation 2.22. Oscillations also occur due to the small scale charge-density perturbations within the plasma with a characteristic plasma frequency given by Equation 2.6. When the electron gyro-frequency $>>$ plasma frequency, radio waves emission occurs (Baines et al., 2018).

During geomagnetic storms magnetic tail reconnection events can increase, accelerating energetic electrons from the plasma sheet region along the magnetic field into the Northern and Southern hemispheres. This radiation emitted from these electrons is then generated by the conversion of their free energy via the CMI. CMI

occur due to mildly relativistic, downward-directed electron beams accelerated by parallel electric fields. At lower altitudes the electrons encounter increasing magnetic fields, which would occur as they approach the hemispheres. Parallel energy of the electron is then converted into perpendicular energy. This conversion of energy creates an unstable positive perpendicular velocity gradient, driving strong wave growth near the local electron cyclotron frequency. These emissions are anisotropic and restricted to a hollow cone that is limited by the local plasma parameters, does not exceed 90°, and whose central axis is aligned to the local magnetic field line of the source (Wu et al. (1979); Zarka (1998); Mutel et al. (2010); Baines et al. (2018)).

Therefore, CMIs occur in strongly magnetised regions (high relative gyro-frequency) of low plasma density (low relative plasma frequency) which restricts SKR to the regions above the planet. CMIs have been confirmed with flybys of Cassini through the high-latitude SKR and auroral source regions where emissions, propagating at large angles from the magnetic field lines have been observed. (Wu et al. (1979); Galopeau et al. (1989); Zarka (1998), Baines et al. (2018)).

When geomagnetic storm-like activity occurs in the magnetotail, accelerated electrons are produced as part of the field aligned current system. Intensification also occurs during auroral brightening, ENA enhancements, plasmoid production, energetic-particle injections, and solar wind dynamic pressure enhancements (Badman et al. (2008); Baines et al. (2018)).

Due to the conical emission caused by CMI, detection of SKR is limited to the position of the observing satellite/instrument around the planet, see Figure 3.9. SKR sources are located at invariant latitudes $\geq 70°$ along local magnetic field lines. Along the local magnetic field line, SKR beaming comes from an angle $\leq 70°$, resulting in

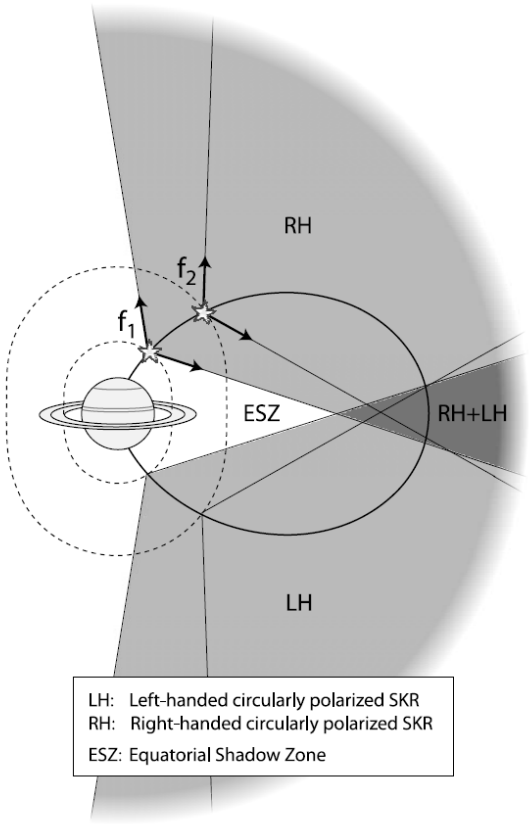

Figure 3.9: SKR emission zones along the local magnetic field lines. Due to the confinement of the hollow cone emissions, satellites must be passing within a cone in order to observe SKR emission. A narrow region does exist about the equator, significantly far out from the planet to detect emissions of both SKR polarisations. Image credit: Lamy, Zarka, et al. (2008).

a shadow zone along the equator as illustrated in Figure 3.9. This shadow zone is dependant on the source's origin along the local magnetic field line and aperture angle of the emission cone. SKR emissions at high and low frequencies were not detected at Cassini altitudes $\geq 55°$ (Lamy, Zarka, et al., 2008).

SKR is strongly circularly polarized, with high intensity emissions at wavelengths

from 3kHz to 1.2 MHz, with a peak intensity between 100 and 400 kHz. SKR also features two components with opposite polarities; a Southern hemisphere originating left-hand (LH) component and a Northern hemisphere originating right-hand (RH) component. This polarisation is well defined from numerous flybys of Cassini across all latitudes. SKR LH and RH powers vary in synchronicity, with peaks and troughs in intensities aligning with a high correlation coefficient at timescales ≥ 30 minutes. This is not a definitive lower bound, shorter timescales may also show strong correlation. Though emissions sources are identifiable between hemispheres, determinable by the polarisation, overlapping emissions from both hemispheres do occur close to the equator (Lamy, Zarka, et al., 2008).

3.6 Closing Remarks

In the second half of our introduction to the background physics necessary to understand and interpret this thesis we have first explored the terrestrial magnetosphere, it's properties, and processes such as the Dungey cycle, magnetic reconnection, and the generation of magnetic currents. The phenomena of coupling functions try to explain the complexity of the solar wind-magnetosphere coupling interactions, whilst geomagnetic indices are generated as measures of the magnetic activity.

Building on the terrestrial system, the driving mechanisms are then used as the foundation to expand into the Saturnian magnetosphere. We explored the rotational driving of Saturn's magnetosphere, in addition to the Dungey cycle, and the production of additional ions and neutrals within from the major moons Enceladus and Titan. Unique properties and structures that differentiate the magnetosphere

of Saturn were described before focusing on the phenomena that is SKR, generated within the Saturnian magnetosphere due to the CMI.

We are now equipped to handle the work of this thesis. However, before we continue into the methods and results of this work, we must first understand the physical manifestation of our understanding. Therefore, the next step in our journey is to explore and understand the data that underpins this work.

Chapter 4

Data

There are two primary goals to this thesis. First, to find a proxy for the solar wind as an external driver for Saturn's magnetosphere dynamics. Secondly, to demonstrate the effectiveness of the application of MI as a novel technique to assess the strength of these proxies.

Implementing MI requires the application of two separate data sets in order to build a joint probability distribution between an input and output data set. This will be defined later in subsection 5.4.1. The interest of the research is in understanding the relationship between an input data set with an output data set. Hence, to build the necessary channel, data sets must be matched by their time of measurement and be equal in size, see section 6.1. Of the data investigated, sampling rates differ between data sources. Hence, where a choice is available, the higher sampling rate is chosen to ensure minimal smoothing and maximal fine-detail of the data is retained when preparing the data.

The physical principles behind the data to be investigated have been explored previously in chapter 2 and chapter 3. Here, the physical data is presented, covering

the sources and instrumentation of the data, investigated parameters and their units, and any relevant information of the data that must be considered when applying MI. In section 4.1 the directly measured solar wind and geomagnetic indices data is described. This direct solar wind data is then used in subsection 4.1.2, to solve the coupling function equations described in section 3.3.

As there is no direct solar wind monitor at the outer planets, section 4.3 presents the propagation model of Tao et al. (2005) and its verification can be found in section A.3. This model will take the directly measured solar wind data and propagate it to the outer planets. In subsection 4.3.2, propagated solar wind data to Saturn is described. This propagated data can then be used to test MI over long-time periods, in the absence of directly measured solar wind data.

The Geocentric Solar Ecliptic coordinate system (GSE) is the frame of reference used for several data sets involving the solar wind. In the GSE system the X-direction points from the Earth to the Sun, the Y-direction is perpendicular to the X-direction in the ecliptic plane opposing planetary motion (pointing duskward), and the Z-direction is parallel to the ecliptic pole. The GSE system has a yearly rotation in an inertial reference frame (Russell, 1971).

4.1 OMNI Data

OMNI uses several different sources to build a complete database of 1-minute, solar wind magnetic field and plasma data sets. The ACE and Wind satellites contribute the majority of the data comprising the OMNI database, spanning from 1998 and 1995 respectively, until the present day. The Cassini mission at Saturn ran from 2004

- 2017, and the period investigated for geomagnetic indices and coupling functions, from 2005 - 2021. OMNI supplements its data for the periods of interest using Geotail data from 1995 until 2006 (Papitashvili et al., 2020).

ACE, standing for Advanced Composition Explorer, orbits the L1 Lagrange point between the Earth and the Sun approximately 235 Earth radii from the Earth. Launched on 25th August 1997, it became officially operational on 21st January 1998 with an expected lifespan of two to five years. It continues to operate in the present day. ACE is fitted with nine instruments, able to provide real-time space weather data and advanced warning of geomagnetic storms. See Siddiqi (2018), Smith, L'Heureux, et al. (1998), and Stone, Frandsen, et al. (1998) for more information on the ACE satellite and its instruments. ACE plasma data was taken from the Solar Wind Electron, Proton, and Alpha Monitor (SWEPAM) instrument, whilst magnetic field data was taken from the Magnetometer (MAG) instrument.

The Wind spacecraft orbits the L1 point between the Earth and the Sun. It was launched on 1st November 1994, settling into the L1 point in early 2004, after spending some time in the magnetosphere. Originally launched with an expected lifespan of three to five years, it continues to operate in the present day. Wind is fitted with eight instruments and from the L1 point can measure real-time solar wind and magnetic fields. See Siddiqi (2018), Lepping et al. (1995), and Wilson III et al. (2021) for more information on the Wind satellite and its instruments. WIND plasma data was taken from the Solar Wind Experiment (SWE) instrument, whilst magnetic field data was taken from the two triaxial fluxgate magnetometer (MFI - Magnetic Field Investigation) instruments.

Geotail operated in a high elliptical Earth orbit and was purposed with investi-

gating the Earth's long magnetotail region. It was launched on 24th July 1992 with an expected lifespan of four years. It continued to operate until 28th November 2022. Geotail was fitted with seven instruments, able to provide real-time magnetic field and plasma data. See Siddiqi (2018) and Nishida (1994) for more information on the Geotail satellite and its instruments. Geotail plasma data was taken from the Comprehensive Plasma Instrument (CPI) instrument, whilst magnetic field data was taken from the Magnetic Fields Measurement Monitor (MGF) instrument.

The satellites that have provided data for the OMNI database are not located in the same fixed position. Even at the L1 point, satellites orbit this position and need constant readjustment around this point of gravitational equilibrium, meaning data can vary by hours and several Earth radii. Therefore, all data is time shifted to the bow shock nose to ensure the data is consistent for use as a single data set. This shifting assumes that values measured by a spacecraft, at any time and place, are propagated as if they lie on a planar surface (phase front), convecting with the solar wind (Papitashvili et al., 2020).

High resolution data is available from 1995 to the present day, covering the lifespan of the Cassini mission from 2004 - 2017 and the investigation of coupling functions and geomagnetic indices. In total, OMNI data from 2004 - 2021 is used. Direct high resolution 1-minute solar wind data used in this research can be found in the OMNI database (Papitashvili et al., 2020).

4.1.1 Solar Wind Data

From the OMNI database, six solar wind parameters are taken into consideration. These have been chosen because they are also the solar wind parameters available

in the Automated Multi-Dataset Analysis (AMDA) database (CDPP, 2005), propagating OMNI data using the model of Tao et al. (2005). For this work, the solar wind parameters considered are radial velocity (v_x), tangential velocity (v_y), tangential magnetic field (B_y), dynamic pressure (p_{dyn}), proton density (ρ), and temperature (T). The solar wind parameters considered and further information on them is available in Table 4.1.

4.1.2 Coupling Functions

Coupling functions, as defined in section 3.3, are solved using solar wind parameters. From the OMNI database, six directly measured high-resolution solar wind parameters, from 2005 - 2021, are used to solve the coupling function equations. For this work, the solar wind parameters considered to solve the coupling functions are radial velocity (v_x), tangential velocity (v_y), the z-component of the velocity (v_z), radial magnetic field (B_x), tangential magnetic field (B_y), and the z-component of the magnetic field (B_z). The solar wind parameters considered and further information on them is available in Table 4.1.

Solar Wind Parameter	Reference Frame	Unit	Fill Value	Sampling Rate
v_x	GSE	$km \cdot s^{-1}$	99999.9	1-min
v_y	GSE	$km \cdot s^{-1}$	99999.9	1-min
v_z	GSE	$km \cdot s^{-1}$	99999.9	1-min
B_x	GSE	nT	9999.99	1-min
B_y	GSE	nT	9999.99	1-min
B_z	GSE	nT	9999.99	1-min
p_{dyn}	-	nPa	99.99	1-min
ρ	-	cm^{-3}	999.99	1-min
T	-	K	9999999	1-min

Table 4.1: Directly measured solar wind data from the OMNI database (Papitashvili et al., 2020). Solar wind parameters: v - velocity, B - IMF strength, p_{dyn} - Dynamic Pressure, ρ - Proton Density, and T - Temperature. Subscripts: x - radial component, y - tangential component, and z - component parallel to the ecliptic pole. These data sets contain fill values, used in place of an absent value, where measurements are not available. The fill value is deliberately large, to ensure no confusion between the real data and the fill value data.

4.2 Geomagnetic Indices: AL Index and SYM/H Index

The geomagnetic indices, AL and SYM/H, were described in section 3.2. Unlike the solar wind and coupling functions, the geomagnetic indices are not governed by

space missions such as ACE and Wind but are measured at the Earth's surface using networks of magnetometers.

Magnetometers measure variations in a surrounding magnetic field. Electric currents, when exposed to an external magnetic field, experience a combined force due to the electric and magnetic fields imposed upon them. This force is known as the Lorentz force and is given by Equation 2.10. When the current flows through an electric conductor, a Lorentz force acting transverse to the flow of the electric current causes an accumulation of charge to one side of the conductor, resulting in a potential difference, this is known as the Hall effect. As the direction and strength of the magnetic field varies, potential difference also varies. Hence, a magnetometer can measure characteristics of the surrounding magnetic field by measuring variations in the magnitude and polarity of the potential difference.

4.2.1 AL Index Data

In the case of the AL index and auroral indices generally, measurements are based on 1-min readings of the northward H component trace from twelve auroral zone observatories. These observatories are located between 60° and 70° magnitude with a longitudinal spacing between 10° and 50° (Li et al. (2007); Baumjohann et al. (2012)). The derivation of these indices were performed by the World Data Center for Geomagnetism in Kyoto (WDC for Geomagnetism, 2005). A brief description of the transformation of readings into the AL index is described in section A.1.

Some uncertainties are present in the data due to the geography of the observatories. Electrojets typically flow along the auroral oval, perpendicular to the terrestrial global eccentric dipole north-south direction, as opposed to perpendicular to the local

H direction. The angle between the local magnetic H component and the global eccentric dipole north-south direction is greater than 30°. Consequently, observatories exhibiting this feature underestimate the electrojet current (Baumjohann et al., 2012).

Longitudinal gaps exist, with the largest gap being in excess of two hours. Geomagnetic storms can occur in shorter periods and consequently be missed by the network of observatories.

Finally, the small latitudinal range covered by the network of observatories presents challenges. During periods of high and low activity, the auroral oval can contract above 70° latitude and expand below 60° latitude, respectively (Li et al. (2007); Baumjohann et al. (2012)).

As the study of this thesis is to investigate over long-time periods, the absence of a minority proportion of sub storms and gaps in the data should not have a detrimental effect. In the worst case, the results relating the strength of the geomagnetic indices with the solar wind will be lower bounds for the MI value (see chapter 5 for a definition of MI).

Direct high-resolution data for the AL Index, from 2005 - 2021, is available from the OMNI database (Papitashvili et al., 2020). Further information on these variables is available in Table 4.2.

4.2.2 SYM/H Index Data

In the case of the SYM/H index the process of data collection is much the same as for the auroral indices. Measurements are made using a network of ground-based magnetometers, ranging between approximately 50° to −50° latitude and distributed longitudinally (Wanliss et al., 2006). Iyemori (1990) solves the transformation of

Geomagnetic Index	Unit	Fill Value	Sampling Rate
AL Index	nT	99999	1-min
SYM/H Index	nT	99999	1-min

Table 4.2: Directly measured geomagnetic indices data taken from the OMNI database (Papitashvili et al., 2020). These data sets contain fill values, used in place of an absent value, where measurements are not available. The fill value is deliberately large, to ensure no confusion between the real data and the fill value data.

readings into SYM/H data, which is briefly covered in section A.2.

Like the AL index, uncertainties are present in the data. On any given month, only six observatories out of eleven are used for background field averaging of the data (Wanliss et al., 2006). As such, different variation fields are observed due to contributions from the magnetotail; these predominantly affect nightside latitudes and longitudes, and are not captured by dayside observatories. Therefore the longitudinal spacing can drastically affect the final index value (Wanliss et al., 2006). However, as stated, the study of this thesis is to investigate over long-time periods. Therefore, whilst on short-time periods this averaging may cause issues in the data, the affect should be minimised over the time period considered.

Direct high-resolution data for the SYM/H Index, from 2005 - 2021, is available from the OMNI database (Papitashvili et al., 2020). Further information on these variables is available in Table 4.2.

4.3 Propagated Solar Wind

4.3.1 Tao Model

Developed as a response to a lack of upstream solar wind monitors, Tao et al. (2005) developed a one-dimensional magneto-hydrodynamic (MHD) model to propagate continuous, directly measured solar wind measurements, taken at the Earth, to Jupiter. Thus, the solar wind is modelled as an ideal MHD fluid affected by solar gravity in a one-dimensional, spherically symmetric coordinate system. In this Cartesian coordinate system, the x-direction is in the equatorial plane, the z-direction points Northward, and the y-direction completes the orthogonal triad,which describes the GSE coordinate system. The MHD model assumes the solar wind propagates with constant solar wind speed, that B_z is zero constant, and that B_x is fixed at 0.001 nT at the inner boundary (1 AU) and drops as $1/r_x^2$ as the plasma parcel propagates anti-sunward.

MHD equations are given in the centimetre-gram-second (CGS) Gaussian system, used by Tao et al. (2005).

The continuity equation

$$\frac{\partial}{\partial t}(\rho S) + \frac{\partial}{\partial x}(\rho v_x S) = 0 \tag{4.1}$$

The x component of the momentum equation

$$\begin{aligned} &\frac{\partial}{\partial t}(\rho v_x S) + \frac{\partial}{\partial x}\left[\left(\rho v_x^2 + p + \frac{B^2}{8\pi} - \frac{B_x^2}{4\pi}\right) S\right] = \\ &\rho\left[g_x + \left(v_y^2 - \frac{B_y^2}{4\pi\rho}\right)\frac{1}{R}\frac{dR}{dx}\right] S + \left(p + \frac{B^2}{8\pi}\right)\frac{dS}{dx} \end{aligned} \tag{4.2}$$

The y component of the momentum equation

$$\frac{\partial}{\partial t}(\rho v_y RS) + \frac{\partial}{\partial x}\left[\left(\rho v_x v_y - \frac{B_x B_y}{4\pi}\right) RS\right] = 0 \tag{4.3}$$

Gauss's law for magnetism

$$\frac{\partial}{\partial x}(B_x S) = 0 \tag{4.4}$$

The induction equation

$$\frac{\partial}{\partial t}\left(\frac{B_y S}{R}\right) - \frac{d}{dx}\left(\frac{(-v_x B_y + v_y B_x)S}{R}\right) = 0 \tag{4.5}$$

The energy equation

$$\begin{gathered}\frac{\partial}{\partial t}\left[\left(\frac{1}{2}\rho v^2 + \frac{p}{\gamma - 1} + \frac{B^2}{8\pi}\right) S\right] + \\ \frac{\partial}{\partial x}\left[\left\{v_x\left(\frac{1}{2}\rho v^2 + \frac{\gamma p}{\gamma - 1}\right) - \frac{1}{4\pi}(B_y(-v_x B_y + v_y B_x))\right\} S\right] \\ = \rho g_x v_x S\end{gathered} \tag{4.6}$$

For equations 4.1, 4.2, 4.3, 4.4, 4.5, and 4.6 ρ is the mass density, v is the solar wind velocity, B is the IMF strength, p is the thermal pressure, and γ, the specific heats ratio, is 7/5.

g_x, the solar gravitational force is given as

$$g_x = \frac{-GM}{x^2} \tag{4.7}$$

where G is the gravitational constant and M is the solar mass. S is the unit surface and is defined as

$$S = x^2 \tag{4.8}$$

where $R(x) \sim x$ is the distance from the solar rotation axis.

The time step is 10s and grid spacing is 1/300 AU. To satisfy Equation 4.4 the inner B_x drops as $1/x^2$ as the solar wind plasma propagates anti-sunward.

The time of the solar wind data, as measured at Earth, is shifted according to

$$\Delta t = \frac{\Phi}{\Omega_{Sun}} \tag{4.9}$$

where Φ is the Earth-Sun-Jupiter angle and Ω_{Sun} is the angular velocity of the Sun's rotation.

MHD equations are solved using the Coordinated Astronomical Numerical Software (CANS), the source code of which can be found at ACT-JST (2005).

There are some limitations to the MHD model given in Tao et al. (2005). The B_x and B_z components of the IMF are fixed in the MHD model, as such the IMF variation on the Jovian magnetosphere is not accounted for. The absence of some pressure enhancement events in the real data, predicted by the MHD model, creates an event selection ambiguity. Finally, when the prediction error between the arrival time and the duration of pressure pulses are comparable, the increasing or decreasing phase of solar wind dynamic pressure becomes undetectable.

Finally, the model is verified to be valid, with a prediction error no greater than $\pm$ 2 days, when $\Phi < 50°$. This prediction error is taken into account with the use of time off-setting, which is explained in section 6.4. A brief review of the verification of the MHD model by Tao et al. (2005) can be found in section A.3.

4.3.2 Propagation to Saturn and Considerations

One of the aspects of this research is to consider the parameters of the solar wind as a driver of Saturn's magnetosphere dynamics, without an apriori assumption towards which parameters will act as strong drivers. As such, all available propagated solar wind parameters, using OMNI data, in the AMDA tool (CDPP, 2005) are considered equally. These parameters are listed in Table 4.3.

The equations and propagation of the MHD model remain the same when considering Saturn in place of Jupiter, with the exception of substituting the Earth-Sun-Jupiter angle for the Earth-Sun-Saturn angle in Equation 4.9.

Whilst B_z is held constant and B_x falls as $1/r_x^2$, it has been established that at the orbital distance of Saturn, due to the Parker Spiral effect (subsection 2.6.1), the majority of the IMF is concentrated in the B_y component, aligned to the azimuthal (tangential) plane. As such, confidence can be held that the B_y component of the IMF is a valid indicator of the IMF strength and variation at Saturn. Additionally, the research of this thesis is not looking at specific enhancement events but the long-term behaviour of the solar wind. As such, the absence of specific enhancement events is not detrimental to this work.

Tao et al. (2005) quotes the outer boundary of the MHD model at 8 AU. However, later works have expanded this distance and verified the use of the MHD model to the orbital distance of Saturn (approximately 10 AU) and beyond (Kimura et al. (2013); Provan et al. (2015); Lamy, Prangé, et al. (2017); Nakamura et al. (2019); Palmerio et al. (2021)).

It is noted that later papers begin to quote the maximum prediction error as up to 2 days when $\Phi < 60°$, with the earliest case seen in Kimura et al. (2013). This quoted

value directly cites Tao et al. (2005), in which no reference to an angle of $\Phi < 60°$ is found. The assumption is made that this value is for the Sun-Earth-Saturn angle, Φ_S, rather than Φ, as the original author of the MHD model is co-author on many of these papers, including Kimura et al. (2013). However, as increasing the angle range would increase the quantity of data, without certainty this would improve the quality of the data, the value of $\Phi < 50°$ from Tao et al. (2005) will be used when preparing data, see section 6.5.

We note that Kimura et al. (2013) investigates Saturn's auroral radio emissions, whereas Tao (2005) conducted their investigation at Jupiter. Kimura et al. (2013) expects that the magnitude of the error will be the same, but may be up to twice that of Jupiter.

Propagated solar wind data, using the MHD model of Tao et al. (2005), can be acquired using the AMDA tool, at the Centre de Données sur la Physique des Plasmas spatiaux (CDPP, 2005). Data is available for the lifetime of the Cassini mission, from 2004 - 2017, and propagation is performed using solar wind data from the OMNI database (Papitashvili et al., 2020).

Solar Wind Parameter	Reference Frame	Unit	Fill Value	Sampling Rate
v_x	GSE	km·s^{-1}	NaN	10-min
v_y	GSE	km·s^{-1}	NaN	10-min
B_y	GSE	nT	NaN	10-min
p_{dyn}	-	nPa	NaN	10-min
ρ	-	cm^{-3}	NaN	10-min
T	-	eV	NaN	10-min

Table 4.3: Propagated solar wind data from CDPP (2005), using the MHD model of Tao et al. (2005). Solar wind parameters: v - velocity, B - IMF strength, p_{dyn} - Dynamic Pressure, ρ - Proton Density, and T - Temperature. Subscripts: x - radial component, and y - tangential component. These data sets contain fill values, used in place of an absent value, where measurements are not available. The fill value is defined as Nan (Not a Number), to ensure no confusion between the real data and the fill value data.

4.4 Saturn Kilometric Radiation

The Radio and Plasma Wave Science (RPWS) Instrument of the Cassini satellite was designed to measure electric and magnetic fields of radio emissions and plasma waves. Included in this instrument is a High Frequency Receiver (HFR) for the measurement of radio waves. These radio waves are collected by three antenna (monopoles), commonly referred to as E_U, E_V, and E_W. These antenna are mounted with an angle of 120° between the E_U and E_V elements and the third element, E_W, perpendicular to the plane formed by them. Two signals are mixed from these antenna signal, E_x,

using a dipole-mode configuration from the voltages of the E_U and E_V monopoles, and E_z, derived from the E_W voltage (Gurnett, Kurth, et al. (2004); Galopeau et al. (1989); Lamy, Zarka, et al. (2008)).

HFR consists of two sets of four analogue receivers. One set of receivers is connected to the E_W monopole, whilst the other set can be connected to either of the E_U and E_V monopoles or the E_X dipole. Three of these receivers have fixed-frequency filters, covering the range from 3.5 to 319 kHz (A, B, and C). The final receiver has two modes (HF1 and HF2), the first covers 100 kHz to 4.125 MHz, in 25 kHz steps, and the second covers 125 kHz to 16.126 MHz, in 50 kHz steps. HFR is therefore able to provide simultaneous auto and cross correlation measurements from two antennas over the frequency range 3.5 kHz to 16 MHz. Switching the two inputs of the receiver between the three monopole electric antennas, the receiver can provide measurements of the radio waves arrival direction as well as the flux and polarisation, known as the Stokes parameters (Gurnett, Kurth, et al. (2004); Galopeau et al. (1989); Lamy, Zarka, et al. (2008)).

A summation of the characteristics of the HFR, first presented in Gurnett, Kurth, et al. (2004), is presented in Figure 4.1.

It is therefore evident than any raw data will be highly inhomogeneous due to the range of frequencies and steps, and the differing integration times. Fortunately, HFR data has been homogenised and cleaned to produce uniform SKR data. The approach of Lamy, Zarka, et al. (2008) describes within the appendix such a means of cleaning and homogenising the data, building long-term time series of emitted flux densities and normalised powers, from which SKR can be extracted. Whilst other references also perform this reduction, principal authors of this paper are the data producers of

Band	Frequency range	Frequency steps	Frequency resolution	Integration times
A	3.5–16 kHz	8, 16, or 32 (logarithmic)	20, 10, or 5%	0.125, 0.25, 0.5, or 1 s
B	16–71 kHz	8, 16, or 32 (logarithmic)	20, 10, or 5%	0.125, 0.25, 0.5, or 1 s
C	71–319 kHz	8, 16, or 32 (logarithmic)	20, 10, or 5%	0.125, 0.25, 0.5, or 1 s
HF1	125 kHz–4.125 MHz	n × 25 kHz; 1, 2, 4, or 8 linear channels within 25-kHz band	3.125, 6.25, 12.5, 25, or n × 25 kHz	20, 40, 80, or 160 ms
HF2	125 kHz–16.125 MHz	n × 50 kHz; 1, 2, 4, or 8 linear channels within 25-kHz band	3.125, 6.25, 12.5, 25, or n × 50 kHz	10, 20, 40, or 80 ms

Figure 4.1: Summation of the characteristics of the High Frequency Receiver of the RPWS instrument on Cassini. Image credit: Gurnett, Kurth, et al. (2004)

SKR from the AMDA tool (CDPP, 2005)[1].

SKR radio data is found across the wavelength range of 3 kHz to 1.2 MHz and peaks in the 100 - 400 kHz range (Galopeau et al., 1989). Hence, we find the available data is split into two sets, from 10 - 1,000 kHz and the peak range of 100 - 400 kHz, where the most intense radiation can be considered.

SKR is also strongly polarised, Voyager missions flybys found that there are two components of SKR with opposite polarization, these are the Right-Hand (RH) polarisation that originates from the Northern hemisphere and the Left-Hand (LH) polarisation that originates from the Southern hemisphere (Warwick, Pearce, et al. (1981); Warwick, Evans, et al. (1982); Kaiser et al. (1982)). This results in the additional division of the data sets between RH and LH data.

[1]The data providers for SKR data are acknowledged: Laurent Lamy and Baptiste Cecconi

Polarisation/ Hemisphere	Frequency Range (kHz)	Unit	Fill Value	Sampling Rate
LH/Southern	100 - 400	$W{\cdot}s^{-1}$	NaN	3 min
LH/Southern	10 - 1,000	$W{\cdot}s^{-1}$	NaN	3 min
RH/Northern	100 - 400	$W{\cdot}s^{-1}$	NaN	3 min
RH/Northern	10 - 1,000	$W{\cdot}s^{-1}$	NaN	3 min

Table 4.4: SKR data from the RPWS instrument of the Cassini satellite. LH - Left Hand polarisation. RH - Right Hand polarisation. These data sets contain fill values, used in place of an absent value, where measurements are not available. The fill value is defined as Nan (Not a Number), to ensure no confusion between the real data and the fill value data.

Consequently, SKR is made available in four data sets, divided by frequency range and polarisation (hemisphere). See Table 4.4 for further details of the division of the SKR data. Though there are four different data sets to analyse the interest will also be in how the relationship between the solar wind and SKR is related across all of these data sets. SKR data, covering 2004 - 2017, can be acquired using the AMDA tool, at the Centre de Données sur la Physique des Plasmas spatiaux (CDPP, 2005).

4.5 Closing Remarks

At this stage the origins of the data and the physical principles have been outlined. It is evident to see that the data, coming from a variety of sources, under different conditions, and at varying levels of availability, is complex. Applying these different data sets to MI is not a straightforward task, and significant effort has been required to

achieve this. In the coming chapters, the principles of MI will be outlined (chapter 5), followed by an explanation of how these varied data sets can be applied (chapter 6), to hopefully achieve new insights into the relationship of the solar wind at the Earth and Saturn.

Chapter 5

Mutual Information

5.1 Why Mutual Information

Traditional metrics, such as Pearson correlation, are limited in their ability to investigate the relationship between data sets. It is only possible for them to explore linear relationships. Mutual information (MI) on the other hand has a distinct advantage over these, it can explore any relationship. As well as being able to investigate linear relationships, it can also identify non-linear ones. It is a more general measure of relationships and thereby opens the possibility of exploring and identifying new kinds of relationships that may not have been so closely observed between the solar wind and the Solar System magnetospheres.

5.2 Defining Information

Fundamentally, before considering the motivations behind the research of this thesis we must understand MI and what this measure tells us. This begs the very first

question,

What is Information?

Information is a broad subject and further reading will demonstrate how vast it is (see texts such as Cover et al. (1991) and MacKay (2003)). For the purposes of this thesis, information is defined and explored only with relevance to the research presented in chapter 7, chapter 8, and chapter 9.

To define information, examples offered by Moser et al. (2012) are presented in new forms to illustrate the concept of information and build the foundations that will lead to MI. Consider then the following statements

- The weather will be clear tomorrow
- The weather was dreary yesterday
- You will win the lottery in this week's draw

It is intuitive to us that each of these statements can be understood as providing information. However, it is reasonable to ask the question, are all of these statements providing the same amount of information? Consider then the following two statements

- Is it raining today in the United Kingdom?
  - There are two answers: *yes* or *no*
- Someone in York won the lottery this week, who was it?
  - This time there are approximately 200,000 possible answers (the rough population of York)

It is again intuitive, that between these two statements, the second is providing more information than the first, as it is far less likely to be able to predict the answer to the second question. Hence, the first step in the journey to defining information.

1. Information is linked to the number of possible answers, r

Consider another scenario, you are playing a game of Dungeons and Dragons, and locked in battle with a fearsome Owlbear. As a mighty Paladin, you swing your warhammer and strike the Owlbear. Observe the following two cases of rolling for damage

- The eight-sided die is thrown. You announce the result to your party.
- You cast Divine Smite and can roll 3 eight-sided dice. You announce the result to your party who leap into the air in celebration as the deadly beast is defeated.

It is evident that the results announced are providing different amounts of information. Rolling three dice provides three times the amount of information as rolling one, leading us to the second step in defining information.

2. Information should be additive in some sense

In the first case the number of possible answers is $r = 8$, and in the second case the number of possible answers is $r = 8^3 = 512$. There are 64 times more potential outcomes in the second case than in the first. If information is additive, how can this be reconciled? The answer: use logarithms.

$$\log_b 8^3 = 3 \cdot \log_b 8 \tag{5.1}$$

Hartley (1928) made these same observations , defining information as

$$\tilde{I}(U) \triangleq \log_b r \tag{5.2}$$

where r is the number of possible outcomes of a random message, U, and b is an arbitrary base. In information theory the convention is to use b in units of *bits*, setting the base $b = 2$. However, any base may be chosen, so long as the base is consistent in any measurements of information. Hartley (1928) also demonstrated the desired property of information being additive

$$\tilde{I}(U_1, U_2, ..., U_n) = \log_2 r^n = n \cdot \log_2 r \tag{5.3}$$

Equation 5.3 suggests the smallest unit of information will come from a binary system, $\tilde{I}(U) = \log_2 2 = 1$. Shannon (1948) demonstrated that this was not the case.

Figure 5.1 shows two hats, *Hat A* and *Hat B*. Each contains 4 balls; in *Hat A* there are two white balls and two black balls, whilst in *Hat B* there are 3 black balls and 1 white ball. At random a single ball is drawn from each hat. U, the random message, is set as the colour. Then, for both hats $r = 2$, as there are only two colour possibilities. Therefore, by our current definition of information, $\tilde{I}(U_A) = \tilde{I}(U_B) = \log_2 2 = 1$ bit. However, it is clear that if we draw a black ball from *Hat B*, we will gain less information than if we were to draw a black ball from *Hat A*. We expect to draw a black ball from *Hat B* because we know there are more black balls than there are white. Thus probability must play a role in defining information, leading to the third step in defining information.

3. A true measure of information needs to take into account the probabilities of the different possible outcomes

Figure 5.1: Left: *Hat A*, contains two black and two white balls. Right: *Hat B*, contains three black and one white balls. In both cases $r = 2$ but it is self evident that if a black ball were to be drawn from *Hat B*, it would contain less information than if a black ball were drawn from *Hat A*.

Consider again *Hat B*, where the probability of drawing a white ball is one in four. The quantity r in Equation 5.2 is the number of all possible outcomes of a random message, U. Hartley's measure of information says one possible outcome out of r possible outcomes will be observed. In this case the white ball is one possible outcome of four possible outcomes, when selecting a ball from the hat

$$\tilde{I}(U) = \log_2 4 = 2 \text{ bits} \tag{5.4}$$

However, there are three chances out of four that a black ball will be drawn from *Hat B*. Here, Hartley's measure of information cannot be used directly, Hartley's form of information must be transformed into one that gives *one* possible outcome out or r. To achieve this the statement can be *normalised*. Dividing through by 3, the number of black balls, gives one realisation out of 4/3 possible realisations.

$$\tilde{I}(U) = \log_2 \frac{4}{3} = 0.415 \text{ bits} \tag{5.5}$$

Now, the system represents two different values of information depending on the colour drawn. To take a single value that represents the information of the system, the result can be averaged, i.e. different information values will be weighed according to the probabilities that they will occur.

$$\tilde{I}(U) = \frac{1}{4}\log_2 4 + \frac{3}{4}\log_2 \frac{4}{3} = \frac{1}{4}2bits + \frac{3}{4}0.415 \text{ bits} = 0.811 \text{ bits} \tag{5.6}$$

This average of Hartley information is Shannon's entropy and is defined as

$$\sum_{r=1}^{r} p_i \log_2 \frac{1}{p_i} = -\sum_{r=1}^{r} p_i \log_2 p_i \tag{5.7}$$

where p_i is the probability of the i^{th} possible outcome. Hence, to define the entropy, H, of a random message, U, that takes on r different values, each with probability p_i, where $i = 1, \ldots, r$ as

$$H(U) = -\sum_{i=1}^{r} p_i \log_2 p_i \tag{5.8}$$

This *derivation* of Shannon's entropy is evidently not rigorous but it is useful to aid in becoming familiar with the concepts. Shannon's Entropy plays a crucial role in deriving MI and so understanding these illustrative examples is as important a step on the journey to MI as its mathematical proof.

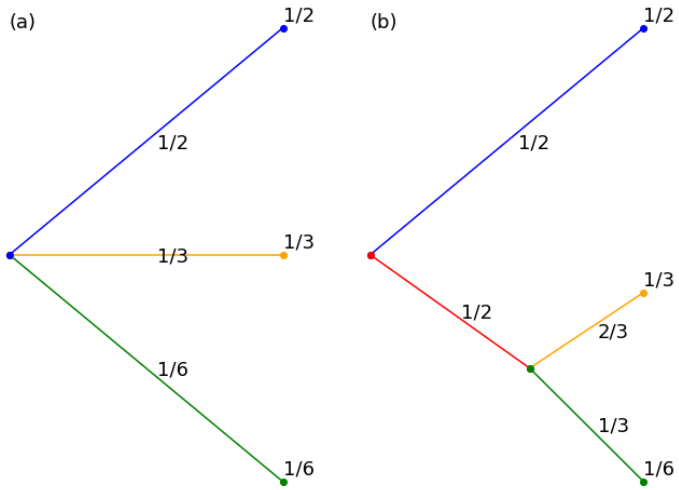

Figure 5.2: Depiction of a possibility tree for three choices. Replicated from Shannon (1948).

5.3 Proving Shannon's Entropy

5.3.1 Shannon's Derivation

Shannon did mathematically derive the equation of entropy in Equation 5.8 and laid out the properties of $H(U)$.

To perform this derivation, take a set of possible events whose probabilities of occurrence are $p_1, p_2, ..., p_r$. Only the probabilities that these events will occur is known but nothing else with regards to which events will occur. Shannon postulated whether it was possible to find a measure of the choice involved in selecting an event. That is to say how uncertain one can be of the outcome.

This measure, defined as $H(p_1, p_2, ..., p_r)$, should therefore have the following properties

1. This measure, H, should be continuous in p_i

2. In the case that all p_i are equal, $p_i = \frac{1}{r}$, and H should be a monotonic increasing function of r. In this case of equally likely events there is therefore more uncertainty in cases where there are more possible events.

3. If a choice can be separated into successive choices, the original choice, H, should be the weighted sum of the successive choices. These successive choices are illustrated in Figure 5.2. (a) The probability tree offers three distinct possibilities with probabilities $p_1 = \frac{1}{2}$, $p_2 = \frac{1}{3}$, and $p_3 = \frac{1}{6}$. (b) The probability tree offers two possibilities of equal probability $\frac{1}{2}$. In this case, should the second possibility occur, another successive choice must be made between two further possibilities with probabilities $\frac{2}{3}$, and $\frac{1}{3}$. The end possibilities of the probability tree in (b) have the same probabilities as the end possibilities of (a). In this special case it is required that

$$H\left(\frac{1}{2}, \frac{1}{3}, \frac{1}{6}\right) = H\left(\frac{1}{2}, \frac{1}{2}\right) + \frac{1}{2}H\left(\frac{2}{3}, \frac{1}{3}\right) \tag{5.9}$$

where the coefficient $\frac{1}{2}$ included in the uncertainty of the successive option is included because this second choice only occurs half of the time.

These properties were originally defined in Shannon (1948), section 6. Using these defined properties, one can now derive Shannon's Entropy, the full derivation of which is in B.1 and results in Equation 5.10.

$$H = -K \sum p_i \log p_i \tag{5.10}$$

where the coefficient, K, must be positive to satisfy the second property. The value of K corresponds to the unit of measure, in our case, 2 (bits).

5.3.2 Khinchin's Conditions

Shannon derived the definition of entropy given in Equation 5.8 mathematically but it was not entirely robust, failing to prove that this was the only form entropy could take. It was not until 1956 that Aleksandr Khinchin (Khinchin, 1956) put forward four conditions that entropy should have and proved definitively that the only definition entropy could take is of the form given in Equation 5.8.

N.b. Due to a lack of access to the English translation of Khinchin's original paper, Khinchin (1957), the four conditions are sourced from Moser et al. (2012).

Once again, $H_r(p_1, p_2, ..., p_r)$ is defined as a function of r probabilities. $p_1, ..., p_r$, that sum to 1.

$$\sum_{i=1}^{r} p_i = 1 \tag{5.11}$$

The function must also satisfy the following four properties

1. $H_r(p_1, p_2, ..., p_r)$ must be continuous and symmetric in $p_1, ..., p_r$ for all values of r. In simpler terms, small changes in p_i only result in small changes to H_r and the value of H_r is unaffected by the order of probabilities.

2. Zero probability events have no effect on H_r

$$H_{r+1}(p_1, ..., p_r, 0) = H_r(p_1, ..., p_r) \tag{5.12}$$

3. When all probabilities for $p_1, ..., p_r$ are the same, forming a uniform distribution, H_r is maximised

$$H_r(p_1, ..., p_r) \leq H_r\left(\frac{1}{r}, ..., \frac{1}{r}\right) \tag{5.13}$$

4. When a group of possible outcomes, $m \cdot r$, are divided into m groups, each with r possible outcomes, then the uncertainty can be split between the uncertainty of choosing a particular group, m, and the uncertainty of a particular outcome of the group, averaged over all groups.

   For a random experiment partitioned into m groups, each containing r elements, it can be performed in two steps

   (a) Determine which group the actual outcome belongs to

   (b) Determine which outcome in the group is the actual outcome

   The probabilities of the outcomes are $p_{j,i}$, $1 \leq j \leq m$, $1 \leq i \leq r$. Thus, the total probability of all the outcomes in group j are

$$q_j = \sum_{i=1}^{r} p_{j,i} \tag{5.14}$$

   and the conditional probability of outcome i from group j is then given by

$$\frac{p_{j,i}}{q_j} \tag{5.15}$$

   $H_{m \cdot r}$ can now be written as

$$H_{m \cdot r}(p_{1,1}, p_{1,2}, ..., p_{m,r}) = H_m(q_1, ..., q_m) + \sum_{j=1}^{m} q_j H_r\left(\frac{p_{j,1}}{q_j}, ..., \frac{p_{j,r}}{q_j}\right) \tag{5.16}$$

Khinchin proved this theorem in his paper (Khinchin, 1957), demonstrating that the only functions of the entropy, H_r, that satisfy the above four conditions are of the form

$$H_r(p_1, ..., p_r) = -c \sum_{i=1}^{r} p_i \log_2 p_i \tag{5.17}$$

where c $\geq$ 0 is a constant that only determines the units of H, which match Equation 5.8.

5.4 The Channel

With entropy defined a mathematical means of relating the before and after of an interaction with the solar wind must be found. That is to say, given a particular solar wind value, how certain is it that a value in an output data set will be observed?

Recall, the premise of this thesis is to try and infer the conditions of the solar wind in other data as a proxy for the solar wind. To assess the suitability of a proxy data set, it must be compared to available solar wind data in order to determine its strength as a proxy when solar wind data is unavailable. Treating the solar wind and proxy data sets as the input and output data sets respectively, how then can these be related mathematically, in a manner that can determine the relationship between the two?

Several factors affect the certainty of perceiving the affects of the solar wind; the arrival time which is uncertain due to the propagation models used, the response time in the magnetosphere, and the extent to which the solar wind affects elements of the magnetosphere to name a few. This uncertainty can be demonstrative of a

$$\mathcal{X} = \left\{ \begin{matrix} x_1 \\ x_2 \\ x_3 \\ . \\ . \\ . \\ x_s \end{matrix} \right\} \rightarrow X \rightarrow \begin{pmatrix} P_{Y|X}(y_1|x_1) & P_{Y|X}(y_2|x_1) & \dots & P_{Y|X}(y_t|x_1) \\ P_{Y|X}(y_1|x_2) & P_{Y|X}(y_2|x_2) & \dots & P_{Y|X}(y_t|x_2) \\ \dots & \dots & \dots & \dots \\ P_{Y|X}(y_1|x_s) & P_{Y|X}(y_2|x_s) & \dots & P_{Y|X}(y_t|x_s) \end{pmatrix} \rightarrow Y \rightarrow \left\{ \begin{matrix} y_1 \\ y_2 \\ y_3 \\ . \\ . \\ . \\ y_s \end{matrix} \right\} = \mathcal{Y}$$

Figure 5.3: The channel model with the channel transition matrix, showing $P_{Y|X}(y_j|x_i)$, at it's centre. Input data set $\mathcal{X}$ and output data set $\mathcal{Y}$ are specified by the joint probability distribution $P_{Y|X}(y_j|x_i)$. This figure is a combination of equation 6.1 and figure 6.3 from Moser et al. (2012).

probabilistic characterization of the input-output relationship. This relationship can be mathematically defined with the use of *the channel*.

5.4.1 Defining the Channel

The channel $(\mathcal{X}, P_{Y|X}(y_j|x_j), \mathcal{Y})$ has the following properties

1. An input data set $\mathcal{X} \triangleq x_1, ..., x_s$, where s denotes the number of input data
2. An output data set $\mathcal{Y} \triangleq y_1, ..., y_t$, where t denotes the number of output data
3. A conditional probability distribution $P_{Y|X}(y_j|x_i)$. This represents the probability of observing $Y = y_j$ in the output given $X = x_j$ has been sent, $1 \leq i \leq s$, $1 \leq j \leq t$

The channel properties thus determine the relationship between the input, $X \in \mathcal{X}$, and output $Y \in \mathcal{Y}$, and are defined by a set of conditional probabilities, termed the *forward conditional probability*, $P_{Y|X}(y_j|x_i)$, which states the probability of receiving an output y_j given an input x_j.

The Channel transition matrix in Figure 5.3 has the following properties

1. Entries on the i^{th} row have probabilities of observing the values of the output data, Y, for the range $y_1, ..., y_t$ given the i^{th} value of the input data set, X, x_i

2. Entries on the j^{th} column have probabilities of observing the values of the input data set, X, for the range $x_1, ..., x_s$ given the j^{th} value of the output data set, Y, y_j

3. The sum of the probabilities in a row always equals 1

$$\sum_{j=1}^{t} P_{Y|X}(y_j, x_i) = 1 \tag{5.18}$$

   meaning for each x_i, there is certainty that something will come out and that $P_{Y|X}(y_j, x_i)$ gives the distribution of these probabilities.

4. If $P_X(x_i)$ is the probability of the i^{th} input, then

$$\sum_{s=1}^{s} \sum_{j=1}^{t} P_{Y|X}(y_j, x_i) P_X(x_i) = 1 \tag{5.19}$$

   meaning, if something is input to the channel, something will come out.

The probabilities in $P_{Y|X}(y_j, x_i)$, $1 \leq i \leq s$, $1 \leq j \leq t$, fully characterise the channel. The channel is assumed to be stationery, that is to say the probabilities are invariable with time.

5.4.2 Channel Relationships

There are s possible inputs $x_1, ..., x_s$. If x_i is input to the channel, the probability of observing the y_j output from the channel is given by the conditional probability $P_{Y|X}(y_j, x_i)$. Hence, the probability of simultaneously observing the joint probability of $X = x_i$ and $Y = y_j$ is

$$P_{X,Y}(x_i, y_j) \triangleq P_{Y|X}(y_j|x_i)P_X(x_i) \tag{5.20}$$

where $P_X(X_i)$ is the probability that x_i is selected.

The probability that y_j will occur at the channel output can be determined by observing the simultaneous pairings of $Y = y_j$ and $X = x_i$ for $1 \leq i \leq s$

$$\begin{aligned} P_Y(y_j) &= P_{Y|X}(y_j|x_1)P_X(x_1) + ... + P_{Y|X}(y_j|x_s)P_X(x_s) \\ &= \sum_{i=1}^{s} P_{Y|X}(y_j|x_i)P_X(x_i), \quad 1 \leq j \leq t \end{aligned} \tag{5.21}$$

Further simplifying equation 5.21 with the definition of equation 5.20 yields

$$P_Y(y_j) = \sum_{i=1}^{s} P_{X,Y}(x_i, y_j), \quad 1 \leq j \leq t \tag{5.22}$$

Consider again Equation 5.20 which relates the probability of both x_i and y_j occurring with the input distribution, X, via the *forward conditional probability*, $P_{Y|X}(y_j|x_i)$, i.e. the probability that y_j will be output given an input value x_i. $P_{X,Y}(x_i, y_j)$ can also be written as

$$P_{X,Y}(x_i, y_j) = P_{X|Y}(x_i|y_j)P_Y(y_j) \tag{5.23}$$

This time the joint probability, $P_{X,Y}(x_i, y_j)$, is based on the output distribution, Y, and the *backward conditional probability*, $P_{X|Y}(x_i|y_j)$, i,e, the probability that an x_i was input given an output y_j. Equating Equation 5.20 and Equation 5.23 results in the well known *Bayes's Theorem* on conditional probabilities (Bayes, 1763)

$$P_{X|Y}(x_i|y_j) = \frac{P_{Y|X}(y_j|x_i)P_X(x_i)}{P_Y(y_j)} \tag{5.24}$$

Subbing Equation 5.21 into Equation 5.24

$$P_{X|Y}(x_i|y_j) = \frac{P_{Y|X}(y_j|x_i)P_X(x_i)}{\sum_{i'=1}^{s} P_{Y|X}(y_j|x_{i'})P_X(x_{i'})} \tag{5.25}$$

and summing over all x_i

$$\begin{aligned}\sum_{i=1}^{s} P_{X|Y}(x_i|y_j) &= \sum_{i=1}^{s} \frac{P_{Y|X}(y_j|x_i)P_X(x_i)}{\sum_{i'=1}^{s} P_{Y|X}(y_j|x_{i'})P_X(x_{i'})} \\ &= \frac{\sum_{i=1}^{s} P_{Y|X}(y_j|x_i)P_X(x_i)}{\sum_{i'=1}^{s} P_{Y|X}(y_j|x_{i'})P_X(x_{i'})} \\ &= 1 \end{aligned} \tag{5.26}$$

It is thus demonstrable that the total probability in the system must sum to 1, i.e. if given some output y_j, some x_i was put into the channel.

5.5 System Entropies

The channel transfers the probabilistic information-carrying message X into the output Y via the conditional probability law, $P_{Y|X}(y_j|x_i)$. The input and output channels are thus by definition uncertain, i.e. it cannot be known with certainty

which input x_i, and which output y_j will be sent and received respectively. The system can only be considered in terms of probabilistic characterizations. This leads to the question, how much *aggregate* information, or amount of uncertainty, is there in the overall channel system? If the channel relationship input and output data, X and Y, are applied to Shannon's Entropy, Equation 5.8 respectively becomes Equation 5.27 and Equation 5.28

$$H(X) = \sum_{i=1}^{s} P_X(x_i) \log_2 \frac{1}{P_X(x_i)} \tag{5.27}$$

$$H(Y) = \sum_{j=1}^{t} P_Y(y_j) \log_2 \frac{1}{P_Y(y_j)} \tag{5.28}$$

5.5.1 Bounds on the Entropy

If a random message, U, has r possible values

$$0 \leq H(U) \leq \log_2 r \text{ bits} \tag{5.29}$$

where

$$H(U) = 0 \qquad \text{if and only if } p_i = 1 \text{ for some } i \tag{5.30}$$

$$H(U) = \log_2 r \text{ bits} \qquad \text{if and only if, } p_i = \frac{1}{r} \; \forall \; i \tag{5.31}$$

It can be shown that $H(U) \geq 0$, $H(U) = 0$ if the input is certain, and $H(X)$ is maximised when all x_i are equally likely. That is to say, unless we are absolutely certain of the message sent and received, x_i and y_j, there is an entropy associated

with the random message and that entropy is maximised if all possible sent messages are equally likely.

See proof in B.2.

5.5.2 Joint Probability

When $X = x_i$ and $Y = y_j$ simultaneously the probability of this event is given by the joint probability $P_{X,Y}(x_i, y_j)$. Analogous to Equation 5.27 and Equation 5.28 the joint entropy for the simultaneous event is defined as

$$H(X,Y) \triangleq \sum_{i=1}^{s}\sum_{j=1}^{t} P_{X,Y}(x_i, y_j) \log_2 \left(\frac{1}{P_{X,Y}(x_i, y_j)} \right) \tag{5.32}$$

which measures the total uncertainty contained in the channel input and output and hence the total channel system. Relating $H(X,Y)$ with $H(X)$ and $H(Y)$, there are two cases to consider, when $H(X)$ and $H(Y)$ are statistically independent of one another, and when $H(X)$ and $H(Y)$ are dependent on one another. In the independent case X and Y are characterised by

$$P_{X,Y}(x_i, y_j) = P_X(x_i) P_Y(y_j) \tag{5.33}$$

(Bertsekas et al., 2002). Hence in the independent case from Equation 5.32 and Equation 5.33

$$H(X,Y) = H(X) + H(Y) \tag{5.34}$$

See B.3 for a full proof.

The following results hold in the case when X and Y are dependent on the relationship between the joint entropy, $H(X,Y)$, and the individual entropies, $H(X)$ or $H(Y)$,

$$H(X,Y) = H(X) + H(Y|X) \tag{5.35}$$

which is typically true since the channel output depends, at least in part, on the channel input. The conditional entropy associated with Y given X is given by

$$H(Y|X) \triangleq \sum_{i=1}^{s} \sum_{j=1} P_{X,Y}(x_i, y_j) \log_2 \left(\frac{1}{P_{Y|X}(y_j, x_i)} \right) \tag{5.36}$$

See B.4 for a full proof.

Thus the joint entropy, $H(X,Y)$, is the sum of the input entropy, $H(X)$, and the conditional entropy, $H(Y|X)$, which measures the uncertainty remaining in Y given X is known. N.B. If X and Y are independent, i.e. one can infer nothing about Y even if X is already known, then $H(Y|X) = H(Y)$ and Equation 5.35 becomes Equation 5.34.

Finally, if starting from Equation 5.23, the alternate expression for $P_{X,Y}(x_i, y_j)$, $H(X,Y)$, can be expressed as

$$H(X,Y) = H(Y) + H(X|Y) \tag{5.37}$$

indicating that the joint entropy is symmetric, i.e. whether we consider the received output, y_j, given a specific input, x_j, or vice versa.

5.6 Mutual Information

Combining the now established definitions of information, or more correctly uncertainty, and the means by which this information is transmitted, the tools are present to define MI. In Figure 5.3, the clear outcome is to know how much information can be gained about the input, based on the observed output $Y = y_j$. The difference in uncertainty before and after receiving y_j measures the gain in information from the reception of y_j.

On the transmission side, the probability that x_i occurs is given by $P_X(x_i)$, known as the *a priori probability* of x_i. On the reception side, the probability that upon receiving y_j, x_i was sent, is defined by the *a posteriori probability* (or *backwards conditional probability*), $P_{X|Y}(x_i, y_j)$. The change in probability from *a priori* to *a posteriori* is closely related to the amount of information that can be learnt about x_i from the reception of y_j.

As such, this gain in information is called *mutual information* and is defined as

$$\underbrace{I(x_i; y_j)}_{\substack{\text{information gain or} \\ \text{uncertainty loss after} \\ \text{receiving } y_j}} \triangleq \underbrace{\log_2\left(\frac{1}{P_X(x_i)}\right)}_{\substack{\text{uncertainty before} \\ \text{receiving } y_j}} - \underbrace{\log_2\left(\frac{1}{P_{X|Y}(x_i|y_j)}\right)}_{\substack{\text{uncertainty after receiving} \\ y_j}}$$

$$= \log_2\left(\frac{P_{X|Y}(x_i|y_j)}{P_X(x_i)}\right) \tag{5.38}$$

If $X = x_i$ and $Y = y_j$ are independent, $P_{X|Y}(x_i|y_j) = P_X(x_i)$ and $I(x_i; y_j) = 0$, i.e. no information about x_i is gained by the reception of y_j. The other extreme is a noiseless channel, $y_j = x_i$, where $P_{X|Y}(x_i|y_j) = 1$. Being completely certain about which input symbol has been sent, mutual information attains the maximum value

$\log_2(\frac{1}{P_X(x_i)})$; hence, all information about x_i is conveyed without any loss through the channel.

Recall from Equation 5.20 and Equation 5.23 that probability is symmetric under certain conditions

$$P_{X|Y}(x_i|y_j)P_Y(y_j) = P_{X,Y}(x_i, y_j) = P_{Y|X}(y_j|x_i)P_X(x_i) \tag{5.39}$$

In this case

$$I(x_i; y_j) = \log_2\left(\frac{P_{X,Y}(x_i, y_j)}{P_X(x_i)P_Y(y_j)}\right) = I(y_j; x_i) \tag{5.40}$$

Therefore, x_i provides the same amount of information about y_j as y_j does about x_i, hence the term *mutual information*.

5.7 System Mutual Information

5.7.1 Define System Mutual Information

Having characterised the MI of a specific input-output pair, it is now important to average the MI with respect to both the input and output. This will account for the statistical behaviour of the channel, caused by the random nature of the source and channel output.

The *system mutual information*, or average MI is defined as

$$I(X;Y) \triangleq \sum_{i=1}^{s}\sum_{j=1}^{t} P_{X,Y}(x_i, y_j) I(x_i; y_j)$$
$$= \sum_{i=1}^{s}\sum_{j=1}^{t} P_{X,Y}(x_i, y_j) \log_2 \left(\frac{P_{X,Y}(x_i, y_j)}{P_X(x_i) P_Y(y_j)} \right) \tag{5.41}$$

System mutual information has the following properties:

1. $I(X;Y) \geq 0$
2. $I(X;Y) = 0$ if and only if X and Y are independent
3. $I(X;Y) = I(Y;X)$

which means the system mutual information must have a positive value unless there is no relationship between the two data sets. Also, the input data informs us about the output data as much as the output data does about the input data.

5.7.2 Continuous Mutual Information

The previous MI definitions have dealt with discrete data. However, there are many cases whereby data is not discrete but continuous, including the data dealt with in the studies of this thesis discussed in chapter 4. In this case, the form of Equation 5.41 changes from a discrete summation to a continuous integral

$$I(X;Y) = \int_{i=1}^{s}\int_{j=1}^{t} P_{X,Y}(x_i, y_j) \log_2 \left(\frac{P_{X,Y}(x_i, y_j)}{P_X(x_i) P_Y(y_j)} \right) dx\ dy \tag{5.42}$$

5.7.3 System Mutual Information and Entropy

Many forms of entropy have been covered thus far, with that in mind, this section ends by relating entropy to mutual Information. Starting from the system mutual information of Equation 5.41

$$I(X;Y) = \sum_{i=1}^{s}\sum_{j=1}^{t} P_{X,Y}(x_i, y_j) \log_2 \left(\frac{P_{X,Y}(x_i, y_j)}{P_X(x_i) P_Y(y_j)} \right) \tag{5.43}$$

$$= \sum_{i=1}^{s}\sum_{j=1}^{t} P_{X,Y}(x_i, y_j) \left(\log_2 P_{X,Y}(x_i, y_j) \right. \tag{5.44}$$

$$\left. - \log_2 P_X(x_i) - \log_2 P_Y(y_j) \right)$$

$$\tag{5.45}$$

subbing in Equation 5.22 for X and Y

$$\tag{5.46}$$

$$= -\sum_{i=1}^{s}\sum_{j=1}^{t} P_{X,Y}(x_i, y_j) \log_2 \left(\frac{1}{P_{X,Y}(x_i, y_j)} \right) \tag{5.47}$$

$$+ \sum_{i=1}^{s} P_X(x_i) \log_2 \left(\frac{1}{P_X(x_i)} \right) + \sum_{j=1}^{t} P_Y(y_j) \log_2 \left(\frac{1}{P_Y(y_j)} \right)$$

$$\tag{5.48}$$

subbing in Equation 5.27, Equation 5.28, and Equation 5.32

$$\tag{5.49}$$

$$= H(X) + H(Y) - H(X,Y) \geq 0 \tag{5.50}$$

Since

$$H(X,Y) = H(X) + H(Y|X) = H(Y) + H(X|Y) \tag{5.51}$$

also

$$I(X;Y) = H(X) - H(X|Y) = H(Y) - H(Y|X) \tag{5.52}$$

5.8 Closing Remarks

Defining entropy and the channel have been crucial steps in the path to *mutual information*. MI is a measure of the reduction in the uncertainty, a more accurate description than information, of a system before and after measuring the input and output events. The uncertainty itself has been shown to derive from the definitions of entropy presented at the start of the chapter and underpins the definition of MI. Thus, the loss in uncertainty, when averaged over the entire system, gives a measure of how strongly an input and output data set are related to one another.

It logically follows that if the amount of uncertainty in the system between the two data sets is reduced by only a small amount, then there is little to learn from one data set about another. However, if the reduction in uncertainty is large, then it is demonstrable that these data sets have a strong relationship with one another.

Thus, the groundwork has now been laid to show that MI provides a useful method for assessing the relationship between the solar wind and the proxy data sets to be investigated.

In summary

$$I(X;Y) = \begin{cases} H(X) + H(Y) - H(X,Y) \\ H(X) - H(Y|X) \\ H(Y) - H(X|Y) \end{cases} \tag{5.53}$$

the equivocation is given by

$$H(X|Y) = H(X) - I(X;Y) \tag{5.54}$$

$$H(Y|X) = H(Y) - I(X;Y) \tag{5.55}$$

the joint entropy is given by

$$H(X,Y) = \begin{cases} H(X) + H(Y) - I(X;Y) \\ H(X) + H(Y|X) \\ H(Y) + H(X|Y) \end{cases} \tag{5.56}$$

and continuous mutual information is given by

$$I(X;Y) = \int_{i=1}^{s} \int_{j=1}^{t} P_{X,Y}(x_i, y_j) \log_2 \left(\frac{P_{X,Y}(x_i, y_j)}{P_X(x_i) P_Y(y_j)} \right) dx \; dy \tag{5.57}$$

Chapter 6

Method

Though MI can be expressed as the singular equation, Equation 5.42, that will be applied to the considered data, the practical application of this technique is significantly more complex. Data must first be prepared so that one can create the channel defined in subsection 5.4.2, in order to calculate the MI. Then, one must decide upon the different estimators that exist to apply MI to the data. We use Kraskov, Stögbauer, and Grassberger, known henceforth as KSG, and describe its methods briefly in section 6.2. Finally, for a rigorous study we must calculate the uncertainties of these results as shown in section 6.3.

In addition, we have an understanding of the response time of the Earth's magnetosphere, the time from initial interaction between the solar wind and magnetosphere to measurement of geomagnetic indices, at approximately 30 - 60 mins for the AL and SYM-H indices, (Stumpo et al. (2020); Wintoft (2005); March et al. (2005)). The response time at Saturn is much more poorly understood. In either case, this phenomena must be explored to better understand the interaction of the solar wind as a driver of magnetospheric dynamics, which is done in section 6.4.

Working with propagated data also creates additional limitations on the data, as the Earth and Saturn are not stationery bodies with respect to the Sun. This effect on the propagation of the data must be accounted for and is discussed in section 6.5.

6.1 Equalising

As discussed in section 5.4, to calculate MI *The Channel* must be constructed, representing the joint probability distribution between a pair of considered data sets. The joint probabilities between variables of both data sets are given by $P_{Y|X}(y_j|x_j)$. In order to build the joint probability between two variables each data set must have a variable that can correspond to the other. Hence, the first step we must consider is how to construct these.

All data sets include time data of variable measurements, as such all variables can be indexed with a corresponding time stamp. The aim is to investigate the interaction of solar wind data with magnetosphere dynamics, by observing the effects this creates. In the case of Saturn this is via SKR data, in the case of the Earth this is via geomagnetic indices and coupling functions. The following assumption is made regarding the data:

- It is assumed the interaction is seen at the same time stamp for the measurement of the solar wind variable and the compared variable.

It is self-evident that this cannot be not the case (at least not consistently). A magnetospheric response time exists, whereby the solar wind must travel through the magnetospheric system before we see its effect in the measured data. Additionally, in

the case of propagated solar wind, uncertainty exists in its arrival time. Therefore, in section 6.4 these uncertainties are accounted for by offsetting the time stamps.

Data sets are not always of a consistent size to one another, the Cassini mission ran from 2014 until 2017, providing 13 years of continuous data, whereas OMNI data is available for decades. Additionally, sampling rates can differ, and data sets can be filled with null data points.

6.1.1 Sampling Rates

In the case of comparing propagated solar wind data to SKR data, they have sampling rates of 10 and 3 minutes respectively (see Table 4.3 and Table 4.4). In order to produce the joint probability distibution, $P_{Y|X}(y_j|x_j)$, that populates the channel, there must be a corresponding data point from each data set. If both data sets have differing time stamps, corresponding data points can not be easily matched. As such the sampling rate of the higher resolution data is adjusted to match the lower resolution data.

The resolutions are matched by using the time stamps of the low resolution data, which we call X. For each time stamp in X, all time stamps of the comparison data set, which we call Y, within the time stamp of X by +/- half the time resolution of X, are gathered. These data points from Y are averaged into a single data point and given the same time stamp used in X.

Though averaging the data involves an element of smoothing, using this method encapsulates the full system of the data. It also avoids neglecting significant amounts of high resolution data and having to tailor a weighting method for each considered data set, in order to determine which data points can be matched to the low resolution

data. Alternative approaches could have been taken, such as aligning each solar wind data point with the nearest time stamp and interpolating the missing solar wind data points to equal the SKR data set size. However, whereas averaging takes the average of real data points, interpolating generates synthetic data points. At such a high resolution it is unlikely there is sufficient variation that the synthetic data would not be representative of the real conditions. Nevertheless, it was therefore decided to use averaging, whereby the smoothed data is still representative of the true solar wind distribution, albeit at a lower resolution.

6.1.2 Final Step to Build the Channel

Once the sampling rates are matched the final step is to remove all null, fill, and zero values as appropriate from both data sets considered. Once these data points have been removed, should they be present, the remaining data sets can be compared by their time stamps. Only data points with a time stamp present in both data sets will be kept. The final point is justified by the following: if there is a data point for a timestamp in one data set and no data point for the same timestamp in the other data set, then Equation 5.10, for the absent data point, becomes $0 \log 0 = 0$, as $x \log x \to 0$ as $x \to 0$. Thus, adding a zero term adds no entropy and by extension no MI value (Cover et al., 1991). There is only value to retaining data, where data is present in both data sets for a given timestamp. The result is two equally sized data sets, with a means of pairing individual data points in order to produce the joint probabilities of *The Channel*.

6.2 KSG Estimator

6.2.1 Estimating the Variance of KSG

In section 5.8, it was shown that MI can be expressed according to Equation 5.53, combining the marginal and joint Shannon entropies. From this equation, Kraskov et al. (2004) proposed an MI estimator, known as a KSG[1] estimator, to calculate these entropies using the k^{th} nearest neighbour method to detect fine structures in the underlying probability distribution. Here, each of the marginal and joint Shannon entropy terms can be expressed as

$$\hat{H}_{KL}(X) = -\psi(k) + \psi(N) + log(c_d) + \frac{d}{N}\sum_{i=1}^{N} log(\epsilon^{(k)}(i)) \tag{6.1}$$

where ϕ is the digamma function, d is the dimensionality of x, N is the total number of samples, c_d is the volume of a unit ball with d dimensions, and $\epsilon^{(k)}(i)$ is twice the distance between the i^{th} data point and its k^{th} neighbour (Kozachenko et al., 1987). The MI is thus estimated as

$$\hat{I}^{(k)}_{KSG} = \psi(k) - \frac{1}{k} - \langle \psi(n_x^{(k)}) + \psi(n_y^{(k)}) \rangle + \psi(N) \tag{6.2}$$

where averaging is over the samples (Kraskov et al. (2004); Stögbauer et al. (2004)). Note that, if $\langle \psi(n_x^{(k)}) \rangle$ and $\langle \psi(n_y^{(k)}) \rangle$ increase, the MI estimate drops.

The meaning behind equation Equation 6.1 and Equation 6.2 is explained in Kozachenko et al. (1987) and Kraskov et al. (2004), respectively. In short, k is a free parameter that must be chosen *a priori*. If $k = 1$, fine scale features in the joint probability distribution will be picked up but result in large scale statistical

[1] KSG is available in the open source python library *SciPy*.

fluctuations. If $k >> 1$, fine scale structures may be missed but statistical fluctuations will be smaller.

The optimal k depends on the structure of the spatial features in the data. These can be non-trivial and exist on multiple scales. The optimal k should also depend on N, since fine features can only be observed at high sample densities. In order to estimate the optimal value of k , one must first estimate the standard error of the estimator, and also estimate the bias of the estimator.

6.3 Uncertainties

An important question when assessing the validity of any MI results for a paired data set is: how confident can one be in the result? In order to make this assessment, the level of uncertainty in the result must be solved. However, the solution is non-trivial. Information is non-linear and as such, simple techniques like bootstrapping, which are only applicable when the quantities are linear in the underlying probability distribution, are non-applicable (Tibshirani et al., 1993).

This can be understood intuitively if one thinks about the process of bootstrapping, where a data set is only a subset of all possible data. Consider a population survey, it can be for many millions of people but it is unlikely to be for *all* people. So, how can there be certainty that any results are statistically accurate? If the sample of the population is sufficiently large, it should be representative of the population as a whole and approximate to a normal distribution. If the original sampling of the population were repeated, the second distribution would be unlikely to perfectly match the first sampling but would approximate its distribution. If this process were

repeated again and again, a range of slightly differing distributions would be sampled, allowing statistics on the accuracy of the data distribution to be calculated, such as the mean or standard error.

However, it is typically impractical or even impossible to keep taking population samples. Instead, when the data is sufficiently large and so approximates the distribution of the true population, bootstrapping can be applied. Bootstrapping takes random subsamples from the original data sample, with replacement, rather than repeating the sampling itself. Using these subsamples, one solves the calculation made on the real data distribution for the bootstrapped samples. The results of these subsamples will give a range of potential values the data distribution could take, much like the variation of repeatedly taking independent population samples. Using this distribution of results, the mean, standard deviation, or other desired statistics can be solved for, overcoming the impracticality of taking repeated population samples.

However, when one attempts to solve MI with bootstrapping, this approach will quickly breakdown. Bootstrapping the data with replacement will result in duplicate data points. Estimators such as KSG will interpret these repetitions as fine-scale, high-information features. Consequently, the MI value will be overestimated. In simpler terms, sampling with replacement will increase the probability of repeated data point pairs, increasing their information worth. This can be easily demonstrated using a bivariate Gaussian distribution, where the analytical value of MI, $I_{analytical}$, is known. $I_{analytical}$ is given as

$$I_{analytical} = -\frac{1}{2}\log_2(1-\rho^2) \tag{6.3}$$

where ρ is the correlation coefficient. Observing Figure 6.1, data is sampled

from a Gaussian distribution with $\rho = 0.6$ and $I_{analytical} \simeq 0.32$. When samples are taken without replacement from this Gaussian distribution (independent population samples) the mean and standard deviation of the these samples is 0.33 ± 0.04 bits, which matches closely to $I_{analytical}$. However, when the distribution is repeatedly bootstrapped, (sampling the same population with resampling) repeated data points are interpreted as high information features, resulting in a mean and standard deviation equal to 0.94 ± 0.1 bits, which greatly exceeds $I_{analytical}$.

There is only one data set per variable in this study; decade spanning data sets have not been be independently sampled hundreds of times. As has just been proven, in the absence of multiple data sets bootstrapping these singular data sets will not work. Yet, Holmes et al. (2019) offers a solution to this problem. With a known analytical value of the MI, as given in Equation 6.3, a bivariate Gaussian distribution can be used to empirically derive the uncertainty of MI. Using data taken from this bivariate Gaussian test case, the methods described in Holmes et al. (2019) are replicated in the remainder of this section.

For $N >> 1$, where N is the size of the data set, the variance of functions such as Equation 6.2 is an average of N independent and identically distributed random variables and scales as $1/N$. For N > 50, this holds true for bivariate Gaussians as illustrated in Figure 6.2. Therefore, the variance of MI for the KSG estimator can be written as

$$\sigma^2_{KSG}(N) = \frac{B}{N} \tag{6.4}$$

where B is an empirically derived value that depends on the distribution considered.

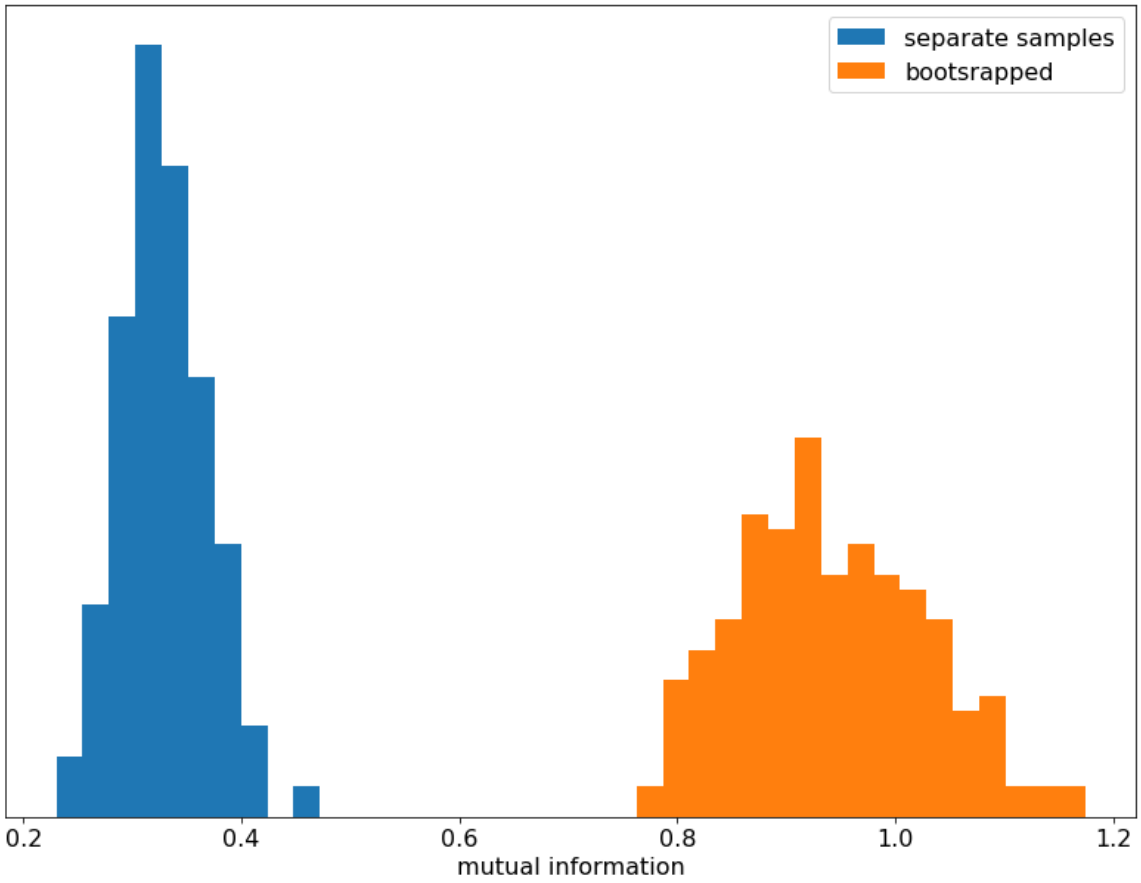

Figure 6.1: Bootstrapping MI. Both distributions represent the MI values of data taken from a bivariate Gaussian, with ρ=0.6, for 1,000 data points. Blue samples show the distribution of MI values when a population is repeatedly sampled. The mean of the distribution is 0.33 $\pm$ 0.04 bits. Orange samples show that when a single population sample is bootstrapped, the resampling is interpreted as high-information features. The result is a broader, and higher value distribution of MI values with a mean of 0.94 $\pm$ 0.1 bits.

In order to estimate B, the data is randomly subsampled by dividing it into n subsets, where n is an integer. These subsets are equal in size, or as close as

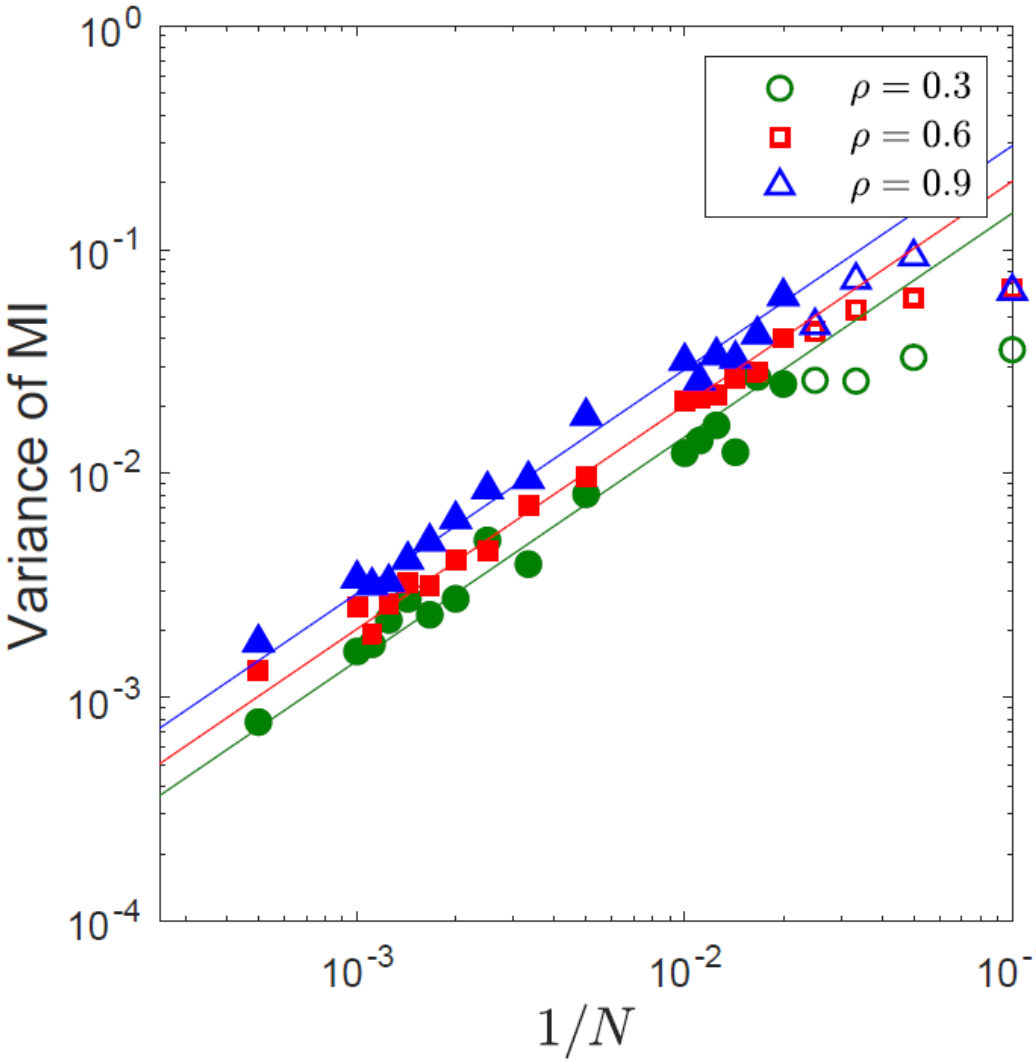

Figure 6.2: An $N = 1{,}000$ data points sample, for a bivariate Gaussian with $\rho = 0.3$, 0.6, and 0.9. 100 independent data sets, of different sizes for N, are generated for each value of ρ. $\sigma^2_{KSG}(N)$ is calculated for each N and plotted vs $1/N$. The resulting linear fit shows that variance scales as $1/N$ for $N >> 1$. Image Credit: Holmes et al. (2019).

is practicably possible. To maintain independent calculations of the variance, the partitions of subsets do not overlap, to ensure the subsets are of a size N/n. Subsets are not to be repeatedly calculated for each n, in an attempt to average the estimates and reduce the variation in variance for different N/n, as this does not produce independent samples of the variance.

$\mathbf{I}^{(k)}_{KSG}$ is calculated for each subset according to Equation 6.2, giving n values of $\mathbf{I}^{(k)}_{KSG}$. For the n values of $\mathbf{I}^{(k)}_{KSG}$, the variance estimate for these values gives the KSG variance, $\sigma^2_{KSG}(N/n)$. Thus, B is solved empirically by solving $\sigma^2_{KSG}(N/n)$ for multiple values of n and fitting Equation 6.4 to these values. With an empirically derived value for B, $\sigma^2_{KSG}(N)$ can be solved directly from Equation 6.4.

With these results, the estimate of the variance of the KSG estimator for the data set, of size N, is given by

$$\sigma^2_{KSG}(N) = \frac{B}{N} = \frac{\sum_i \frac{n_i - 1}{n_i} \sigma^2_{KSG}(N_i)}{\sum_i (n_i - 1)} \tag{6.5}$$

and the standard error of the variance is given by

$$var\ \sigma^2_{KSG}(N) = \frac{2B^2_{ML}}{\sum_i (n_i - 1) N^2} \tag{6.6}$$

where B_{ML}, the maximum likelihood of B, is given by

$$B_{ML} = \frac{\sum_i \frac{n_i - 1}{n_i} N \sigma^2_{KSG}(N_i)}{\sum_i (n_i - 1)} \tag{6.7}$$

the derivation of which can be found in the appendix of Holmes et al. (2019). In Figure 6.3 this method is independently applied to calculate the variance of a bivariate Gaussian of $\rho = 0.6$, successfully reproducing Fig 2 of (Holmes et al., 2019).

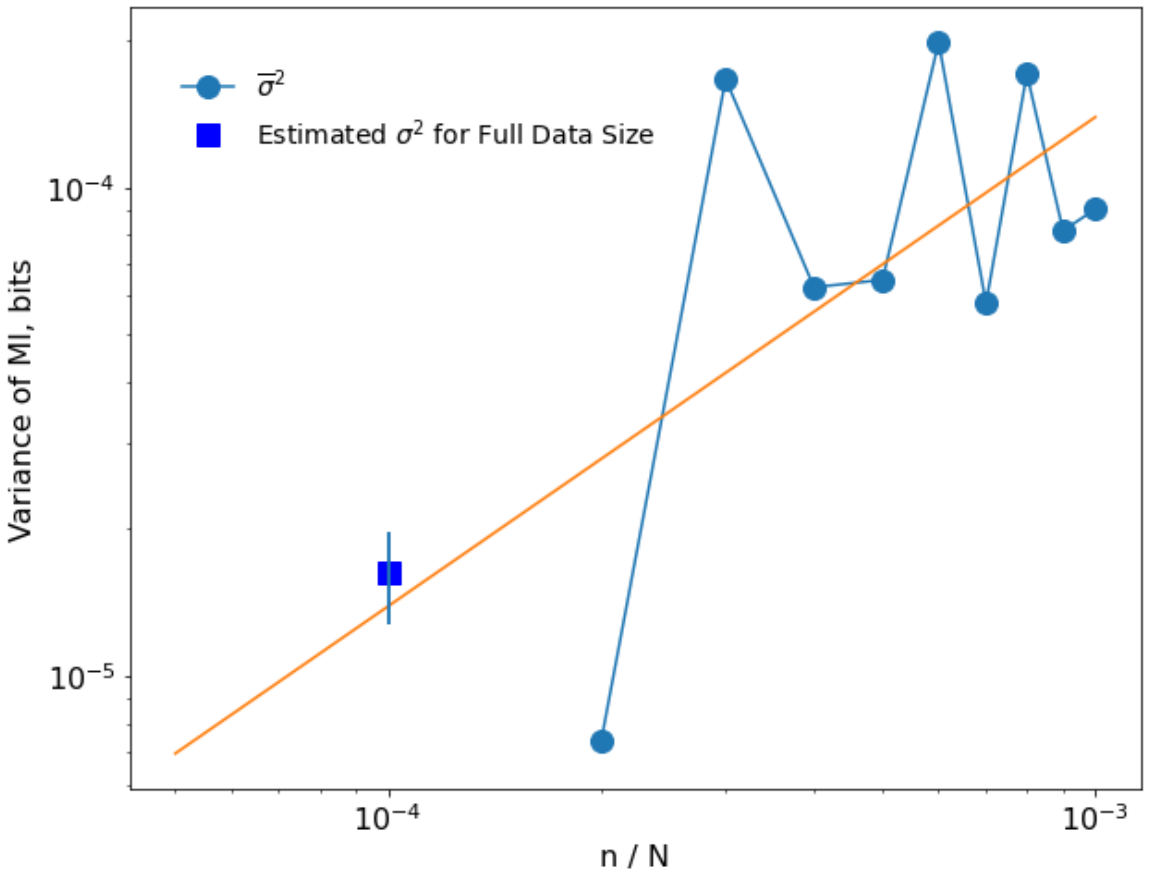

Figure 6.3: Reproduction of Fig 2 of (Holmes et al., 2019). An $N = 1{,}000$ data points sample, for a bivariate Gaussian with $\rho = 0.6$. The variance of KSG, with $k = 1$, for N/n data points is calculated. Circular data points represent the calculation of the variance of I, for each N/n subset. The square data point shows the estimate of the variance of the KSG estimator, with its own standard error given by Equation 6.5 and Equation 6.6 respectively. The slope is an unweighted linear fit, replicated as a guide to illustrate the variance of the estimator to the full data set size.

6.3.1 Detecting the Estimation Bias and Choosing k

The KSG estimator is biased for finite N and as such is sample size dependent. Holmes et al. (2019) uses the following approach to detect the bias for KSG.

The number of nearest neighbours, k, used by the KSG estimator can dramatically affect the MI value. For a large value of k the fine-scale features of the probability distribution will be overlooked by the KSG estimator resulting in an underestimation of the MI. Also, n_x^k and n_y^k, from Equation 6.2, grow with k. Thus, the expectation is that the standard deviation will be smaller at large k. For small values of k, statistical fluctuations will be larger and two factors may affect the bias of the KSG estimator. First, by choosing a small k, fine-scale features will be explored, rather than overlooked and reduce bias towards a smaller estimation of the MI. Secondly, that the larger fluctuations in n_x^k and n_y^k will create a larger, upward, N-dependent bias in $-\langle\psi(n_x^k)\rangle$ and $-\langle\psi(n_y^k)\rangle$ from Equation 6.2.

The affect of k on the KSG estimation of MI can be explored as a function of N for a range of k values. Selection of an optimal k will be under the following conditions:

- There is no sample-size-dependent drift compared to the estimator standard deviation, and
- the standard deviation is smallest.

The effect of varying k values on the KSG estimation of MI, for a range of n, is shown in Figure 6.4, successfully reproducing Fig 3 in Holmes et al. (2019). In agreement with Holmes et al. (2019), $k = 4$ is the most stable choice for the KSG estimator in the case of a bivariate Gaussian of $\rho = 0.6$.

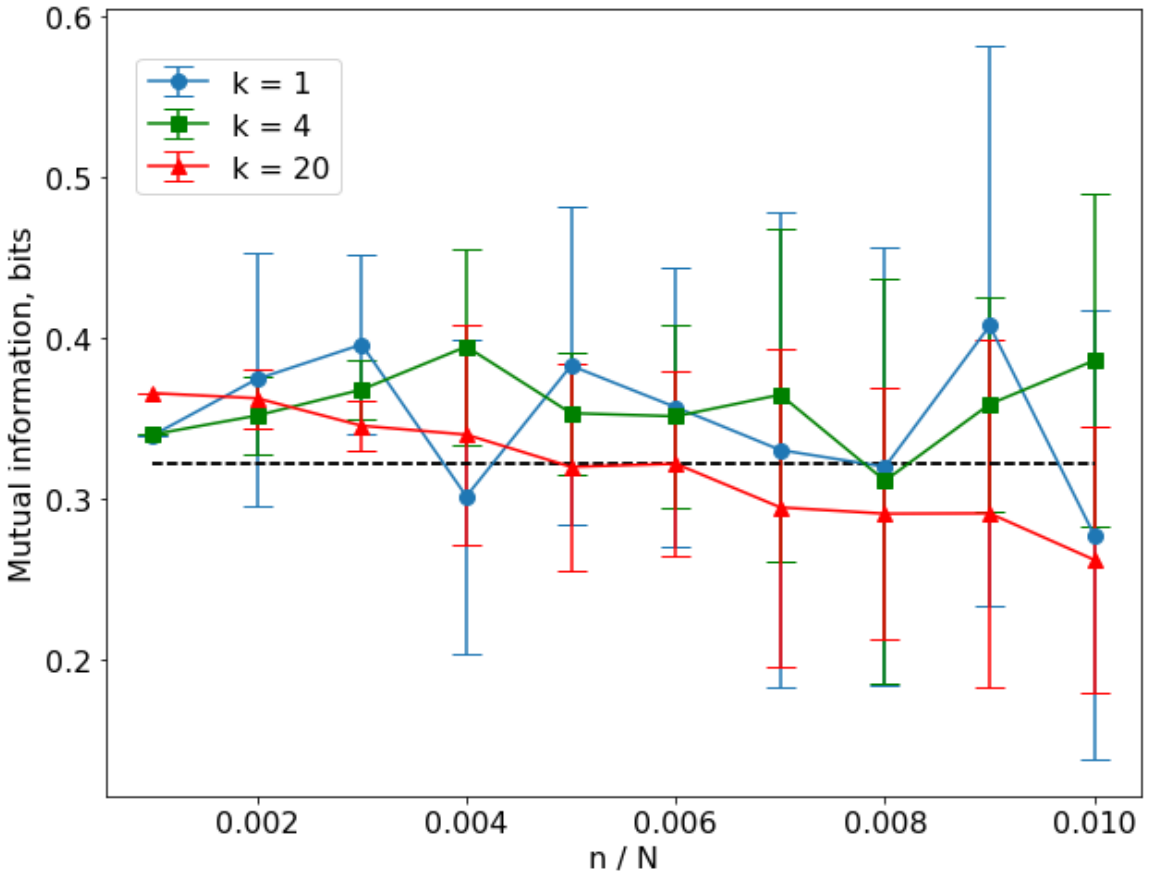

Figure 6.4: Reproduction of Fig 3 of Holmes et al. (2019). An $N = 1{,}000$ data points sample, for a bivariate normal Gaussian with $\rho = 0.6$. The data is separated into n_i non-overlapping subsets, where $i = 1, 2, ..., 10$ resulting in n/N data points for each subset. The mean I and σ is calculated for each subset using the KSG estimator for $k = 1$, 4, and 20. For $n = 1$, representing the full data set size, no value for σ can be estimated. A strong downward bias in I is observed for $k = 20$. $k = 1$ and $k = 4$ show a relatively stable estimation of I although $k = 1$ shows a much larger variance. Note, a larger number of data points was chosen than in Fig 3 for Holmes et al. (2019), to be consistent with this studies testing.

6.3.2 Renormalising the Heavy Tail

KSG has large biases for heavy-tailed distributions, which are present in all real data considered in this thesis. This bias can be traced back to the non-symmetric distribution of data points in ϵ - balls, found in Equation 6.1. For a bivariate log-normal Gaussian distribution with $\rho = 0.6$, Figure 6.5 reproduces Fig 4a of Holmes et al. (2019) by calculating the KSG estimation of I for different values of n and k. It is evident that the heavy-tailed data has a strong bias towards underestimation, as the value of MI, I, ranges from 0 to 0.03 bits, well below the expected value of $I_{analytical} \simeq 0.32$ bits.

Thanks to a special property of MI known as invariance, heavy-tailed distributions data can still be resolved without underestimation. MI is invariant under invertible transformations, which is also known as reparameterisation (Cover et al., 1991). As such, the marginal variables, x and y, can be reparameterised to a standard normal variable, for which the KSG estimator works well with little bias. Defining $r_i = 1, \ldots, N$ as the rank of the corresponding value for x_i, the reparameterisation is given by

$$x_i^{'} = \sqrt{2}\mathrm{Erf}^{-1}(2r_i - (N+1)) \tag{6.8}$$

where Erf^{-1} is the inverse of the error function.

Reparameterisation is thus applied to the same bivariate log-normal Gaussian distribution with $\rho = 0.6$. The resultant MI values are illustrated in Figure 6.6, reproducing Fig 4b of Holmes et al. (2019). It is clear reparameterisation has removed the bias caused by the heavy-tail data when compared with Figure 6.5. The scaling of the variance with $1/N$ after reparameterisation, as illustrated in Figure 6.2, is maintained.

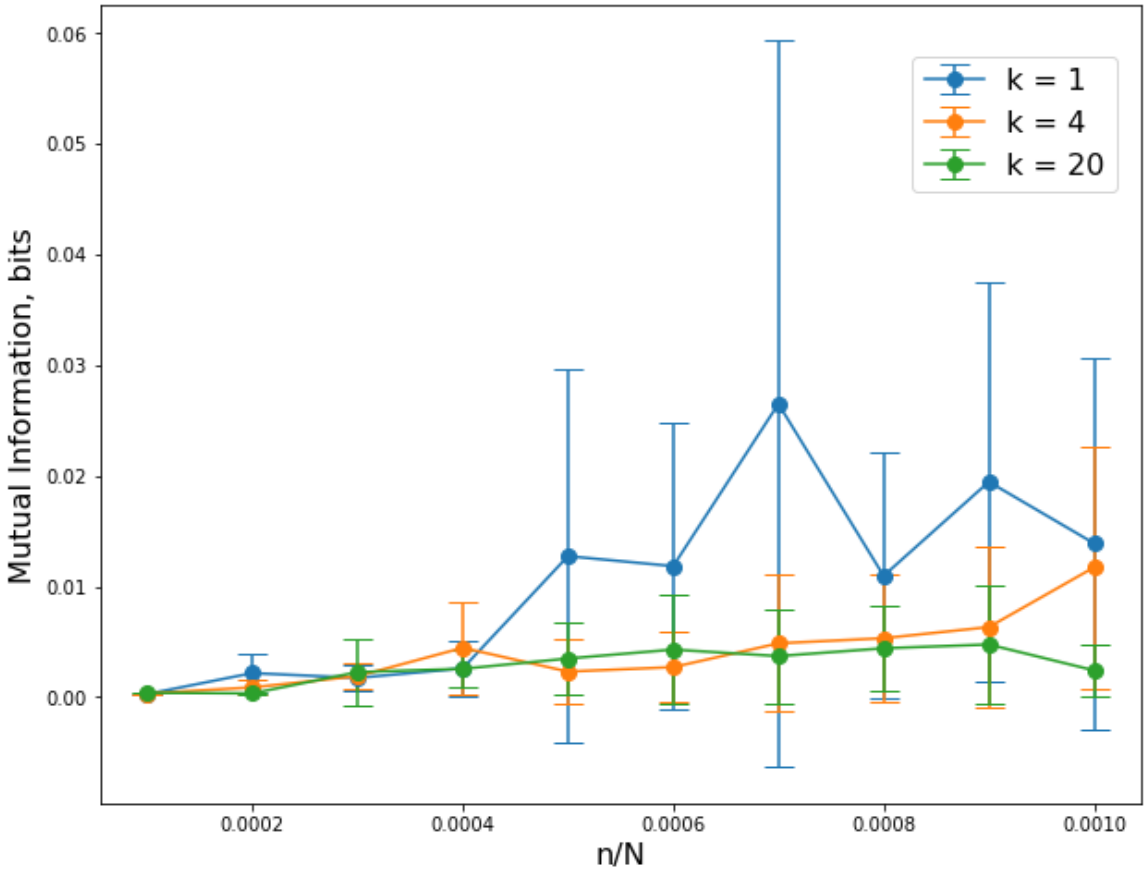

Figure 6.5: Reproduction of Fig 4a of Holmes et al. (2019). An $N = 1{,}000$ data points sample, for a bivariate log-normal Gaussian $P(x, y)$, with $\rho = 0.6$. The same method, as illustrated in Figure 6.4, is applied to this heavy-tailed data. $P(x, y)$ is solved as $x = e^{s_i}$, for $i = 1, \ldots, N$, where s_i is a sample drawn from a Gaussian distribution, S, and $y = e^{e^{u_i}}$, where $u = \rho \cdot s_i + (1 - \rho^2)^{0.5} \cdot t_i$, where t_i is a sample drawn from a Gaussian distribution, T. MI is severely underestimated from the expected value of $I_{analytical} \simeq 0.32$ bits, as a result of the heavy-tail distribution.

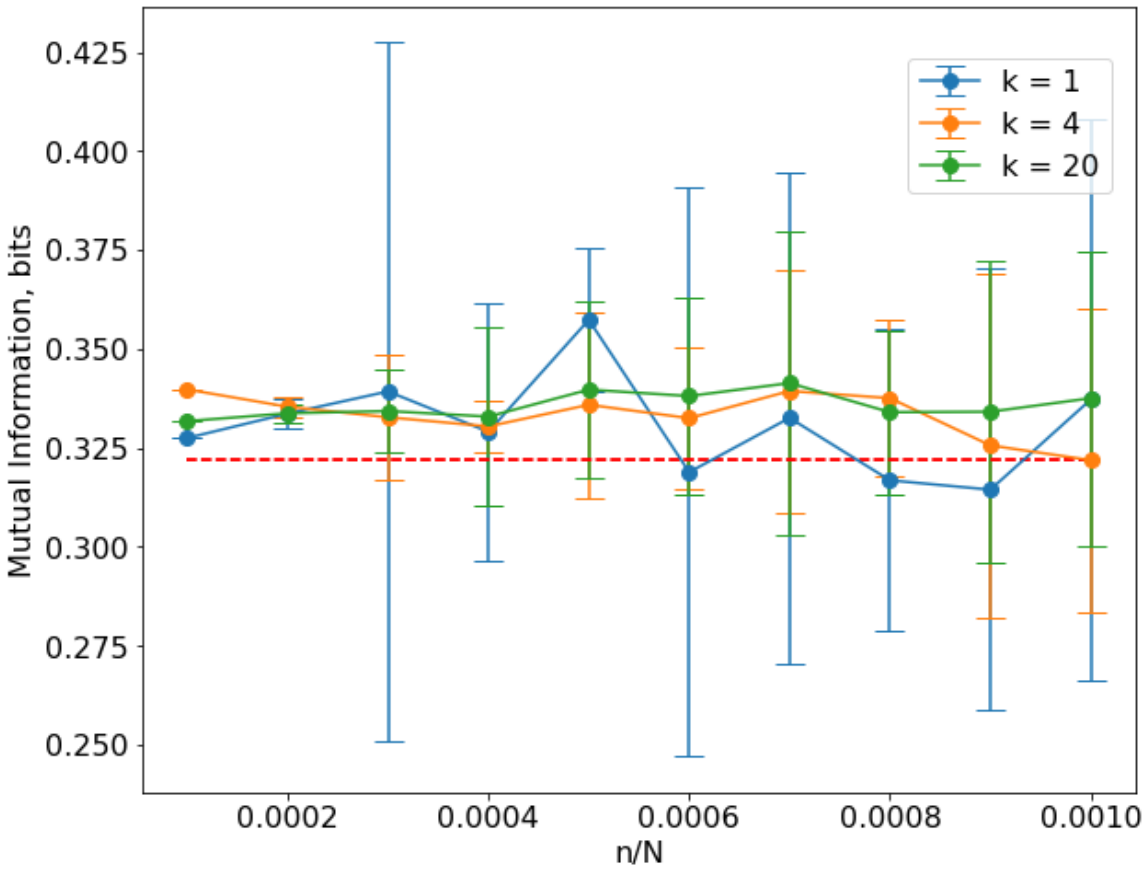

Figure 6.6: Reproduction of Fig 4b of Holmes et al. (2019). An $N = 1{,}000$ data points sample, for a bivariate log-normal Gaussian, $P(x, y)$, with $\rho = 0.6$, after undergoing reparameterisation. The same method, as illustrated in Figure 6.4, is applied to this reparameterised heavy-tailed data. $P(x, y)$ is solved as $x = e^{s_i}$, for $i = 1, \ldots, N$, where s_i is a sample drawn from a Gaussian distribution, S, and $y = e^{e^{u_i}}$, where $u = \rho \cdot s_i + (1 - \rho^2)^{0.5} \cdot t_i$, where t_i is a sample drawn from a Gaussian distribution, T. After reparameterisation, the heavy-tailed data returns to values approximating $I_{analytical} \simeq 0.32$ bits. This affirms the use of reparameterisation to account for the bias of heavy-tail data when using the KSG estimator.

6.3.3 Application to Real Data

Reparameterisation is now applied to real data as a final demonstration of its applicability. In this case the solar wind radial velocity variable, v_x, propagated using the propagation model of Tao et al. (2005), and the SKR variable, LH 100 - 400 KHz. Figure 6.7, a Kernel Density Estimate of the combined data's probability distribution, shows a prominent heavy-tailed distribution with no reparameterisation yet performed. When reparameterisation is applied according to Equation 6.8 the data is transformed into a standard normal variable, illustrated in Figure 6.8. Before reparameterisation the MI for real, heavy-tailed data can be assumed to be underestimated, as was the case in Figure 6.5 when considering the results of the Gaussian test case.

It should be noted that in the case of the real data, the size of the splits, n, has been adjusted upwards. This is to account for the larger number of data points in the real data, approximately 10^5, as opposed to 10^3 for the simulated Gaussian test data.

In total, 9 k values were tested: 1, 2, 3, 4, 5, 7, 10, 15, and 20. The conditions given in subsection 6.3.1 were applied by taking the gradient of the mean MI values for each k. According to the conditions, the sample-size-dependent drift compared to the estimator standard deviation should be non-existent. However, this is only the case when applied to an ideal Gaussian data set. Even after reparameterisation, the data is much larger and more complex. In no data set tested is the drift negligible. Therefore, the k value gradient closest to 0, and thus with the minimum sample-size-dependent drift, is chosen as the best value of k. This is valid when considering the estimated standard deviation, which for almost all values of the mean MI bounds all other mean MI values, keeping with the conditions considered.

When applying these methods to real data, a k value can be chosen and the bias of the heavy-tailed data accounted for. The method is applied to the real data illustrated in Figure 6.7 and Figure 6.8, where the smallest gradient both before and after reparameterisation is for $k = 1$. The resultant estimation of MI is 0.072 ± 0.005 bits before reparameterisation and 0.096 ± 0.006 after, see Figure 6.9 and Figure 6.10. By considering the gradient, it is found in almost all cases that the correct k value to choose is $k = 1$, which suggests the presence of fine-scale features in the data.

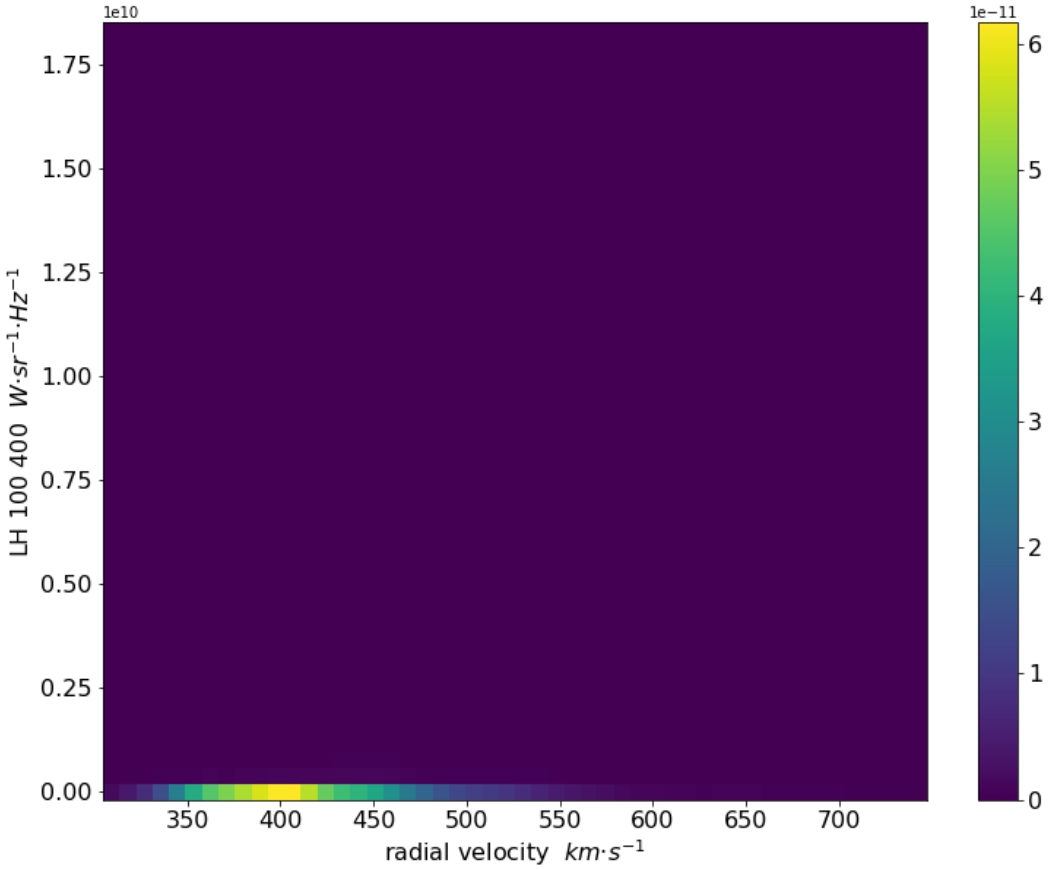

Figure 6.7: A Kernel Density Estimate plot of Left-Hand polarised (LH) SKR data, across the 100 - 400 KHz range (Table 4.4), against the propagated solar wind variable, radial velocity (Table 4.3). The data in both data sets have heavy-tail extensions. The resultant MI value is underestimated at 0.072 ± 0.005 bits, as described for heavy-tail data in subsection 6.3.2.

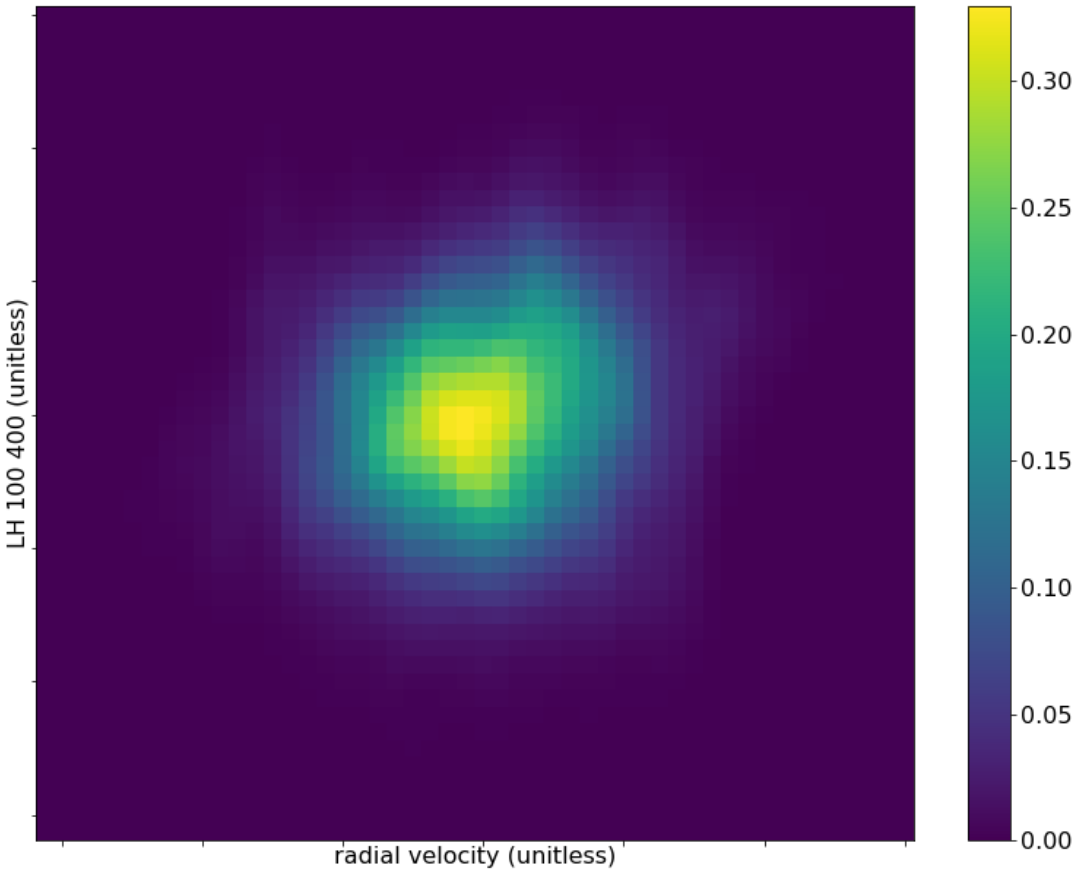

Figure 6.8: A Kernel Density Estimate plot of Left-Hand polarised (LH) SKR data, across the 100 - 400 KHz range (Table 4.4), with the propagated solar wind variable, radial velocity (Table 4.3). By reparameterising the data into a standard normal variable according to Equation 6.8, the presence, and consequent bias, of heavy-tails is largely eliminated from the data, ensuring a better MI estimate of 0.096 $\pm$ 0.006 bits.

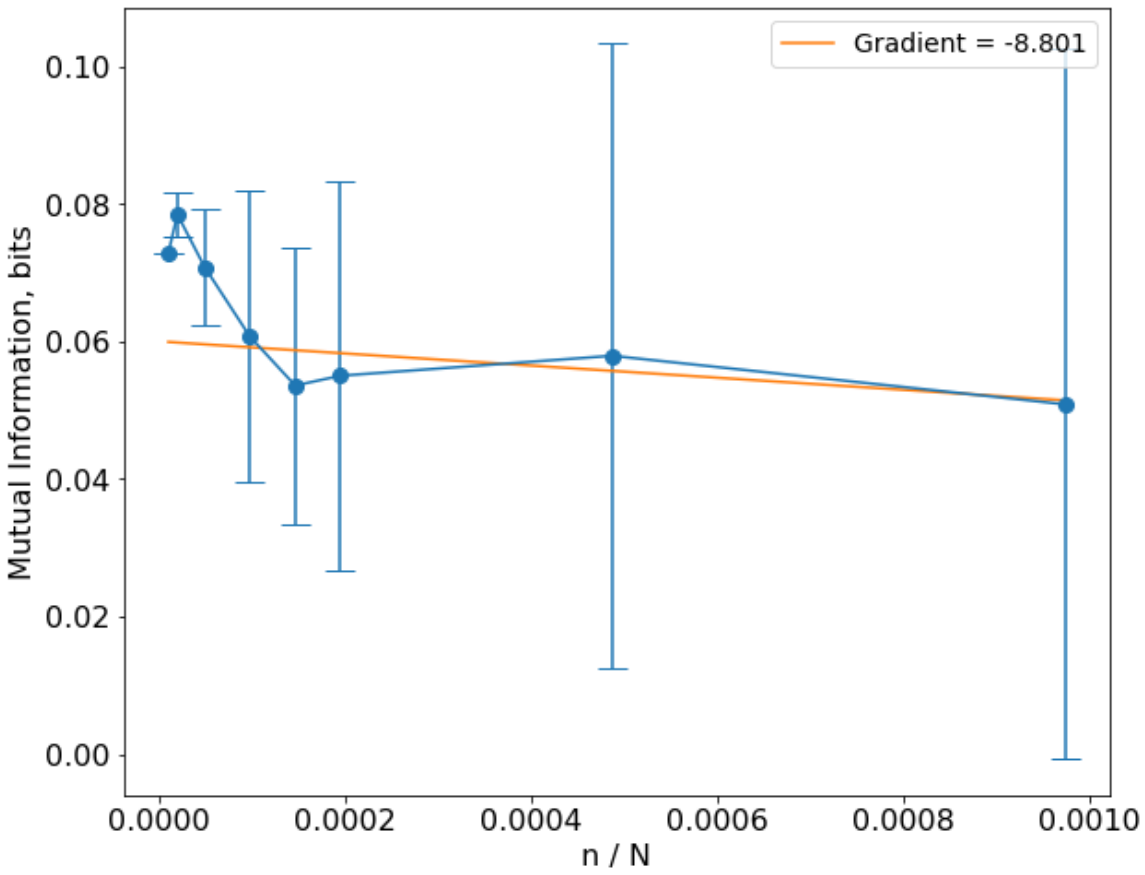

Figure 6.9: Left-Hand polarised (LH) SKR data, across the 100 - 400 KHz range (Table 4.4), with propagated solar wind variable, radial velocity (Table 4.3), before reparameterisation. k=1, where k is the number of nearest neighbour values used by the KSG estimator. MI drops as the number of subsets increases, indicating that there is greater fine structure in the real data as opposed to the Gaussian test data.

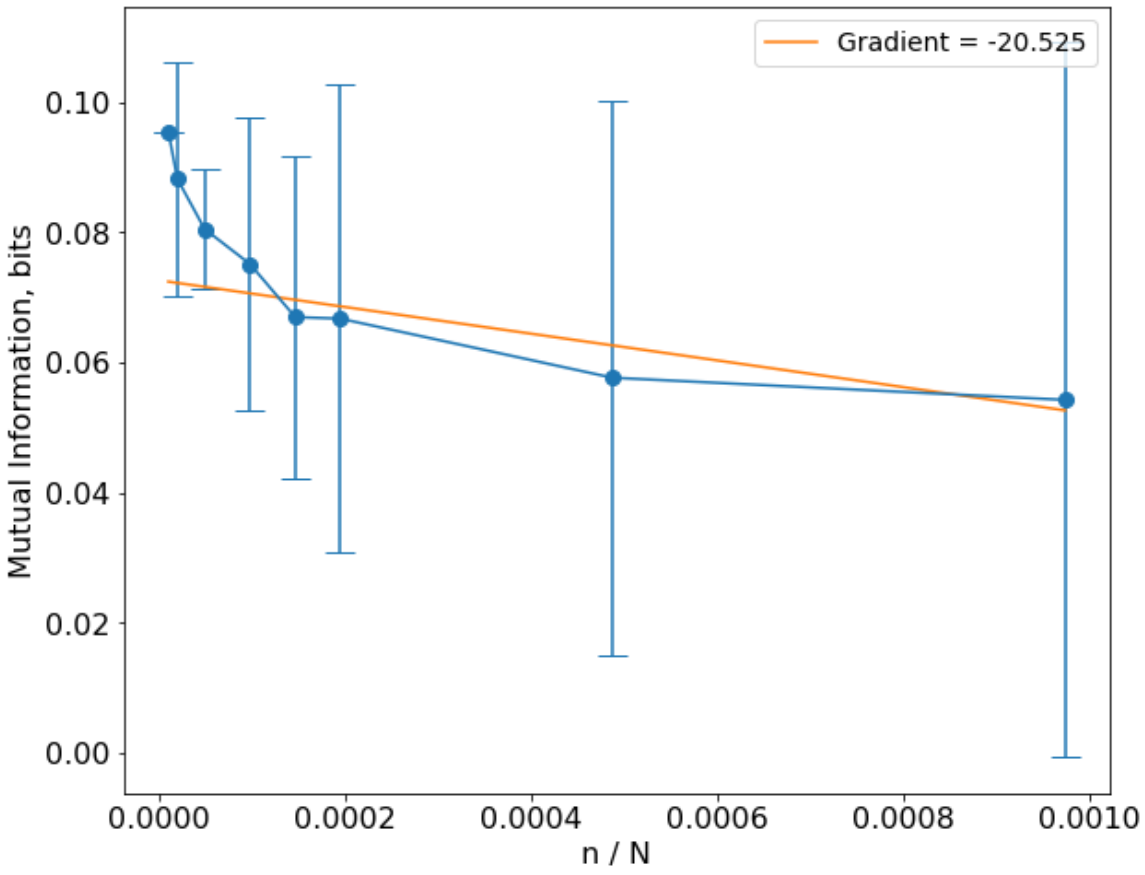

Figure 6.10: Left-Hand polarised (LH) SKR data, across the 100 - 400 KHz range (Table 4.4), with propagated solar wind variable, radial velocity (Table 4.3), after reparameterisation. k=1, where k is the number of nearest neighbour values used by the KSG estimator. As the number subsets become very large, $n > 20$, MI plateaus to similar values as the unreparameterised data in Figure 6.9, suggesting a lower limit for MI is achieved. However, at lower values of n, MI for reparameterised data is higher than the same data before reparameterisation, demonstrating the improvements of reparameterisation in eliminating the biases created by heavy-tail data.

6.4 Time Offset

There are different reasons to offset the data, such as the prediction error in the arrival time of propagated solar wind data (Tao et al., 2005) or the delayed response of the magnetosphere to the solar wind (Stumpo et al. (2020); Wintoft (2005); March et al. (2005)). Whilst the offset is specifically discussed for each data set in chapter 7, chapter 8, and chapter 9 it is acknowledged here as part of the *method* that data can be and is offset by time.

Each data point has an associated time stamp for its measurement or estimated arrival time due to propagation. As such, it is a straightforward application to adjust the time stamps of one data set by an offset. This ensures that any considerations as to why the given time stamp may not be accurate, when considering how it compares to the comparison data set, can be accounted for.

To give an example, let us consider the response time of a magnetosphere, that is the time it takes for plasma to travel through the magnetospheric system, from contact between the solar wind and magnetosphere to the measurement of its effects. In the case of the solar wind's arrival at Earth's magnetospheric system, to measurement of the AL index, it is estimated that the response time ranges from 30 to 60 minutes (March et al. (2005); Wintoft (2005); Stumpo et al. (2020)). In order to measure the MI, and by extension the relationship, between the solar wind and the AL Index, the time stamp of the solar wind can be offset by 30 minutes. Now, when building *the channel* (section 5.4), the measured AL index is paired with the solar wind variable that caused the change in the strength of the AL Index, after travelling through the magnetosphere for 30 minutes. Without an offset, one is pairing two unrelated variables, e.g. the AL Index value measured at a specific time and a solar wind

variable measured at that same time, that will not have an affect on the AL index value for another 30 minutes.

We acknowledge one consequence of our approach, in subsection 6.1.1 the high resolution SKR data is averaged from 3 minutes to 10 minutes, matching the resolution of the propagated solar wind data. This is done before any offsetting, so that the same data set is used for all offsets. One might consider that if the reverse were to be performed (determine the offset before averaging), this would vary the data used to create the lower resolution SKR data. However, this should only create dramatic effects in the case that the solar wind data were highly variable at the minute-scale resolution, whereby a single data point of an extreme value would cause the averaged (post-shifted) solar wind value to be radically different from the approach taken. For a significant effect on MI (which considers the entire distribution) this would then need to occur continuously and at a high frequency to have an effect, which is not seen in the data.

6.5 Earth-Sun-Saturn Angle

The methods previously described in this chapter are broadly applicable and are applied to all data sets considered in the following results chapters. However, in the case of the solar wind data at Saturn, the additional consideration of the arrival time must be taken into account as a result of propagation.

As outlined in section 4.3, the prediction error of the MHD simulation is no more than $\pm$ 2 days at an Earth-Sun-Jupiter angle of $\phi < 50°$. This condition is maintained for the data propagated out to Saturn. As such, in the case of the propagated data,

we cannot consider the continuous 13 year data set, but only consider the data when $\Phi_S < 50°$. As can be illustrated in Figure 6.11, the data, when restricted to $\Phi_S < 50°$, still encompasses data taken from across the mission lifetime of Cassini.

6.6 Closing Remarks

Now, finally, at the end of this chapter, one is able to apply MI to the real data using the KSG estimator method. Importantly, with the inclusion of an empirically derived and verified uncertainty value, using the methods of Holmes et al. (2019), and understanding of how data, particularly in the case of propagated data, must be treated in this approach, these results can be solved with confidence.

Not only can there now be confidence in the results, but also in the use of the data, as its format, limitations, and origins have been fully explored in chapter 4, allowing for any caveats to also be considered and accounted for. Finally, with an understanding of the physical principles outlined at the beginning of this thesis, not only can the MI results for all considered data sets be presented, but in the following chapters it will be possible to interpret these MI values in the wider context of existing research. Should new and interesting results present themselves, the foundations have been set to interpret the potential causes behind these new results.

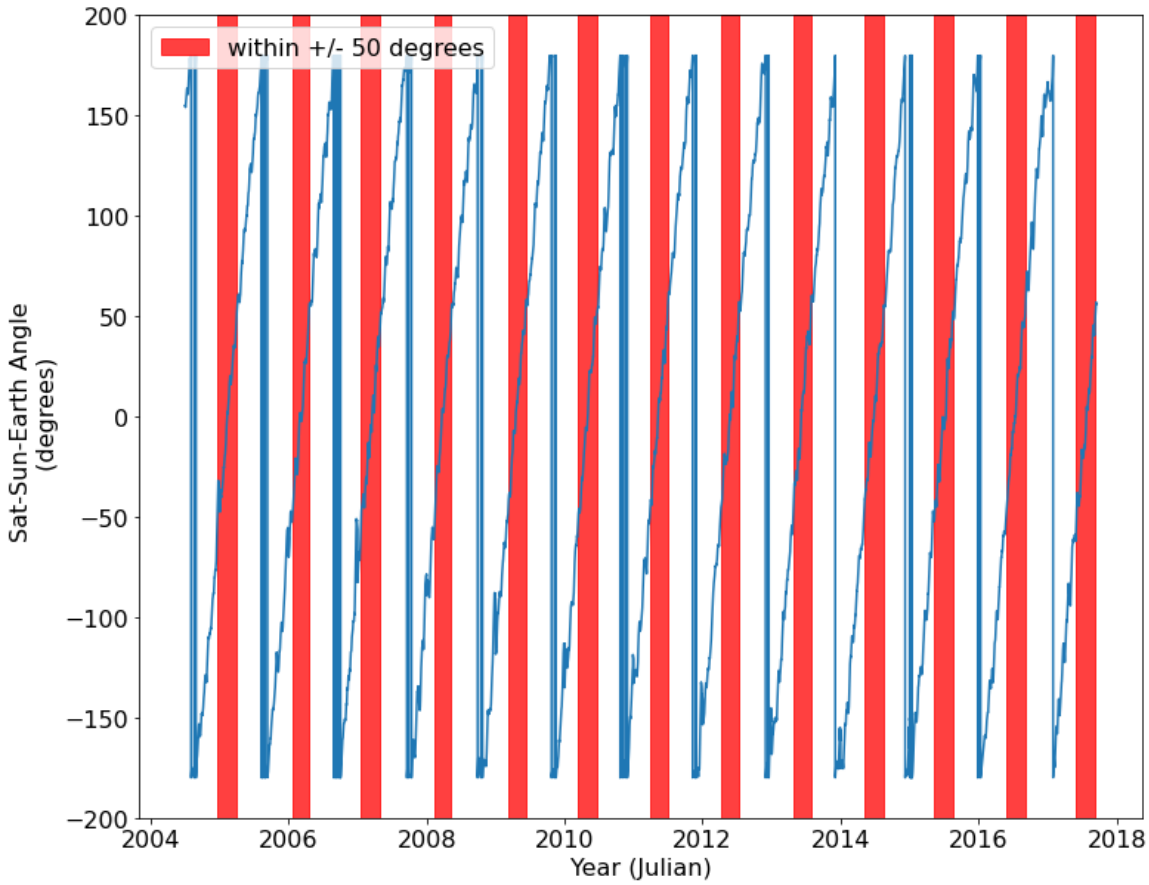

Figure 6.11: Earth-Sun-Saturn angle as a function of time for the Cassini mission life time. Areas highlighted in red represent where $\Phi_S \leq 50^\circ$ and may be considered valid for use in this research.

Chapter 7

Geomagnetic Indices and the Magnetospheric Response Time

This chapter contains an investigation of the solar wind interactions with the Earth's magnetosphere and subsequent measurement of geomagnetic indices, AL and SYM/H. This work was conducted in collaboration with the European Space and Astronomy Centre (ESAC) as part of a 6 month research visit. The primary focus of this investigation is to verify the means of applying MI described in earlier chapters, to real space plasma physics data over long time periods. Verification is performed using geomagnetic indices data as it has been extensively investigated and measured over decades, with an already well described relationship between indices and the solar wind. Verification is measured by seeking out know relationships and the response time of the terrestrial magnetosphere. Not only is verification sought but as this approach is a novel means of investigating the relationship of the solar wind, the possibility of seeing new interpretations is explored. The response time of the

magnetosphere is verified against existing literature, verifying the application of the methods in this thesis, whilst the IMF magnetic field component, B_z, and solar wind radial velocity component, v_x, are identified as influential parameters on the strength of the geomagnetic indices.

7.1 Introduction

We have investigated the origins and caveats of our data in chapter 4, understood the theory behind MI in chapter 5, and given an evidenced method of application and uncertainty calculation in chapter 6. The work of these chapters has led to the development of a means of applying MI to a range of data sets in the space and plasma physics domain, independent of time, with results we can take confidence in the value of. This development now begets the singular and perhaps most important question of this thesis, *Will it work*? If there is to be confidence in any results that come from applying the methods, it must first be applied to well understood real data where the relationship between data sets is known *a priori*. Extracting these known relationships here, with the methods developed, will act as the means of validation for applying to data sets where the relationship is unknown in chapter 9.

In section 6.4, the well understood behaviour of the solar wind's interactions with the Earth's magnetosphere were introduced in the form of the magnetospheric response time. This is the time taken for the solar wind energy/momentum to permeate through the magnetosphere and cause the associated phenomena observed; that is, the time from solar wind and IMF contact with the magnetosphere, to measurement of the phenomena. The response time of the terrestrial magnetospheric

system, to measurement of the AL and SYM/H indices, is estimated to range from 30 to 60 minutes (March et al. (2005); Wintoft (2005); Stumpo et al. (2020)). That the response time of the magnetospheric system is a range of times, rather than a definite value, aligns with our understanding. The solar wind and IMF are not constant values, strength, speed, temperature, and density all vary; events such as CMEs, geomagnetic storms, and substorms create even more turbulence. As these values vary so do the mechanisms by which plasma moves through the magnetosphere environment as explored in chapter 3. No one time can therefore describe the response time of the magnetosphere.

It therefore follows that the MI values will be at their greatest when the time offset (section 6.4) between the solar wind and geomagnetic indices data is equal to this response time. The measured indices are caused by the solar wind energy/momentum that travels through the magnetospheric system for the response time. As the response time is not definite, the MI of the considered data sets is not expected to remain low and suddenly return a maximum value at one time. Some solar wind responses will move quickly through the system, others more slowly. Therefore, one expects that the MI value will gradually increase from a minimum at the lowest quoted response time ($\sim$ 30 minutes), to a maximum around the mean response time ($\sim$ 45 minutes), before gradually decreasing back to a minima ($\sim$ 60 minutes).

In this chapter, we first delve more extensively into a review of several models that have taken different approaches to understanding the response time and have each worked to identify the primary drivers of the geomagnetic indices in the solar wind and IMF parameters. As we shall see, the response time of the AL and SYM/H indices differ. A summary of the findings from this review can be found in Table 7.1.

Following a review of existing work, we present our results. Firstly, comparing the AL index, directly measured at the Earth, to directly measured solar wind and IMF data. Secondly, repeating this verification with the SYM/H index in place of the AL index. An understanding of the geomagnetic indices has already been described in section 3.2 and information on the data in section 4.1, and so will not be repeated here.

The use of the AL and SYM/H index are critical to the later investigations within this work. Cassini data compared with propagated solar wind and IMF data, which has highly uncertain arrival times due to the propagation errors, means any results will be meaningless without wider context. How can we know that the MI values we see are representative of the drivers of SKR? The driving of the magnetosphere dynamics at Saturn by the solar wind is poorly understood, with case studies covering brief periods of time, due to the sparsity of satellite flybys, from which to compare the results. By performing the study of this chapter, we can provide certainty that the results output by this method are robust. Confidence is provided by showing that when well understood systems are investigated with these methods, known relationships can be drawn out of the data, such as the response time and primary drivers of the AL and SYM/H indices.

The following solar wind parameters are investigated against the geomagnetic indices: the IMF components, B_x, B_y, and B_z, respectively; IMF magnitudes, B_{xz}, and B_{yz}, given by Equation 7.1; and solar wind dynamic pressure, p_{dyn}; proton density, ρ; temperature, T; and radial and tangential velocities, v_x, and v_y, respectively.

$$B_{ik} = \sqrt{B_i^2 + B_k^2} \tag{7.1}$$

Finally, we interpret these results in the context of the existing work reviewed. The response time measured is compared to existing estimates in order to verify the methods outlined in this thesis, before then drawing out the most influential solar wind and IMF parameters.

7.2 Literature Review

Here, several previous studies of the AL and SYM/H index are examined and their results summarised for comparison with the results of this thesis. Using existing publications, the well understood magnetospheric system at Earth can be explored to expose relationships between the solar wind and magnetosphere dynamics, solidifying confidence in any results that come in chapter 9. Also, by confirming with several existing studies, it is demonstrated that the methods of this thesis can be applied in support of existing research as a new tool of investigation.

Bargatze, Baker, et al. (1985) investigates the temporal relationship between the solar wind and magnetospheric activity using high resolution solar wind data from the IMP8 mission and the AL index from terrestrial magnetometers (subsection 4.2.1). Data spans 34 events across November 1973 - December 1974, of which 30, 5 hour events are the main focus of the data. Bargatze, Baker, et al. (1985) expands the works of Clauer et al. (1981), which uses linear filtering routines to aid modelling the response of the AL index to solar wind variations. The filter, $H(T)$, models a general linear relationship between measured magnetospheric and solar wind quantities. Used in combination with the solar wind input time series, $I(T)$, the solar wind driven component of geomagnetic activity can be estimated using convolution theorem

$$O(T) = \int_0^\infty H(T)((t-T)dt) \tag{7.2}$$

Clauer et al. (1981) measures the response of AL index to solar wind variations. The solar wind inputs are given by vB_s, v^2B_s, and ϵ (the Akasofu parameter given by Equation 3.8), where B_s is formed from B_z under specific conditions; if $B_z \geq 0$ nT (zero or northward), B_s is equal to zero; if B_z is negative (southward), B_s is equal to the absolute value of B_z, and v is the instantaneous solar wind bulk speed. Bargatze, Baker, et al. (1985) expands this study to compare the response filter of solar wind-AL index variations with the overall geomagnetic activity.

Two response pulses, giving the activity of the AL index, are subsequently observed at 20 and 60 minutes. These pulse peaks are independently reproducible and both are present in more than half the filters investigated. It should be noted that these pulses do vary, the 20 minute pulse ranges from 15 to 30 minutes, and the 60 minute pulse ranges from 55 to 70 minutes. Part of the variation can be attributed to variations in the response time of the magnetosphere.

Two competing models are assessed to explain this relationship, the driven-model and the unloading model. In the driven model, solar wind energy is directly carried into the magnetosphere via magnetic reconnection, which responds directly to the variations in the solar wind conditions. This would be a rapid interaction, where the only time delay between the solar wind arrival at the bow shock and the measurement of a corresponding change in the geomagnetic indices, is the convection time of the solar wind energy from the energy-coupling region to the energy dissipation region. In the unloading model, solar wind energy is convected through the magnetosphere and stored in the magnetotail as magnetic flux. The stored energy is then released at

the expansion phase onset, adding to the energy dissipated via convection. The time delay in this case is, as before, the travel time through the magnetosphere, plus the time until release from the magnetotail. In the case of the unloading model, Bargatze, Ogino, et al. (1999) postulates this corresponds to an increase in the electrojet current flow due to tail wedge, and near-Earth neutral line formation and energy release from the tail.

Bargatze, Ogino, et al. (1999) uses a 3-D MHD model, that models the interaction of the solar wind with the terrestrial magnetosphere, to assess variability in the response time of the magnetosphere. MHD equations have been previously discussed in one form (section 4.3), and the reader is directed to Bargatze, Ogino, et al. (1999) for the MHD equations in the form used for this model. The response time is defined by determining the growth phase duration, which is governed by the variations in B_z, and the onset of the substorm expansion phase (section 3.2).

A parameter search is performed, using differing values of the IMF B_z component strengths. B_z is held constant for 4 hours prior to and after southward turnings, when B_z goes from a northward to a southward orientation (+ve to -ve). Across the parameter search, differing combinations of northward and southward B_z values generate a range of response times, $\sim 60 \pm 30$ minutes. Bargatze, Ogino, et al. (1999) then proceeds to verify the model predictions using empirical means, from the data of 117 substorm events from Feb 1978 to Apr 1979 (Blanchard et al., 1995), connecting the AL index to corresponding time series solar wind data (vB_s). The combination of empirical results from previous studies with the MHD simulation supports the model prediction time.

Eriksson et al. (2000) uses a linear correlation comparison between geomagnetic

indices, including SYM/H, with solar wind and IMF parameters to investigate the magnetospheric response to changes in the solar wind. These are conducted to support an investigation of the cross-polar potential drop, Φ_{pc}, which is correlated with the coupling quantities, ϵ (the Akasofu parameter given by Equation 3.8), vB_z, and $vB_{YZ}\sin^k(\theta/2)$, where B_{YZ} is the transverse component of the IMF given by Equation 3.6, θ_c is the clock angle given by Equation 3.7, and k is an integer (3 or 4). Magnetospheric response results for Φ_{pc} are then compared to the magnetospheric response of the *SYM/H* index against solar wind and IMF parameters.

Data is included from 7^{th} July until 24^{th} July 1997; SYM/H data is then taken as described in subsection 4.2.2. Φ_{pc} is determined from 37 FAST satellite passes in the Northern hemisphere, measuring the in-situ electric field using a three-axis dipole antennae, which span 10-20 minute time periods. Additionally, solar wind and IMF measurements make a continuous series from the WIND satellite at a 5-minute resolution. Though SYM/H data is at a 1-minute resolution, it is averaged over the same period as the individual cross polar potentials.

SYM/H is offset with a given solar wind or IMF parameter in 5 minute intervals, for each of the 37 events, where the response time is taken as the time offset with the largest correlation coefficient. This offsetting also is performed for a time averaged Φ_{pc}.

Eriksson et al. (2000) finds a clear 70 minute delay, the response time for the *SYM/H* index, with a less prominent secondary peak preceding at 45 minutes, independent of solar wind and IMF parameter. As in Bargatze, Baker, et al. (1985) and Bargatze, Ogino, et al. (1999) for the AL index, these two peaks for the *SYM/H* index are attributed to the direct carrying of solar wind energy into the magnetosphere

during dayside reconnection and the unloading of built up energy during magnetotail reconnection.

Using Wind data for 176 days in the first half of 1995 (day 24 to 200), March et al. (2005) uses MI to consider correlation coefficients between time-lagged solar wind data from separate satellites. By comparing the coefficients from different satellites, one can quantify the success of one time-lagging approach over another. This method is then continued to compare correlation of a solar wind parameter, once incident on the Earth's magnetosphere, to geomagnetic indices, including AL and Dst (a lower-resolution SYM/H). By first calculating the time from solar wind contact with a satellite to the Earth's magnetosphere, and then time from contact with a satellite to measurement of geomagnetic indices, one can take the difference of the two to be left with the magnetospheric response time. MI is then employed as the means of measuring the relationship.

10 solar wind and IMF parameters are considered: B_x, B_y, B_z, B, v_xB_z, v_x, ϵ (the Akasofu parameter given by Equation 3.8), ρ, ρv, and ρv^2.

Results in this study find B_z and v_x are the strongest drivers with the largest enhancement of MI; even stronger than the components individually, v_xB_z achieves the greatest enhancement of MI. For v_xB_z against the AL index, the MI enhancement peaks at approximately 45 minutes, whilst against Dst, MI peaks at approximately 60 minutes.

Though the approach of this study also uses MI, it does differ in that data has been selected over a specific period, approximately 176 days in early 1995 to coincide with the solar minimum. March et al. (2005) also uses discrete mutual information, with only 8 bins, where as this thesis uses continuous mutual information.

Alberti et al. (2017) is a case study of differing timescales for the coupling of the solar wind and IMF conditions with the magnetospheric dynamics. Two events are considered, spanning 21 day periods in 2013 and 2015, respectively. During these events, geomagnetic storms occurred due to CMEs. In addition, this study explores the response time of the magnetosphere. Data is taken from the ACE satellite at the L1 Lagrange position. An alternative form of MI is used to measure the coupling, referred to as Delayed Mutual Information (DMI), which modifies the joint probability of Equation 5.41 with a time offset variable, Δ, giving:

$$I(X;Y|\Delta) = \sum_{i=1}^{s}\sum_{j=1}^{t} P_{X,Y}(x_i(t), y_j(t+\Delta)) \log_2 \left(\frac{P_{X,Y}(x_i(t), y_j(t+\Delta))}{P_X(x_i)P_Y(y_j)} \right) \tag{7.3}$$

Several parameters are considered, including B_x, B_y, B_z, v, ϵ (the Akasofu parameter given by Equation 3.8), and the geomagnetic indices: AE, AU, AL, SYM/H, and ASYM/H. Results for the coupling features shows that for all timescales considered, it is the B_z component that most strongly couples with the geomagnetic indices. When considering the response time, a time of 70 - 80 minutes is found for the AL index, and a time of 100 - 150 minutes for the SYM/H index. The response times are longer than in other studies considered.

However, Alberti et al. (2017) acknowledges that the response times quoted do not account for the travel time from the L1 Lagrange point to the Earth's magnetopause boundary. Wintoft (2005) notes that the typical time it will take a structure in the solar wind at L1 to reach the Earth's magnetopause varies from 30 to 80 minutes, which would bring the results of Alberti et al. (2017) to timescales consistent with the other studies investigated.

Poudel et al. (2019) investigates the coupling of the solar wind with the terrestrial

magnetosphere using cross-correlation analysis. 5 geomagnetic disturbance events are considered, each spanning between 1 - 3 days. Each event is a unique event type: quiet, intense, High Intensity Long Duration Continuous Auroral Activity (HILDCAA), substorm, and super-substorm. The following parameters are considered: v, ρ, B_z, and the geomagnetic indices SYM/H and AE (recall AE is composed of the AL and AU indices, subsection 4.2.1).

Cross-correlation shows B_z most strongly couples with the SYM/H index, with the largest correlation values for each event at a time lag of 30 (substorm), 170 (intense), 71 (HILDCAA), 0 (super-substorm), and 328 (quiet) minutes. In the case of the super-substorm event, the average energy levels deposited in the magnetosphere are up to two orders of magnitude higher (10^{12} vs $10^{11/10}$ Watts per minute), explaining the rapid response of the SYM/H index. Response times in this study are not representative for the generalised approach taking in this thesis but serve to both further support the evidence of a response time and to show how highly variable it is, dependent on the solar wind conditions. Data with many intense storms may bring down the average response time, and vice versa increase the response time in their absence. Poudel et al. (2019) also notes that some portion of the magnetospheric response time is due to the transit time from spacecraft to magnetopause, which would further effect its variability. The use of unique events demonstrate the solar wind and IMF are under specific and unique conditions when coupling with the magnetosphere. As such, it is expected that the results of each event would differ, with each short timescale event considered individually, rather than representing the general conditions of the solar wind and IMF.

Stumpo et al. (2020) uses information theory to investigate the complex dynamics

of the solar wind coupling with the magnetospheric and ionospheric systems. Coupling is investigated for B_z and ϵ (the Akasofu parameter given by Equation 3.8) to the geomagnetic indices SYM/H and AE (made of the AU and AL indices). Data spans for 1 year from 1 Jan 2000 - 2001, during which several geomagnetic storms and substorms occur and is shifted from the L1 Lagrange point to the bow shock of the magnetosphere.

Results show that for B_z coupling with the geomagnetic indices, the response time stands at 30 minutes when considering solar wind flows to the auroral ionosphere, given by the AE index. Whilst the response time stands at 60 minutes when considering the transfer from the solar wind to the inner and equatorial magnetospheric regions of the ring current, given by the SYM/H index.

7.3 Results

7.3.1 AL Index

Observing Figure 7.1 the IMF magnetic field component, B_z, and solar wind radial velocity component, v_x, return the strongest MI values in relation to the AL index. B_z, at a 0 minute offset, begins with an MI value of 0.1758 $\pm$ 0.004 bits and reaches a peak MI value of 0.1968 $\pm$ 0.0004 bits at a 45 minute offset. v_x, at a 0 minute offset, begins with an MI value of 0.1535 $\pm$ 0.0005 bits and reaches a peak MI value of 0.1548 $\pm$ 0.0009 bits at the 30 minute offset. The third value of significance is the temperature, T, with an initial MI value of 0.1235 $\pm$ 0.0006 bits and reaching a peak MI value of 0.1244 $\pm$ 0.0011 at the 115 minute offset. Other IMF and solar wind parameters explored in relation to the AL index reveal much weaker MI values.

MI results comparing IMF and solar wind parameters with the AL index are visualised, with associated errors, in Figure 7.2, full MI values can be found in the following appendix tables: Table C.1, for IMF parameter results, and Table C.2, for solar wind parameter results, and for visualisations of the data, see section C.2.

7.3.2 SYM/H Index

Observing Figure 7.3, B_z, at a 0 minute offset, begins with an MI value of 0.0981 $\pm$ 0.0008 bits and reaches a peak MI value of 0.1292 $\pm$ 0.0008 bits at a 45 minute offset. In contrast to the AL index results, B_z does not return the strongest MI value in relation to the SYM/H index, starting as the fifth strongest parameter, before becoming the fourth strongest from the 30 minute offset (overtaking p_{dyn}). v_x returns the strongest value with an MI value of 0.261 $\pm$ 0.0005 bits at an offset of 0 minutes. v_x then varies between 0.2610 and 0.2657 bits until an offset of 135 minutes, with a peak MI value of 0.2657 $\pm$ 0.0008 bits at a 120 minute offset.

The second strongest driver is the solar wind proton density, ρ, with an MI value of 0.2461 $\pm$ 0.0005 bits at an offset of 0 minutes, which is also its peak MI value. The third strongest driver is Temperature, T, with an MI value of 0.1747 $\pm$ 0.0005 bits at a 0 minute offset and peaks at an MI value of 0.1930 $\pm$ 0.0009 bits at a 75 minute offset, at which time it becomes the second strongest driver, overtaking ρ, which has rapidly decreased with increasing offset value.

The fourth strongest driver, at a 0 minute offset, is the dynamic pressure, p_{dyn}, with an MI value of 0.1246 $\pm$ 0.0005 bits, which becomes the fifth strongest driver from the 30 minute offset (overtaken by B_z).

MI results comparing IMF and solar wind parameters with the SYM/H index are

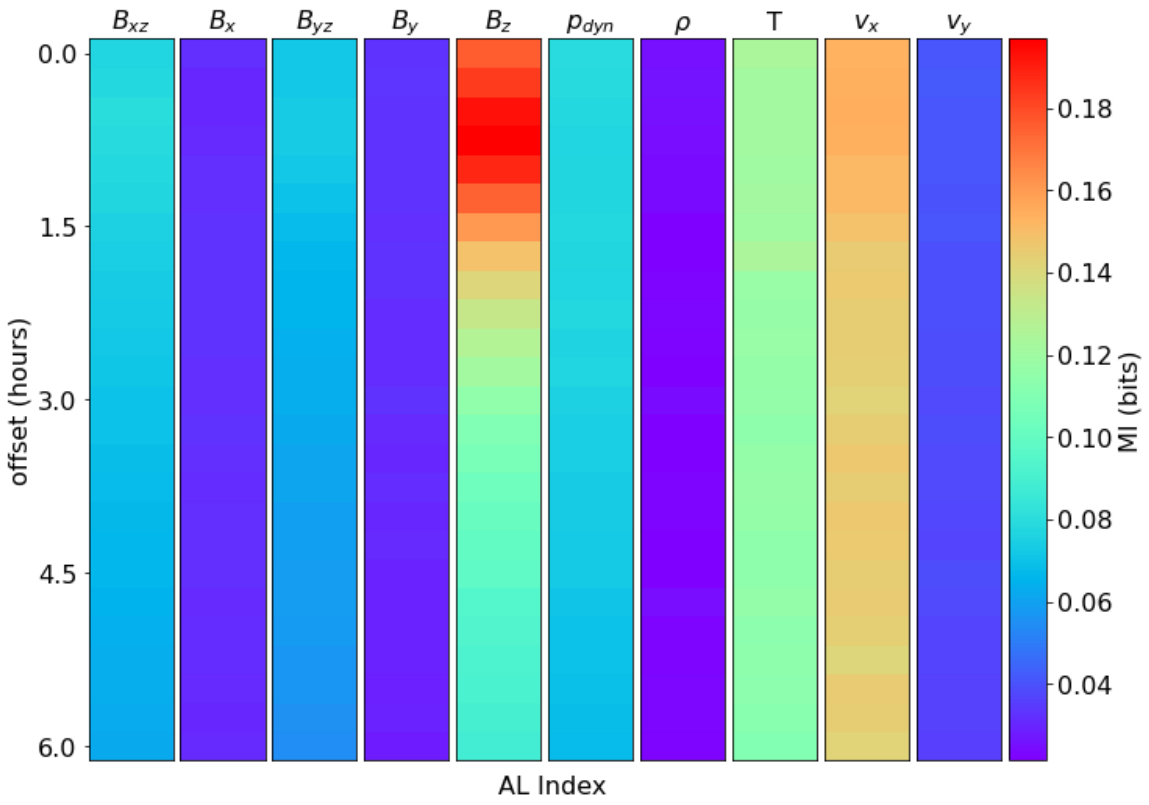

Figure 7.1: Comparison of MI values for the AL index when compared to parameters of the propagated solar wind. x-axis: (top) solar wind and IMF variables (bottom) all data sets compare to the AL index. The y-axis represents the time offset, in hours, between the solar wind variables and the AL index data set's timestamps, as described in section 6.4. Individual heat maps, where the relative MI is not relative to other data sets and the response time is observable in almost all cases can be seen in section C.2.

visualised, with associated errors, in Figure 7.4, full MI values can be found in the following appendix tables: Table C.3, for IMF parameter results, and Table C.4, for solar wind parameter results, and for visualisations of the data, see section C.4.

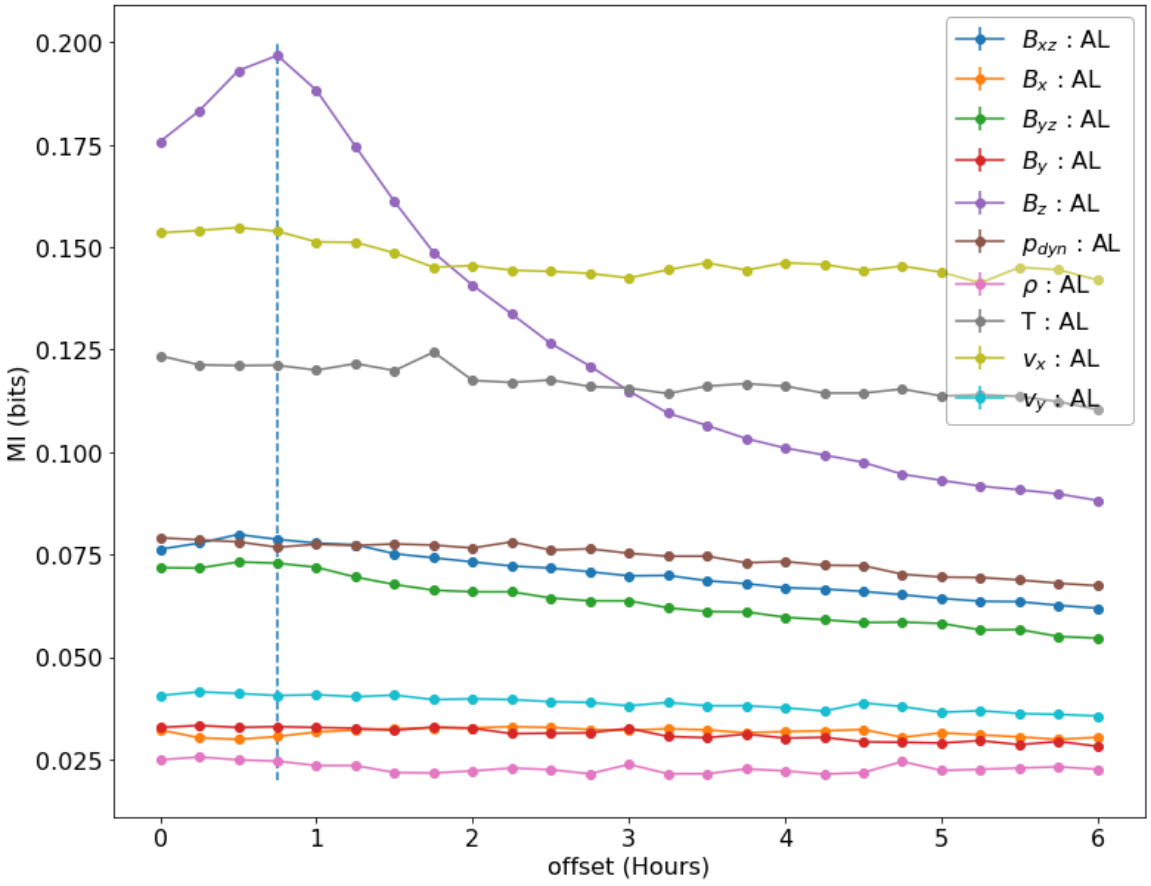

Figure 7.2: MI results for the solar wind and IMF parameters' relationship with the AL index. The B_z component of the IMF is the strongest driver of the AL index and clearly draws out the magnetospheric response time of the terrestrial magnetosphere, at the 45 minute offset (dashed vertical line). v_x is identifiable as the secondary driver of the AL index with T, third. T is likely an artefact of the v_x parameter. Offset indicates the extent of time offsetting between data sets (section 6.4). Individual values of the MI can be found in Table C.1 for the IMF parameters and Table C.2 for solar wind parameters.

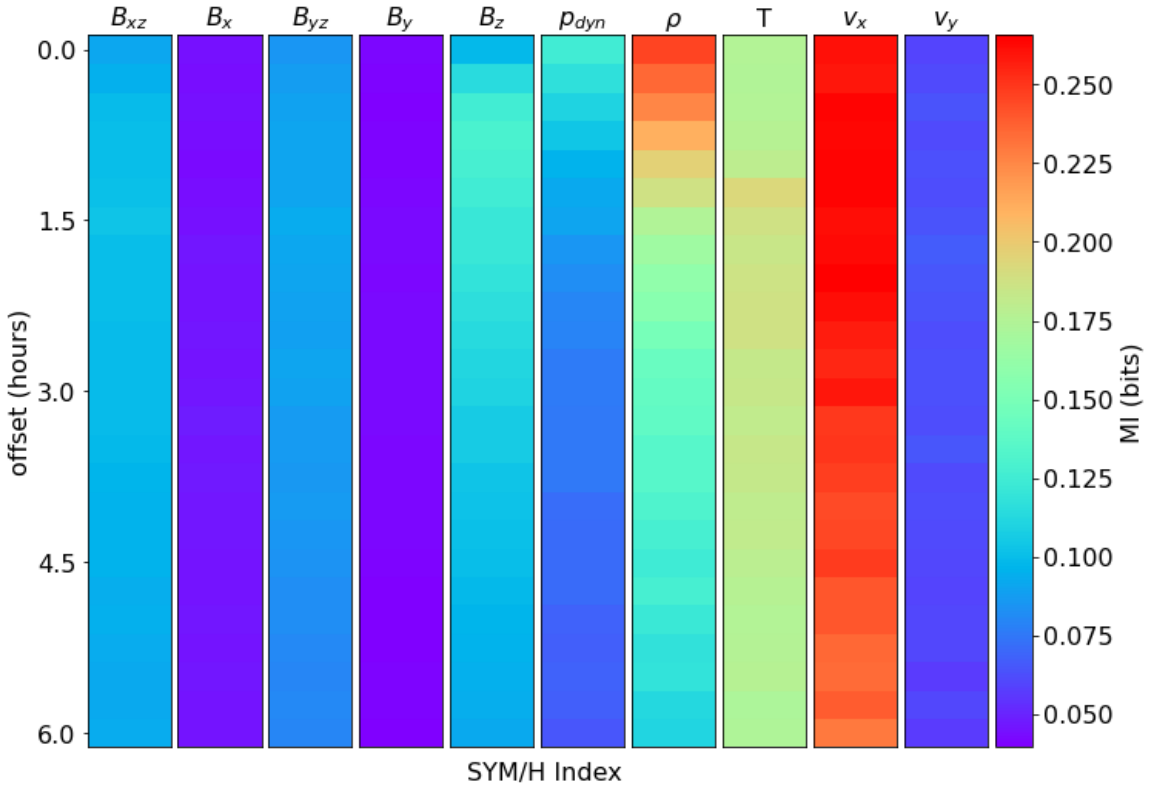

Figure 7.3: Comparison of MI values for the SYM/H index when compared to parameters of the propagated solar wind. x-axis: (top) solar wind and IMF variables (bottom) all data sets are compared to the SYMH/H index. The y-axis represents the time offset, in hours, between the solar wind variables and the *SYM/H* index data set's timestamps, as described in section 6.4. Individual heat maps, where the relative MI is not relative to other data sets and the response time is observable in several cases can be seen in C.4.

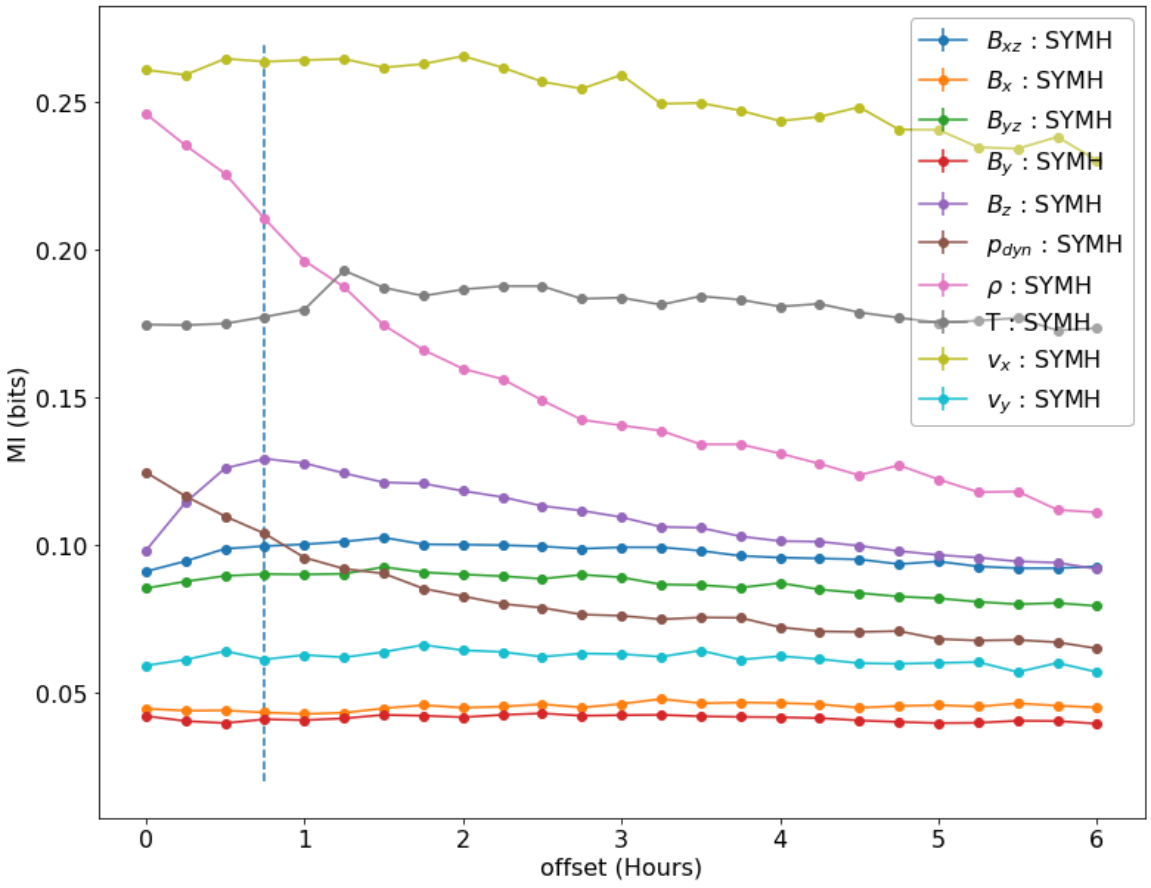

Figure 7.4: MI results for the solar wind and IMF parameters' relationship with the SYM/H index. v_x is identifiable as the strongest driver of the SYM/H index. The B_z component of the IMF is not the strongest driver of the SYM/H index but clearly draws out the magnetospheric response time of the terrestrial magnetosphere, at the 45 minute offset (dashed vertical line). ρ begins as the second strongest driver, before T takes over, peaking at 75 minutes, as ρ rapidly drops off with increasing time offset. Individual values of the MI can be found in Table C.3 for the IMF parameters and Table C.4 for solar wind parameters. Offset indicates the extent of time offsetting between data sets (section 6.4).

Source	Response Time (minutes)		Parameters of Note
	AL	SYM/H	
Bargatze, Baker, et al. (1985)	20/60	-	v, B_z
Bargatze, Ogino, et al. (1999)	60 ± 30	-	B_z
Eriksson et al. (2000)	-	45/70	v, B_z, B_{YZ}
March et al. (2005)	45	60	v_x, B_z, v_xB_z
Alberti et al. (2017)	70 - 80*	100 - 150*	B_z
Poudel et al. (2019)	-	30,170,71,0,328*	B_z
Stumpo et al. (2020)	30	60	B_z

Table 7.1: Summary of response times for geomagnetic indices of interest from existing studies. Included are the key parameters of solar wind and IMF coupling with the terrestrial magnetosphere, that drive AL and SYM/H measurement. * propagation from the L1 point has not been included, which can reduce the response times by 30 minutes (v = 800 km·s^{-1}) to 80 minutes (v = 300 km·s^{-1}) (Wintoft, 2005).

7.4 Discussion

Reviewing Table 7.1, one would conclude that the two primary drivers of the AL and SYM/H indices are the IMF, B_z, and solar wind, v_x, parameters. Whilst other parameters were considered in the reviewed studies, these parameters have often been found to be comparatively weaker or even negligible.

In subsection 3.2.1 we outlined the AL index, expressing the strongest westward current intensity of the Auroral Electrojets (AE). It is a well understood geomagnetic

index, measured over several decades with the use of Earth based magnetometers, leaving a wealth of data to explore (subsection 4.2.1). The AL index is therefore an ideal case study to verify the methods developed in this thesis. Additional studies, such as Li et al. (2007) further connect the solar wind to the AL index, demonstrating that the IMF and its direction primarily drive magnetospheric activity but that the solar wind velocity is also a significant driver, with the solar wind density playing a negligible role. These conclusions are further supported by Petrukovich et al. (2005) and Luo et al. (2013).

Furthermore, in subsection 3.2.2 we outlined the SYM/H index, which is a measure of the ring current intensity. SYM/H represents another well understood geomagnetic index, that has been documented over several decades with the use of Earth based detectors (subsection 4.2.2). Therefore, the SYM/H index presents another ideal case to verify the methods of this thesis and support/contrast the findings of subsection 7.3.1. Additional studies, such as Bhaskar et al. (2019), forecast SYM/H linked geomagnetic storms, using the IMF and solar wind velocity and density parameters, because of their importance to the solar wind-magnetosphere coupling. The use of these parameters is further supported by Wanliss et al. (2006), Cai et al. (2009) Siciliano et al. (2021), and Manu et al. (2022).

7.4.1 Drivers

In the case of the AL index, observing Figure 7.1, our results match expectations with the IMF, B_z, and solar wind, v_x, parameters presenting as the strongest primary and secondary drivers of the AL index from the considered solar wind variables.

In the case of the SYM/H index, observing Figure 7.3, the picture differs. Here the

v_x component of the solar wind is the primary driver of the SYM/H index. Perhaps in contrast to expectations, B_z moves from the fifth to fourth strongest driver of the SYM/H index, retaining a MI value of some significance, though evidently a less significant driver than for the AL index.

In the case of B_z, due to frozen-in theorem (subsection 2.5.1), IMF field lines are carried with the solar wind. The terrestrial magnetosphere is north-south aligned in the positive northward direction with most magnetic reconnection occurring where oppositely aligned field lines meet (subsection 3.1.1). This means that negative southward directed IMF lines would be the expected primary IMF driver of the geomagnetic indices, as the circumstance in which the greatest proportion of the solar wind energy is transferred into the magnetosphere and able to drive the magnetic disturbances measured in the AL and SYM/H indices. As such, the IMF B_z component should be one of the most important for geomagnetic indices activity.

For v_x, the solar wind is emitted perpendicular to the Sun's surface and as such the solar wind velocity is concentrated in the radial direction at the point of emission (section 2.6). As the solar wind velocity dominates in the radial direction, one can expect the v_x component of the solar wind velocity to be the strongest velocity driver. Furthermore, as high speed solar wind results in compressed high density regions of the solar wind, increasing plasma coupling into the magnetosphere when these regions contact the terrestrial system, one would expect enhancements of the geomagnetic indices. In the SYM/H case, the higher dependency on v_x may be due to the enhanced rate of magnetotail reconnection into the inner magnetosphere, with the sudden arrival of fast, dense solar wind that occurs during substorms and geomagnetic storms. During these events, ring current is intensified by the increased loading of plasma

to the inner magnetosphere at low latitudes. Although substorms and geomagnetic storms create intensifications in the AL index, ring current intensification events (and consequently SYM/H intensification) last longer, and peak later (Gonzalez et al., 1994).

Considering the fundamental physics occurring between the solar wind and IMF magnetosphere coupling, one can therefore conclude from the nature of the IMF and solar wind, that the strongest drivers of the AL and SYM/H indices would be from B_z and v_x. Which was largely supported by past observations (section 7.2). That they are the strongest drivers should therefore be evidenced by the strongest MI values corresponding to these parameters. However, as we have noted in the case of the SYM/H index, there are values stronger than B_z, which we now address.

Returning to Figure 7.3, the second strongest driver returned is the solar wind density, ρ. The solar wind ram pressure, p_{dyn}, depends on the solar wind density, ρ, which plays an important role in ring current intensification (Smith, Hoffman, et al., 1976). Observing Figure 7.4, we can see that the MI value of p_{dyn} decreases with time offset as the MI value of ρ does, suggesting we can observe this relationship in the results. Gonzalez et al. (1994) notes that the solar wind ram pressure can modulate the Earth's magnetic field; as ρ is an important factor in ring current intensification, the results for the SYM/H index are interpreted as showing two driving mechanisms. There is also the possibility of a third driving mechanism from p_{dyn}, which with the strongest MI value at a time offset of 0 minutes, may be showing compression induced field enhancements.

Finally, we note the temperature, T, of the solar wind, which in each case is the third strongest driver returned of the geomagnetic indices, and eventually

second strongest returned for the SYM/H index, after ρ declines in strength. T is linearly correlated with the solar wind velocity (subsection 2.6.2), which in a physical interpretation would relate the kinetic energy of the particle to the temperature (dependent on particle velocity). In the case of both geomagnetic indices we can see that the strength of T approximately follows this relationship with v_x.

7.4.2 Response Time

In addition to understanding the physical interpretation of the MI values for the IMF and solar wind parameters driving the geomagnetic indices, our goal was to validate the use of a time offset to show the response time. The relationships investigated should strengthen (approach their true MI value) when the time offset matches the response time of the Earth's magnetosphere. This is the time from solar wind contact with the magnetopause for the solar wind energy to travel through the magnetospheric system and generate perturbations in the magnetometers, measured as the AL and SYM/H indices. Noting the observations in case studies (Table 7.1), it is expected that there may be two response times each for the AL and SYM/H indices, the shortest from dayside magnetic reconnection and the longest due to tail ward reconnection. Furthermore, the SYM/H index should return a later response time than that of the AL index.

For the AL index, B_z clearly draws out the response time of the magnetosphere, increasing the MI result from 0.1758 ± 0.004 bits to a peak MI value at the 45 minute interval of 0.1968 ± 0.0004 bits, in agreement with the response time of past studies (Table 7.1). Although less prominent, v_x peaks at the 30 minute interval, with an MI of 0.1548 ± 0.0009 bits. Observation of individual relationships further reveals

the response time of the Earth's magnetosphere in the B_{XZ}, B_{YZ}, B_Y, ρ, and v_y parameters' MI results, further reinforcing the capability of the methods in this thesis to find the response time. See Table C.1 for IMF parameter result values, Table C.2 for solar wind parameter result values, and section C.2 for illustrations of the data.

Bargatze, Baker, et al. (1985) observes intensification of the AL index at two time offsets of B_z, at 20 and 60 minutes, with an average response time of 40 minutes. With a resolution of only 15 minutes (as opposed to 2.5 minutes), two distinct peaks are not seen in the results of this work, though the peak of MI strength does persist across the 15 and 60 minute intervals, supporting our findings.

For the SYM/H index, the response time of the strongest driver returned, v_x, is difficult to draw out, with MI values holding their peak values (almost) continuously from 30 until 135 minutes at ~ 0.264 bits. However, as noted prior, ring current intensification events, and consequently SYM/H intensification last longer, and peak later (Gonzalez et al., 1994). There is clearer evidence of two distinct MI peaks, which can be attributed to the different driving mechanisms seen through the IMF component, B_z, and solar wind temperature, T. The first mechanism may be a consequence of the typical Dungey cycle (subsection 3.1.1 and subsubsection 3.1.1.1). This mechanism is represented by the clear peak in the MI value of B_z, 0.1292 ± 0.0008 bits at 45 minutes. The second mechanism, attributed to ring current intensification due to enhanced tail reconnection during substorms and geomagnetic storms, can be seen through T. T is well correlated with v_x (subsection 2.6.2) and achieves a clear peak value of 0.1930 ± 0.0009 bits at 75 minutes. A secondary response time is further supported by B_{XZ} and B_{YZ} at 90 minutes, and v_y at 115 minutes. See Table C.3 for IMF parameter result values, Table C.4 for solar wind parameter result values, and

section C.4 for illustrations of the data.

Eriksson et al. (2000) found dual peaks in more than half the data sets explored for the SYM/H index, at 45 and 70 minutes for B_z, which supports the findings here. Though two peaks are not seen in the results for B_z here, the work of Eriksson et al. (2000) is aided by a higher resolution. The first correlation peak at 45 minutes falls until past the 60 minute point, then rapidly peaking and dropping to a lower value. At 15 minute intervals this study only gives offsets at 45, 60, 75, and 90 minutes (compared to a 5 minute interval step). It is therefore possible the secondary MI peak has been missed in our own analysis of B_z. However, as noted the later peak for T is likely revealing the second response time.

7.5 Conclusions

Using the two geomagnetic indices has provided complimentary results in support of the magnetosphere response times and provided validation of the methods of this thesis. As is expected by an understanding of the physics and review of past studies, the IMF B_z component, and solar wind v_x component are strongly related to driving of the magnetosphere and measurement of the geomagnetic indices AL and SYM/H.

Drawing out the response time of the Earth's magnetosphere in these results is a critically significant success. Validation of the methods developed in this thesis, shows that an *a priori* relationship can be observed in the MI values output. Consequently, this demonstrates that the method applied is capable of finding relationships between the solar wind and other data.

It also shows the importance of the time offset (section 6.4) to demonstrate that

the data has a degree of temporal sensitivity. Using MI to assess the strength of the relationship between solar wind and IMF parameters with magnetospheric (and proxy) data sets, therefore, must be temporally aligned. This accounts for the time taken for the effects of the solar wind condition's at the bow shock of the magnetosphere to be measured by detectors, such as the magnetometers for the geomagnetic indices. In addition to this consideration, temporal alignment will be especially important when considering the results of comparing SKR data to propagated solar wind measurements at Saturn. Here, the propagated solar wind has an uncertainty in the arrival time of up to $\pm$ 2 days, in addition to the response time of Saturn's magnetosphere for SKR emission, estimated at $\approx$ 13 - 50 hours (Taubenschuss et al., 2006).

It is important to note that when discussing temporal sensitivity, this is not in contradiction to the original goal, to find an approach that is independent of time. It does not matter if the data is discontinuous, nor what order the data is introduced to build *the channel* (section 5.4). What is important is how individual pairs of x and y data points are paired. When pairing x and y data points, to create a probability for *the channel*, that pairing accounts for the response and/or propagation time. In effect, we could consider MI, for this study, to be temporally independent on the macro scale and temporally dependent on the micro scale.

A future investigation at a higher temporal resolution would indicate if the results in this chapter further support the distinct peaks found by Bargatze, Baker, et al. (1985) and Eriksson et al. (2000). At a minimum, the results of this thesis, at this resolution, are in agreement with the broad response times of the magnetosphere found in previous studies. It should of course be also noted that there is no one

specific response time to be drawn out, only an approximate, which is why previous studies are not all in perfect agreement (only approximate). All plasma transferred into the magnetospheric system does not travel at the same rate, plasma particles will have a distribution of energies at any moment in time during reconnection.

However, significantly different results have come from this approach to the investigation in previous studies. Temperature, T, is absent from the previous studies explored here, despite results here demonstrating a strong relationship between T and the geomagnetic indices. Perhaps this is due to the linear relationship, and T being seen as an artefact of velocity. Whilst T is linearly correlated with the solar wind velocity (subsection 2.6.2), the drawing out of the response time via T demonstrates the importance of considering all parameters. Equally, in the case of the SYM/H index, despite past studies of specific events discounting ρ, the deliberately long time-scale approach of this works, ignoring (or averaging out) phenomena such as CMEs, geomagnetic storms, and substorms, reveals that other parameters may be stronger drivers than expected overall. For example, Wintoft (2005) acknowledges the solar wind velocity, v, and density, ρ as possible drivers but finds no discernible influence from them over a 6-month period.

The consensus of past case studies would support the assertion that it is primarily B_z that plays a significant role in the evolution of magnetosphere dynamics and subsequent influence of the geomagnetic indices with v_x as a secondary driver. The results of past studies do not consistently agree with the results here, with T and ρ acting as stronger drivers than B_z in the case of the SYM/H index.

A possible explanation is the unique approach of this study, to be time-independent over long time periods. There has been no event selection, and no attempts to choose

optimal time periods. In addition, the solar wind parameters investigated in this thesis have not been curated to only include parameters existing literature suggests are the strongest drivers. In this thesis, all parameters have been included, without any optimization. The only changes made to the data are described in chapter 6, whose sole purpose is to filter out unusable, not sub-optimal, data. In opposition to this approach, other methods may have introduced a bias in their selection process, seeking to investigate the IMF relationship as a known driver without exploring other parameters freely. In all cases data appears chosen to maximise/meet the expected results by investigating specific periods of intense activity. Stumpo et al. (2020) and March et al. (2005) use information theory over a period of up to a year. In the former, dates are chosen to be at the maximum of a solar cycle. For the latter, dates are chosen because they cover a period at solar minimum.

Temperature, T, and proton density, ρ, may be artefacts of the solar wind radial velocity, v_x, interaction. In the case of the SYM/H index, v_x has a strong relationship with T and ρ as stronger drivers than B_z (at approximately double the MI value). What is of particular interest is just how large the MI values of v_x, T, and ρ are, see Table 7.2. Recall, that the MI value in an ideal Gaussian case, with a correlation coefficient of 0.6 is $\simeq 0.32$ bits. In the case of v_x, and ρ, the MI values are $\geq 75\%$ the value of an ideal case, whilst $T \geq 60\%$, these are significant values and suggests a much stronger, direct relationship with the solar wind velocity. If T and ρ are artefacts, this explains their strength above B_z.

	AL		SYM/H	
	S	45	S	45
B_z	0.1968 ± 0.0004	0.1968 ± 0.0004	0.1292 ± 0.0008	0.1292 ± 0.0008
T	0.1244 ± 0.0011	0.1212 ± 0.0004	0.1930 ± 0.0009	0.1773 ± 0.0003
v_x	0.1548 ± 0.0009	0.1539 ± 0.0006	0.2657 ± 0.0008	0.2638 ± 0.0004
ρ	0.0256 ± 0.0006	0.0246 ± 0.0004	0.2461 ± 0.0005	0.2105 ± 0.0004

Table 7.2: Significant mutual information values (in bits) are listed for solar wind parameters of particular interest: B_z, T, v_x, and ρ. S represents the strongest mutual information value for that particular pairing of geomagnetic index and solar wind parameter. 45 represents the mean response time (in minutes) of the magnetosphere and the MI value at that time is displayed. Individual values of the MI can be found in Table C.1 and Table C.3 for the IMF parameters, and Table C.2 and Table C.4 for solar wind parameters.

7.6 Closing Remarks

The methods used in this thesis have been confirmed by identifying the *a priori* relationships in existing literature and drawing out the response time of the magnetosphere. By confirming existing relationships, it is now possible to move forward with a measure of confidence in exploring new data sets, where the corresponding relationship may be less certain or even unknown. Additionally, by not seeking out optimal time periods to investigate, and freely considering all parameters, it has been shown that additional relationships can be found.

Chapter 8

On the Utility of Coupling Functions

Following development of the geomagnetic indices investigation of chapter 7, as part of a collaboration placement with ESAC, the remaining time was spent conducting a short investigation on the utility of coupling functions to characterise the solar wind and IMF coupling to the Earth's magnetosphere, using the methods developed in this thesis. This chapter therefore seeks to ascertain whether coupling functions can provide a better description of this characterisation than the IMF parameter, B_z. Source papers of the coupling functions are reviewed to understand their utility in short time-scale, ideal conditions, as a baseline for comparison. The methods of this thesis applied to the IMF component, B_z, with a clear coupling relationship, is used as a comparative solar wind parameter to determine the value of coupling functions as general measures of the solar wind and IMF coupling to the magnetosphere. The geomagnetic indices, AL and SYM/H, are well connected to this behaviour, and as in

the previous chapter, will be used as a measure of the coupling effect for solving *the channel* and hence MI. Coupling functions are determined to be effective as measures of solar wind and IMF coupling with the terrestrial magnetosphere, with MI results more significant than B_z by $\sim 100\%$ for the AL index and $\sim 40\%$ for the SYM/H index at the peak time offsets.

8.1 Introduction

The IMF parameter, B_z, is considered a strong indicator of magnetospheric driving and was confirmed by our own investigation in chapter 7. However, as given by Newell et al. (2007), B_z predicts only a quarter of the variance in magnetospheric state variables. This can be improved upon; for example, knowledge of the previous Dst index (low-resolution SYM/H index) can greatly improve the predictive power of B_z for the next value.

Coupling functions then, were introduced as an attempt to find an improved measure of the solar wind and IMF coupling to the magnetosphere. They are equations that seek to characterise magnetospheric activity from the coupling of the solar wind with the magnetosphere and are typically of the form given by Equation 3.2. To achieve this characterisation, they combine solar wind and IMF parameters with the clock angle (Equation 3.7), and empirically derived coefficients and powers, which are solved from the observation data considered. Following the investigation of geomagnetic indices in chapter 7, and confirmation that the methods of this thesis can be successfully used to determine relationships between the solar wind and terrestrial phenomena, we have chosen to then investigate the use of coupling functions as an

extension of the solar wind and IMF relationship with the geomagnetic indices, AL and SYM/H.

As concluded in the previous chapter, B_z, when considered as a general parameter, is strongly related to the geomagnetic indices. Although in the case of the SYM/H index, the solar wind radial velocity, v_x, and by relation proton density, ρ, and temperature, T, stood as the strongest parameters, B_z most clearly showed the magnetospheric response time and has a consistently strong relationship across both geomagnetic indices (section 7.3). Therefore, B_z will be considered against a range of coupling functions as a baseline relationship. Coupling functions are solved using the same data as the investigation of B_z in chapter 7, ensuring the MI results are a valid comparative dataset. Data for the solar wind, IMF, and geomagnetic indices come from the OMNI database (section 4.1) and are for the same length and period of time, 2005 - 2021 (subsection 4.1.2).

8.2 Literature Review

Three coupling functions will be considered, Akasofu parameter, ϵ, the Kan and Lee Electric Field, E_{KL}, and the dayside reconnection rate, Φ_D, given by Equation 3.8, Equation 3.9, and Equation 3.10, respectively.

The first coupling function, ϵ, is one of the most well known. First described by Perreault and Akasofu (1978), ϵ measures the energy input into the magnetosphere via variation of the Poynting flux. This energy input is split between ring current particle injection, Joule dissipation into the ionosphere, and auroral particle injection. Due to the difficulties of measuring these from first principles, geomagnetic indices were used

as proxies ((Perreault and Akasofu, 1978); (Milan, Gosling, et al., 2012)), making the relationship between coupling functions and the geomagnetic indices highly suitable to investigate.

Comparing 15 major geomagnetic storms and substorms from 1967 - 1970, each 1-2 days in length, Perreault and Akasofu (1978) compares a range of parameters including the IMF magnitude, B, its north-south component, B_z, the AL index, and the Dst index. It is seen that ϵ is closely related to the growth of geomagnetic storms by the total energy dissipation, $u(t)$, given by

$$u(t) = u_i(t) + u_j(t) + u_p(t) \tag{8.1}$$

where $u_i(t)$ is the ring current particle injection rate, $u_j(t)$ is Joule dissipation rate into the ionosphere, and $u_p(t)$ auroral particle injection rate. Though relation to B_z is also seen in the data, the strength of B_z in comparison to ϵ is not quantitatively given. However, an investigation of coupling functions in Newell et al. (2007) calculates the correlation coefficient of B_z and ϵ across 10 indices, finding ϵ more strongly accounts for the variance of the indices, as an average, than B_z, summarised in Table 8.1. It should be noted that in the case of Dst, the correlation coefficient of B_z does exceed that of ϵ. Newell et al. (2007) uses geomagnetic index data from WDC for Geomagnetism (2005), the AL index was assessed for the period of 1983-1987, and the Dst index was assessed for the periods of 1984-1994 and 1995-2005.

The second function considered, E_{KL}, of Kan et al. (1979), stands for the reconnection electric field at the magnetopause. More specifically, magnetic field line reconnection results in parallel electric fields on open-field lines in high-latitude cusps and the polar cap regions. These parallel electric fields are then found to be potential

components in the formation of cusp and polar cap aurora (Kan et al., 1979).

Kan et al. (1979) does not give a quantitative assessment of E_{KL}, nor compare it to B_z, although it is noted that a relation to ϵ is found. However, Newell et al. (2007) also assesses E_{KL} in its investigation of coupling functions. Newell et al. (2007) concludes that E_{KL}, across 10 indices, accounts for a greater percentage of the variance in geomagnetic indices than B_z and ϵ, the results of which are summarised in Table 8.1.

Finally, we consider Φ_D, of Milan, Gosling, et al. (2012), which measures the dependence of the dayside reconnection rate as a function of the solar wind and IMF parameters, where it is assumed no nightside reconnection occurs, allowing Φ_D to equal the rate of change of polar cap flux, dF_{PC}/dt. F_{PC} is estimated using the location of the polar cap, determined using auroral imaging data from the Far Ultraviolet (FUV) instrument onboard the Imager for Magnetopause-to-Aurora Exploration (IMAGE) spacecraft. By using a means that assumes no nightside reconnection, events are chosen where nightside reconnection remains low through a period of southward IMF, whereby the polar cap expands following a long period of northward IMF and constant polar cap size. Thus events are short, with 26 events considered from May 2000 - April 2002, totalling 49.2 hours. Each event accounts for any delays in the arrival time of the solar wind parameters.

Milan, Gosling, et al. (2012) does not investigate Φ_D in comparison to B_z but does for ϵ and other coupling functions by calculating the correlation coefficient between the coupling function and observed data. The correlation coefficient for Φ_D is calculated from the variation between the modelled F_{PC} and the F_{PC} calculated from data, across the time for each event. In the case of the modelled F_{PC}, the parameters of

Parameter	AL	Dst	Variance	Milan, Gosling, et al. (2012)
B_z	.440	.476	26.4%	-
ϵ	-.338	-.770	36.6%	0.899
E_{KL}	-.443	-.797	51%	-
Φ_D	-	-	-	0.972

Table 8.1: (column 1) IMF parameter, B_z and coupling functions. (columns 2 - 3) correlation coefficient for B_z and coupling functions with the AL and Dst (low-resolution SYM/H) geomagnetic indices (Newell et al., 2007). (column 4) variance of the indices accounted for by B_z and the coupling functions, as an average of 10 indices (Newell et al., 2007). (column 5) Correlation coefficient for coupling functions (Milan, Gosling, et al., 2012).

Equation 3.2 are modified to achieve the best correlation coefficient. Φ_D exceeds ϵ, as seen in Table 8.1, demonstrating a continued improvement of characterisation of the solar wind and IMF coupling to the magnetosphere.

8.3 Results

8.3.1 AL Index

Observing Figure 8.1, the dayside reconnection rate, Φ_D, returns the strongest MI value. At a 0 minute offset, Φ_D, is 0.2683 $\pm$ 0.0007 bits, reaching a peak offset of 0.4118 $\pm$ 0.0009 bits at a 45 minute offset. The second strongest MI result is the Kan and Lee Electric Field, E_{KL}. At a 0 minute offset, E_{KL}, is 0.2661 $\pm$ 0.0004 bits, reaching a peak offset of 0.3723 $\pm$ 0.0005 bits at a 45 minute offset. The third

strongest result is the Akasofu parameter, ϵ. At a 0 minute offset, ϵ, is 0.2551 $\pm$ 0.0004 bits, reaching a peak offset of 0.3614 $\pm$ 0.0007 bits at a 45 minute offset.

As noted in chapter 7, the southward facing IMF parameter, B_z, at a 0 minute offset, begins with an MI value of 0.1758 $\pm$ 0.004 bits and reaches a peak MI value of 0.1968 $\pm$ 0.0004 bits at a 45 minute offset. This is the fourth strongest MI result but is relatively weaker when compared with the coupling functions, Φ_D, E_{KL}, and ϵ.

MI results comparing B_z, Φ_D, E_{KL}, and ϵ, with the AL index are visualised, with associated errors, in Figure 8.2. Full MI values for the results can be found in the appendix table Table D.1, and for individual visualisations of the data, see section D.2.

8.3.2 SYM/H Index

Observing Figure 8.3, the three strongest MI results, at 0 minutes offset, are the coupling functions once again, albeit in reverse order of significance. The strongest MI result is, initially, ϵ. At a 0 minute offset, ϵ, is 0.1385 $\pm$ 0.0003 bits, reaching a peak offset of 0.1938 $\pm$ 0.0004 bits at a 90 minute offset. The second strongest MI result is E_{KL}. At a 0 minute offset, E_{KL}, is 0.1344 $\pm$ 0.0004 bits, reaching a peak offset of 0.1941 $\pm$ 0.0004 bits at a 90 minute offset. The third strongest result is Φ_D. At a 0 minute offset, Φ_D, is 0.1270 $\pm$ 0.0005 bits, reaching a peak offset of 0.1921 $\pm$ 0.0005 bits at a 90 minute offset.

As noted in chapter 7, the southward facing IMF parameter, B_z, at a 0 minute offset, begins with an MI value of 0.1758 $\pm$ 0.004 bits and reaches a peak MI value of 0.1968 $\pm$ 0.0004 bits at a 45 minute offset. This is the fourth strongest MI result but again, is relatively weaker when compared with the coupling functions, Φ_D, E_{KL}, and ϵ.

MI results comparing B_z, Φ_D, E_{KL}, and ϵ, with the SYMH index are visualised, with associated errors, in Figure 8.4. Full MI values for the results can be found in the appendix table Table D.2 and for individual visualisations of the data, see section D.4.

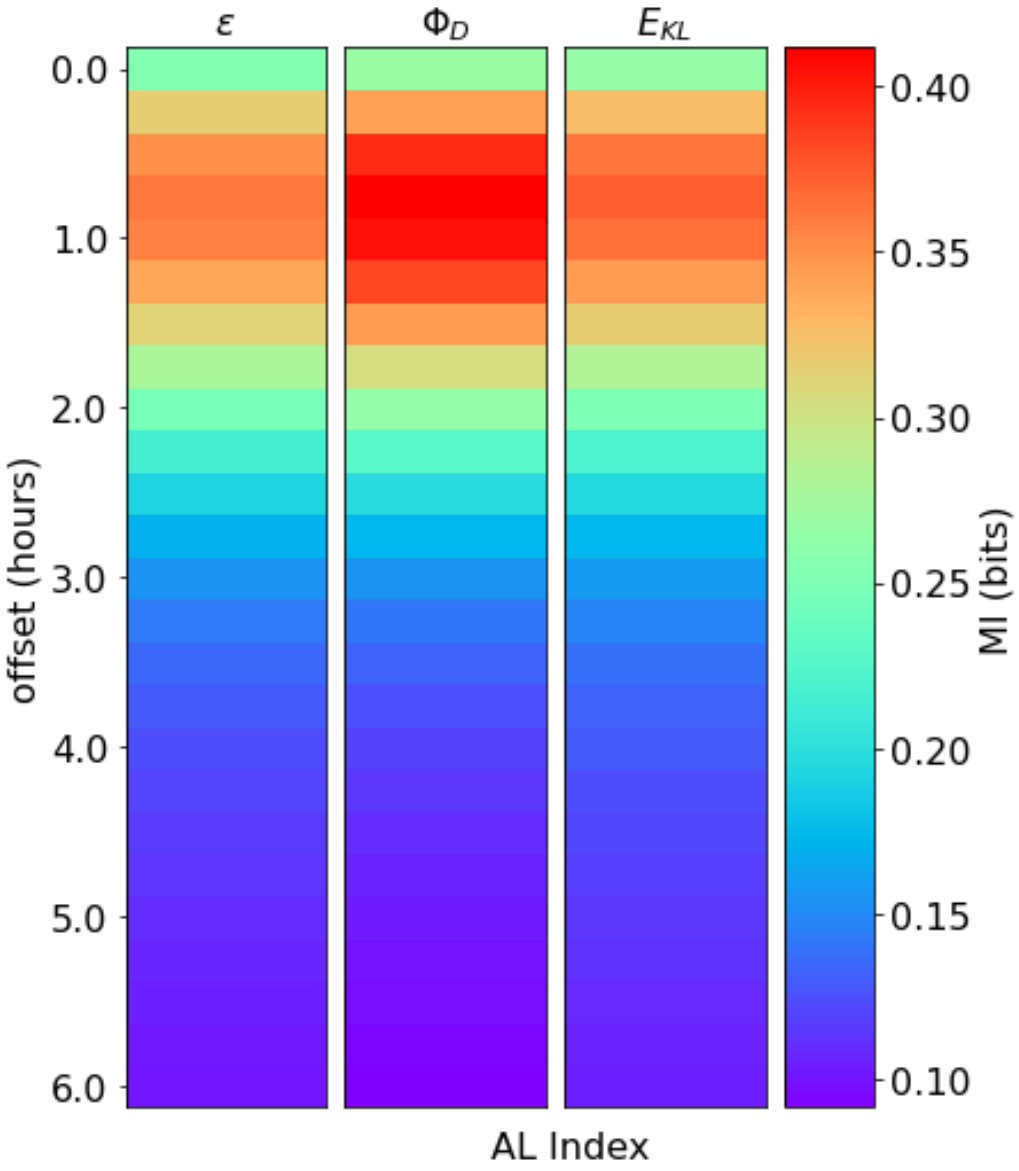

Figure 8.1: Comparison of MI values for B_z, Φ_D, E_{KL}, and ϵ, as observed via the AL index. x-axis: (top) coupling function (bottom) all data sets use the AL index. The y-axis represents the time offset, in hours, between the coupling functions and the AL index timestamps, as described in section 6.4. Individual heat maps, where the MI value is not relative to other data sets can be seen in section D.2.

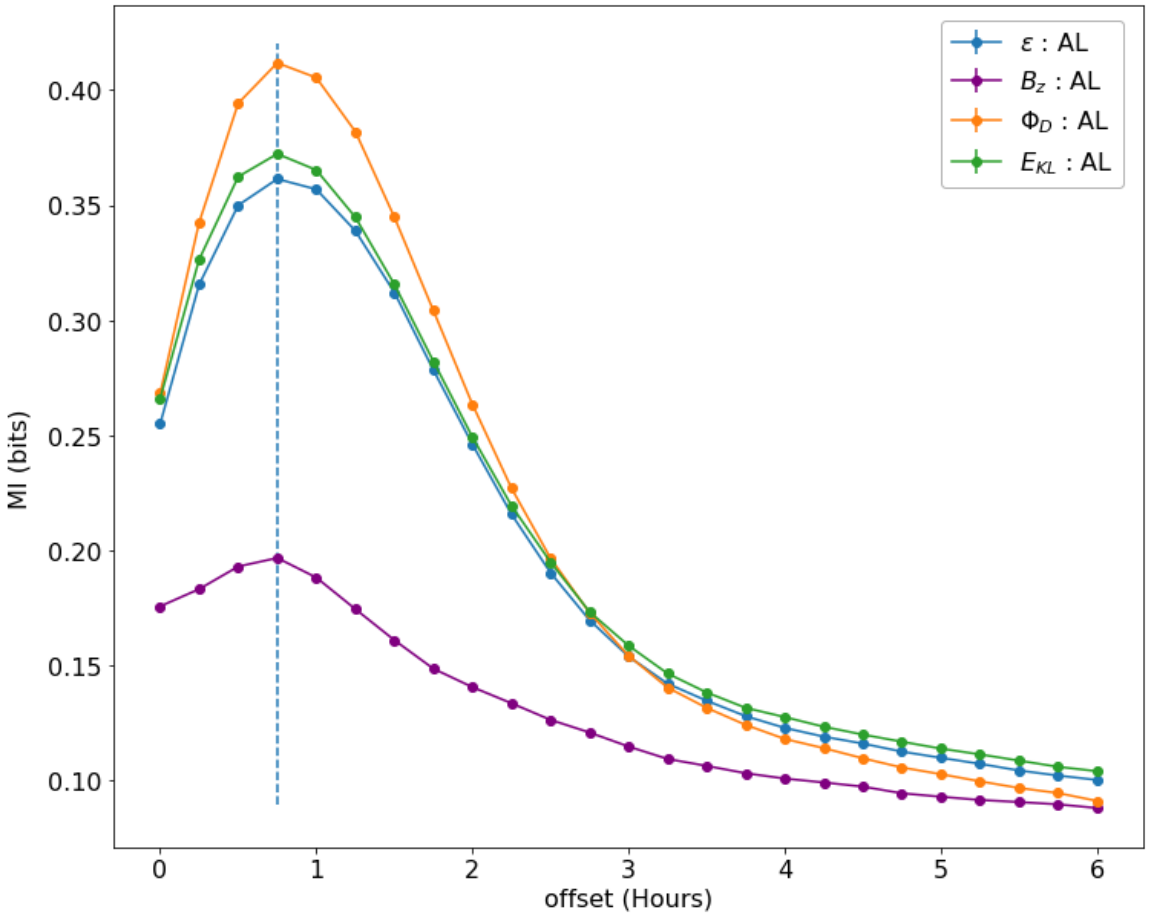

Figure 8.2: MI results for B_z, Φ_D, E_{KL}, and ϵ, with the AL index. The coupling functions, B_z, all clearly draw out the magnetospheric response time of the terrestrial magnetosphere, at the 45 minute offset (dashed vertical line). Offset indicates the extent of time offsetting between data sets (section 6.4). Individual values of the MI can be found in Table D.1.

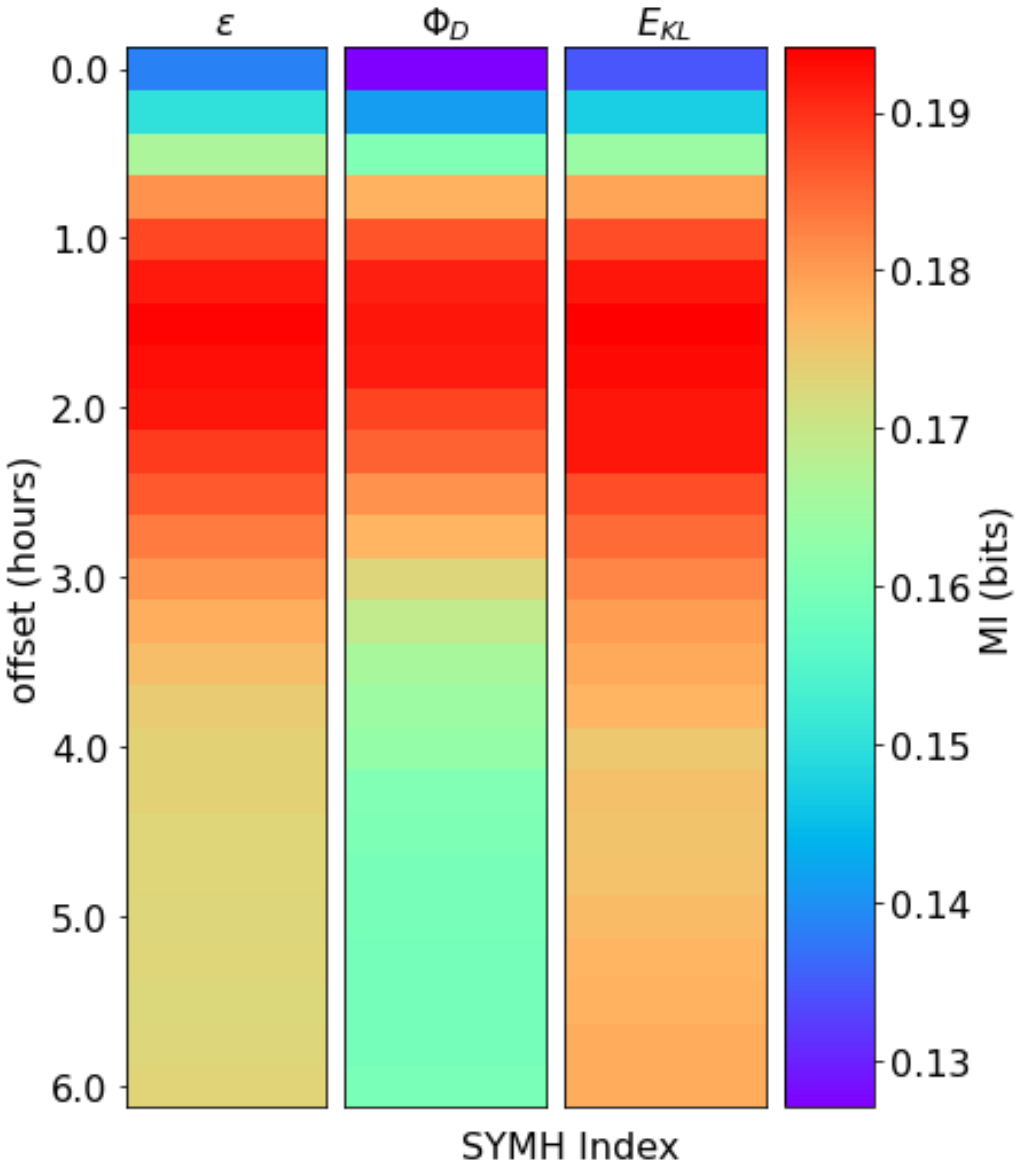

Figure 8.3: Comparison of MI values forB_z, Φ_D, E_{KL}, and ϵ, as observed via the SYM/H index. x-axis: (top) coupling functions (bottom) all data sets use the SYM/H index. The y-axis represents the time offset, in hours, between the coupling functions and the SYM/H index timestamps, as described in section 6.4. Individual heat maps, where the MI value is not relative to other data sets can be seen in section D.4.

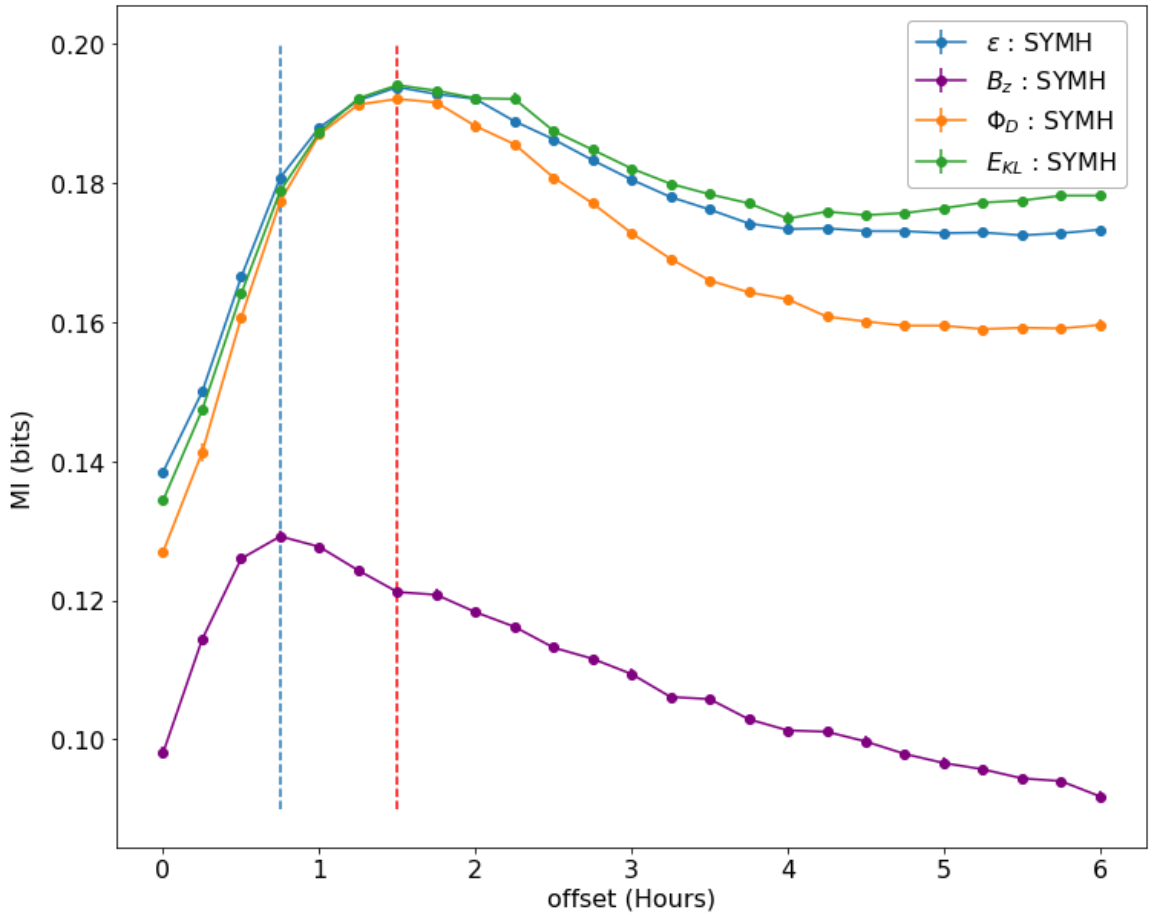

Figure 8.4: MI results for B_z, Φ_D, E_{KL}, and ϵ, with the SYM/H index. The coupling functions all clearly draw out the magnetospheric response time of the terrestrial magnetosphere. at the 90 minute offset (red dashed vertical line), which occurs later (as expected) that the 45 minute offset for B_z (blue dashed vertical line). Offset indicates the extent of time offsetting between data sets (section 6.4). Individual values of the MI can be found in Table D.2.

8.4 Discussion

Following section 8.2 it can be inferred that the coupling functions considered, the Akasofu parameter, ϵ, Kan and Lee electric field, E_{KL}, and Dayside reconnection rate, Φ_D, should more strongly characterise the solar wind and IMF coupling to the magnetosphere than the IMF component, B_z. The precise ordering the coupling functions should take is difficult to draw out. Firstly, each coupling function characterises different behaviours in the solar wind and IMF coupling to the magnetosphere, and one must take note of the fact that the methods and data applied between Newell et al. (2007) and Milan, Gosling, et al. (2012) are not the same.

Coupling function coefficients are empirically derived and the data used in considered studies appears, typically, to be of short time-scales under ideal conditions, with considered studies spanning hours to a few days for events. Therefore, the novel approach of using MI, which can draw out both linear and non-linear relationships as opposed to correlation, presents an opportunity to conduct a new assessment of coupling functions with decades of available data. Thus, we can assess their use in characterising the solar wind and IMF coupling to the magnetosphere generally. Additionally, as the coefficients of coupling functions are solved under ideal conditions, often in short time scales, it opens the question as to whether they are generally useful for characterising the coupling relationship or if the IMF parameters, B_z, stands as a better measure of coupling. The exception of the studies considered is Newell et al. (2007), which investigates parameters for several years. The measure of this relationship is the Pearson coefficient, not MI, however, it does offer a large scale investigation to compare our results against.

The AL index, expressing the strongest westward current intensity of the Auroral Electrojets (AE), has been explored in-depth in subsection 3.2.1 and proven to show the response time of the magnetosphere, $\approx$ 45 minutes, with a strong relationship to B_z, following our investigation in subsection 7.3.1. It has been used to support the investigation of coupling functions in previous studies, including Perreault and Akasofu (1978); Kan et al. (1979); Bargatze, Baker, et al. (1985); Bargatze, Ogino, et al. (1999); Newell et al. (2007); Alberti et al. (2017); and Milan, Gosling, et al. (2012). It is a well understood geomagnetic index, measured over several decades with the use of Earth based magnetometers, leaving a wealth of data to explore (subsection 4.2.1). The AL index is therefore an ideal index to investigate the use of coupling functions.

Additionally, the SYM/H index, a measure of the ring current intensity, has been explored in-depth in subsection 3.2.2 and supports expected values of the response time, varying from 45 minutes to 135 minutes, with a strong relationship to B_z following our investigation in subsection 7.3.2. Whilst the response time of the SYM/H index has greater variation, results have been in line with previous studies and the knowledge that ring current intensification events which generate SYM/H intensification last longer, and peak later (Gonzalez et al., 1994). It has been used to support the investigation of coupling functions in previous studies, including Eriksson et al. (2000); Milan, Gosling, et al. (2012); Alberti et al. (2017); and Stumpo et al. (2020), as well as the low resolution counterpart, Dst, in Newell et al. (2007); and Perreault and Akasofu (1978). SYM/H therefore represents another well understood geomagnetic index, that has been documented over several decades with the use of Earth based detectors (subsection 4.2.2). The SYM/H index is therefore an ideal

index to investigate the use of coupling functions.

8.4.1 Drivers

In the case of the AL index, assessing the results presented in subsection 8.3.1, it is clear to see that the three coupling functions, Φ_D, ϵ, and E_{KL}, are confirmed as much stronger indicators of the characterisation of the solar wind and IMF coupling to the magnetosphere by measurement of the AL index. They exceed the value of B_z by 100% at their peak MI result at an offset of 45 minutes. Whilst all three coupling functions are closely valued, by the 45 minute offset, Φ_D becomes unequivocally the most significant MI result and indicator of AL index driving, although the MI results show a clear relationship for all coupling functions.

Furthermore, in the case of the SYM/H index, assessing the results presented in subsection 8.3.2 a similar picture is seen. All three coupling functions, Φ_D, ϵ, and E_{KL}, are confirmed as stronger indicators of the characterisation of the solar wind and IMF coupling to the magnetosphere by measurement of the SYM/H index. They exceed the value of B_z by 60% at their peak MI result at an offset of 90 minutes, or by 50% when comparing their peak offset to the B_z peak offset, 90 and 45 minutes respectively. Unlike the AL index, no coupling function becomes a clear indicator of the SYM/H index driving compared to one another.

In the case of the dayside reconnection rate, Φ_D, observing Equation 3.10, we see the dependency of Φ_D is on the solar wind radial velocity, v_x, IMF magnitude, B_{YZ}, and clock angle, θ_c. Observing our results in chapter 7, we determined that in the case of the AL index, B_z and v_x are the parameters that most strongly determine the driving of the AL index. Furthermore, we determined that v_x was the strongest

driver of the SYM/H index and that B_{YZ}, although the fourth strongest driver, was a significant parameter. Furthermore, we have shown from both our results and physical understanding outlined in chapter 2 and chapter 3, that B_z, indicating the strength of the southward orientated IMF, and v_x, indicating the rate of plasma coupling from high speed events creating compressed regions of the solar wind, are two parameters that would strongly determine the rate of energy insertion to the magnetosphere. B_{YZ}, representing the transverse component of the IMF, given by Equation 3.6, may more fully encompass the rate of reconnection, as not all field lines are perfectly aligned north-south, and hence reconnection is not solely confined to the north-south orientation, just a significant portion of it. Finally, θ_c, the angle of the IMF vector projected onto the Y-Z plane, helps to further refine the measurement of reconnection. Hence, these variables combine to an expected and demonstrably more powerful measure of the Φ_D, shown by the measured relationship of Φ_D with both geomagnetic indices.

For the Akasofu parameter, ϵ, given by Equation 3.8, and the Kan and Lee electric field, E_{KL}, given by Equation 3.9, similar conclusions can be drawn. Both coupling functions are also dependent on the solar wind velocity, IMF, and clock angle. In the case of ϵ, the dependency is on the solar wind speed, v, and IMF strength, B, given by Equation 3.4 and Equation 3.5, respectively. Unlike Φ_D, the dependency on these parameters is independent of orientation along any vector axis. As such, it is unsurprising that whilst a strong indicator, at the expected peak response time of 45 minutes, for the AL index results, there is separation between Φ_D and ϵ, as the vector orientation is important to the rate of reconnection and energy insertion to the magnetospheric system. This assertion is supported by E_{KL},

where it returns a stronger MI result than ϵ, as E_{KL}, whilst also dependent on v, is related to B_{YZ} rather than B. Finally, when considering the SYM/H index results, we see almost no separation between the coupling functions, with ϵ and E_{KL} differing with Φ_D by ≈ 0.0017 bits. The lack of distinction between the coupling functions could be attributed to the later occurring and longer lasting behaviour of SYM/H intensification. SYM/H being created through ring current intensification via magnetotail reconnection, meaning energy coupled to the magnetosphere may be more homogenised due to the energy build up in the magnetotail of variable timescales before reconnection occurs. This cause of the delayed measurement of the SYM/H index likely also determines why the MI results for SYM/H are lower than the respective MI results for the AL index.

8.4.2 Response Time

Alongside the physical interpretation of the MI values for coupling functions indicating driving of the geomagnetic indices, we again validate the use of a time offset to validate the response time. Repeating our assertion in subsection 7.4.2, the relationships investigated should strengthen (approach their true MI value) when the time offset matches the response time of the Earth's magnetosphere. This is the time from solar wind contact with the magnetopause for the solar wind energy to travel through the magnetospheric system and generate perturbations in the magnetometers, measured as the AL and SYM/H indices. Noting the observations in case studies (Table 7.1), it is expected that there may be two response times each for the AL and SYM/H indices, the shortest from dayside magnetic reconnection and the longest due to tail ward reconnection. Furthermore, the SYM/H index should return a later response

time than that of the AL index.

For the AL index, Φ_D, E_{KL}, and ϵ all draw out the response time of the magnetosphere with clear values matching the established time of 45 minutes (Table 7.1). Starting from their MI results at a 0 minutes offset, respectively: 0.2683 $\pm$ 0.0007 bits, 0.2661 $\pm$ 0.0004 bits, and 0.2551 $\pm$ 0.0004 bits, each coupling function rises to a peak MI result at the expected offset of 45 minutes, respectively: 0.4118 $\pm$ 0.0009 bits, 0.3723 $\pm$ 0.0005 bits, and 0.3614 $\pm$ 0.0007, in agreement with the response time of past studies. See section D.1 for all MI results and section D.2 for visualisations of the data.

For the SYM/H index, Φ_D, E_{KL}, and ϵ all draw out a clear response time in contrast to the SYM/H index results of subsection 7.4.2, which returned the response time as a range of times. The response time is also later, with each coupling function peaking at 90 minutes, rather than 45 minutes. Starting from their MI results at a 0 minutes offset for Φ_D, E_{KL}, and ϵ respectively: 0.1270 $\pm$ 0.0005 bits, 0.1344 $\pm$ 0.0004 bits, and 0.1385 $\pm$ 0.0003 bits, each coupling function rises to a peak MI result at an offset of 90 minutes, respectively: 0.1921 $\pm$ 0.0005 bits, 0.1941 $\pm$ 0.0004, and 0.1938 $\pm$ 0.0004 bits. See section D.3 for all MI results and section C.4 for visualisations of the data.

Our results in chapter 7 supported the investigation of past studies that the AL and SYM/H indices have differing response times. In the case of the SYM/H index this was much less clearly pronounced, with our results and past studies not giving a clear response time. However, this was expected as SYM/H events last for longer periods of time due to ring current intensification which depletes with time. Our results in chapter 7 supported this assertion with peak MI results from approximately

30 to 135 minutes. In this study we note that there is a much clearer MI peak and hence a quantifiable response time of 90 minutes. However, comparing Figure 8.2 and Figure 8.4, it can be seen that whilst the coupling functions for the AL index, decline quickly to MI values $\approx 25\%$ of the peak MI values, coupling functions for the SYM/H index, after 6 hours, have only declined to $\approx 50\%$ of the peak MI values, demonstrating that they are being sustained longer than the AL index intensification.

Evidence of two distinct MI peaks, which can be attributed to the different driving mechanisms, is partially supported, but equally unclear in this study. Observing Figure 8.4, one can see an increase from the previous MI result at 135 minutes for E_{KL}, and a reduction in the negative gradient at the same time for Φ_D. These results match similar times seen in the solar wind variables of the SYM/H index study, seen in Figure 7.4.

8.5 Conclusions

Investigating three well established coupling functions that characterise the solar wind and IMF coupling with the magnetosphere has provided further evidence in support of the methods of this thesis. The works of Perreault (1974); Kan et al. (1979); Newell et al. (2007); and Milan, Gosling, et al. (2012) indicated that coupling functions should exceed the IMF, B_z, parameter as a measure of the coupling, via the geomagnetic indices AL and SYM/H. This has been shown to be the case, with the coupling functions exceeding B_z by $\approx 100\%$ and 50% for the AL and SYM/H indices, respectively.

Furthermore, by drawing out the response time of the Earth's magnetosphere more

clearly than the investigation of chapter 7 confirms that an *a priori* relationship can be observed in the MI values output. With two studies demonstrating the effectiveness of the methods outlined in this thesis, further work can be taken forward with confidence that relationships between the solar wind and other data can be found.

The benefits of this study, are not only reliant on the capability of MI to draw out non-linear relationships, but to validate the use of coupling function parameters. Coupling functions rely on the empirical derivation of the coefficients and powers of Equation 3.2, using data measurements. In the studies considered, these derivations are often conducted in each case with events spanning only a few hours or days. In these short time spans, the combination of solar wind and IMF parameters are adjusted to best fit the coupling function to the variance of the compared data which may could be considered creating a bias. The work of this thesis uses significantly larger data sets from 16 years of data, at a higher sampling rate (15 minutes vs 1 hr) and does not attempt to *fit* MI to optimise the result against the comparative data. Predetermined conditions are applied in the methods (chapter 6) and applied uniformly to find what may be considered the *correct* MI value for the relationship between two data sets. Furthermore, the coefficients and powers are empirically derived under periods of optimal physical conditions, for the considered phenomena. Thus, this may act to ensure any measured strength of a coupling function, compared to B_z and other coupling functions, would exceed others. By assessing these coupling functions with these methods, not only have we shown the utility of our methods, but provided confirmation of their capability to better characterise the solar wind and IMF coupling with the magnetosphere under general conditions.

In Newell et al. (2007) continuous data sets spanning several years are used to

calculate correlation coefficients that indicate coupling functions account for a greater measure of the variation in the geomagnetic indices than B_z, at 1 hour sampling rates. Coupling functions are noted to primarily describe the dayside reconnection phenomena, whereas our own investigation in chapter 7 into B_z and the geomagnetic indices, indicates that tail reconnection may be the primary driver of magnetospheric plasma into the inner magnetosphere. In the case of Φ_D, Milan, Gosling, et al. (2012) relies on the absence of nightside reconnection to determine the coefficients and powers, and to investigate the strength of the coupling. Therefore, working under this understanding, if coupling functions are focussed on considering the dayside reconnection rate, when tail reconnection is the primary driver, it is unsurprising that we have not seen two distinct peaks in the results of this chapter. It may be that values seen in chapter 7 are showing driving from tail reconnection, and the results of this chapter, a better measure of driving from dayside reconnection.

It is worth nothing here, again, that one of the key differences of this work, as opposed to past studies, is in the difference between MI and correlation. MI information is able to quantify all relationships between two sets of variables by exploring both linear and non-linear relationships, whereas correlation is only able to quantify linear relationships.

8.6 Closing Remarks

With the approach of this thesis, it has been determined that coupling functions are strong indicators of the solar wind and IMF coupling to the magnetosphere as a whole. B_z, whilst useful, is a less reliable indicator of the variation in the geomagnetic indices

than coupling functions. This investigation was done as a limited exploration of the coupling functions strength of characterisation, as observed in the AL and SYM/H indices. Therefore, confirmation of this conclusion should be made with an expanded investigation. Additional coupling functions should be considered, and a greater range of comparison data sets included, such as additional geomagnetic indices, and a wider range of phenomena connected to solar wind and IMF coupling to the magnetosphere. Furthermore, a study done at a higher temporal resolution, < 15 minutes, may be able to define the two driving mechanisms from day side reconnection and ring current intensification due to tail ward reconnection, that was not drawn out through the MI results associated with any singularly paired data sets.

Chapter 9

Saturn Kilometric Radiation and the Solar Wind

This chapter presents the primary investigation of this thesis work, to assess the viability of using SKR as a proxy for the solar wind and IMF conditions at Saturn. This work was conducted at the Space and Planetary Physics group, Lancaster University.

The objective of this work is to apply MI as the measure of the strength of the relationship between specific solar wind and IMF parameters with SKR. Determination of SKR as a suitable proxy for the solar wind and IMF conditions is performed by propagating the directly measured parameters at Earth, using the propagation model of Tao et al. (2005). Accounting for limitations of the propagated data, such as uncertainty in the arrival time and data availability restrictions from the Sun-Earth-Saturn alignment, the methods of this thesis are used to apply MI between the propagated parameters and SKR. Propagated parameters that show a strong MI

relationship with SKR then indicate the suitability of SKR to act as a proxy for the conditions of a given solar wind or IMF parameter. The tangential IMF parameter, B_y, is identified as the strongest MI relationship, and only significant parameter in comparison to the results of chapter 7 and chapter 8. B_y is inferred to be an indicator for the IMF strength and rate of magnetic reconnection, and thus driving of SKR.

9.1 Introduction

With the close of chapter 8, all the elements have been drawn together to investigate the primary motivations of this thesis. With a lack of upstream solar wind monitors at the outer planets, directly measured data has been restricted to a handful of short events, from the passing of past satellite missions such as the Voyager probes. Consequently, the lack of available data has made it challenging to explore the impact of the solar wind on planetary magnetospheres outside the terrestrial system. Is the model of the terrestrial system a universal model or restricted to the conditions of its own magnetosphere? Is the solar wind a significant driver of all planetary magnetosphere dynamics? Without continuous data of the solar wind conditions at other planets, at large enough time scales to encapsulate the evolution of the solar wind and magnetospheres, it is challenging to answer these and other questions relating to the solar wind's impact. Therefore, in this chapter we outline our investigation of SKR as a proxy for the solar wind and IMF conditions at Saturn. The Cassini mission offers 13 years of continuous, directly measured data for investigation, from 2004 - 2017.

We have explored the physical principles underlying the solar wind and IMF interactions with magnetospheres throughout chapter 2 and chapter 3. An understanding

of the Saturnian magnetosphere and SKR has been described in section 3.4 and section 3.5, respectively. As such, information explored in these chapters will not be repeated here unless directly relevant to the interpretation of results.

In chapter 4, we have explored the data of both the solar wind and SKR, their origins, processing, format, and limitations. The solar wind, measured at the L1 Lagrange point with several satellites offers a data set for investigation that spans decades (section 4.1). Using the propagation model of Tao et al. (2005), this data has been propagated to Saturn, where it is used as a substitute for direct solar wind measurements (section 4.3). There are two primary limitations of the propagation model. The first is the need for the alignment of bodies, with a Sun-Earth-Saturn angle, Φ_S, $< 50°$, limiting the availability of data (subsection 4.3.1). The second is the uncertainty in the arrival time of the solar wind to Saturn, approximately $\pm$ 2 days, which is dependent on Φ_S (subsection 4.3.2).

SKR, measured by the RPWS instrument of the Cassini satellite, is presented in four distinct data sets. We consider four different SKR data sets for two reasons. The first is due to the opposing polarisation of SKR between the two hemispheres of Saturn, discovered during the Voyager flybys. These are the Right-Hand (RH) polarisation that originates from the Northern Hemisphere and the Left-Hand (LH) polarisation that originates from the Southern hemisphere. As can be seen in Figure 3.9, this creates two distinct regions in which SKR can be detected due to the nature of SKR emissions. This results in the first division of the data between hemispheres, which we separate in order to investigate any difference in the relationship to SKR based on polarisation and the physical boundaries limiting SKR detection. Secondly, each of these data sets is split in two as SKR is found across the wavelength range of 3 kHz to

1.2 MHz and peaks in the 100 - 400 kHz range. Hence, we find the available data is split into two sets, from 10 - 1,000 kHz and the peak range of 100 - 400 kHz, where the most intense radiation can be considered. By separating out the peak SKR frequency range, we may find stronger relationships if the additional frequency ranges are returning weak signals and not strongly connected to the solar wind. Alternatively, if the relationship is seen across all frequencies, we would expect to see a more significant MI result across the complete frequency range, demonstrating a better characterisation of the relationship. Consequently, SKR is considered in four data sets, divided by frequency range and polarisation (hemisphere). See section 4.4 for further details of the division of the SKR data.

The theory behind MI has been explored in chapter 5. Crucially, in chapter 6, we have explored the application of MI to ideal Gaussian data with a known analytical value (Equation 6.3). Furthermore, with the challenges of acquiring data we presented an alternative means of calculating uncertainties to give confidence in the values achieved, from singular solar wind and SKR data sets. Finally, we explored real data in chapter 7 and chapter 8, investigating the application of MI and uncertainty calculation to the solar wind and geomagnetic indices, answering the central question, *Will it work?*. Successfully drawing out the response time of the terrestrial magnetosphere answered this question, with confidence, that significant results in the relationship between the solar wind and phenomena associated with the magnetospheric systems can be found.

In this chapter, the time offset outlined in section 6.4 will be even more important than in the terrestrial based studies. The solar wind and IMF are not constant values, strength, speed, temperature, and density all vary; events such as CMEs,

geomagnetic storms, and substorms create even more turbulence. As these values vary so do the mechanisms by which the solar wind moves through the magnetospheric environment, to emission of SKR. Taubenschuss et al. (2006) finds different response times for different variables: 13 hours for the solar wind dynamic pressure, p_{dyn}, 44 hours for tangential IMF component, B_y, and 52 hours for solar wind bulk velocity, $\mathbf{v}$. As seen in chapter 7, the response time is not a definite value. The solar wind plasma moves through the system at different rates, as seen in the gradation of MI results for the geomagnetic indices. Furthermore, no clear relationship between Φ_S and the propagation uncertainty is presented in Tao et al. (2005). As such, even though an individual offset could be calculated for each solar wind and IMF parameter according to Φ_S, before pairing with an SKR parameter (section 5.4), it is not feasible to solve this with any confidence. No one time offset can therefore describe the temporal uncertainties in the data. We must treat the data as a whole, and apply an offset uniformly to investigate the Saturnian magnetospheric response time and the uncertainty in the propagation arrival time, neither of which are easily accounted for.

If the application of a uniform offset can account for these uncertainties, it follows that the MI values will be at their greatest when the time offset (section 6.4) between the solar wind and SKR data equals the correct value. However, it is not anticipated that this will be clearly defined in these results, as the combined temporal uncertainties creates a complex issue to account for. Following an assessment of the results, we discuss possible future solutions.

We begin this chapter by reviewing several papers investigating the relationship between the solar wind driving of the magnetosphere and emission of SKR. We investigate earlier works from the limited available data prior to the Cassini mission

and works that have followed using the RPWS SKR data. A summary of the findings from this review and the expected parameters that should present a strong MI relationship with SKR can be found in Table 9.1.

Following a review of existing work, we present the results of the research in this thesis. Results are analysed according to each SKR data set independently, interpreting these results in the context of the existing work reviewed. We attempt to draw out the response time of the Saturnian magnetosphere and account for the uncertainties in the propagation model arrival time. We also draw out the most influential solar wind and IMF parameters of SKR and determine which parameters SKR can act as a proxy for. Furthermore, we assess these results wholly to one another, understanding the commonalities and differences between the data sets.

The following parameters are investigated in this chapter: the IMF tangential component; B_y, and solar wind parameters: dynamic pressure, p_{dyn}; proton density, ρ; temperature, T; and the radial velocity components, v_x, and v_y. These parameters are compared to each of the four SKR data sets: LH 10 - 1,000 kHz, LH 100 - 400 kHz, RH 10 - 1,000 kHz, and RH 100 - 400 kHz, creating 24 unique data sets to consider.

9.2 Literature Review

Here, several previous studies of the relationship between SKR and the solar wind are examined and their results summarised for comparison with the results of this thesis. Using existing publications, the available evidence in support of solar wind driving of SKR can be explored to building a consensus of the parameters we expect to see display strong relationships. Earlier studies, prior to the Cassini mission, are limited

by the availability of data, primarily from the flybys of the Voyager probes. From 2004 onwards, Cassini provides the wealth of data that has been awaited to expose relationships between the solar wind and SKR. By exploring these past studies we can understand the present understanding of the relationship, to which the results of this chapter may act as confirmation or provide new insights.

In 1980 and 1981, respectively, the Voyager 1 and 2 probes visited Saturn. No sooner had the probes sent back their data than investigations of the solar wind's connection with SKR began. The Plasma Science (PLS) experiment aboard the probes measured the solar wind bulk velocity and dynamic pressure, $\mathbf{v}$ and p_{dyn}, respectively. Modulation of SKR was already known to be of time-scales greater than the rotation period of Saturn, ~ 10.39 hours, Desch (1982) sought to connect the solar wind with SKR modulation as a solution. Investigating two intervals of 161 and 164 days from Voyager 1 and 2, respectively, a long term modulation period of the SKR was observed corresponding to the solar cycle. Strong correlation coefficients (0.57 and 0.58) between p_{dyn} and SKR were found, with moderate correlation to $\mathbf{v}$ (0.24 and 0.45).

These results were followed up in 1983 by Desch and Rucker (1983), investigating the link between an increased number of solar wind parameters and SKR emissions. Increased numbers of parameters were resolved by the inclusion of data from the Voyager 1 probe, for 170 days in 1980. IMF data was sourced from the magnetometer (MAG) experiment, radio emissions from the Planetary Radio Astronomy (PRA) experiment, and plasma data from the PLS experiment. Expansion of the study found a continuing high correlation with p_{dyn}, with a peak correlation occurring at a time lag of 0 hours, indicating an expected response time of less than 1 Saturn

rotation period. Other pressure related variables show strong correlations also, most notably **v**, though these are attributed as artefacts of the p_{dyn} relationship. Notably, although initial links give an equal measure to p_{dyn} and the IMF, this is decreased with randomisation of the data and dismissed as a driver of SKR as an artefact of p_{dyn}. Final peak correlation coefficients are found for the solar wind parameters, dynamic pressure, p_{dyn}: 5.9/4.9; proton density, ρ: 5.5/4.7; solar wind bulk velocity, **v**: 4.2/2.7; and IMF component, B_y: 3.7(3.3)/2.6(3.2) for toward (and away) from the Sun.

These early insights offer an important first look into investigations of the solar wind relationship to SKR. However, Detsch acknowledges some issues in the calculation of results, such as inaccuracies in the propagation of the solar wind from Voyager to Saturn, and unknown interactions between the solar wind coupling with the magnetosphere and emission of SKR. With data limited to only a 6 month period in 1981, we should not take these findings in isolation but as an early indicator of relationships. The following studies now make use of the availability of Cassini missions data, offering more diverse, well processed data to investigate.

Taubenschuss et al. (2006) follows on from works such as Desch (1982) and Desch and Rucker (1983), performing an analysis of solar wind driving of SKR with an investigation of early Cassini data. The IMF results of Desch and Rucker (1983) are directly commented upon, with the low correlation coefficient potentially attributed to the downstream measurements at 1.6 AU, ballistically propagated to the point of the planet and ignoring hydrodynamic interactions of high and low speed streams inside the solar wind. Cassini data is limited to 124 days in late 2004 coinciding with two instances of SKR intensification. Analysis for Taubenschuss et al. (2006) is performed using Linear Prediction Theory (LPT), to predict an output function, Y,

by convolving a filter function, f, with an input function, X. The strength of the prediction is measured as an efficiency, which measures the variance of the modelled output data to the variance of the actual data, an efficiency of 100% indicates a perfect reproduction of the actual data by LPT. LPT gives four parameters equal weight as drivers of SKR emissions: solar wind dynamic pressure, p_{dyn}; 55% (13 hours), solar wind bulk velocity, $\mathbf{v}$; 55% (52 hours), IMF strength, B; 60% (40 hours), and tangential IMF strength, B_y; 53% (27 hours), where values indicate the efficiency of the parameter and the lag time (time offset). In this study, temperature, T, is also assessed but found to have an efficiency of only 20%, and the IMF components, B_x and B_z, ≤ 25 % indicating poor connections to SKR. However, if greater time lags are considered, it is not discounted that the efficiency of these parameters will increase.

Zarka et al. (2007) investigates the modulation period of SKR, P_{SKR}, using Fast Fourier Transforms (FFT) for peak SKR power data (100 - 400 kHz). Data covers a 1,186-day interval, from 30 June 2003 to 27 September 2006. P_{SKR} is typically quoted as ~ 10.39 minutes but can vary by several minutes over timescales of months to years. Zarka et al. (2007) finds that modulation of P_{SKR} occurs on a timescale of 20 - 30 days. This timescale strongly aligns with the modulation seen in the FFT of $\mathbf{v}$ data, with P_{SKR} peaks aligning with $\mathbf{v}$ peaks. Follow up investigation finds a correlation coefficient between P_{SKR} and $\mathbf{v}$ of $C > 40\%$ and gives a correlation coefficient between SKR power and $\mathbf{v}$ of $C > 44\%$. Other parameters are investigated against P_{SKR} but no significant correlation is found for p_{dyn}, ρ, and B. However, this study is not directly connected to SKR power and so only acts to reinforce the importance of $\mathbf{v}$ to SKR, rather than discounting other parameters. That other parameters do not affect the modulation of P_{SKR} does not indicate a lack of driving SKR power.

Badman et al. (2008) investigates the relation between intensification and pulsing of SKR under solar wind compression conditions. This relationship is sought out by investigating intensifications of the SKR power, following arrival of a solar wind compression, any subsequent "drop-out" of the emission detected by Cassini, the phasing of the intensified or reduced emission peaks during the compression event, and the relative phasing and intensity of the emission peaks before and after the compression. Cassini data is analysed from October 2003 to October 2004. This period spans Cassini's approach to Saturn in the first 6 months and its first extended orbit following Saturn orbit insertion in the latter. These intervals were chosen as Cassini was measuring both the interplanetary conditions upstream of Saturn and SKR emissions from Saturn, providing directly measured data in both cases. The IMF magnitude, B, is used as a proxy for p_{dyn}, due to frozen-in theorem a compressed region of the solar wind will correspond to an intensification of the IMF. Investigation of events in the data reveal several features. The key feature of relevance to this work is that high intensity SKR power bursts are coincident with solar wind compressions arrival at the Saturnian magnetosphere. A positive correlation is seen for variations in SKR power with B, acting as a proxy for p_{dyn} with a correlation coefficient of $C = 0.37$.

Early studies of the Cassini mission data, limited to 2004, feature several data gaps. Therefore Rucker et al. (2008) investigates the use of Ulysses satellite data as a proxy, whilst its orbit was close to the ecliptic plane and at $\sim$ 4 AU, with an azimuthal separation to Cassini of 50°. Investigation of the suitability for Ulysses data was done using the SKR relationship to the solar wind with data propagated using an alternative MHD propagation code, ZEUS MHD (Stone and Norman (1992a); Stone

and Norman (1992b)), from 5 AU to Cassini's orbit at 9 AU in three-dimensions using spherical coordinates, R, ϕ, θ. Solar wind is assumed to be uniform in the azimuthal direction as measurement can only occur at a single source. Cassini and Ulysses (SWOOPS experiment) data spans from 1 January 2004 to 31 December 2004. Cross correlation is performed between SKR and the solar $\mathbf{v}$ and p_{dyn} parameters. Use of Ulysses data is confirmed and correlation coefficients between the SKR and solar wind parameters are solved for both Cassini and Ulysses data of C = 0.38 and C = 0.48, respectively for v, and C = 0.57 and C = 0.52, respectively for p_{dyn}.

Clarke et al. (2009) focuses their efforts on connecting the intensification of the auroral oval of Jupiter and Saturn to the solar wind p_{dyn} and v_x parameters. Additionally, SKR power is investigated for several shock events, using Cassini data, of later dates, up to early 2008, of previous studies. Although correlation coefficients are not quoted in this study for SKR and the solar wind, we briefly note that a strong relationship is found between intensification of SKR power and the arrival of increased solar wind v_x and p_{dyn}.

Jackman et al. (2010) investigates the effects of shock compressions from the solar wind on enhancement of SKR emissions. Earlier studies noted in Jackman et al. (2010) reveal that a strong solar wind compression of the magnetosphere during the onset of Saturn Orbit Insertion (SOI) results in intensification of SKR. Furthermore, the magnetic field became depressed and changed orientation, with electron and ion observations revealing Cassini was surrounded by hot, tenuous plasma. The interval surrounding SOI was interpreted as representing a large magnetotail reconnection event accompanied by hot plasma injection. Taking advantage of Cassini's Saturn orbit insertion from 2006, several passes through the magnetotail have occurred, which

Source	Parameters of Note
Desch (1982)	p_{dyn}
Desch and Rucker (1983)	p_{dyn}, $\mathbf{v}$, B_y, ρ
Taubenschuss et al. (2006)	p_{dyn}, $\mathbf{v}$, B_y, ρ
Zarka et al. (2007)	$\mathbf{v}$
Badman et al. (2008)	B, p_{dyn}
Rucker et al. (2008)	p_{dyn}, $\mathbf{v}$
Clarke et al. (2009)	p_{dyn}, v_x
Jackman et al. (2010)	p_{dyn}
Thomsen et al. (2019)	p_{dyn}

Table 9.1: Summary of solar wind and IMF parameters of interest from existing studies that drive SKR emission.

offered several event opportunities to investigate this hypothesis. Jackman et al. (2010) then uses this data to conduct a case study example from Saturn's magnetotail, the purpose of which is to illustrate the response of Saturn's magnetotail to solar wind compression. Changes in the magnetotail flaring and flux content are investigated and the response of SKR emissions to sudden solar wind changes. An alternative one-dimensional MHD solar wind propagation model is used to propagate solar wind data from 1 AU to Saturn, $\sim$ 10 AU (Zieger et al., 2008). Jackman et al. (2010) investigates a 10 day period in 2006, DOY 123-133. A compressions event is attributed to a sudden uptick in p_{dyn} and SKR intensification. This compression event is then attributed to a magnetotail reconnection event, creating plasma release and a travelling compression region, which further intensifies SKR.

Thomsen et al. (2019) develops an analytical method to infer the solar wind parameters, v, and p_{dyn}, from Cassini magnetosheath measurements. Of relevance to this study is the verification of inferred p_{dyn} measurements with SKR intensifications. Five periods are considered for SKR: a) 2004 Day 308-312; b) 2006 Day 39-51; c) 2006 Day 101-105; d) 2010 Day 357 - 2011 Day 2; e) 2012 Day 126-139. In each of these periods, inferred p_{dyn} is compared to SKR power in the 100 - 300 kHz range. Correspondence between SKR and the inferred p_{dyn} is not consistent across data sets. Some events feature strong correspondence between the data and others weakly, if at all. The reasoning behind this is attributed to the conical emissions of SKR and the source region visible by the position of Cassini. When Cassini is close to the equator, the spacecraft preferentially detects radio sources along field lines whose LT differs by less than a few hours from the sub-spacecraft meridian. Thomsen et al. (2019) concludes from the result that the SKR source is most responsive to p_{dyn} variations in regions visible from the morning region of the magnetosphere, the location of the dominant source region.

9.3 Results

Observing the MI values for the data set LH 10 - 1,000 kHz in Figure 9.1, the IMF component, B_y, returns the strongest MI value in relation to SKR. However, unlike the results of the terrestrial based studies in chapter 7 and chapter 8, the distinctions between parameters are not clear. Observing Figure 9.2, variation between MI values for different time offsets of the same parameter have no clear relationship. In the case of B_y, the maximum MI value is 0.1523 ± 0.0056 bits at an offset of 30 hours, whilst

the lowest MI value is 0.0885 ± 0.0014 bits at an offset of -69 hours, with no linear relationship connecting the two through steps of the time offset. This variability is then also seen in the solar wind radial and tangential velocity components, v_x and v_y, respectively, and temperature, T, becoming less pronounced with proton density, ρ, and at a minimum, relatively, with dynamic pressure, p_{dyn}. Furthermore, parameters repeatedly change relative strengths, returning larger MI values than adjacent parameters at some time offsets, and vice versa at others. Parallel levels of variation in the parameters with time offset can be seen across all data sets: LH 10 - 1,000 kHz, LH 100 - 400 kHz, RH 10 - 1,000 kHz, and RH 100 - 400 kHz.

The consequences of this will be discussed in section 9.4. However, because there is no clear response time, there is no single MI value quotable for a specific time offset that has any significance relative to other time offsets across the ± 3 days considered. Nor is there a value, such as at 0 hours offset, that can be considered a baseline MI value to begin from as it is not just a response time being measured but also the uncertainty introduced by the Sun-Earth-Saturn angle, Φ_S. Therefore MI results for a given solar wind/IMF parameter and SKR data set pairing are presented as the average MI values over all time offsets, to give the relative strengths of parameters relative to one another, and as an average measure of their MI relationship to SKR.

9.3.1 LH 10 - 1,000

Observing Figure 9.2, the IMF parameter, B_y, returns the strongest average MI value in relation to the LH 10 - 1,000 kHz SKR data, with an average MI value of 0.1245 ± 0.0033 bits. The second strongest relationship is v_x, with an average MI value of 0.1052 ± 0.0040 bits. The parameters ρ, v_y, and T return average MI values of 0.0518

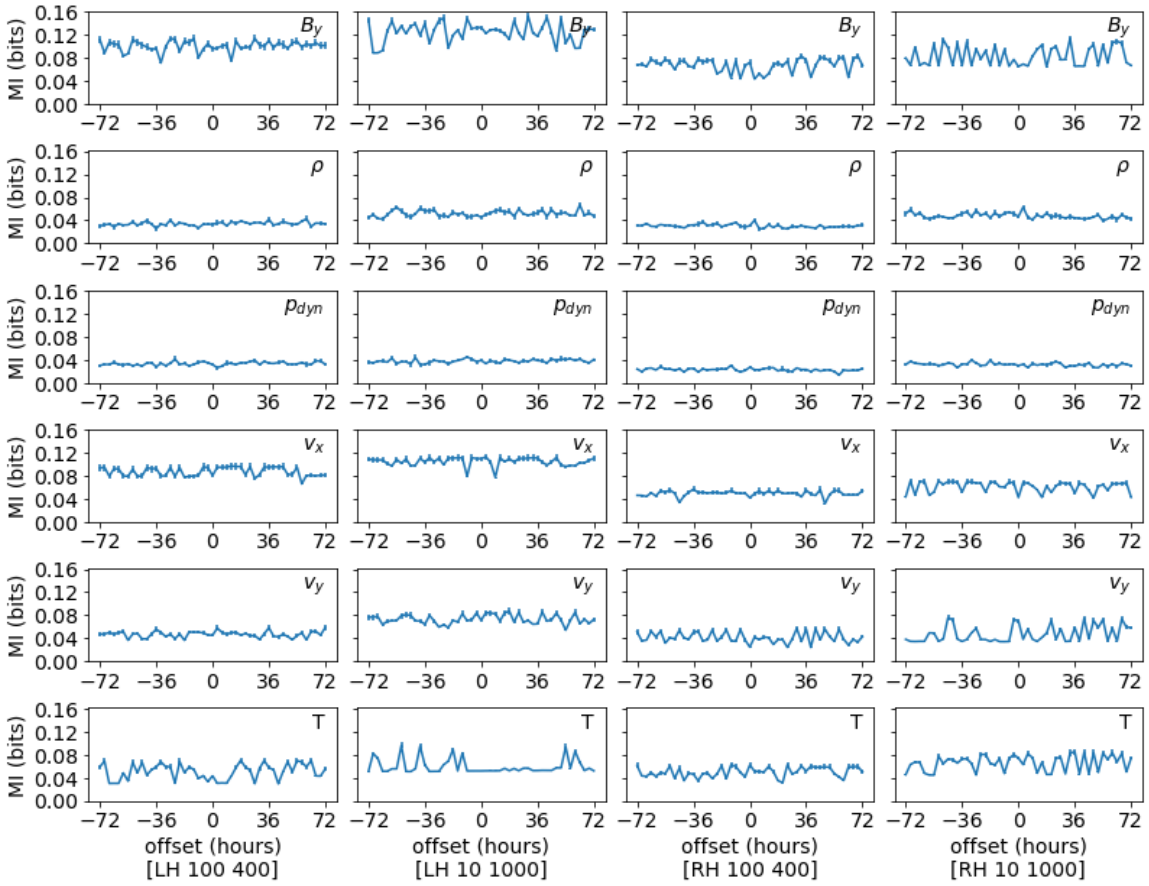

Figure 9.1: MI results for all propagated solar wind variables against SKR data sets. Data is set relative to 50% of an ideal Gaussian relationship of $\sim$ 0.16 bits. Offset indicates the extent of time offsetting between data sets (section 6.4). Individual values of the MI can be found in the appendix tables: section E.1.

$\pm$ 0.0041 bits, 0.0732 $\pm$ 0.0036 bits, and 0.0595 $\pm$ 0.0016 bits, respectively. Finally, the weakest relationship is p_{dyn}, with an average MI value of 0.0375 $\pm$ 0.0031 bits.

MI results comparing B_z, v_y, v_x, T, ρ, and p_{dyn} with the LH 10 - 1,000 kHz SKR data are visualised, with associated errors, in Figure 9.3. Full values for the results can be found in the appendix tables Table E.1 and Table E.2, and for individual

visualisations of the data, see subsection E.2.1.

9.3.2 LH 100 - 400

Observing Figure 9.4, the IMF parameter, B_y, returns the strongest average MI value in relation to the LH 100 - 400 kHz SKR data, with an average MI value of 0.1006 ± 0.0051 bits. The second strongest relationship is v_x, with an average MI value of 0.0873 ± 0.0048 bits. The parameters ρ, v_y, and T return average MI values of 0.0341 ± 0.0031 bits, 0.0469 ± 0.0033 bits, and 0.0507 ± 0.0030 bits, respectively. Finally, the weakest relationship is p_{dyn}, with an average MI value of 0.0331 ± 0.0029 bits.

MI results comparing B_z, v_y, v_x, T, ρ, and p_{dyn} with the LH 100 - 400 kHz SKR data are visualised, with associated errors, in Figure 9.5. Full values for the results can be found in the appendix tables Table E.3 and Table E.4, and for individual visualisations of the data, see subsection E.2.2.

9.3.3 RH 10 - 1,000

Observing Figure 9.6, the IMF parameter, B_y, returns the strongest average MI value in relation to the RH 10 - 1,000 kHz SKR data, with an average MI value of 0.0835 ± 0.0024 bits. The second strongest relationship is T, with an average MI value of 0.0658 ± 0.0029 bits. The parameters v_x, ρ, and v_y return average MI values of 0.0615 ± 0.0030 bits, 0.0477 ± 0.0037 bits, and 0.0476 ± 0.0021 bits, respectively. Finally, the weakest relationship is p_{dyn}, with an average MI value of 0.0316 ± 0.0025 bits.

MI results comparing B_z, v_y, v_x, T, ρ, and p_{dyn} with the RH 10 - 1,000 kHz SKR data are visualised, with associated errors, in Figure 9.7. Full values for the results can be found in the appendix tables Table E.5 and Table E.6, and for individual

visualisations of the data, see subsection E.2.3.

9.3.4 RH 100 - 400

Observing Figure 9.8, the IMF parameter, B_y, returns the strongest average MI value in relation to the RH 100 - 400 kHz SKR data, with an average MI value of 0.0675 $\pm$ 0.0039 bits. The second strongest relationship is T, with an average MI value of 0.0499 $\pm$ 0.0034 bits. The parameters v_x, ρ, and v_y return average MI values of 0.0495 $\pm$ 0.0033 bits, 0.0304 $\pm$ 0.0027 bits, and 0.0415 $\pm$ 0.0030 bits, respectively. Finally, the weakest relationship is p_{dyn}, with an average MI value of 0.0226 $\pm$ 0.0024 bits.

MI results comparing B_z, v_y, v_x, T, ρ, and p_{dyn} with the RH 100 - 400 kHz SKR data are visualised, with associated errors, in Figure 9.9. Full values for the results can be found in the appendix tables Table E.7 and Table E.8, and for individual visualisations of the data, see subsection E.2.4.

9.3.5 Averaged Results

For ease of reference, all MI data sets of propagated solar wind and IMF parameters, paired with respective SKR data sets are summarised in Table 9.2.

	B_y		ρ		p_{dyn}	
Data Set	MI	±	MI	±	MI	±
LH 10	0.1245	0.0033	0.0518	0.0041	0.0375	0.0031
LH 100	0.1006	0.0051	0.0341	0.0031	0.0331	0.0029
RH 10	0.0835	0.0024	0.0477	0.0037	0.0316	0.0025
RH 100	0.0675	0.0039	0.0304	0.0027	0.0226	0.0024
	v_x		v_y		T	
	MI	±	MI	±	MI	±
LH 10	0.1052	0.004	0.0732	0.0036	0.0595	0.0016
LH 100	0.0873	0.0048	0.0469	0.0033	0.0507	0.003
RH 10	0.0615	0.003	0.0476	0.0021	0.0658	0.0029
RH 100	0.0495	0.0033	0.0415	0.003	0.0499	0.0034

Table 9.2: Average MI information results for SKR data sets and propagated solar wind variables.

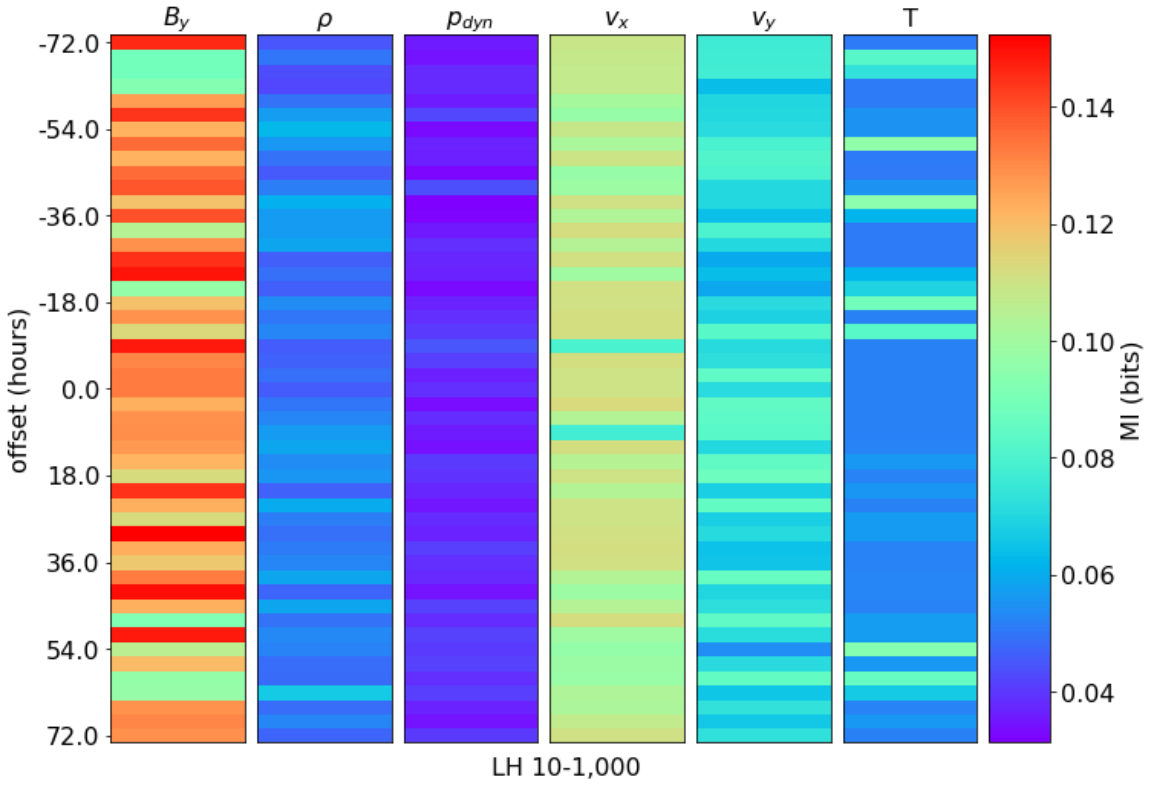

Figure 9.2: Comparison of MI values for propagated solar wind parameters compared with the LH 10 - 1,000 kHz SKR emissions. x-axis: (top) propagated solar wind parameter (bottom) all data sets use the LH 10 - 1,000 kHz SKR data. The y-axis represents the time offset, in hours, between the propagated solar wind and SKR timestamps, as described in section 6.4. The time offset fails to reveal a response time nor reveal a clear strengthening of MI when accounting for the propagation time of the solar wind. Individual heat maps, where the MI value is not relative to other data sets can be seen in subsection E.2.1.

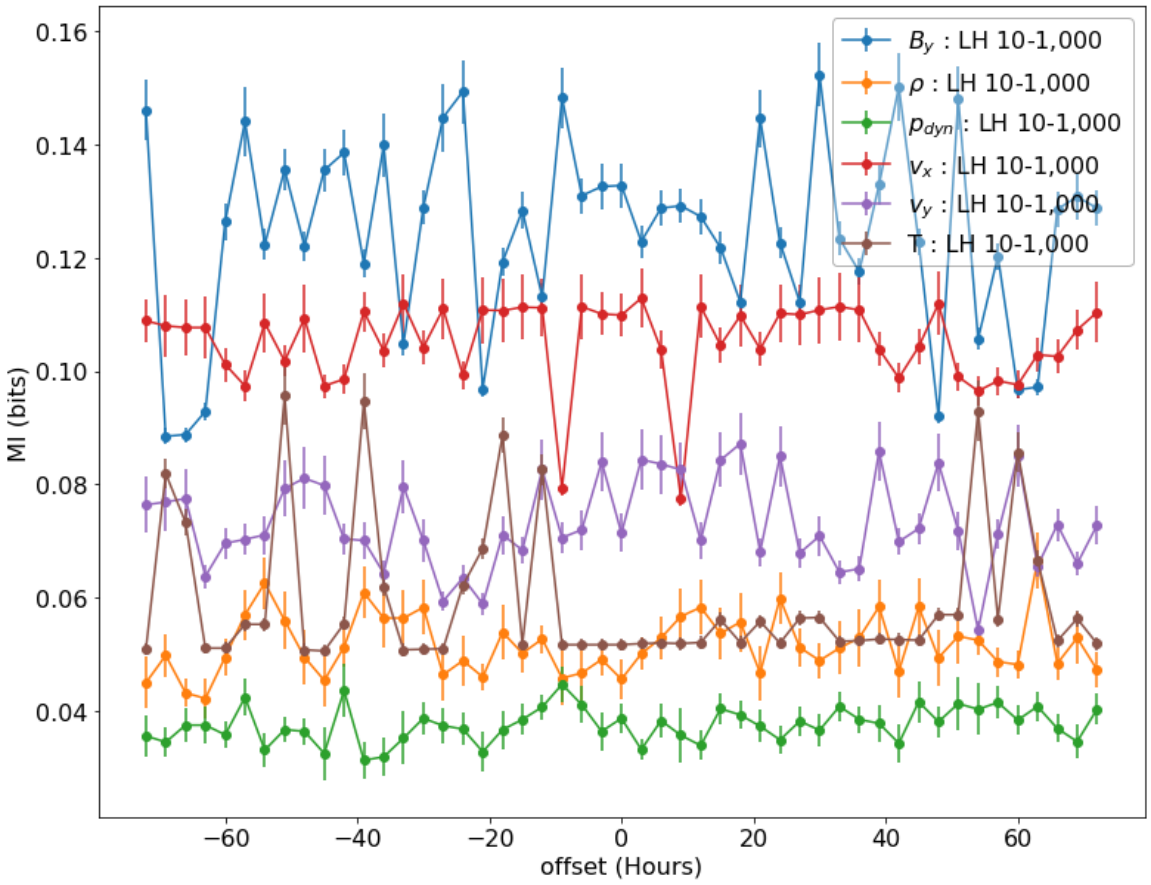

Figure 9.3: MI results for propagated solar wind parameters compared with the LH 10 - 1,000 kHz SKR emissions. Offset indicates the extent of time offsetting between data sets (section 6.4). Individual values of the MI can be found in the appendix tables: Table E.1 for B_y, ρ, and p_{dyn}, and Table E.2 for v_x, v_y, and T.

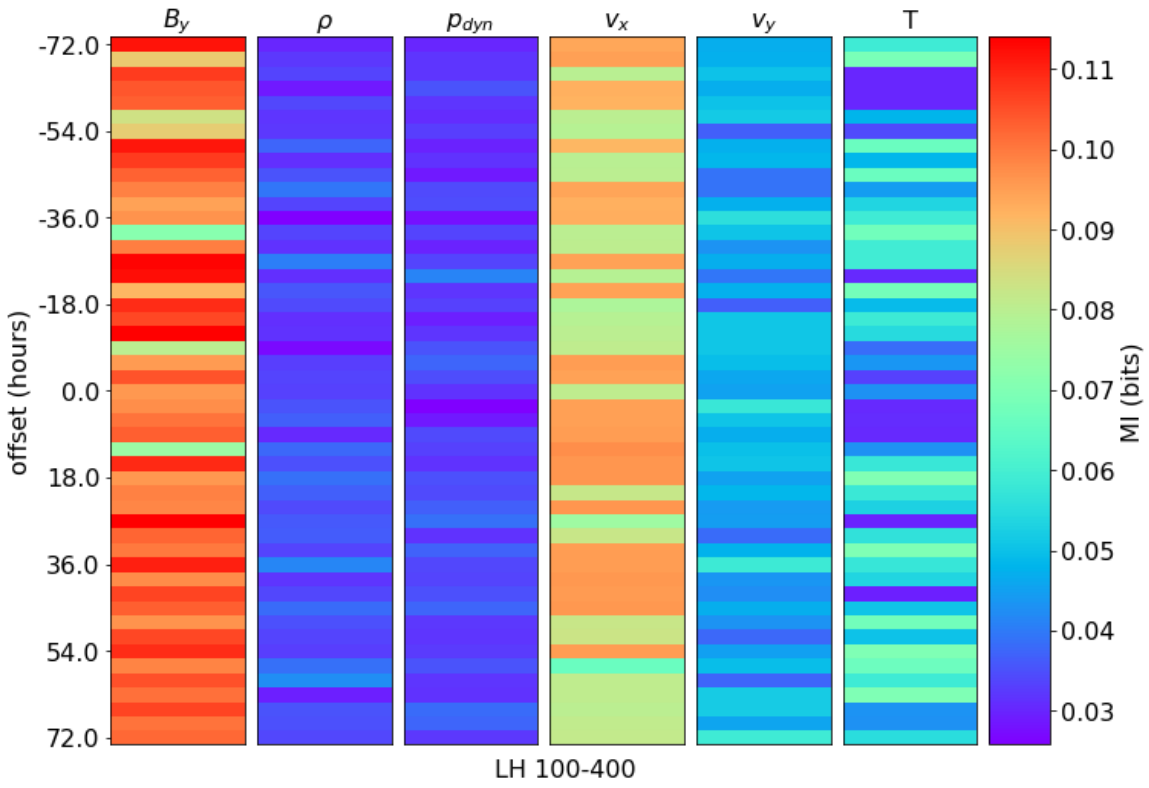

Figure 9.4: Comparison of MI values for propagated solar wind parameters compared with the LH 100 - 400 kHz SKR emissions. x-axis: (top) propagated solar wind parameter (bottom) all data sets use the LH 100 - 400 kHz SKR data. The y-axis represents the time offset, in hours, between the propagated solar wind and SKR timestamps, as described in section 6.4. The time offset fails to reveal a response time nor reveal a clear strengthening of MI when accounting for the propagation time of the solar wind. Individual heat maps, where the MI value is not relative to other data sets can be seen in subsection E.2.2.

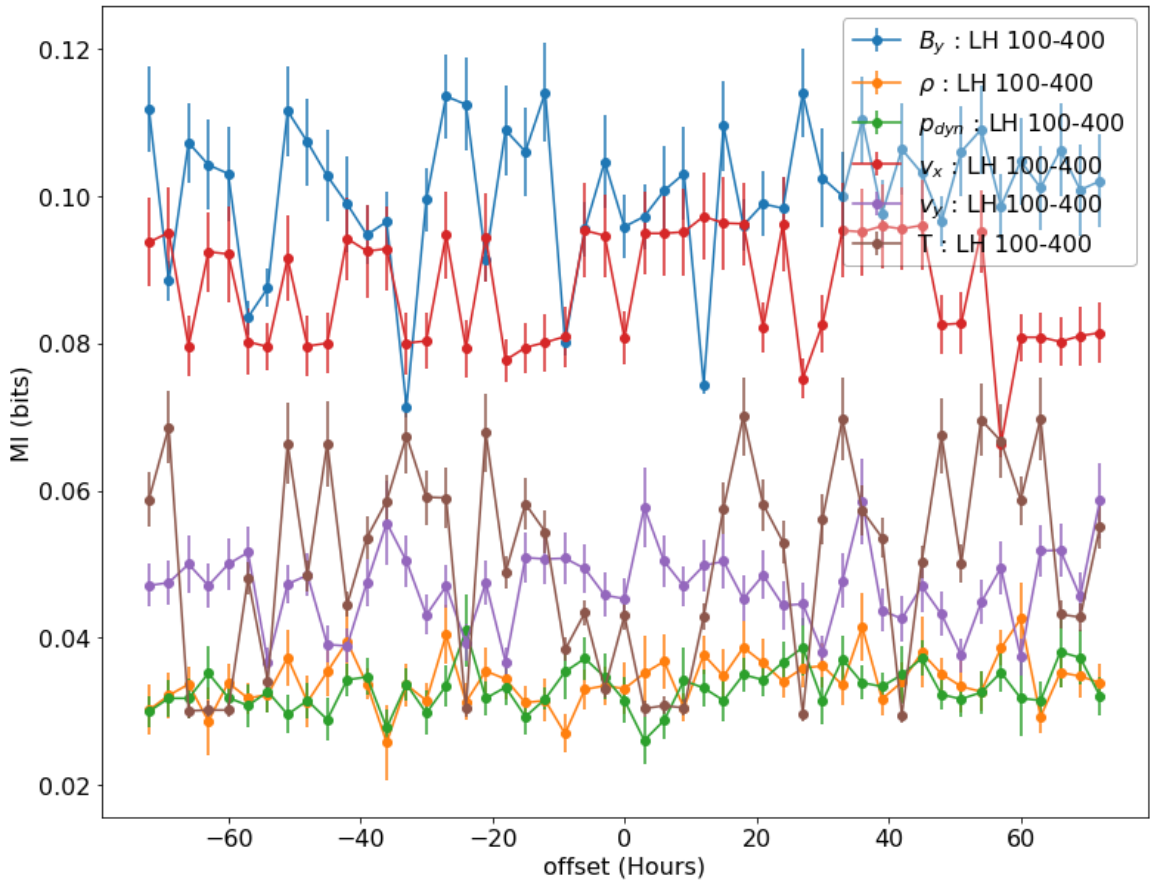

Figure 9.5: MI results for propagated solar wind parameters compared with the LH 100 - 400 kHz SKR emissions. Offset indicates the extent of time offsetting between data sets (section 6.4). Individual values of the MI can be found in the appendix tables: Table E.3 for B_y, ρ, and p_{dyn}, and Table E.4 for v_x, v_y, and T.

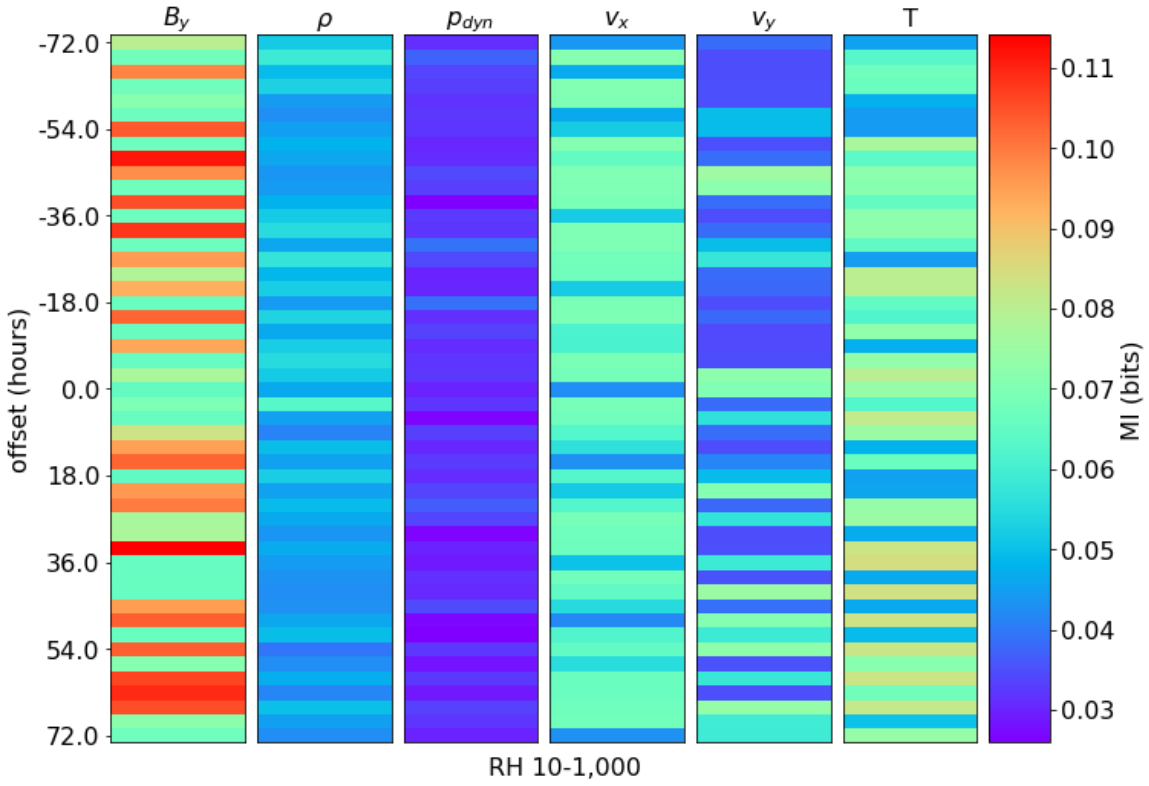

Figure 9.6: Comparison of MI values for propagated solar wind parameters compared with the RH 10 - 1,000 kHz SKR emissions. x-axis: (top) propagated solar wind parameter (bottom) all data sets use the RH 10 - 1,000 kHz SKR data. The y-axis represents the time offset, in hours, between the propagated solar wind and SKR timestamps, as described in section 6.4. The time offset fails to reveal a response time nor reveal a clear strengthening of MI when accounting for the propagation time of the solar wind. Individual heat maps, where the MI value is not relative to other data sets can be seen in subsection E.2.3.

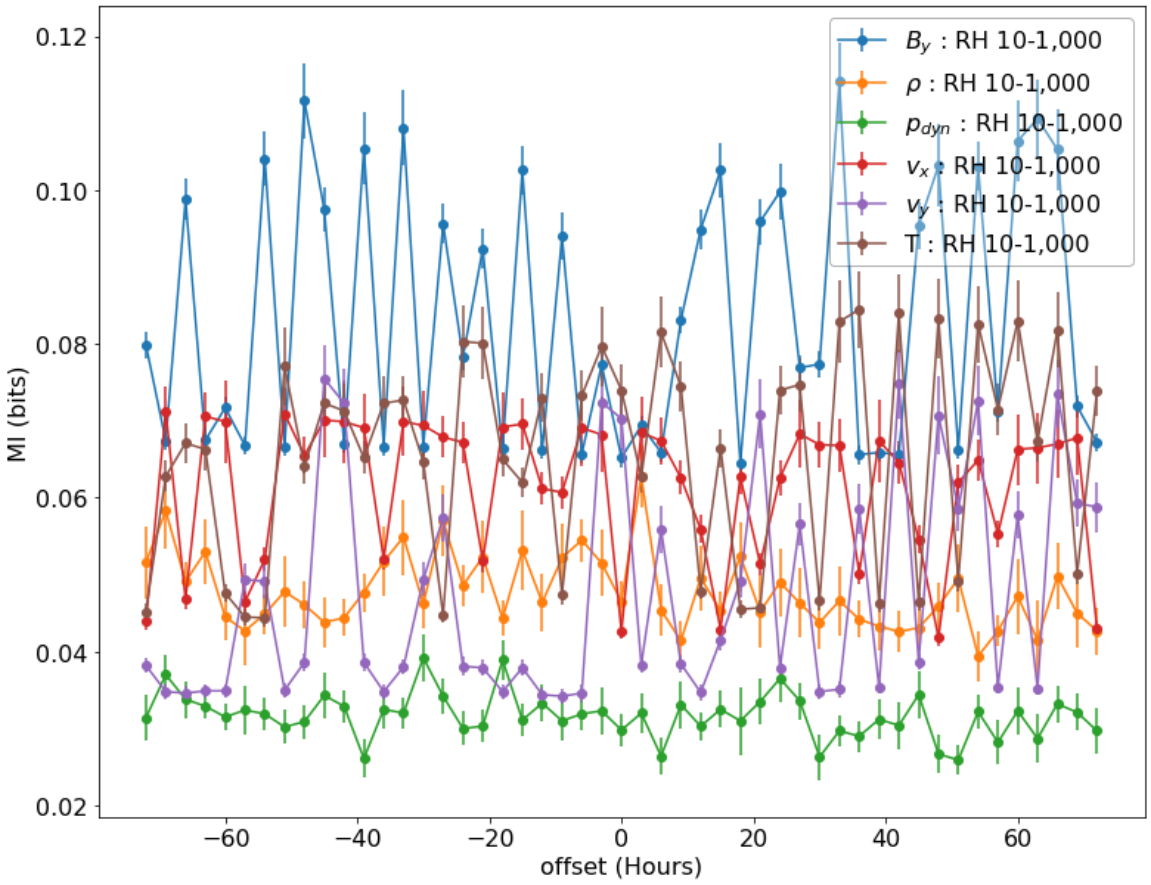

Figure 9.7: MI results for propagated solar wind parameters compared with the RH 10 - 1,000 kHz SKR emissions. Offset indicates the extent of time offsetting between data sets (section 6.4). Individual values of the MI can be found in the appendix tables: Table E.5 for B_y, ρ, and p_{dyn}, and Table E.6 for v_x, v_y, and T.

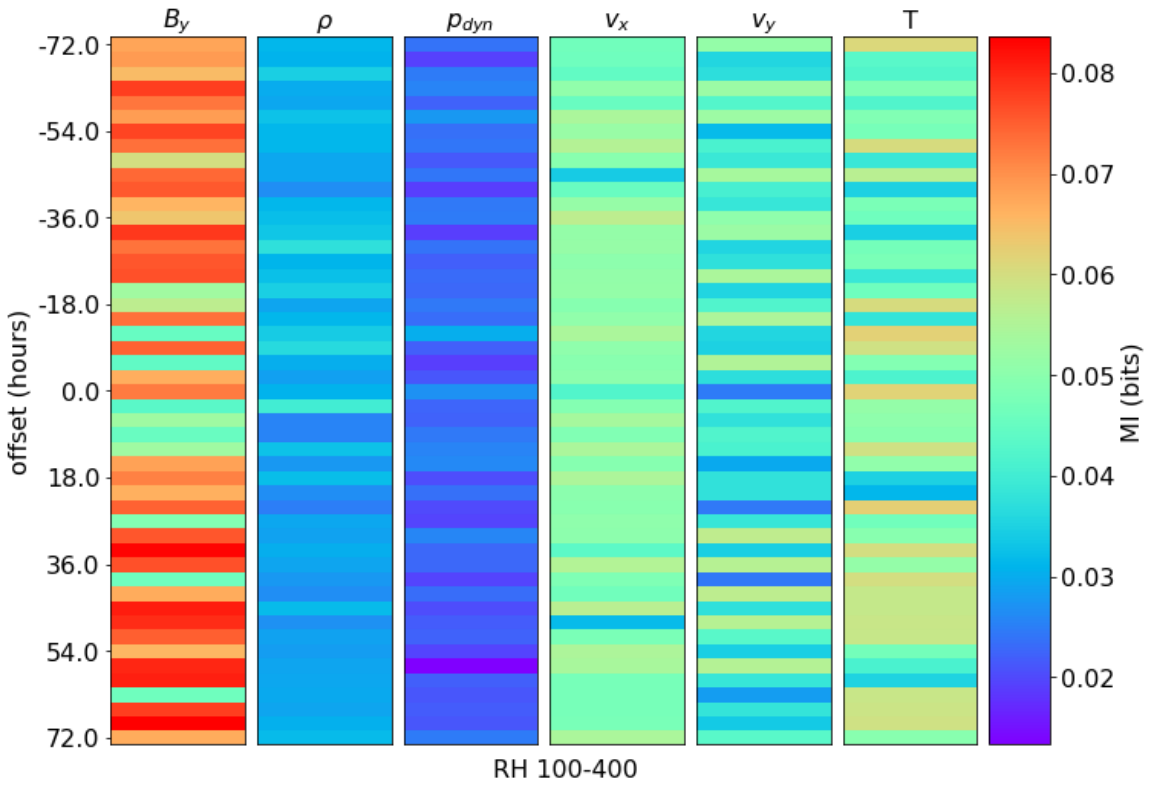

Figure 9.8: Comparison of MI values for propagated solar wind parameters compared with the RH 100 - 400 kHz SKR emissions. x-axis: (top) propagated solar wind parameter (bottom) all data sets use the RH 100 - 400 kHz SKR data. The y-axis represents the time offset, in hours, between the propagated solar wind and SKR timestamps, as described in section 6.4. The time offset fails to reveal a response time nor reveal a clear strengthening of MI when accounting for the propagation time of the solar wind. Individual heat maps, where the MI value is not relative to other data sets can be seen in subsection E.2.4.

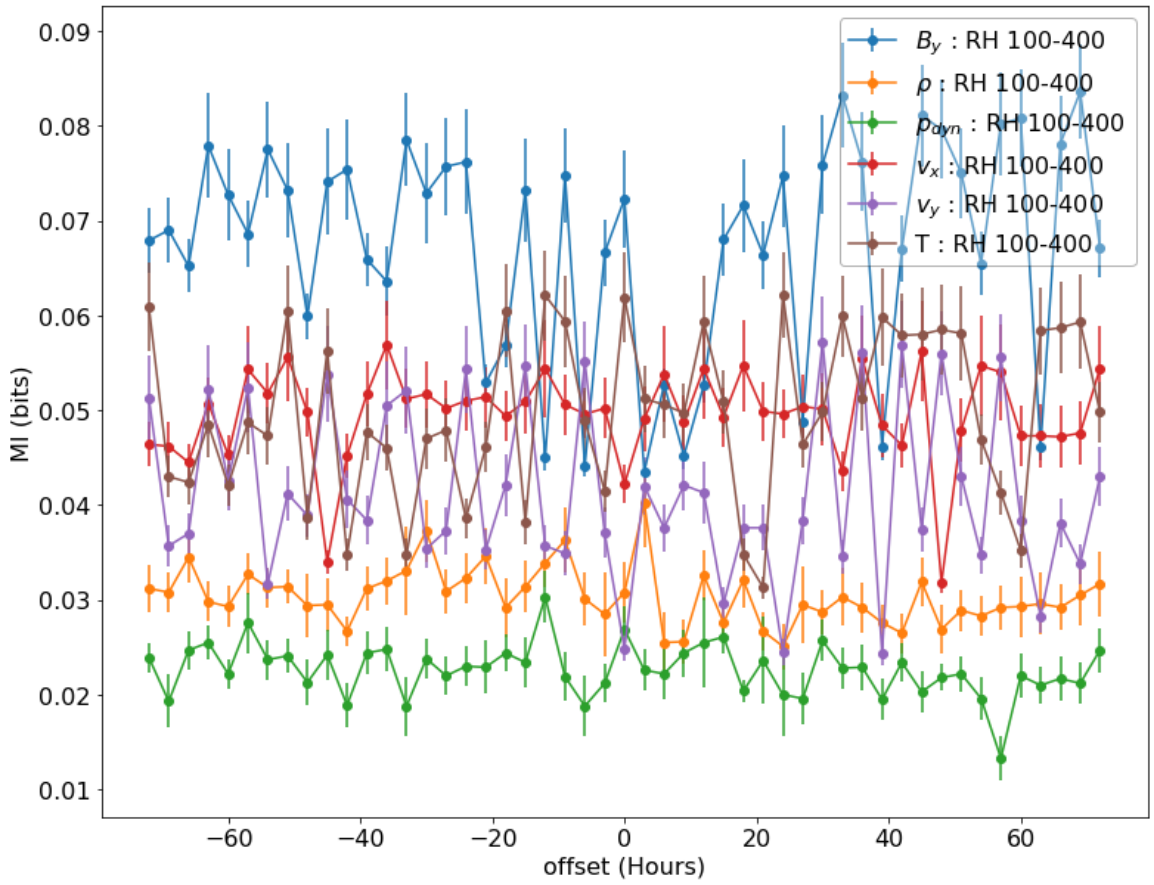

Figure 9.9: MI results for propagated solar wind parameters compared with the RH 100 - 400 kHz SKR emissions. Offset indicates the extent of time offsetting between data sets (section 6.4). Individual values of the MI can be found in the appendix tables: Table E.7 for B_y, ρ, and p_{dyn}, and Table E.8 for v_x, v_y, and T.

9.4 Discussion

SKR, introduced in section 3.5, is the most intense radio wave emission from Saturn located at high altitudes. It rotates with the planet with a periodicity of $\sim$ 10h 39m, with enhanced power in the pre-morning to noon sectors, and is a signature of auroral emissions generated by CMIs. CMIs are unstable to the precipitation of electrons into the auroral zones. During magnetotail reconnection, energetic electrons are accelerated from the plasma sheet into the Northern and Southern hemispheres, which convert their free energy via CMIs. During energetic events, such as geomagnetic storms, magnetic tail reconnection is enhanced. This connection, between the generation of SKR from CMIs and enhanced plasma insertion due to geomagnetic storms, and thereby variable solar wind conditions, makes SKR an appropriate phenomena to study in connecting Saturn's magnetosphere to the solar wind.

One of the most difficult aspects of determining the strength of a relationship seen between the propagated parameters and an SKR band is determining the threshold at which an MI value constitutes a significant relationship. In the terrestrial study of chapter 7 we expected to see significant relationships between the geomagnetic indices and IMF and solar wind parameters, B_z and v_x, respectively, based on an extensive review of literature over 40 years of investigations, see Table 7.1. The results of chapter 7 met with expectations, in the case of the AL index, B_z and v_x were the first and second strongest drivers, and in the case of the SYM/H index, v_x was the strongest driver with B_z the fourth, although proton density, ρ, and temperature, T, (second and third) were considered potential artefacts of v_x. As the considered solar wind and IMF parameters in chapter 7 are the same propagated parameters considered in this

chapter, we can compare the MI results of these parameters to the analytical value of MI given in Equation 6.3, where $I_{analytical} \simeq 0.32$ bits for a correlation coefficient of 0.6, and use this as one way to baseline what may be a significant value.

For B_z, results range from 40% to 62% of $I_{analytical}$ and for v_x, results range from 48% to 83% of $I_{analytical}$ at peak values (expected response time). As these are known relationships, we can therefore consider any MI value returned $\geq$ 40% of $I_{analytical}$ (0.1280 bits) to be considered a significant value.

As outlined in section 3.5, SKR occurs in strongly magnetised regions of low plasma density. Reviewing Table 9.1, it would appear that the primary solar wind parameter driving SKR should be dynamic pressure, p_{dyn}, as it is considered by all but one study across 40 years of investigation, though most are from 2006 onwards due to limited data availability. Some early studies investigated ρ with success, and v and its component v_x has been investigated consistently across the 40 years also. As $p_{dyn} = \rho v^2$ it follows that v would be the stronger influence on any relation with p_{dyn}, and so expect a strong relationship from v also. Additionally, v_x, along which most of the solar wind velocity will be concentrated at 10 AU, due to the Parker Spiral effect (Figure 2.5). B, and its component B_y, then naturally emerges as another potential candidate, as a measure of the IMF field strength. B is strengthened in compressed CIRs, and can act as a proxy for p_{dyn} during reconnection which may enhance Saturn's magnetic field (Badman et al., 2008).

9.4.1 Drivers of SKR

Observing Table 9.2, the relationship between B_y and the LH 10 - 1,000 kHz SKR data set provides the only significant result by our own metric. With an averaged MI

value of 0.1245 ± 0.0033 bits, the B_y and LH 10 - 1,000 kHz MI result is ∼ 39 % of $I_{analytical}$. That B_y has proven to be a result that is comparable to the results of chapter 7 is perhaps expected. As a consequence of frozen-in theorem, the IMF travels with the solar wind through the IPM. Upon contact with a magnetosphere, magnetic reconnection will occur, the rate of which is affected by the IMF strength which is enhanced in compressed CIRs and during storms. When IMF intensity is enhanced, the greater magnetic flux increases the rate of reconnection, generating/enhancing the strongly magnetised regions required for SKR emission. Through reconnection, plasma is also able to enter the magnetospheric system, whereby it travels through the magnetosphere until the measured phenomena, in this case SKR, are emitted. The remaining regions provide comparative strengths below significance to $I_{analytical}$; LH - 100: ∼ 31%, RH - 10: ∼ 26%, and RH - 100: ∼ 21% for the average MI results of B_y.

The next variable approaching our measure of significance is the relationship between v_x and the LH 10 - 1,000 kHz SKR data set. With an MI value of 0.1052 ± 0.0040 bits, the v_x and LH 10 - 1,000 kHz MI result is ∼ 33 % of $I_{analytical}$. Thus, it is difficult to draw further conclusions on other propagated parameters generating emission of SKR and acting as drivers for Saturn's magnetosphere.

As the MI values currently considered are for the average MI values, we now also consider the largest MI results for each propagated parameter. In doing this we make the assumption that the true MI values of the relationships are being suppressed by some means, indicated in the variability of the MI values across all time steps, showing no relationship with offset as seen in chapter 7 and chapter 8. We will investigate why the MI results are not showing the true relationships in subsubsection 9.4.1.1.

	B_y		ρ		p_{dyn}	
Data Set	MI	±	MI	±	MI	±
LH 10	0.1523	0.0056	0.0666	0.0049	0.0447	0.0031
LH 100	0.114	0.0067	0.0426	0.0049	0.041	0.0049
RH 10	0.1141	0.005	0.0628	0.004	0.0392	0.0031
RH 100	0.0836	0.005	0.0402	0.0046	0.0303	0.0027
	v_x		v_y		T	
	MI	±	MI	±	MI	±
LH 10	0.1129	0.0053	0.0872	0.0055	0.0957	0.0051
LH 100	0.0972	0.0059	0.0587	0.0051	0.0701	0.0053
RH 10	0.0713	0.0032	0.0755	0.0044	0.0845	0.005
RH 100	0.0569	0.0047	0.0572	0.0048	0.0622	0.0045

Table 9.3: Peak MI information results for SKR data sets and propagated solar wind variables.

We are observing a range of potential values within which the time offset for the true peak MI may reside. Under this assumption the given Peak MI results are seen in Table 9.3.

Observing Table 9.3, the picture changes slightly. B_y and the LH 10 - 1,000 kHz SKR data set still provides the only significant result, though increasing to $\sim 50\%$ of $I_{analytical}$, by our own metric. However, B_y paired with the LH 100 - 400 kHz and RH 10 - 1,000 kHz SKR data sets both achieve an MI result ~ 36 % of $I_{analytical}$. Solar wind radial velocity, v_x, and the LH 10 - 1,000 kHz relationship also achieves an MI result ~ 35 % of $I_{analytical}$.

Dynamic pressure, p_{dyn}, has returned the weakest MI values across all SKR data sets, achieving results of $\sim 14\%$ for LH - 10, $\sim 13\%$ for LH - 100, $\sim 12\%$ for RH - 10, and $\sim 9\%$ for RH - 100 of $I_{analytical}$. Whilst p_{dyn} has returned the lowest values, and even with its components v_x and ρ, counter-intuitively achieving stronger MI values, it is not appropriate to physically interpret these results directly. That MI results of expected relationships are returning insignificant MI values, when the methods of this thesis have been confirmed in chapter 7 and chapter 8, and yet confirming B_y as a measure of general IMF strength, indicates that it is unlikely to be the case that our results alone disprove a connection between the parameters and SKR.

The physical reason that there may not be an observable connection to SKR may be that Saturn is not like the terrestrial system. As explored in section 3.5, it is not only the solar wind that drives SKR emission but the presence of internal drivers, namely ion outflows from Enceladus that provide a major source of plasma, contributing to the internal plasma environment of Saturn. Therefore, were the internal plasma drivers to dominate over the solar wind, the relationship between propagated parameters and SKR may be concealed. However, the solar wind should still have an effect on the plasma environment of Saturn, as demonstrated by B_y providing a significant relationship in the LH 10 - 1,000 kHz SKR data set case, which indicates magnetic reconnection events would play their part. Although MI results may not reach significant values, we may expect to see relative strengths between parameters match expectations, with p_{dyn} dominating, and ρ and v_x return MI values less than p_{dyn} as artefacts. Therefore, we conclude that the MI results may not be representative of their true relationship and that our results are suppressed by uncertainties in the system.

9.4.1.1 A Possible Explanation

We now explore the possibility that our results represent the true relationship of the parameters, relatively. The IMF tangential component, B_y, is the strongest driver of SKR emissions across all SKR data sets and other propagated parameters are not.

In all cases, contrary to expectations, p_{dyn} is the weakest relationship, showing negligible impact on SKR emissions. Observing Figure 9.1, data sets can be more clearly compared, with all MI values set relative to 0.16 bits, 50% of an ideal Gaussian relationship. Whilst Desch and Rucker (1983) and Taubenschuss et al. (2006) conducted an investigation of B_y in connection with solar wind driving, the relationship, whilst present, was less than $\mathbf{v}$ and p_{dyn}.

A potential solution to this question is in solar wind compressions. Solar wind compressions are regions of slow dense plasma, as a result of fast solar wind impacting a slow solar wind region (subsection 2.6.3). In compressed regions, all IMF components can become enhanced (Figure 2.6).

SKR is connected to compressions during CMI events, (Kurth et al. (2005); Palmerio et al. (2021)). As discussed in the review of past studies, Badman et al. (2008) investigated compression events on the triggering of SKR, able to use B as a proxy for p_{dyn} from frozen-in theorem. SKR bursts are connected (coincident) with auroral intensification. Auroral intensifications were then attributed to magnetic tail reconnection, which is intensified by compression events through destabilisation of the tail, enhancing field-line currents (Cowley et al., 2005). Badman et al. (2008) then relates several further events, noting similar reconnection events drive auroral kilometric radiation in the terrestrial system on contact with compression events. Tail reconnection driving SKR enhancement during compression events is further

supported by Clarke et al. (2009) and Thomsen et al. (2019).

However, in this case one should see the MI of p_{dyn} strengthening with B_y if compression events are the cause of the IMF driving of SKR. Past studies have consistently put p_{dyn} forward as the strongest driver of SKR by the solar wind, if not equal to other solar wind and IMF parameters. However, the data span of each study is limited, with most covering unique events of particularly strong SKR enhancement and variability over brief time spans. What this reveals may be attributed to one of the successes of this approach, that investigating non-linear relationships with MI, combined with the benefit of long time series data availability from the Cassini mission, can more accurately describe the true relationship of the solar wind and IMF parameters and that p_{dyn}, outside enhancement events, may not be a strong driver.

It may also be a consequence of the internal drivers of Saturn magnetosphere dynamics. A relationship between B_y and SKR indicates a connection to IMF strength and the reconnection rate. An enhanced reconnection rate will introduce more plasma into Saturn's magnetosphere, enhancing the rate of tail reconnection and driving more SKR generation. However, the inclusion of energetic ions and neutrals from internal sources may dominate or homogenise the plasma conditions internally, and thereby weaken the effect of solar wind conditions, such as p_{dyn}, for the generation of SKR.

Finally, propagated data does not account for CMEs and compression events. Averaging from the solar wind outside of compression events may provide explanation. A necessary follow up to confirm this would be to identify all compression events during the Cassini mission, and to compare the propagated solar wind and IMF parameters to SKR for data in these periods.

9.4.2 Propagation Uncertainty

Drivers of Saturn's magnetosphere should see MI values strengthen (approach their true value) when the time offset matches the response time of the Saturnian magnetosphere, and the uncertainty of the propagation model. No response time has been observed in the results. Taubenschuss et al. (2006) gave a range of expected response times for various solar wind parameters, a consequence of the more complex magnetosphere dynamics found at Saturn, p_{dyn}; 13 hours, $\mathbf{v}$; 52 hours, B; 40 hours, and B_y; 27 hours. At the maximum limit of solar wind propagation uncertainty, $\pm$ 2 days, and expected response time, 52 hours, time offsets may be as high 100 hours ($\sim$ 4.16 days). However, it is highly unlikely that the response times are hidden outside of the investigated range of time offsets ($\pm$ 72 hours). Results for this chapter have shown that MI can be highly variable from one time offset to another and at this limit it would require all propagated data to be out by 3 days, when including a response time, which contradicts the propagation uncertainty being dependent on the Sun-Earth-Saturn angle, Φ_S.

One might consider the time offset to be an explanation for this variability, as the data is non-continuous due to the Sun-Earth-Saturn angle condition. However, this cause can be discounted; invalid data points are labelled NaN, so that values are only averaged around the relevant times, which is based on the data's timestamps. An adjacent, valid data point (in the data array) with a timestamp greater than the averaging window could therefore not be included in the averaging. It may be possible that the data, where a continuous period is of a shorter time than the maximum offset, would be aligned with a time where there is no SKR data. For example, at a transition point from one hemisphere to the next, where the respective LH or RH data was no

longer measured. However, again, this is a low-likelihood event and not one that would occur consistently. If this transition boundary were encountered it should show a drop to 0 MI at high time-shifts only, where the lack of data results in a joint probability of 0, recalling that $0 \log 0 = 0$ as $x \log x \to 0$, as $x \to 0$ (Cover et al., 1991), see subsection 6.1.2.

In chapter 7 and chapter 8, where the response times were visible, it was seen that MI gradually increased to a peak MI value. Time offsetting increases the propagation uncertainty equally for all data points. However, as propagation uncertainty is dependent on Φ_S, the time offset will only be correct at any given offset for a subset of data points.

We must also pay attention to the difference in MI uncertainty. Observing the results in chapter 7 and chapter 8, the uncertainty for MI results in this chapter is an order of magnitude larger than for previous studies. In the previous chapters, the relationships between the terrestrial magnetosphere and solar wind were well understood, whereas here, the evidence is more tenuous in comparison.

We therefore conclude that the high variability seen in MI values indicates the propagation uncertainty is the most likely explanation for the MI results. The difficulty drawing out expected relationships from propagated parameters is most likely a consequence of this and the MI results we see for the propagated parameters are not reaching their true value, individually or, potentially, relative to one another.

9.4.3 Variation Across SKR Data

Finally, we note the presence of a north-south asymmetry between the MI values of the RH and LH data sets. It is observed that the strongest drivers, according

to our results, reveal stronger MI relationships (both average and peak) in the LH data than the RH data, irrespective of whether full or peak frequency ranges are considered, which can be seen by observing Figure 9.1. Nakamura et al. (2019) investigates the seasonal variations of SKR Power in the Northern and Southern hemispheres for the entire Cassini mission, 2004 - 2017. It was shown that Northern hemisphere power remained relatively constant throughout the Cassini mission whilst Southern hemisphere power varied, decreasing as Southern summer transitioned to Southern winter. Whilst Nakamura et al. (2019) was unable to connect Northern hemisphere power to the solar cycle, Kimura et al. (2013) found suggestion of a solar cycle connection to the Southern hemisphere power. It is therefore suggested that the increased strength of the MI relationship with SKR in the RH data is a consequence of the Southern hemisphere connection to the solar cycle, which would affect solar wind and IMF intensity. Presently, the absence of a relationship between the solar cycle and the Northern hemisphere is poorly understood, and investigation of SKR variation in the hemispheres would add useful weight to this argument.

9.4.4 Conclusions

Investigating propagated solar wind and IMF parameters with SKR has produced interesting results that have not met with initial expectations. Our results contrast to the established understanding of solar wind connection to SKR investigated from flybys of past satellite missions, see Table 9.1, indicating p_{dyn} and v should be strong indicators of SKR driving. The exception is B_y, which is considered to indicate the strength of the IMF and thereby the rate of reconnection.

Mutual information has advantages over traditional techniques such as correlation,

due to its ability to find non-linear relationships. The possibility that a new understanding of the IMF and solar wind interaction with SKR is considered. However, no strength of argument is given to this possibility at this stage, as a more likely explanation exists to explain the discrepancy from expectations and must be addressed first.

As discussed, even where we account for the differences in the Saturnian system, with a dominance of internal drivers, the effects of the solar wind should be visible where parameters contribute to the generation of SKR. Past studies, using directly measured data of the solar wind and IMF from passing satellites, shows that the physical relationship between the solar wind and IMF to the Saturnian magnetosphere, as we currently understand it, is detectable. In our own study we have observed this through the B_y parameter of the IMF as a proxy for magnetic reconnection, with MI results comparable to the known relationships in the terrestrial system.

Therefore, the conclusion we draw to explain the discrepancy is in the relationship between the propagation uncertainty to the Sun-Earth-Saturn angle, Φ_S. The time offsetting factor, combined with the advantages of MI, excelled in revealing the terrestrial relationships between the solar wind and IMF with the geomagnetic indices, AL and SYM/H, in chapter 7. This was further demonstrated when we investigated the use of coupling functions in chapter 8. The time offsetting is applied linearly, shifting the time offset in fixed increments. However, in this chapter the time offset was not the only factor of uncertainty to consider. The uncertainty associated with Φ_S changes from 0 at $\Phi_S = 0°$, to a peak of $\pm$ 2 days for $\Phi_S = 50°$. The combination of the uncertainties introduced by the time offset and Φ_S is a more complicated picture

than first expected.

The uncertainty due to Φ_S means that for any time offset, only a fraction of the data considered will be offset at the "correct time offset". Even at the expected peak offset times, any data that is uncertain with Φ_S, will not be correctly offset. As we have seen in the terrestrial studies, the relationship with time offset is not an absolute condition. The MI value increases as the time offset approaches the response time, demonstrating the nature of the magnetosphere dynamics; that the solar wind takes on a range of energies at any given time, and that it takes a range of times for the solar wind energy to travel through the magnetosphere. Therefore, we can consider that some proportion of the relationship between a propagated parameter is represented through the MI value, and that the MI results given in this chapter can be considered minimum values, with the upper, true, MI value unclear.

We are able to therefore conclude that B_y, as an indicator of IMF strength, and with MI results comparable to those of B in chapter 7 and chapter 8, is a genuine relationship with SKR.

The first step in any further investigation should seek to connect the time offset of the data to Φ_S, to more accurately account for the propagation uncertainty. However, to do this may pose challenges, as all data points must be offset to match a corresponding data point in the comparative data. Thus any function, $f(X(t), \Phi_S)$, must return a data set with offsets to uniquely match each data point to corresponding data.

9.5 Closing Remarks

With the approach of this thesis, the IMF azimuthal component, B_y, has demonstrated a significant relationship with SKR driving, viewed as a proxy for the IMF strength and the rate of magnetic reconnection. This relationship may exist as an artefact of compression events driving enhanced SKR emission. However, in contrast to expectations of this explanation, p_{dyn}, predicted to be the strongest driver, shows a weak relationship to SKR when considering the MI results presented. This may be due to internal drivers of the Saturnian magnetosphere dynamics. Also, for p_{dyn} and other propagated parameters not meeting expectations, the poor relationships presented by low MI results are attributed to the uncertainty in the arrival time associated with the Sun-Earth-Saturn angle, Φ_S. We therefore conclude that the MI results of this chapter are likely minimum MI values, and that accounting for this uncertainty further will improve the MI results. Finally, we note that stronger relationships exist for Southern hemisphere data over Northern hemisphere data, which is linked to the solar cycle.

Although some results are unexpected, the results of chapter 7 and chapter 8 demonstrate that the use of MI is a successful and valid approach to take. Therefore, confidence can be taken that the methods of this thesis are successfully drawing out known relationships. Significant observations should therefore be considered real and future work should investigate both the uncertainty issues associated with Φ_S, and the consequence of separating out the solar wind and SKR data attributed with compression events using these methods, to answer the open question around p_{dyn}.

Chapter 10

Conclusions

10.1 Discussion of Results

The work of this thesis has been performed to try and find a means of advancing our understanding of solar wind driving of Saturn's magnetosphere. In the absence of upstream monitors of the solar wind, we have investigated the use of Saturnian Kilometric Radiation (SKR) as a proxy for the solar wind conditions at Saturn.

With the absence of upstream monitors, there is a significant deficit of solar wind data at Saturn, limiting our ability to investigate the solar wind driving of Saturn's magnetospheric system. Flybys of the Voyager probes in 1981 and 1982 resulted in the time limited case studies of Desch (1982) and Desch and Rucker (1983). Notably, there is a significant absence of publications between them and the onset of the Cassini mission at Saturn in 2014, with Taubenschuss et al. (2006) one of the first subsequent studies of significance found as part of the background research of this thesis. Solar wind driving is significant at the Earth, responsible for the production of auroras and a range of geomagnetic phenomena that can cause devastation to electronic systems.

Although there are no electronics at Saturn, the impact of the solar wind on Earth's systems is evident of the important role it plays in magnetosphere dynamics and in turn, the role a magnetosphere plays in a planet's evolution and behaviour. Evidence shows the solar wind has an impact on Saturn's magnetosphere, yet the extent of this is unclear, particularly in the presence of internal drivers (e.g. particle emissions from Enceladus). Thus, the absence of any solar wind data is evidently of huge detriment to scientific understanding.

Our investigation of SKR as a proxy for the solar wind therefore offers the potential to introduce a 13 year, continuous data set for the solar wind from which to investigate solar wind driving of the Saturnian magnetosphere. The work carried out in chapter 5 introduced mutual information theory, a means of measuring the strength of a relationship between two correlated data sets and therefore how much can be inferred from one data set about the another.

Challenges were presented in the application of mutual information. The absence of secondary, coincident data sets, gave no additional data sets from which to calculate uncertainties of the MI results. Therefore, in chapter 6, we adapted the works of Holmes et al. (2019) to develop a means of solving uncertainties by dividing the data and using k^{th} nearest neighbour mutual information estimators. Furthermore, in order to ascertain confidence in the uncertainty calculations, we applied the methods to Gaussian data with a given correlation coefficient (0.6) and a known analytical mutual information value ($\simeq 0.32$). Results were found inline with analytical values of mutual information, confirming the methods in this thesis can successfully implement mutual information and solve the uncertainties of measurements.

Three investigations were conducted following verification of the methods in this

thesis. The first was an investigation of the relationship between the solar wind and enhancement of the geomagnetic indices, AL and SYM/H (chapter 7). Geomagnetic indices are measurements of variations in the terrestrial magnetic field, measured by a series of magnetometers on the Earth's surface. Investigation of the indices were chosen as they are a well understood relationship with decades of available direct solar wind and geomagnetic indices data. Analysis of the solar wind driving of geomagnetic indices revealed strong mutual information relationships from both indices to the IMF southward facing component, B_z, and solar wind radial velocity, v_x, confirming expected relationships. In addition we investigated the response time of the magnetosphere, the time taken from solar wind contact with the magnetosphere, to emission of the considered phenomena. That is, the time taken for the solar wind driving to travel through the magnetosphere and trigger AL and SYM/H intensification. Confirmation of the response time in both indices ($\sim$ 45 minutes) confirmed the ability of the methods in this thesis to draw out relationships.

The second investigation was conducted as a short investigation, allowed by remaining time during an industrial placement. Following confirmation of the methods in this thesis, the decision was made to use this additional time to investigate the utility of coupling functions, equations that describe the solar wind-magnetosphere coupling in the terrestrial system. Coupling functions use equations in the form of Equation 6.3, adjusting coefficients and powers to achieve optimal values to data used for analysis of the coupling functions. As geomagnetic indices had been connected in several studies (Newell et al. (2007); Milan, Gosling, et al. (2012)), they were deemed an appropriate data set to assess coupling function utility. Results indicate that coupling functions are much stronger measures of the solar wind-magnetosphere

coupling to geomagnetic indices when compared with the IMF north-south parameter, B_z, and the analytical value for mutual information.

Finally, with confidence in the use of mutual information to drawn out relationships, we investigated the solar wind driving of SKR. We compared the following solar wind parameters: IMF tangential component; B_y, radial velocity; v_x, tangential velocity; v_y, density; ρ, dynamic pressure; p_{dyn}, and temperature; T. Solar wind parameters were compared to four SKR data sets, LH and RH, representing the Southern and Northern hemispheres, and 10 - 1,000 kHz and 100 - 400 kHz, representing the complete and peak frequency ranges of SKR. Consistent relationships were found across all four SKR data sets, surprisingly revealing the strongest MI relationship between SKR and B_y, whilst p_{dyn}, the expected strongest relationship based on past studies, returns a negligible relationship with SKR. However, only B_y for LH 10 - 1,000 KhZ SKR data returned a statistically significant result. MI results are taken as a minimum MI value. The possibility of improving the MI values is attributed to better modelling the effects of the Sun-Earth-Saturn angle on the arrival time of propagated solar wind and IMF data.

10.2 Future Work

We present here several potential future works that could be conducted in support of the work of this thesis.

- Following the results of chapter 7, we propose a higher resolution analysis of the solar wind relationship with the geomagnetic indices. The IMF southward facing component, B_z, results indicate the presence of the magnetospheric response

time in both the AL and SYM/H data. However, the resolution of our results is too low to discern the twin peaks of the SYM/H found in Eriksson et al. (2000), attributed to dayside reconnection and night side tail reconnection. A repeat of this analysis at higher resolution would confirm whether both response times of the magnetosphere to SYM/H can be drawn out, and further reinforce the ability of these methods to analyse relationships.

- In chapter 8, our investigation of coupling functions was limited to 3 functions compared with the geomagnetic indices considered in the previous chapter. Coupling functions considered were primarily focused on dayside reconnection, whereas geomagnetic indices were primarily drawn from tail reconnection. Therefore, before any conclusions are drawn regarding the confidence of the results, a further investigation should be conducted. The follow up investigation should expand the number of coupling functions, and compare them to a greater range of geomagnetic indices and other phenomena connected to solar wind-magnetosphere coupling.

- The results of chapter 9, returning a statistically significant result for the relationship between the IMF tangential component, B_y, and the LH 10 - 1,000 kHZ SKR data, sits in isolation. The conclusion drawn is that the MI results for this chapter are lower limits. The variability of MI results is attributed to the uncertainty introduced by the arrival time relating to the Sun-Earth-Saturn angle, Φ_S. Furthermore, we investigated but were unable to find the presence of the magnetosphere response time of various solar wind parameters in the MI results. The absence of the response time has been attributed to the propagation uncertainty also. Better modelling of this relationship to the

propagated solar wind data should reveal a more accurate MI value for the relationships considered and the response times of the magnetospheres revealed, as was done in chapter 7 and chapter 8.

Appendix A

Data

A.1 AL Calculation

At each observatory, H component readings are compared to H_o, a baseline quiet day level. H_o is calculated each month as the average over all readings for the 5 quietist days that month. Data for all twelve observatories is then plotted as a function of UT with the upper and lower envelopes defined as AU and AL respectively, AE is defined as the separation between these two. As discussed in section 3.2, it has been established that the AU and AL indices represent the maximum eastward and westward electrojets, respectively. The indices are thus defined as

$$AU(t) = \max_{i=1,12}\{H(t) - H_o\}_i \tag{A.1}$$

$$AL(t) = \min_{i=1,12}\{H(t) - H_o\}_i \tag{A.2}$$

$$AE(t) = AU(t) - AL(t) \tag{A.3}$$

where t represents UT.

A.2 SYM/H Calculation

SYM/H is calculated (Iyemori (1990); Wanliss et al. (2006)) using the following method:

- The averaged effect of the ionospheric dynamo current, S_q, calculated using the 5 quietest days of the month, is subtracted from the magnetometer readings.
- For the H component, the effect of the ring current, also averaged over the 5 quietest days, is subtracted to determine the baseline. These subtractions form the background field.
- After subtracting the background field, the residual monthly 1-min disturbance field remains. Recall, SYM/H is a high resolution version of the Disturbance storm time index (Dst), see section 3.2.
- The disturbance field is then transformed into a magnetic dipole system. It is rotated by an angle between the direction of the geomagnetic dipole field and the direction of the geomagnetic main field (the direction of the horizontal vector) to avoid mixing of the ring current with the east-west (D) component. The assumption is made that the ring current is flowing parallel to the dipole equatorial plane.

- The symmetric H component, SYM/H, is then calculated by averaging it longitudinally (by averaging the result of all 1min values from each station).
- SYM/H is finally divided by the cosines of the dipole latitude, $\cos\theta_m$, where θ_m is the averaged geomagnetic longitude of the observing stations. This is to normalise and correct for the latitudinal variation of the ring current effect.

A.3 MHD Model Verification

Verification of the MHD model is performed using Ulysses spacecraft data when traversing at an approximate distance to Jupiter, at 5.2 $\pm$ 0.3 AU, for 5 months each (1 Jan to 1 June) in 1998 and 1999. The similar distance makes the solar wind measurements taken by Ulysses at this time an ideal marker to test against the MHD model. Figure A.1 overlays the MHD model predictions with the real, directly measured, Ulysses data, as well as an additional advection shift method. In this verification, dynamic pressure variations of the solar wind are compared, successfully aligning 12 events between the real data and the MHD model. However, this method of verification is uncertain, due to predicted low pressure events not appearing in observation data.

Figure A.2a improves upon the verification accuracy, focusing on the arrival time and absolute values of the 12 pressure enhancement events. A better prediction error for the MHD model, compared with an advection shift method, is found with a maximum prediction error of $\pm$ 2 days when $\Phi < 50°$. Finally, in Figure A.2b, the maximum value of the 12 observed dynamic pressure events are plotted, as modelled by the MHD model against the real Ulysses data. A linear correlation coefficient of

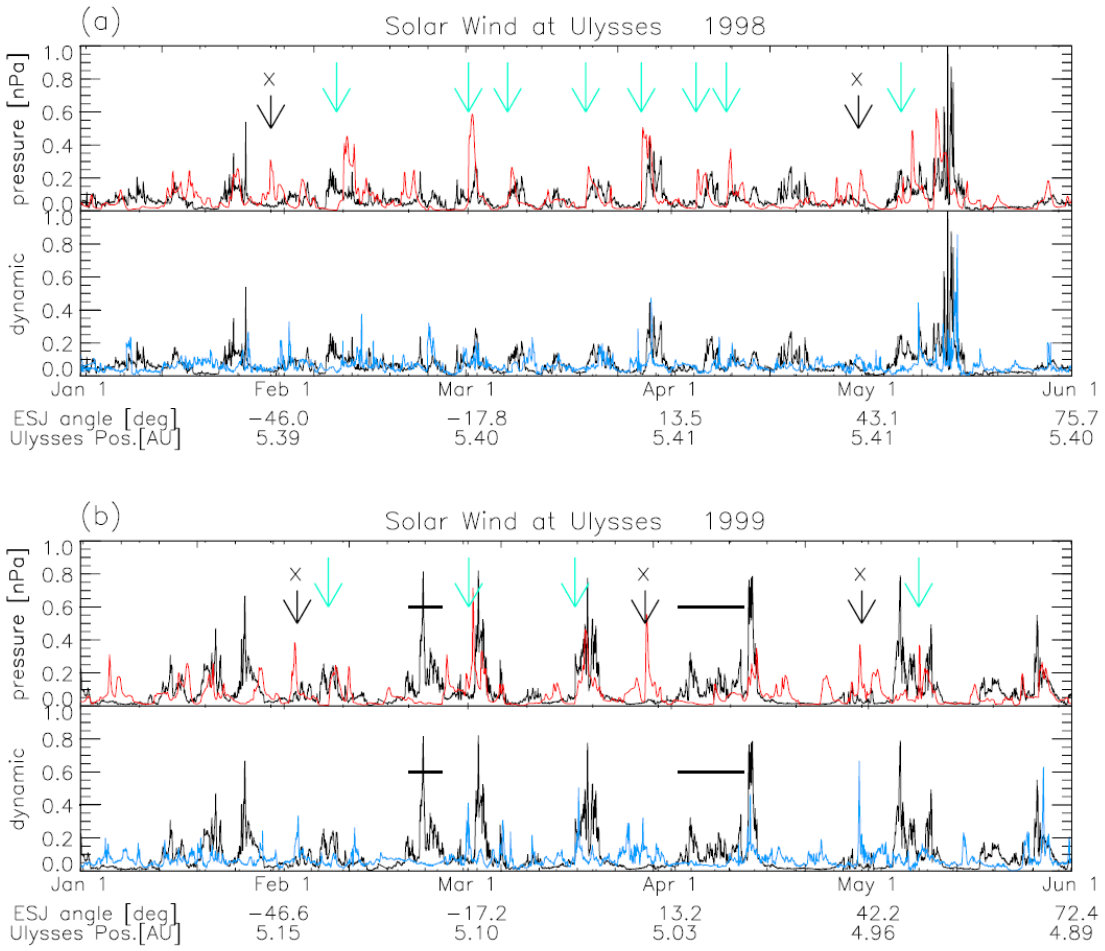

Figure A.1: 12 solar wind dynamic pressure events are indicated by blue arrows. Ulysses data (Black) from two periods, 1 Jan to 1 Jun in both 1998 (a) and 1999 (b), are used to confirm the predicted events of the MHD model (Red). An advection shift method is included as comparison (Blue) Black crosses indicate falsely predicted solar wind dynamic pressure enhancements. Black lines indicate intervals with absent data. Image credit: Tao et al. (2005)

0.66 is found.

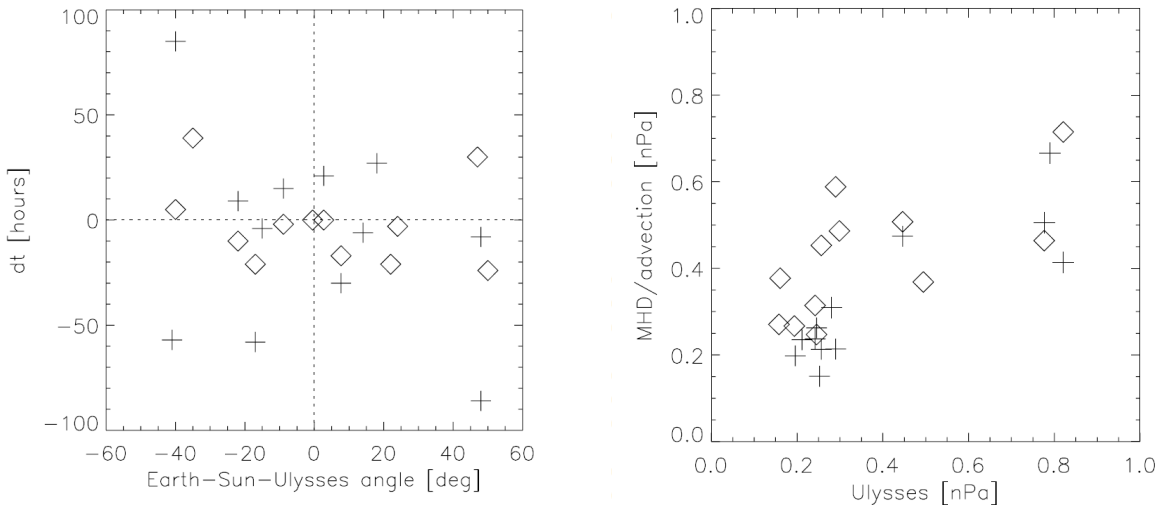

(a) (b)

Figure A.2: Symbols: MHD model - diamonds, advection shift method - crosses. (a) Scatter plot of MHD model and advection shift method prediction errors for pressure enhanced time vs Earth-Sun-Ulysses angle, Φ. (b) Scatter plot of maximum predicted values (vertical) vs actual values (horizontal), from Ulysses, for the 12 dynamic pressure enhancement events. Image credits: (a) and (b) Tao et al. (2005)

Appendix B

Mutual Information

B.1 Shannon's Entropy

N.b. B.1 is quoting from (Shannon, 1948), appendix 2.

$$H(\frac{1}{n}, \frac{1}{n}, ..., \frac{1}{n}) = A(n) \tag{B.1}$$

Shannon's third condition (subsection 5.3.1) allows us to decompose a choice from s^m equally likely possibilities into a series of m choices, each from s equally likely possibilities

$$A(s^m) = mA(s) \tag{B.2}$$

t^n choices can equally be decomposed into a series of n choices, from t equally likely possibilities

$$A(t^n) = nA(t) \tag{B.3}$$

Choosing n to be arbitrarily large and finding an m to satisfy

$$s^m \leq t^n \leq s^{m+1} \tag{B.4}$$

Subsequently taking logarithms of both sides

$$m \log s \leq n \log t \leq (m+1) \log s \tag{B.5}$$

and dividing by $n \log s$ gives

$$\frac{m}{n} \leq \frac{\log t}{\log s} \leq \frac{m}{n} + \frac{1}{n} \tag{B.6}$$

or

$$\left| \frac{m}{n} - \frac{\log t}{\log s} \right| < \epsilon \tag{B.7}$$

where ϵ is arbitrarily small.

The monatonic property of $A(n)$ results in

$$A(s^m) \leq A(t^n) \leq A(s^{m+1}) \tag{B.8}$$

$$mA(s) \leq nA(t) \leq (m+1)A(s) \tag{B.9}$$

Then dividing by $nA(s)$ gives

$$\frac{m}{n} \leq \frac{A(t)}{A(s)} \leq \frac{m}{n} + \frac{1}{n} \tag{B.10}$$

or

$$\left|\frac{m}{n} - \frac{A(t)}{A(s)}\right| < \epsilon \tag{B.11}$$

Take out a constant of proportionality on the L.H.S. of Equation B.11 and divide through to retain ϵ as arbitrarily small, resulting in

$$\frac{m}{n} = \epsilon + \frac{A(t)}{A(s)} \tag{B.12}$$

sub Equation B.12 into Equation B.7 to get

$$\left|\epsilon + \frac{A(t)}{A(s)} - \frac{\log t}{\log s}\right| < \epsilon \tag{B.13}$$

which can become

$$|\epsilon| + \left|\frac{A(t)}{A(s)} - \frac{\log t}{\log s}\right| < \epsilon \tag{B.14}$$

$$\left|\frac{A(t)}{A(s)} - \frac{\log t}{\log s}\right| < \epsilon - |\epsilon| \tag{B.15}$$

$$\left|\frac{A(t)}{A(s)} - \frac{\log t}{\log s}\right| < 2\epsilon \tag{B.16}$$

becoming

$$A(t) = -K \log t \tag{B.17}$$

Where K is a positive constant to satisfy condition 2 in Shannon's conditions (subsection 5.3.1).

If a choice is available from n possibilities with commeasurable probabilities $p_i = \frac{n_i}{\sum n_i}$, where n_i are integers, one can break down a choice from $\sum n_i$ possibilities into

a choice from n possibilities with probabilities $p_i ... p_n$. Then, if one chooses the i^{th}, a choice from n_i with equal probabilities. Once again, taking Shannon's third condition (see subsection 5.3.1), the total choice from $\sum n_i$ as computed by two methods can be equated.

$$K \log \sum n_i = H(p_i, ..., p_n) + K \sum p_i \log n_i \tag{B.18}$$

Therefore

$$H = k \left[\sum p_i log \sum n_i - \sum p_i \log n_i \right] \tag{B.19}$$

$$= -K \sum p_i \log \frac{n_i}{\sum n_i} \tag{B.20}$$

$$= -K \sum p_i \log p_i \tag{B.21}$$

Should the p_i be incommeasurable, rationals can be used to approximate them and the same expression must hold according to Shannon's first condition of continuity. Thus the expression holds in general. The coefficient K is a choice of convenience determining the unit of measure.

B.2 Bounds on the Entropy

By definition

$0 \leq p_i \leq 1$

$$-p_i \log_2 p_i \begin{cases} = 0 & \text{if } p_i = 1 \\ > 0 & \text{if } 0 \leq p_i < 1 \end{cases} \tag{B.22}$$

Therefore, also by definition $H(U) \geq 0$, which is the first bound.

It is only possible to achieve equality if $p_i = 0$ for all i, which requires $p_i = 1$ for one i and $p_i = 0$ for all remaining i.

To derive the second bound, $H(U) = \log_2 r$ bits, if and only if $p_i = \frac{1}{r} \forall i$, take the difference and demonstrate that it must be non-positive. If the probabilities are arranged in descending order and it is assumed that r', where $r' \leq r$, of the r values of the probabilities p_i are strictly positive, i.e. $p > 0$ for all $i = 1, ..., r'$, and $p_i = 0$ for $i = r' + 1, ..., r$.

$$H(U) - \log_2 r = -\sum_{i=1}^{r} p_i \log_2 p_i - \log_2 r \tag{B.23}$$

$$= -\sum_{i=1}^{r'} p_i \log_2 p_i - \log_2 r \cdot \underbrace{\sum_{i=1}^{r'} p_i}_{=1} \tag{B.24}$$

$$= -\sum_{i=1}^{r'} p_i \log_2 p_i - \sum_{i=1}^{r'} p_i \log_2 r \tag{B.25}$$

$$= -\sum_{i=1}^{r'} p_i \log_2 (p_i \cdot r) \tag{B.26}$$

$$= \sum_{i=1}^{r'} p_i \log_2 \underbrace{\left(\frac{1}{p_i \cdot r}\right)}_{\triangleq \xi} \tag{B.27}$$

$$\leq \sum_{i=1}^{r'} p_i \left(\frac{1}{p_i \cdot r} - 1\right) \cdot \log_2 e \tag{B.28}$$

$$= \left(\sum_{i=1}^{r'} \frac{1}{r} - \underbrace{\sum_{i=1}^{r'} p_i}_{=1}\right) \cdot \log_2 e \tag{B.29}$$

$$= \left(\frac{r'}{r} - 1\right) \cdot \log_2 e \tag{B.30}$$

$$\leq (1 - 1) \cdot \log_2 e = 0 \tag{B.31}$$

Equation B.28 follows from the IT Inequality (see Equation B.32).

Equation B.31 follows because $r' \leq r$.

Hence, $H(U) \leq \log_2 r$.

Equality can only be achieved if both

1. in the IT Inequality $\xi = 1$, i.e. if $\frac{1}{p_i r} = 1$ for all i, i.e. if $p_i = \frac{1}{r}$ for all i

2. $r' = r$

IT Inequality, see Moser et al. (2012), section 5.2.3 for full proof:

$$\left(1 - \frac{1}{\xi}\right) \log_b e \leq \log_b \xi \leq (\xi - 1) \log_b e \tag{B.32}$$

B.3 Independent System Entropy

Taken from Moser et al. (2012), section 6.5, pg 124

$$H(X,Y) = \sum_{i=1}^{s}\sum_{j=1}^{t} P_X(x_i)P_Y(y_j) \log_2\left(\frac{1}{P_X(x_i)P_Y(y_j)}\right) \tag{B.33}$$

$$= \sum_{i=1}^{s}\sum_{j=1}^{t} P_X(x_i)P_Y(y_j)\left(\log_2\left(\frac{1}{P_X(x_i)}\right) + \log_2\left(\frac{1}{P_Y(y_j)}\right)\right) \tag{B.34}$$

$$= \sum_{i=1}^{s}\sum_{j=1}^{t} P_X(x_i)P_Y(y_j) \log_2\left(\frac{1}{P_X(x_i)}\right)$$

$$+ \sum_{i=1}^{s}\sum_{j=1}^{t} P_X(x_i)P_Y(y_j) \log_2\left(\frac{1}{P_Y(y_j)}\right) \tag{B.35}$$

$$= \sum_{j=1}^{t} P_Y(y_j) \underbrace{\sum_{i=1}^{s} P_X(x_i) \log_2\left(\frac{1}{P_X(x_i)}\right)}_{H(X)}$$

$$+ \sum_{i=1}^{s} P_X(x_i) \underbrace{\sum_{j=1}^{t} P_Y(y_j) \log_2\left(\frac{1}{P_Y(y_j)}\right)}_{H(Y)} \tag{B.36}$$

$$= \underbrace{\sum_{j=1}^{t} P_Y(y_j)}_{=1} H(X) + \underbrace{\sum_{i=1}^{s} P_X(x_i)}_{=1} H(Y) \tag{B.37}$$

$$= H(X) + H(Y) \tag{B.38}$$

as by definition

$$\sum_{j=1}^{t} P_Y(y_j) = \sum_{i=1}^{s} P_X(x_i) = 1 \tag{B.39}$$

B.4 Dependent System Entropy

Taken from Moser et al. (2012), section 6.5, pg 125

By means of the relation in Equation 5.20 it follows that:

$$H(X,Y) = \sum_{i=1}^{s}\sum_{j=1}^{t} P_{X,Y}(x_i,y_j)\log_2\left(\frac{1}{P_{Y|X}(y_j|x_i)P_X(x_i)}\right) \tag{B.40}$$

$$= \sum_{i=1}^{s}\sum_{j=1}^{t} P_{X,Y}(x_i,y_j)\log_2\left(\frac{1}{P_X(x_i)}\right)$$

$$+ \sum_{i=1}^{s}\sum_{j=1}^{t} P_{X,Y}(x_i,y_j)\log_2\left(\frac{1}{P_{Y|X}(y_j|x_i)}\right) \tag{B.41}$$

$$= \sum_{i=1}^{s}\log_2\left(\frac{1}{P_X(x_i)}\right)\underbrace{\sum_{j=1}^{t} P_{X,Y}(x_i,y_j)}_{P_X(x_i)}$$

$$+ \sum_{i=1}^{s}\sum_{j=1}^{t} P_{X,Y}(x_i,y_j)\log_2\left(\frac{1}{P_{Y|X}(y_j|x_i)}\right) \tag{B.42}$$

$$= \sum_{i=1}^{s} P_X(x_i)\log_2\left(\frac{1}{P_X(x_i)}\right)$$

$$+ \sum_{i=1}^{s}\sum_{j=1}^{t} P_{X,Y}(x_i,y_j)\log_2\left(\frac{1}{P_{Y|X}(y_j|x_i)}\right) \tag{B.43}$$

$$= H(X) + H(Y|X) \tag{B.44}$$

Appendix C

Geomagnetic Indices and the Magnetosphere Response Time

C.1 AL Index Values

	B_{XZ}		B_x		B_{YZ}		B_y		B_z	
Time (Hours)	MI	±	MI	±	MI	±	MI	±	MI	±
0	0.0763	0.0005	0.0322	0.0009	0.0718	0.0003	0.0328	0.0006	0.1758	0.0004
0.25	0.0778	0.0004	0.0303	0.0003	0.0717	0.0004	0.0333	0.0003	0.1833	0.0006
0.5	0.0799	0.0009	0.0299	0.0008	0.0732	0.0009	0.0328	0.0003	0.1931	0.0005
0.75	0.0787	0.0006	0.0306	0.0006	0.0729	0.0004	0.033	0.0006	0.1968	0.0004
1	0.0778	0.0003	0.0317	0.0004	0.0719	0.0006	0.0328	0.0005	0.1883	0.0004
1.25	0.0774	0.0004	0.0322	0.0003	0.0695	0.0004	0.0326	0.0003	0.1746	0.0004
1.5	0.0752	0.0003	0.0325	0.0003	0.0677	0.0003	0.0321	0.0003	0.1611	0.0004
1.75	0.0742	0.0004	0.0327	0.0003	0.0663	0.0005	0.0329	0.0002	0.1487	0.0004
2	0.0732	0.0004	0.0327	0.0005	0.0659	0.0005	0.0326	0.0005	0.1407	0.0005
2.25	0.0722	0.0004	0.033	0.0006	0.0659	0.0008	0.0313	0.0006	0.1337	0.0006
2.5	0.0717	0.0003	0.0328	0.0003	0.0644	0.0005	0.0314	0.0004	0.1265	0.0004
2.75	0.0708	0.0002	0.0323	0.0003	0.0637	0.0003	0.0315	0.0005	0.121	0.0004
3	0.0698	0.0003	0.0321	0.0006	0.0637	0.0004	0.0326	0.0009	0.1149	0.0005
3.25	0.0699	0.0003	0.0325	0.0002	0.062	0.0003	0.0306	0.0009	0.1095	0.0004
3.5	0.0686	0.0002	0.0322	0.0003	0.0611	0.0004	0.0303	0.0005	0.1065	0.0005
3.75	0.0679	0.0004	0.0315	0.0009	0.061	0.0006	0.0312	0.0006	0.1033	0.0004
4	0.0669	0.0008	0.0318	0.0005	0.0597	0.0004	0.0302	0.0003	0.101	0.0005
4.25	0.0666	0.0004	0.032	0.0003	0.0591	0.0003	0.0304	0.0004	0.0993	0.0009
4.5	0.066	0.0003	0.0323	0.0008	0.0584	0.0004	0.0293	0.0004	0.0975	0.0006
4.75	0.0652	0.0003	0.0304	0.0004	0.0585	0.0004	0.0292	0.0003	0.0946	0.0003
5	0.0643	0.0003	0.0315	0.0003	0.0582	0.0008	0.029	0.0004	0.0931	0.0004
5.25	0.0636	0.0003	0.031	0.0005	0.0566	0.0003	0.0296	0.0004	0.0917	0.0006
5.5	0.0635	0.0003	0.0305	0.0004	0.0567	0.0004	0.0286	0.0009	0.0908	0.0006
5.75	0.0626	0.0004	0.0299	0.0006	0.055	0.0004	0.0294	0.0005	0.0898	0.0005
6	0.0619	0.0003	0.0304	0.0004	0.0546	0.0003	0.0282	0.0003	0.0882	0.0004

Table C.1: MI information results for the IMF parameters with the AL geomagnetic index.

	p_{dyn}		ρ		T		v_x		v_y	
Time (Hours)	MI	±	MI	±	MI	±	MI	±	MI	±
0	0.0791	0.0005	0.0249	0.0006	0.1235	0.0006	0.1535	0.0005	0.0406	0.0003
0.25	0.0786	0.0005	0.0256	0.0006	0.1213	0.0004	0.1541	0.0004	0.0415	0.0009
0.5	0.0781	0.001	0.0249	0.0005	0.1211	0.0003	0.1548	0.0009	0.0411	0.0006
0.75	0.0768	0.0009	0.0246	0.0004	0.1212	0.0004	0.1539	0.0006	0.0406	0.0004
1	0.0775	0.001	0.0235	0.0006	0.12	0.0005	0.1513	0.0005	0.0408	0.0004
1.25	0.0772	0.0009	0.0235	0.0004	0.1216	0.0007	0.1512	0.0005	0.0403	0.0004
1.5	0.0776	0.0007	0.0218	0.0002	0.1199	0.0005	0.1486	0.0005	0.0407	0.001
1.75	0.0773	0.0003	0.0217	0.0004	0.1244	0.0011	0.1451	0.0003	0.0396	0.0004
2	0.0766	0.0005	0.0222	0.0005	0.1175	0.0005	0.1455	0.0005	0.0398	0.0004
2.25	0.0781	0.0006	0.0229	0.0006	0.117	0.0004	0.1444	0.0004	0.0396	0.0006
2.5	0.0761	0.0006	0.0225	0.0005	0.1176	0.0005	0.1441	0.0005	0.0391	0.0004
2.75	0.0764	0.0003	0.0215	0.0004	0.116	0.0004	0.1436	0.0005	0.0389	0.001
3	0.0753	0.0005	0.0238	0.0006	0.1156	0.0004	0.1425	0.0004	0.0381	0.0006
3.25	0.0746	0.0005	0.0215	0.0003	0.1143	0.0003	0.1445	0.0007	0.0389	0.0005
3.5	0.0746	0.0006	0.0215	0.0005	0.1161	0.0005	0.1462	0.001	0.0381	0.0005
3.75	0.073	0.0007	0.0227	0.001	0.1167	0.0006	0.1444	0.0004	0.0381	0.0004
4	0.0733	0.0007	0.0222	0.0005	0.1161	0.0005	0.1462	0.0009	0.0376	0.0005
4.25	0.0724	0.0003	0.0214	0.0009	0.1144	0.0003	0.1458	0.001	0.0368	0.0003
4.5	0.0723	0.0006	0.0218	0.0006	0.1144	0.0004	0.1443	0.0006	0.0388	0.0005
4.75	0.0702	0.0005	0.0245	0.0009	0.1154	0.0005	0.1454	0.0009	0.0379	0.0008
5	0.0695	0.0004	0.0223	0.0003	0.1137	0.0005	0.1439	0.0005	0.0365	0.0006
5.25	0.0694	0.0004	0.0226	0.0005	0.114	0.0004	0.1413	0.0003	0.0369	0.0007
5.5	0.0688	0.001	0.0229	0.0006	0.1136	0.0005	0.1451	0.0006	0.0362	0.0005
5.75	0.068	0.0004	0.0232	0.0005	0.1123	0.0003	0.1445	0.0006	0.036	0.001
6	0.0674	0.0004	0.0226	0.0005	0.1104	0.0003	0.142	0.0004	0.0356	0.0003

Table C.2: MI information results for the solar wind parameters with the AL geomagnetic index.

C.2 AL Index Figures

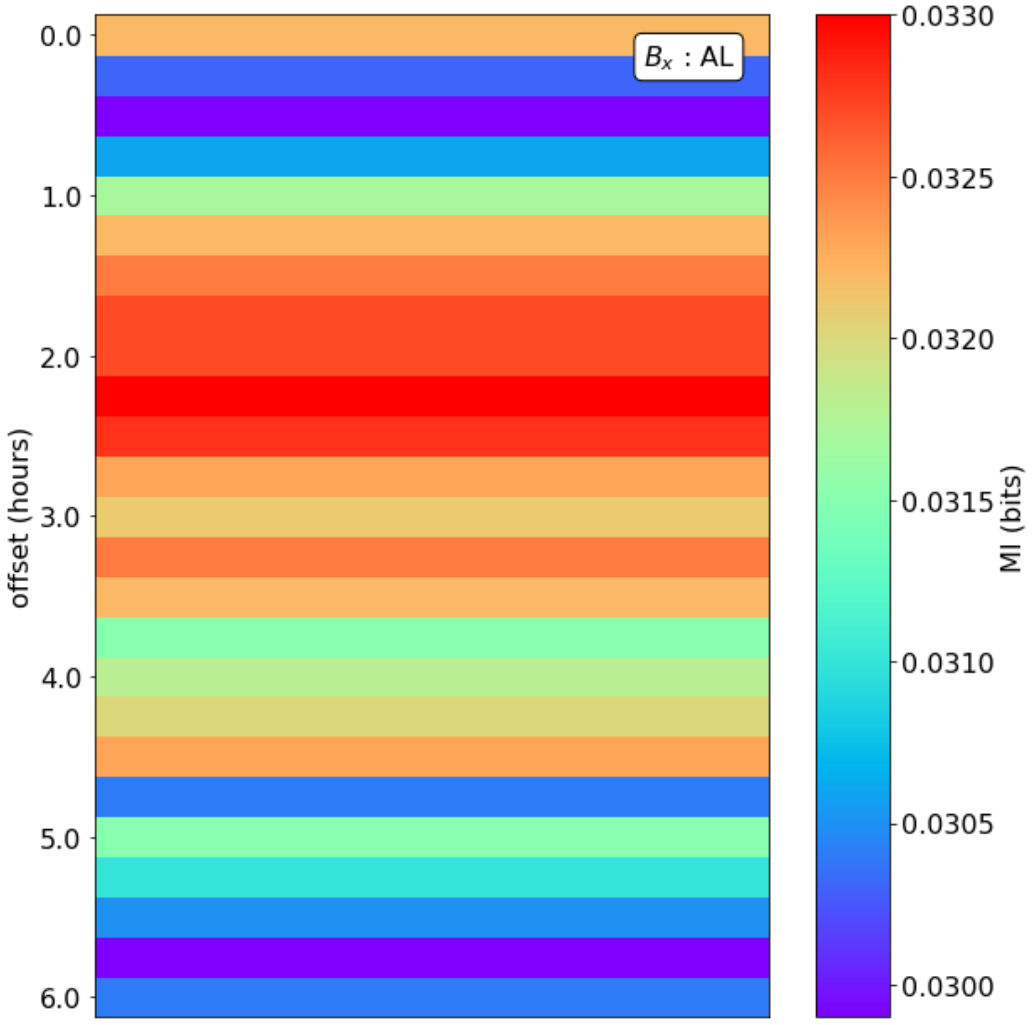

Figure C.1: Mutual information results for the solar wind parameter, B_x when compared to the geomagnetic index, AL. The y-axis represents the time offset, in hours, between the solar wind variables and the AL index data set's timestamps, as described in section 6.4.

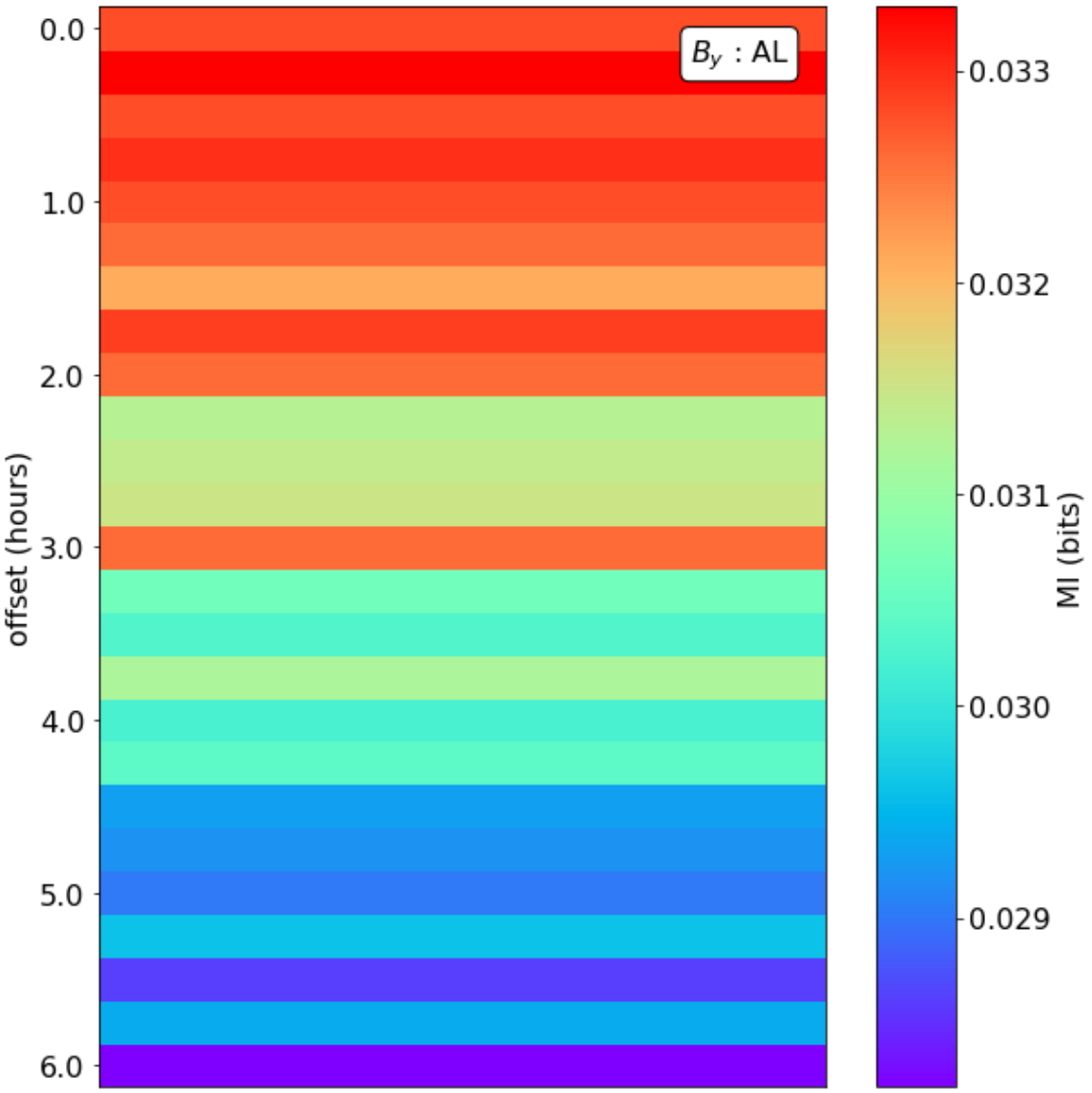

Figure C.2: As Figure C.1 for B_y of the solar wind

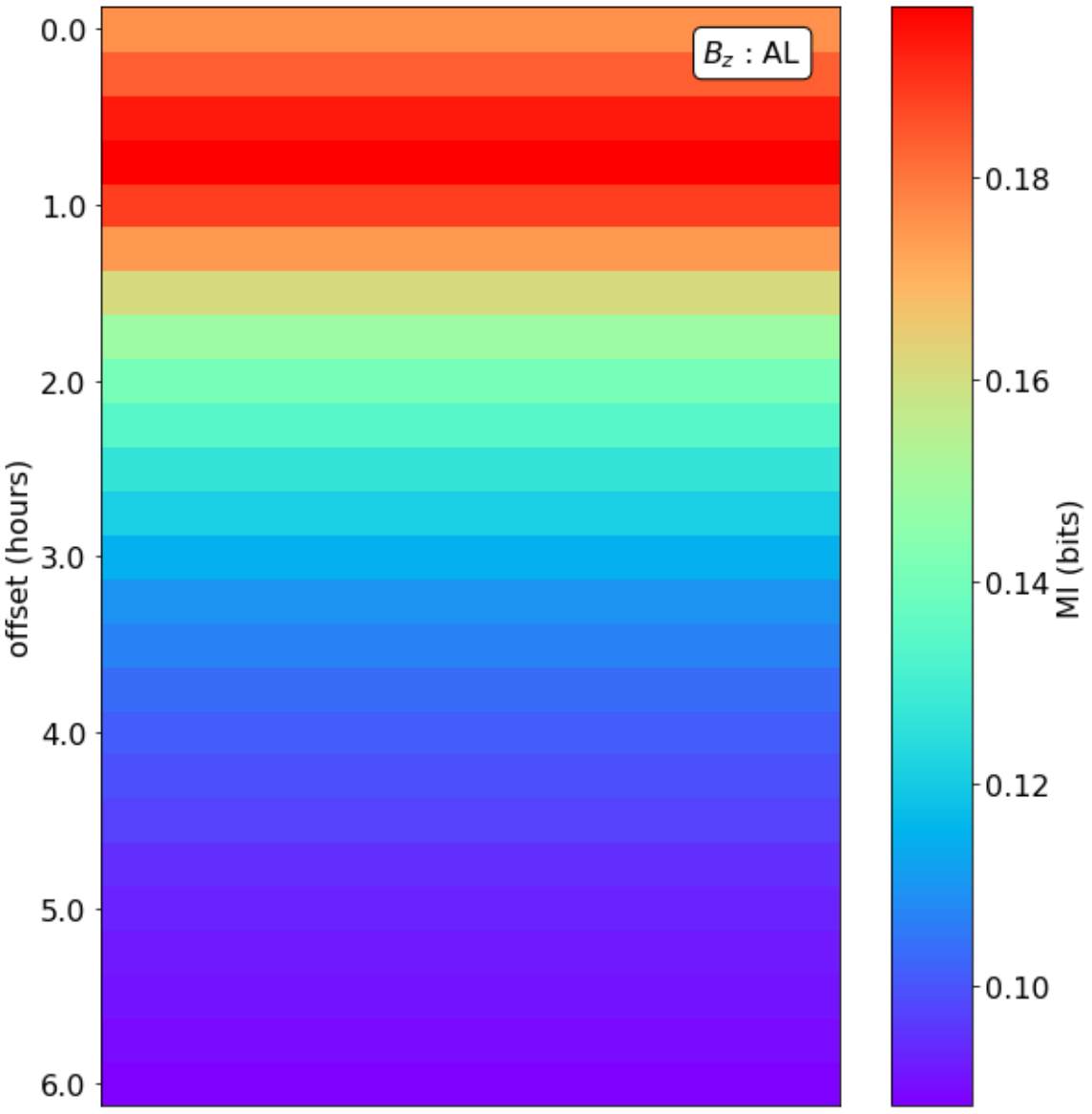

Figure C.3: As Figure C.1 for B_z of the solar wind

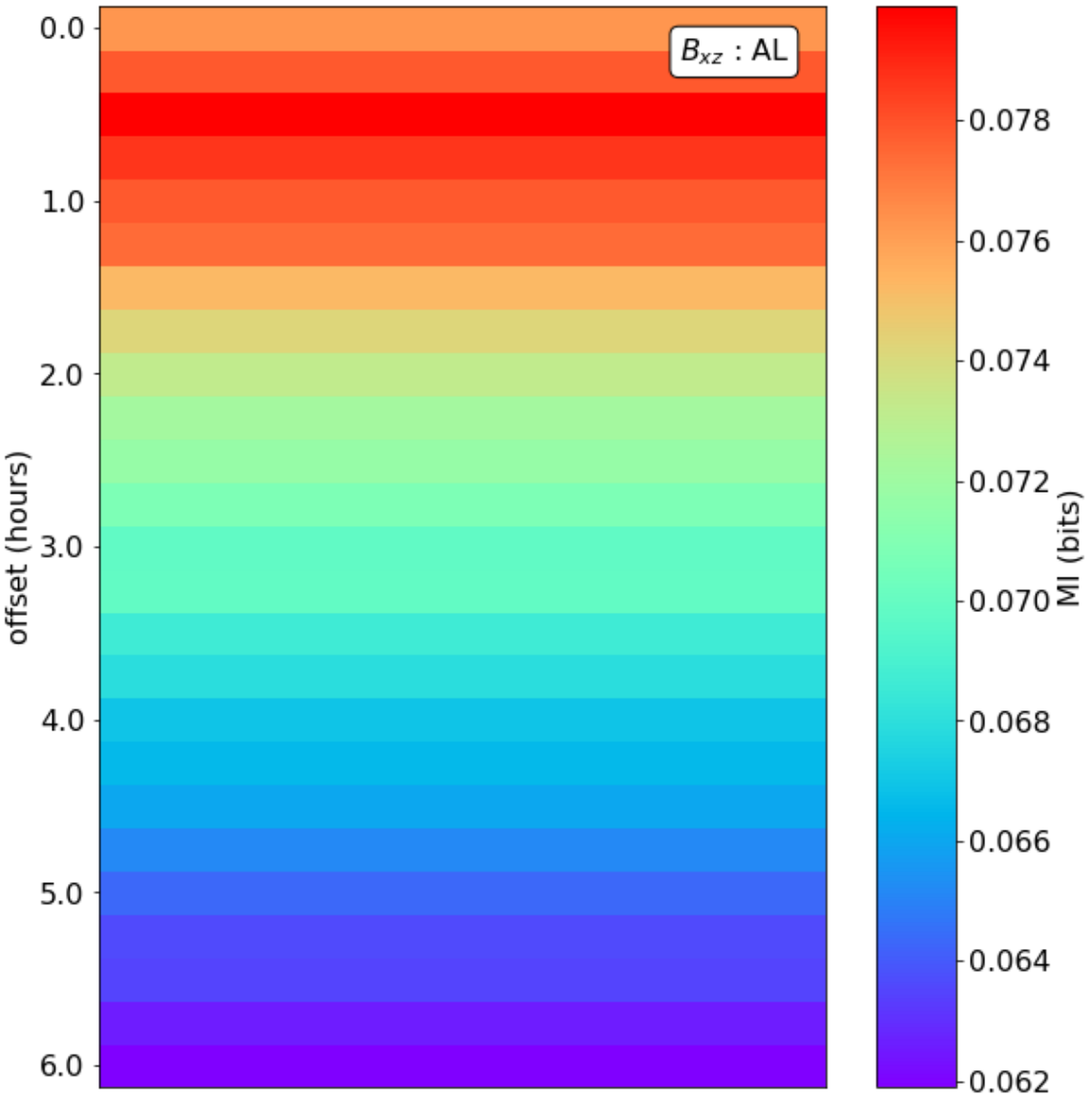

Figure C.4: As Figure C.1 for B_{xz} of the solar wind

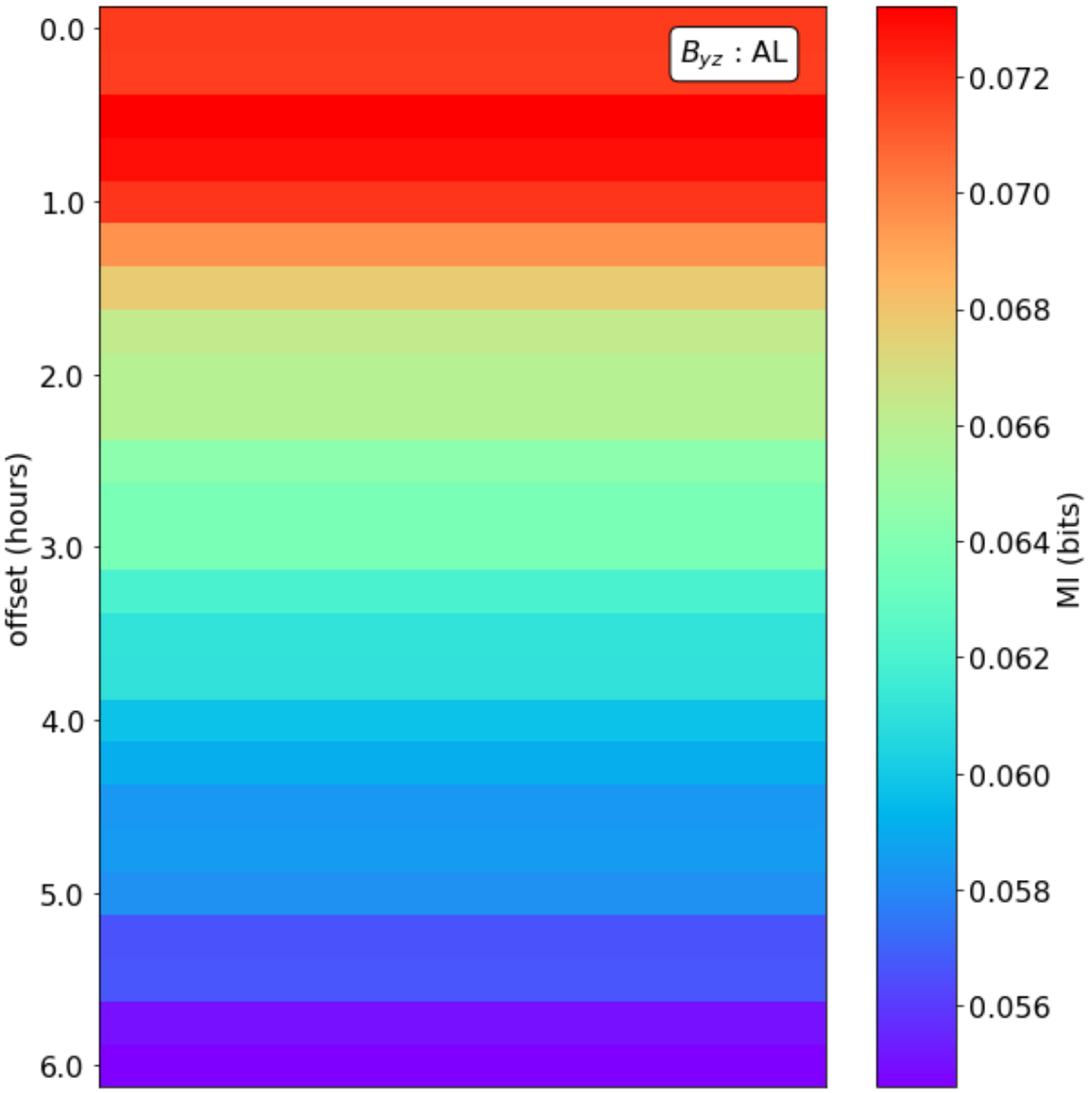

Figure C.5: As Figure C.1 for B_{yz} of the solar wind

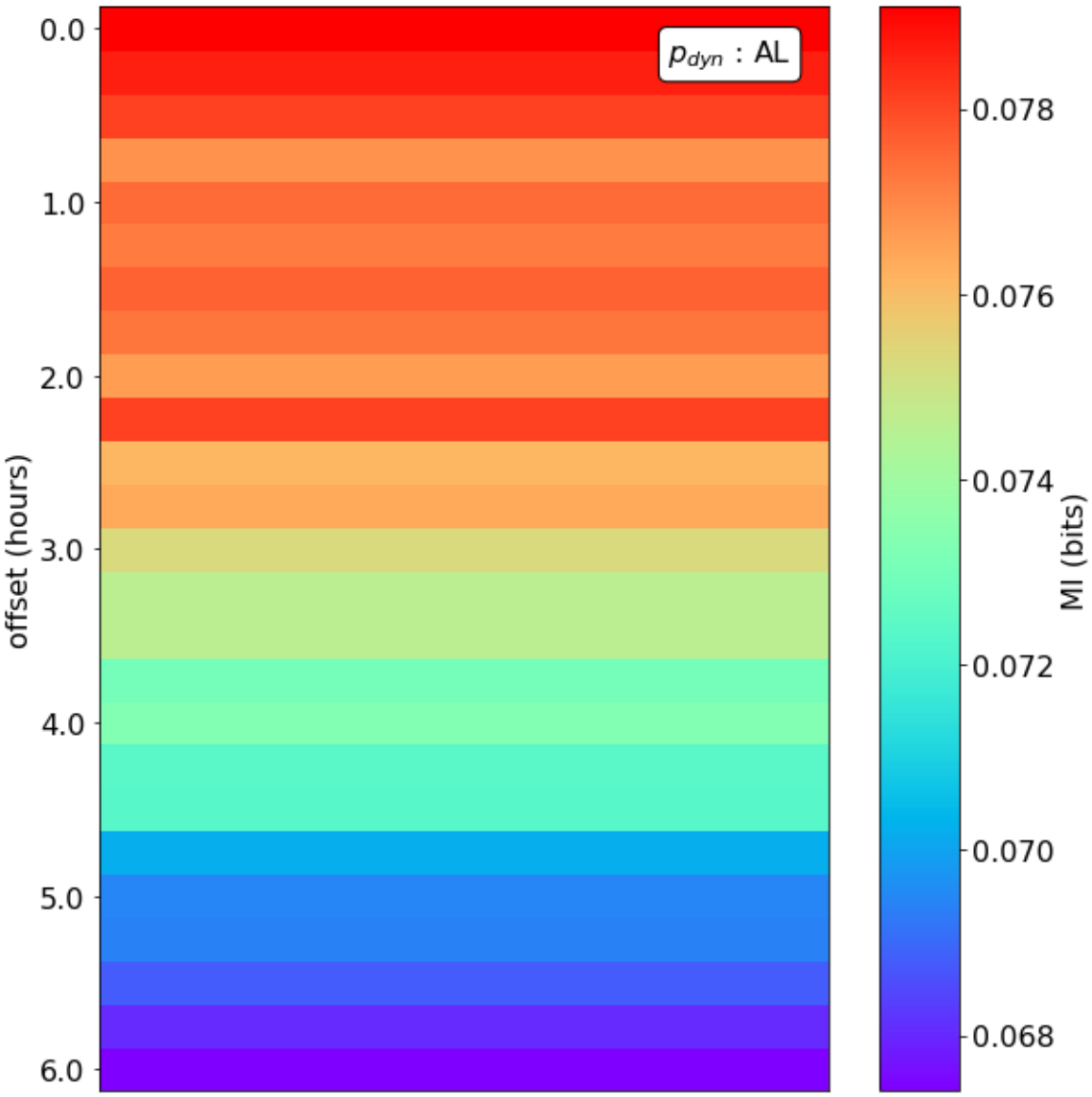

Figure C.6: As Figure C.1 for p_{dyn} of the solar wind

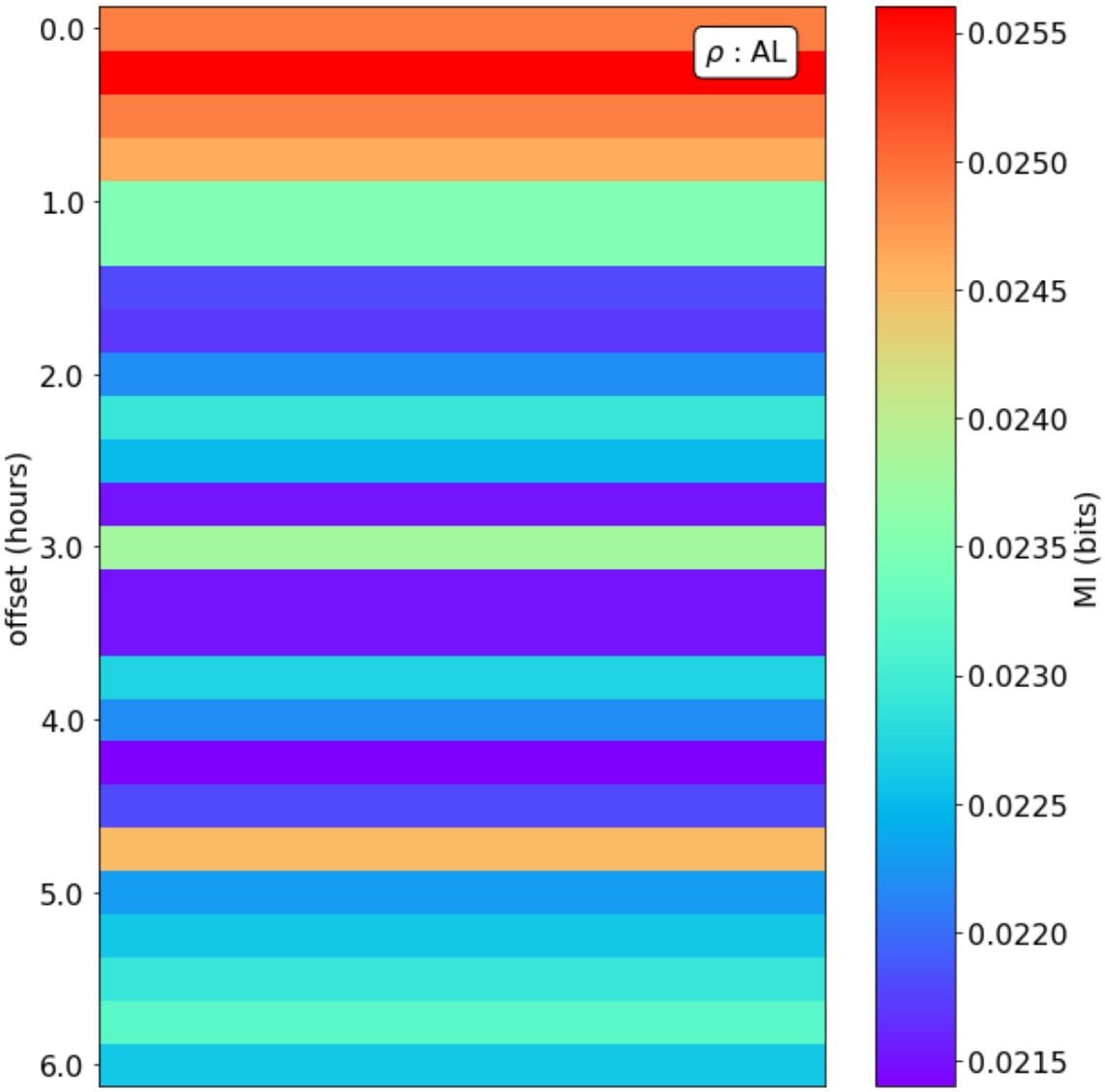

Figure C.7: As Figure C.1 for ρ of the solar wind

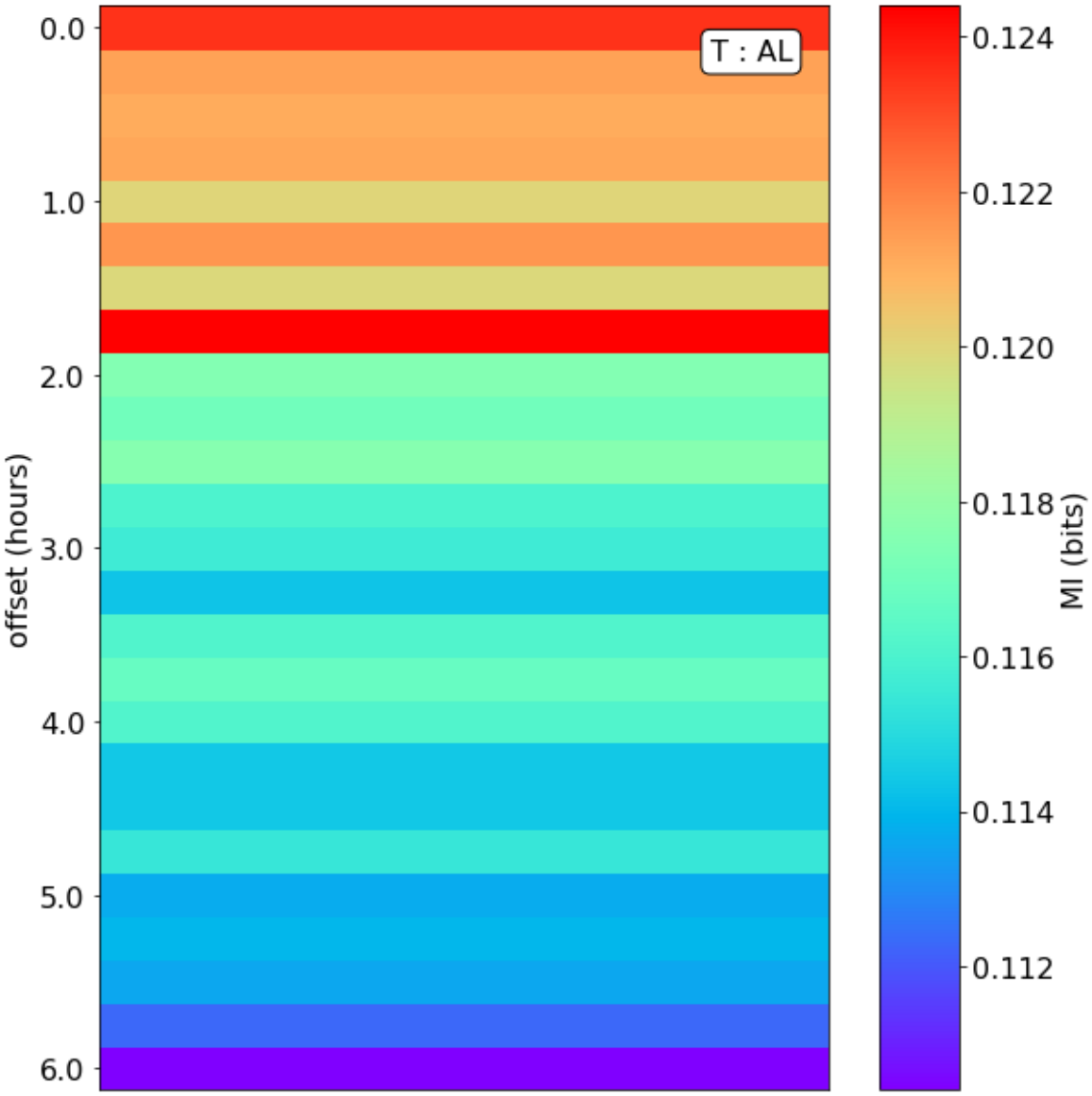

Figure C.8: As Figure C.1 for T of the solar wind

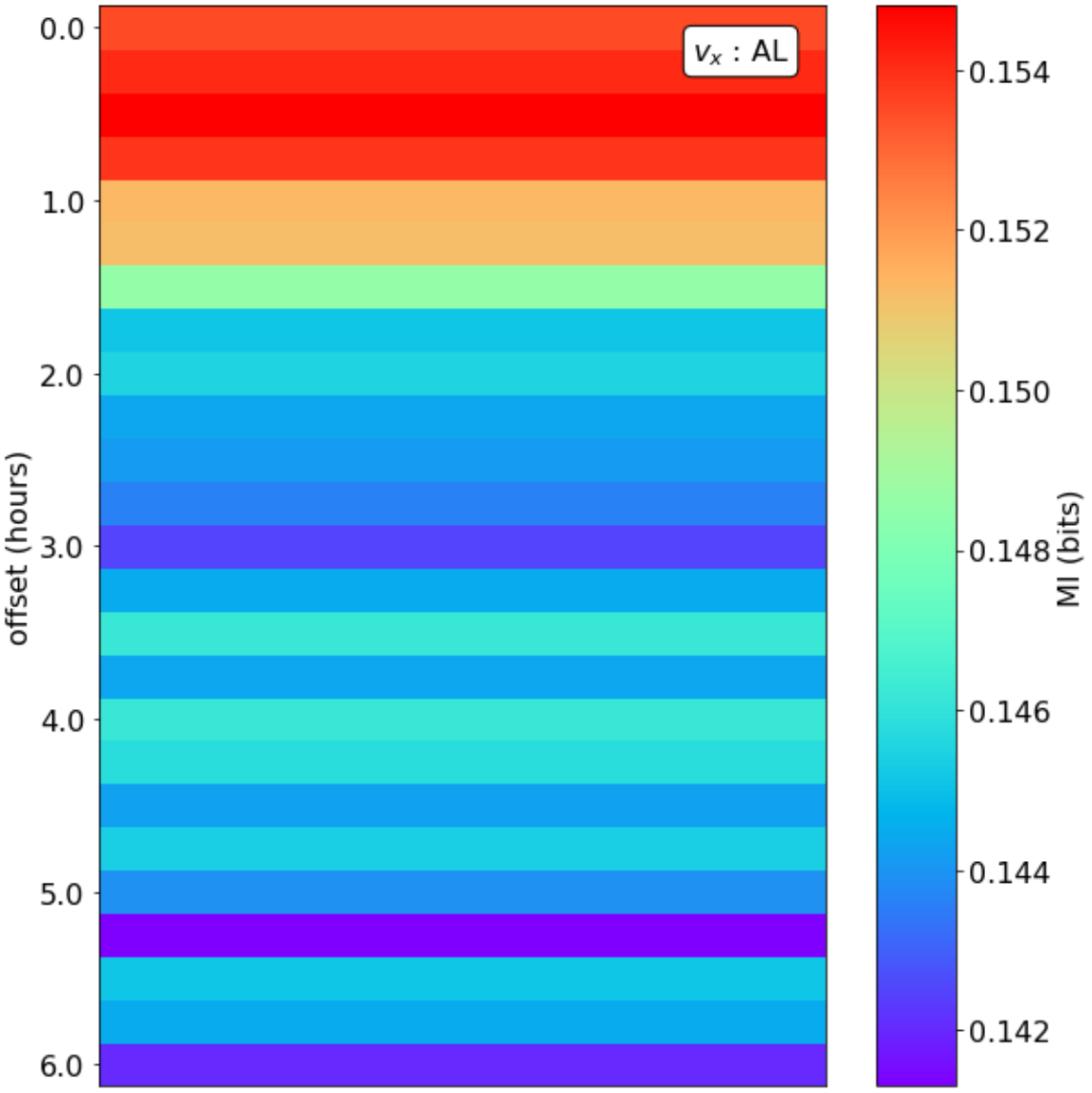

Figure C.9: As Figure C.1 for v_x of the solar wind

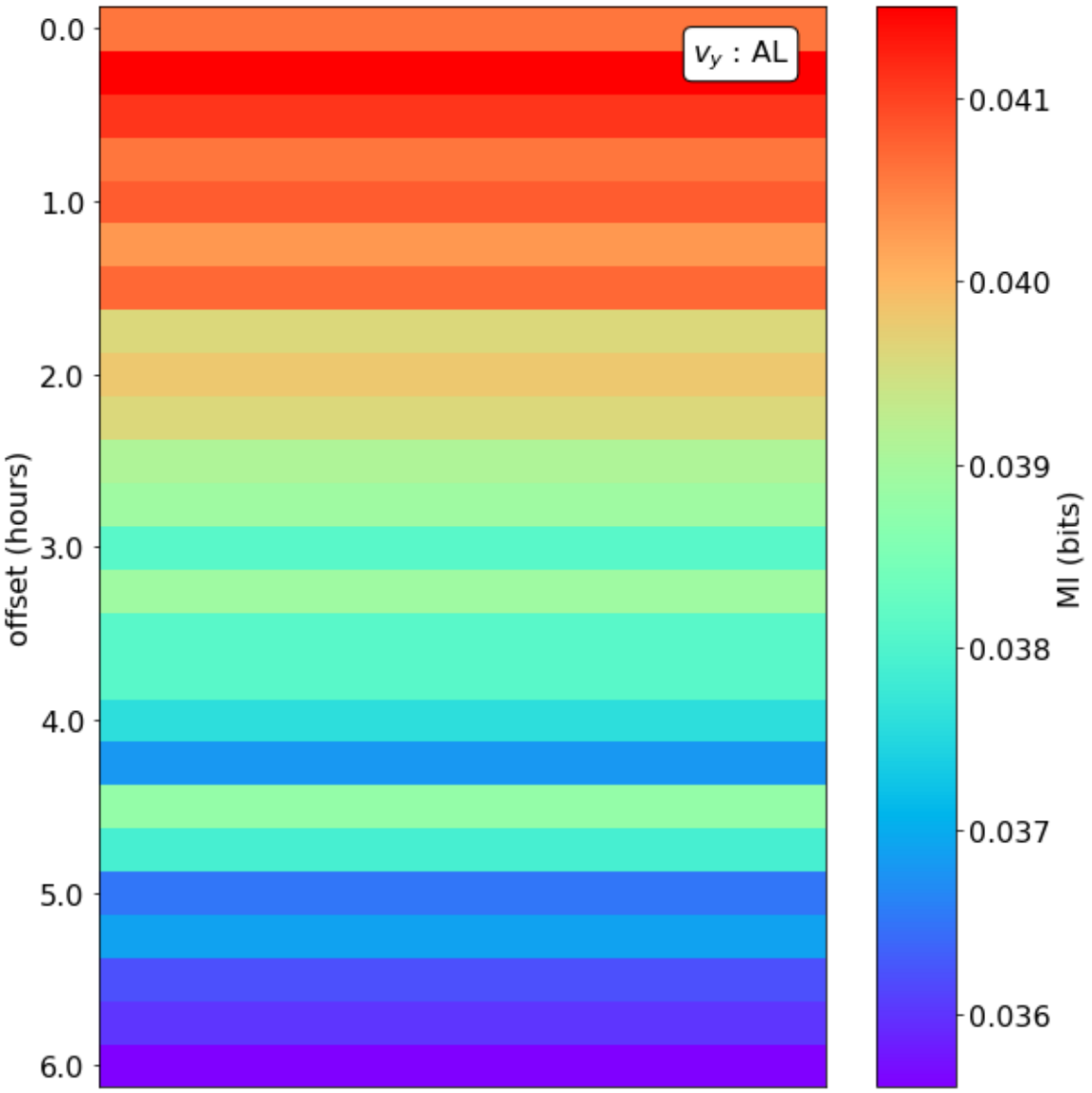

Figure C.10: As Figure C.1 for v_y of the solar wind

C.3 SYM/H Index Values

	B_{XZ}		B_x		B_{YZ}		B_y		B_z	
Time (Hours)	MI	±	MI	±	MI	±	MI	±	MI	±
0	0.091	0.0004	0.0445	0.0008	0.0853	0.0004	0.042	0.0005	0.0981	0.0008
0.25	0.0945	0.0003	0.0438	0.0003	0.0876	0.0007	0.0403	0.0005	0.1144	0.0004
0.5	0.0987	0.0004	0.0439	0.0007	0.0895	0.0008	0.0396	0.0004	0.126	0.0004
0.75	0.0996	0.0003	0.0432	0.0004	0.0901	0.0005	0.0409	0.0007	0.1292	0.0008
1	0.1002	0.0003	0.0427	0.0008	0.09	0.0004	0.0406	0.0008	0.1277	0.0004
1.25	0.1011	0.0005	0.0431	0.0004	0.0902	0.0008	0.0412	0.0008	0.1243	0.0005
1.5	0.1025	0.0008	0.0446	0.0007	0.0925	0.0007	0.0424	0.0008	0.1212	0.0008
1.75	0.1002	0.0003	0.0457	0.0005	0.0907	0.0003	0.0421	0.0004	0.1208	0.0008
2	0.1001	0.0007	0.0448	0.0007	0.09	0.0005	0.0416	0.0004	0.1183	0.0004
2.25	0.0999	0.0005	0.0452	0.0005	0.0894	0.0002	0.0424	0.0008	0.1162	0.0004
2.5	0.0995	0.0005	0.046	0.0005	0.0885	0.0003	0.0429	0.0005	0.1132	0.0004
2.75	0.0987	0.0003	0.0449	0.0005	0.0899	0.0008	0.0421	0.0007	0.1116	0.0004
3	0.0992	0.0005	0.0461	0.0005	0.089	0.0008	0.0423	0.0007	0.1094	0.0008
3.25	0.0992	0.0007	0.0478	0.0008	0.0866	0.0002	0.0424	0.0005	0.1061	0.0003
3.5	0.098	0.0007	0.0463	0.0008	0.0864	0.0004	0.0419	0.0007	0.1058	0.0005
3.75	0.0963	0.0003	0.0466	0.0005	0.0855	0.0004	0.0417	0.0003	0.1029	0.0003
4	0.0957	0.0004	0.0464	0.0005	0.0871	0.0007	0.0416	0.0003	0.1013	0.0005
4.25	0.0954	0.0003	0.046	0.0003	0.0849	0.0005	0.0413	0.0004	0.1011	0.0004
4.5	0.0951	0.0003	0.0448	0.0008	0.0837	0.0008	0.0405	0.0004	0.0997	0.0008
4.75	0.0935	0.0003	0.0454	0.0008	0.0825	0.0005	0.04	0.0005	0.0979	0.0004
5	0.0944	0.0008	0.0457	0.0004	0.0819	0.0005	0.0396	0.0005	0.0966	0.0008
5.25	0.0927	0.0002	0.0452	0.0004	0.0807	0.0002	0.0397	0.0008	0.0957	0.0003
5.5	0.0921	0.0008	0.0463	0.0008	0.0799	0.0002	0.0404	0.0005	0.0944	0.0004
5.75	0.0921	0.0005	0.0455	0.0008	0.0803	0.0004	0.0403	0.0006	0.094	0.0004
6	0.0927	0.0008	0.0449	0.0007	0.0793	0.0005	0.0394	0.0004	0.0918	0.0008

Table C.3: MI information results for the IMF parameters with the SYM/H geomagnetic index.

	p_{dyn}		ρ		T		v_x		v_y	
Time (Hours)	MI	±	MI	±	MI	±	MI	±	MI	±
0	0.1246	0.0005	0.2461	0.0005	0.1747	0.0005	0.261	0.0005	0.0591	0.0003
0.25	0.1165	0.0004	0.2354	0.0009	0.1745	0.0004	0.2593	0.0003	0.0611	0.0005
0.5	0.1097	0.0003	0.2258	0.0008	0.175	0.0003	0.2648	0.0006	0.064	0.0009
0.75	0.1038	0.0004	0.2105	0.0004	0.1773	0.0003	0.2638	0.0004	0.0612	0.0002
1	0.0957	0.0003	0.1963	0.0004	0.1798	0.0003	0.2643	0.0005	0.0627	0.0003
1.25	0.0919	0.0004	0.1874	0.0006	0.193	0.0009	0.2647	0.0004	0.0619	0.0003
1.5	0.0903	0.0009	0.1745	0.0003	0.1872	0.0005	0.2618	0.0003	0.0637	0.0006
1.75	0.0852	0.0006	0.1661	0.0005	0.1844	0.0003	0.263	0.0004	0.0661	0.0008
2	0.0826	0.0006	0.1597	0.0005	0.1866	0.0004	0.2657	0.0008	0.0643	0.0006
2.25	0.08	0.0004	0.1562	0.0009	0.1877	0.0004	0.2618	0.0006	0.0637	0.0006
2.5	0.0787	0.0006	0.149	0.0005	0.1877	0.0004	0.257	0.0004	0.0621	0.0003
2.75	0.0764	0.0004	0.1424	0.0004	0.1834	0.0003	0.2546	0.0004	0.0632	0.0006
3	0.076	0.0005	0.1405	0.0004	0.1838	0.0003	0.2593	0.0009	0.063	0.0004
3.25	0.0748	0.0003	0.1387	0.0006	0.1814	0.0003	0.2495	0.0003	0.0621	0.0005
3.5	0.0754	0.0009	0.1341	0.0003	0.1843	0.0005	0.2498	0.0005	0.0642	0.0008
3.75	0.0753	0.0008	0.1341	0.0006	0.1831	0.0005	0.2472	0.0004	0.0611	0.0005
4	0.0721	0.0009	0.131	0.0006	0.1808	0.0004	0.2437	0.0003	0.0623	0.0005
4.25	0.0707	0.0003	0.1275	0.0004	0.1817	0.0005	0.2451	0.0005	0.0613	0.0008
4.5	0.0705	0.0005	0.1236	0.0003	0.1788	0.0004	0.2484	0.0009	0.0599	0.0004
4.75	0.0708	0.0008	0.127	0.0009	0.177	0.0004	0.2408	0.0004	0.0597	0.0004
5	0.0681	0.0004	0.1222	0.0006	0.1753	0.0004	0.2407	0.0005	0.06	0.0004
5.25	0.0676	0.0004	0.1179	0.0006	0.176	0.0005	0.2348	0.0003	0.0603	0.0006
5.5	0.0678	0.0005	0.1181	0.0008	0.1769	0.0007	0.2343	0.0004	0.0569	0.0003
5.75	0.067	0.0008	0.1119	0.0004	0.1727	0.0004	0.2383	0.0009	0.06	0.0009
6	0.0649	0.0009	0.111	0.0004	0.1735	0.0006	0.2303	0.0003	0.0569	0.0003

Table C.4: MI information results for the solar wind parameters with the SYM/H geomagnetic index.

C.4 SYM/H Index Figures

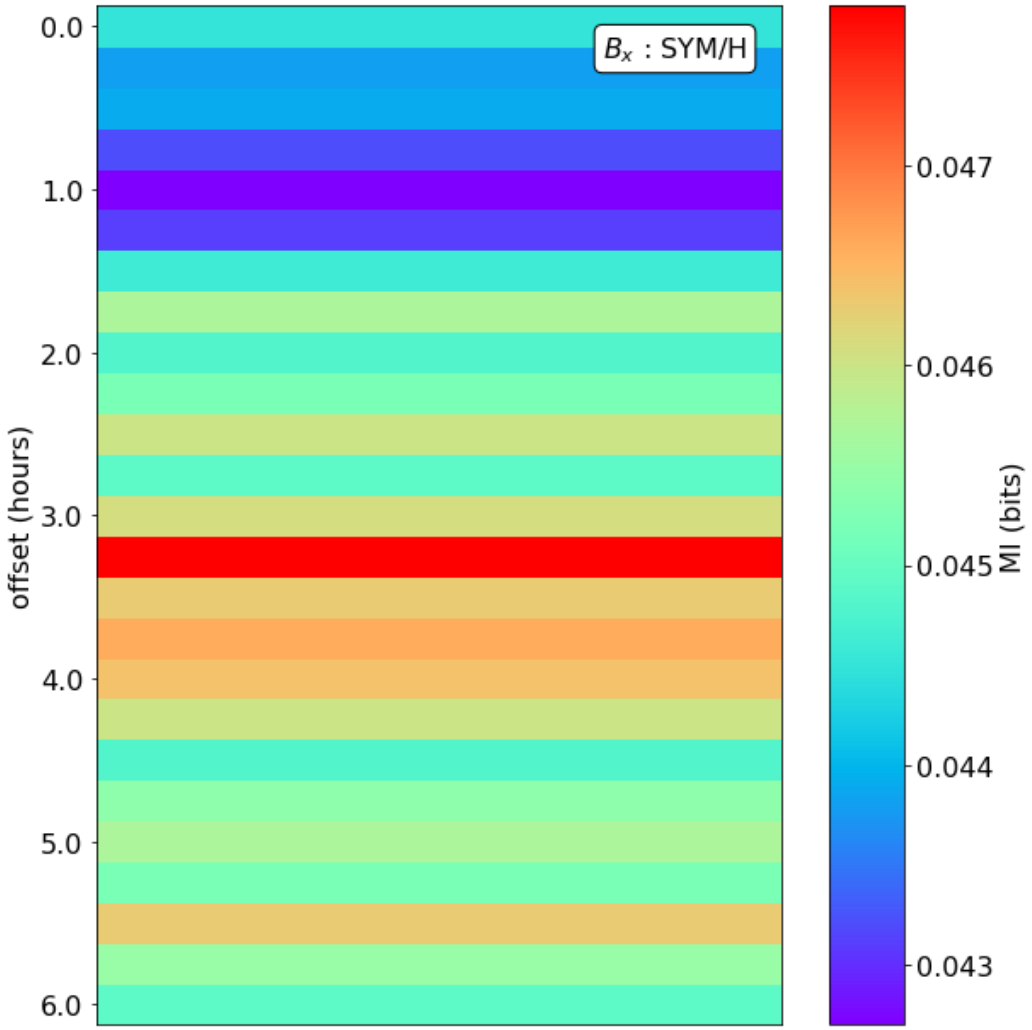

Figure C.11: Mutual information results for the solar wind parameter, B_x when compared to the geomagnetic index, SYM/H. The y-axis represents the time offset, in hours, between the solar wind variables and the SYM/H index data set's timestamps, as described in section 6.4.

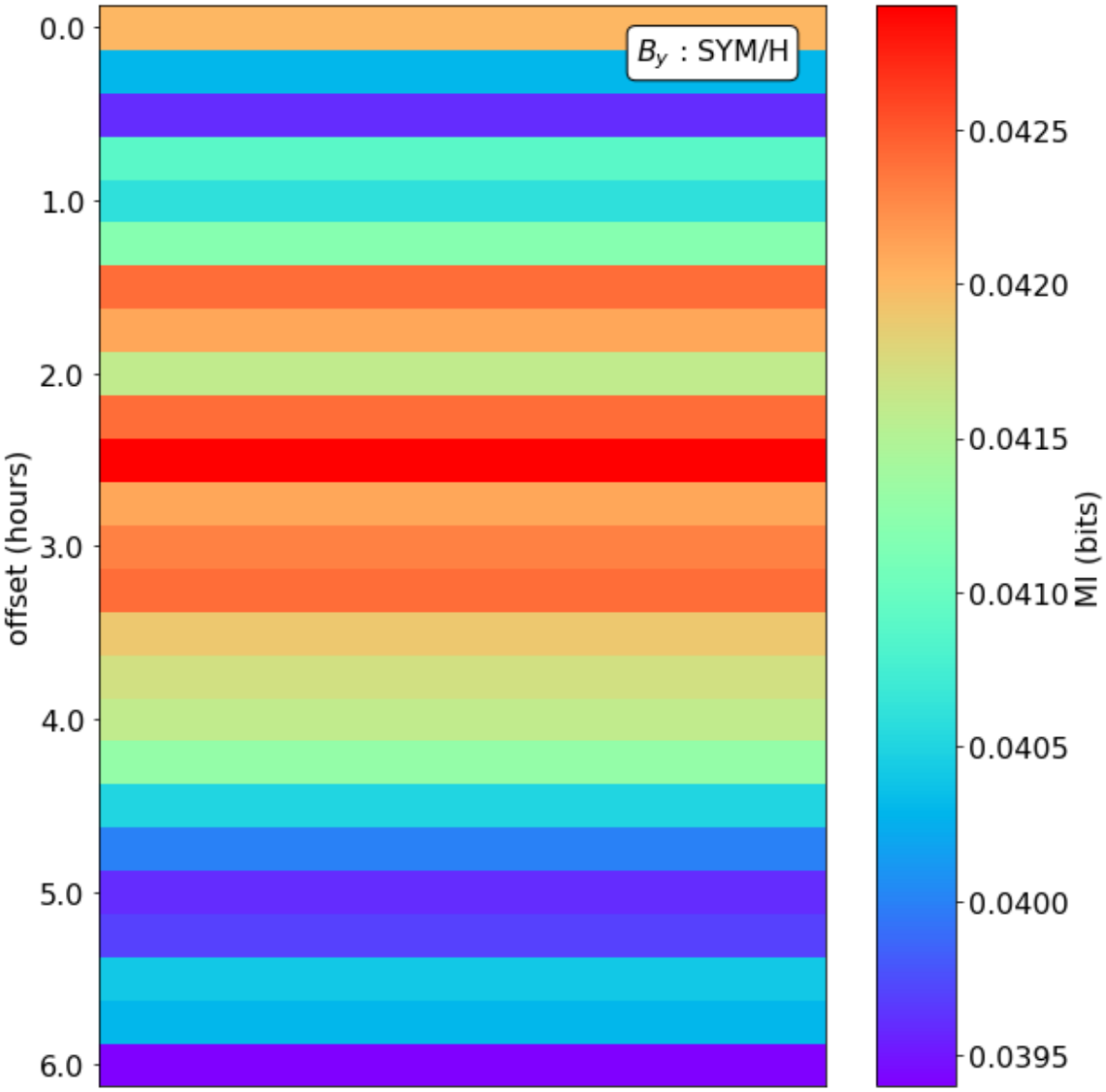

Figure C.12: As Figure C.11 for B_y of the solar wind

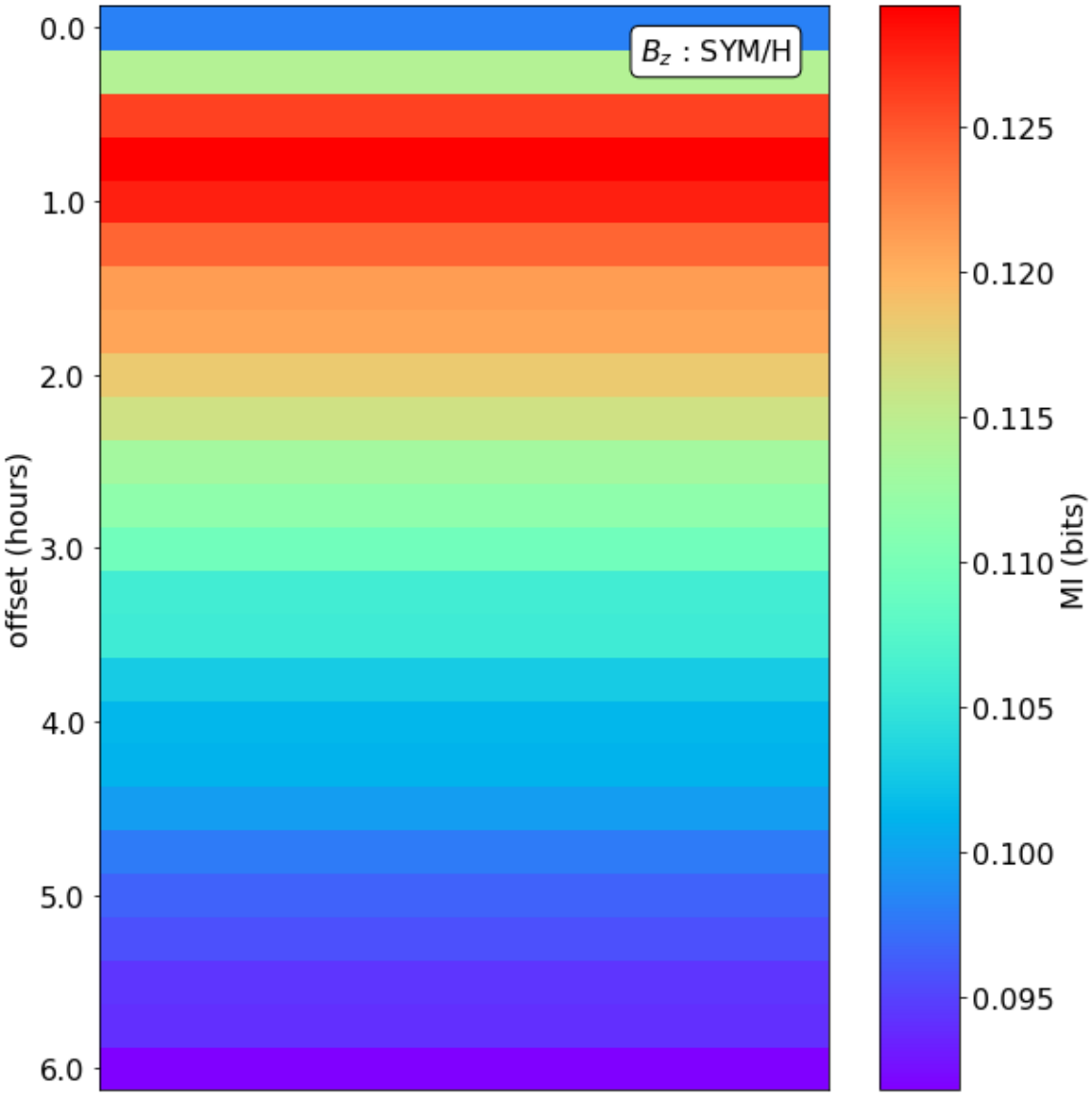

Figure C.13: As Figure C.11 for B_z of the solar wind

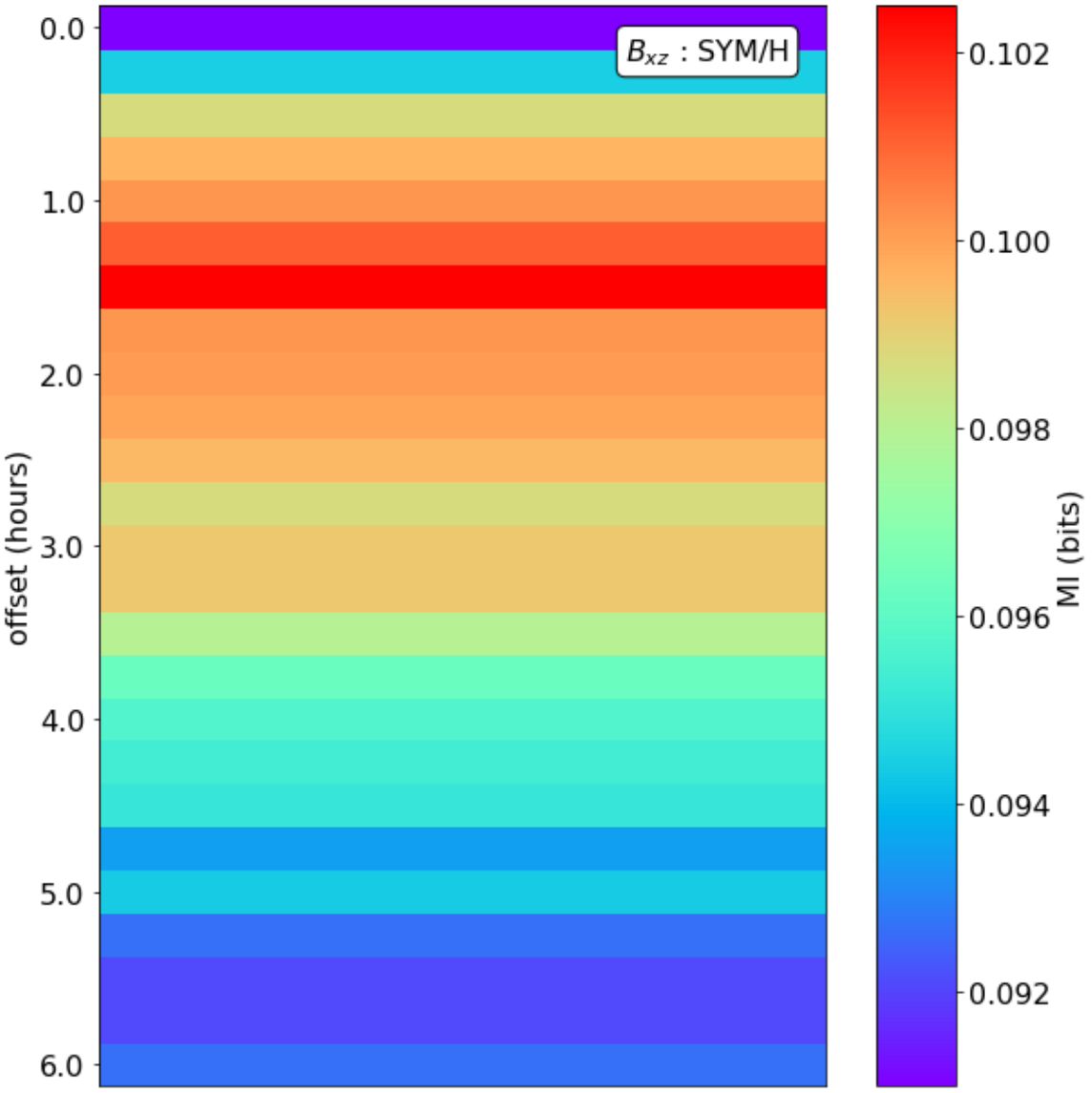

Figure C.14: As Figure C.11 for B_{xz} of the solar wind

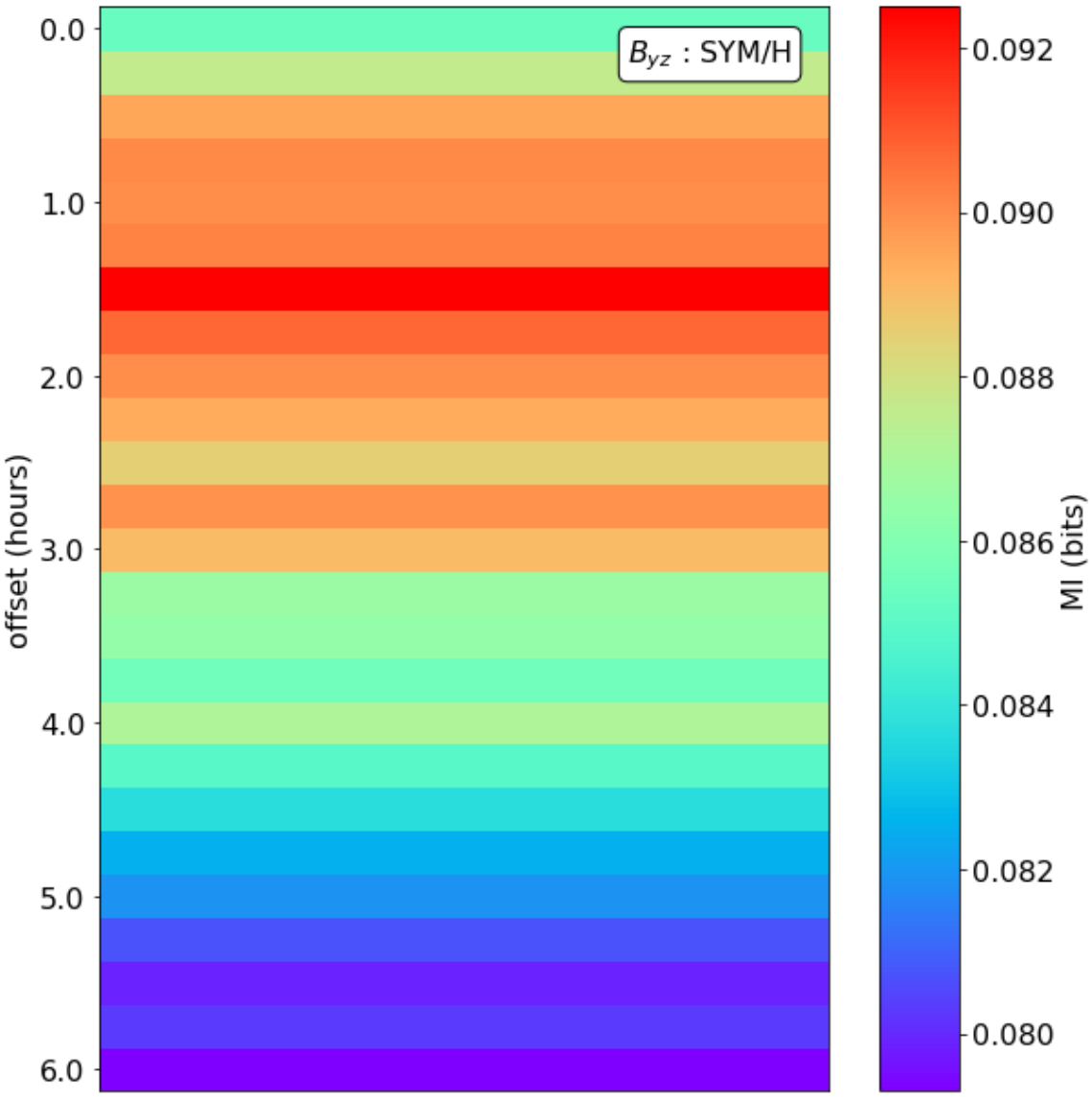

Figure C.15: As Figure C.11 for B_{yz} of the solar wind

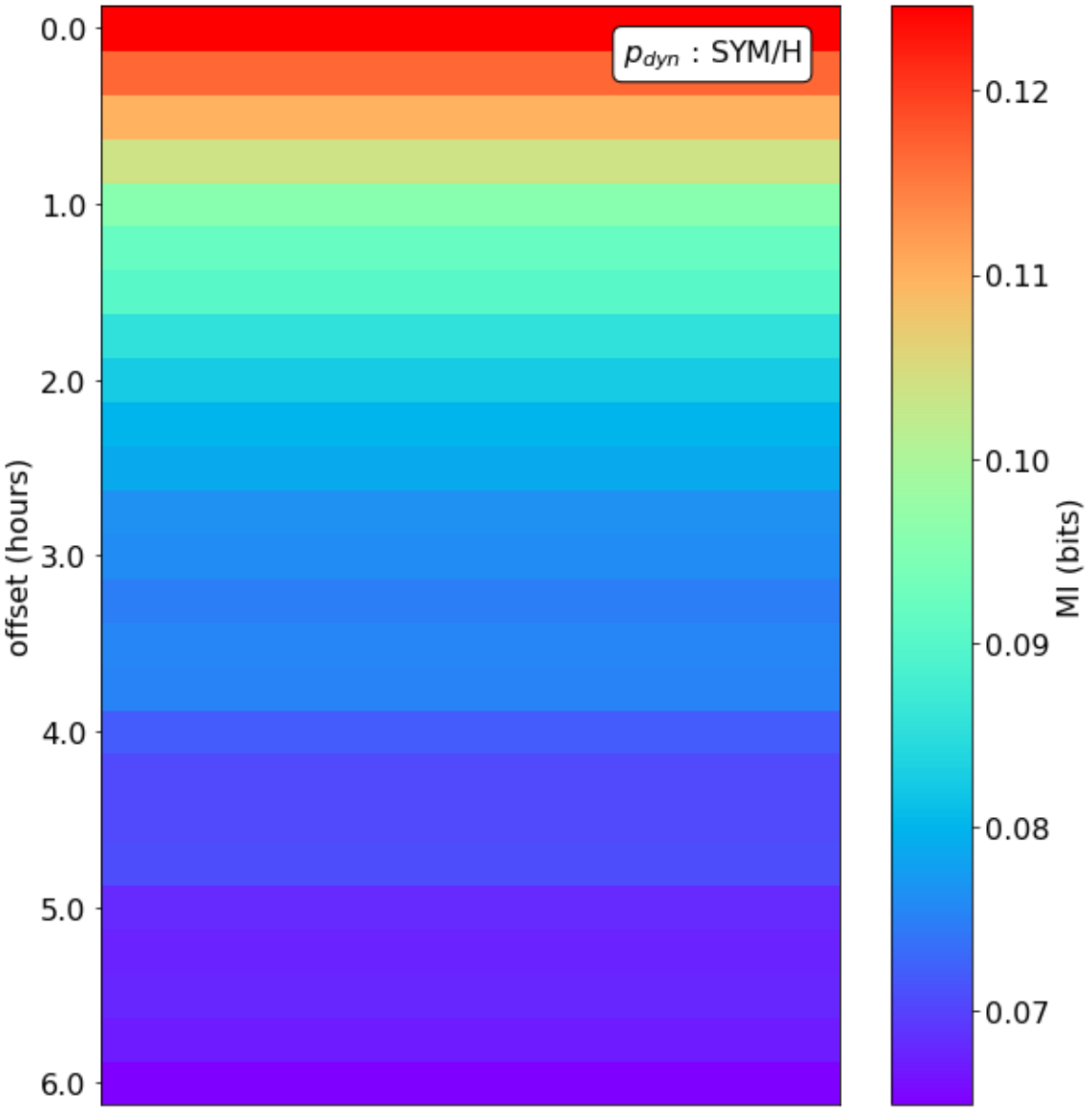

Figure C.16: As Figure C.11 for p_{dyn} of the solar wind

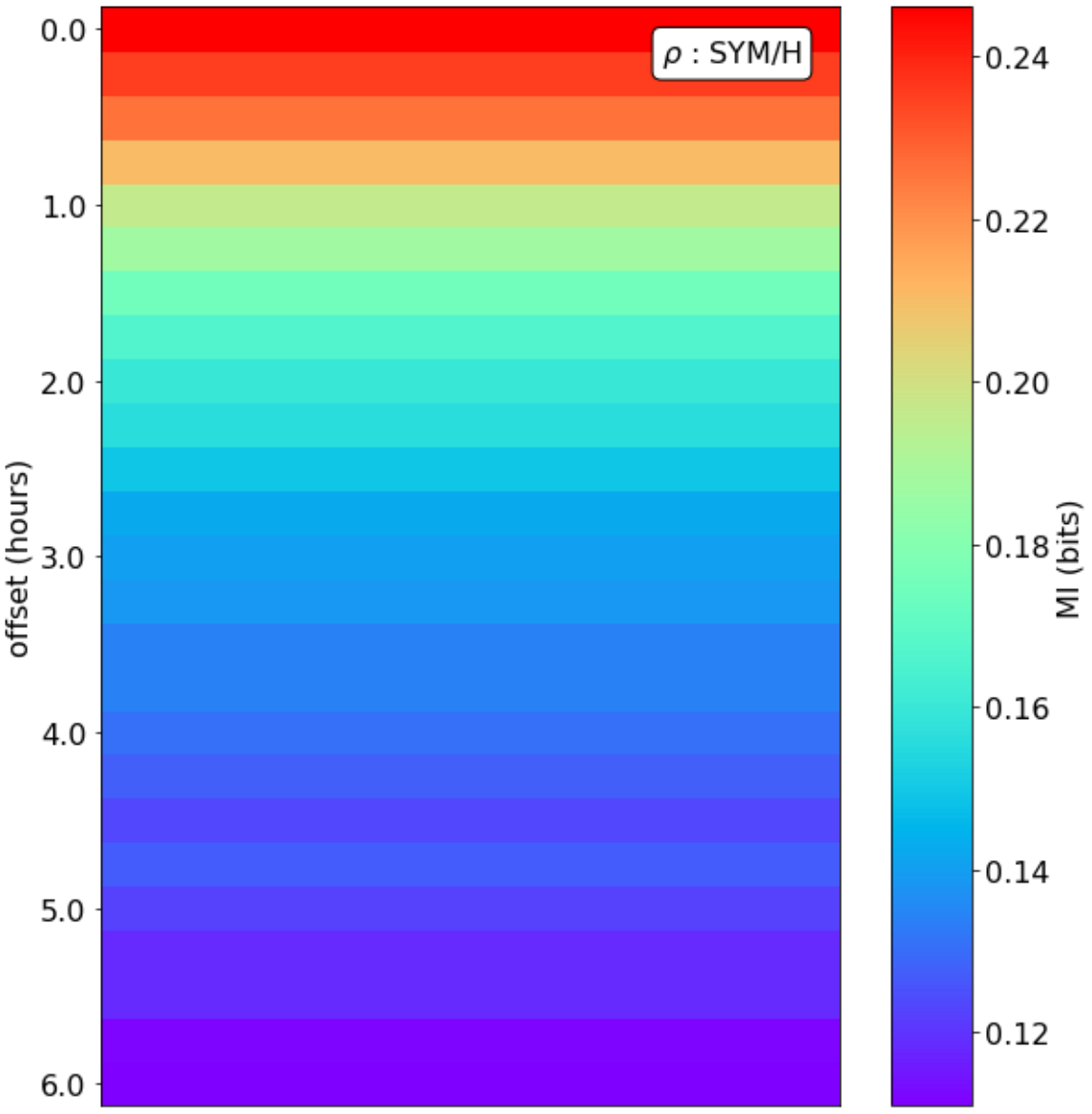

Figure C.17: As Figure C.11 for ρ of the solar wind

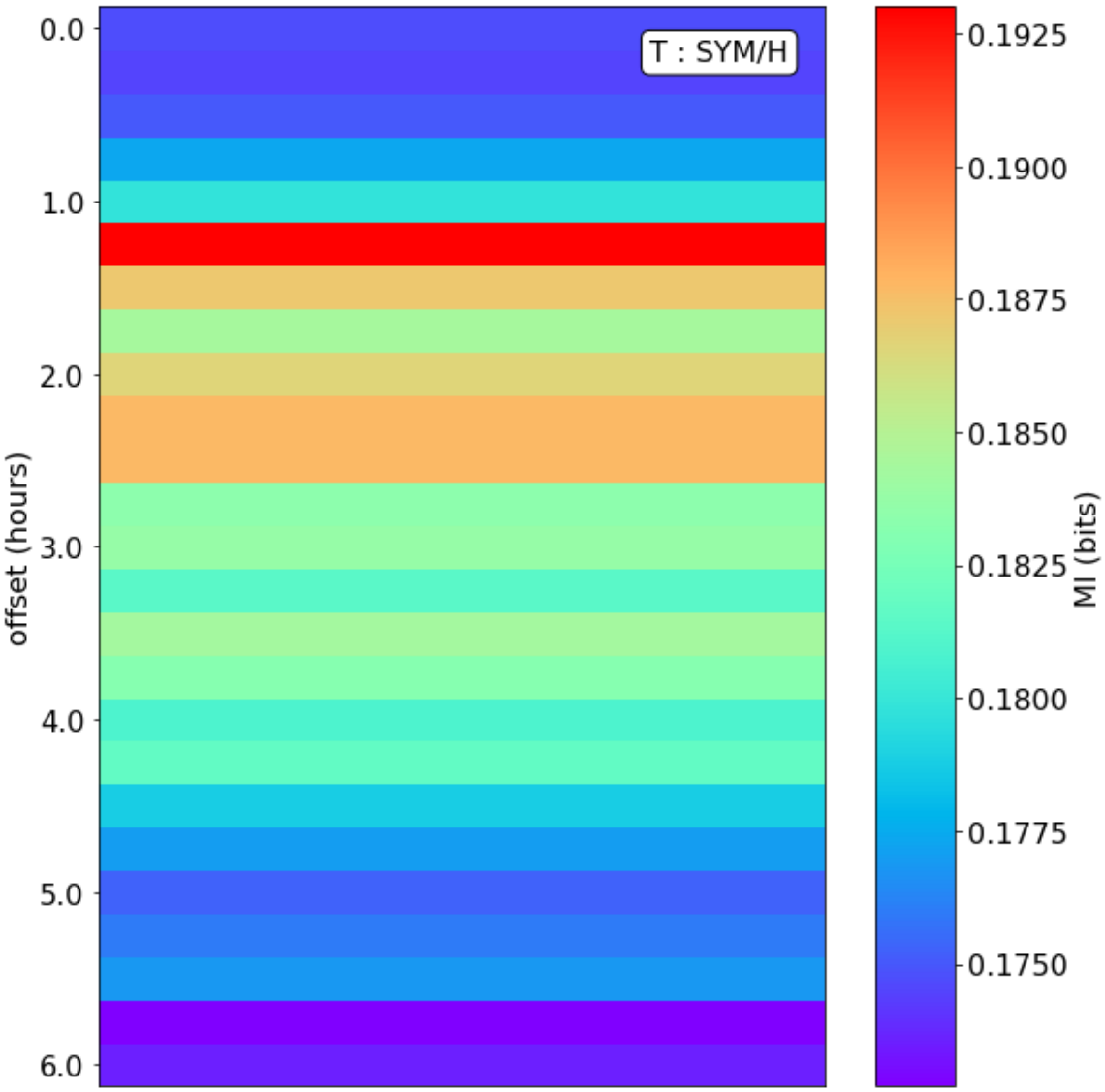

Figure C.18: As Figure C.11 for T of the solar wind

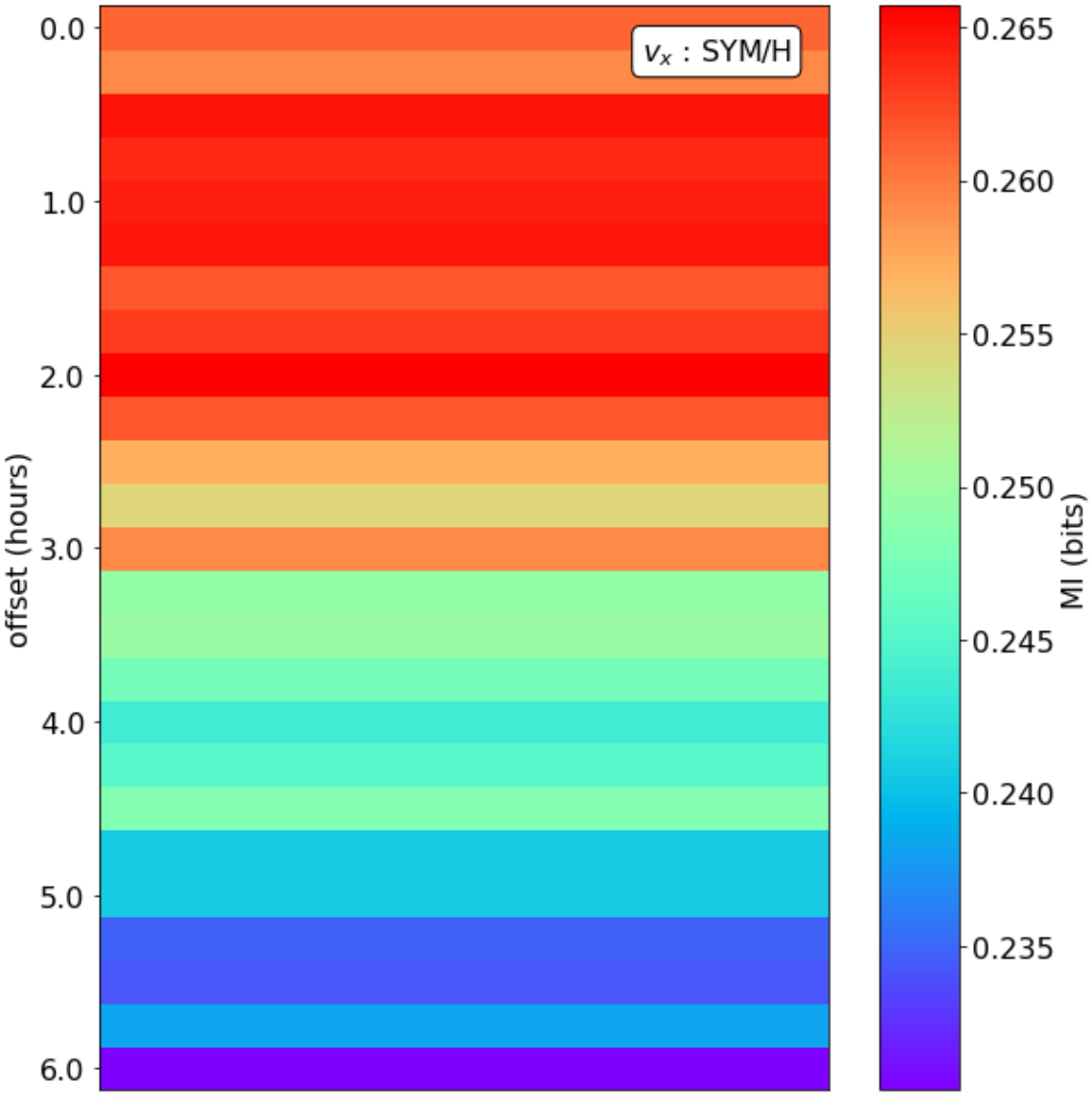

Figure C.19: As Figure C.11 for v_x of the solar wind

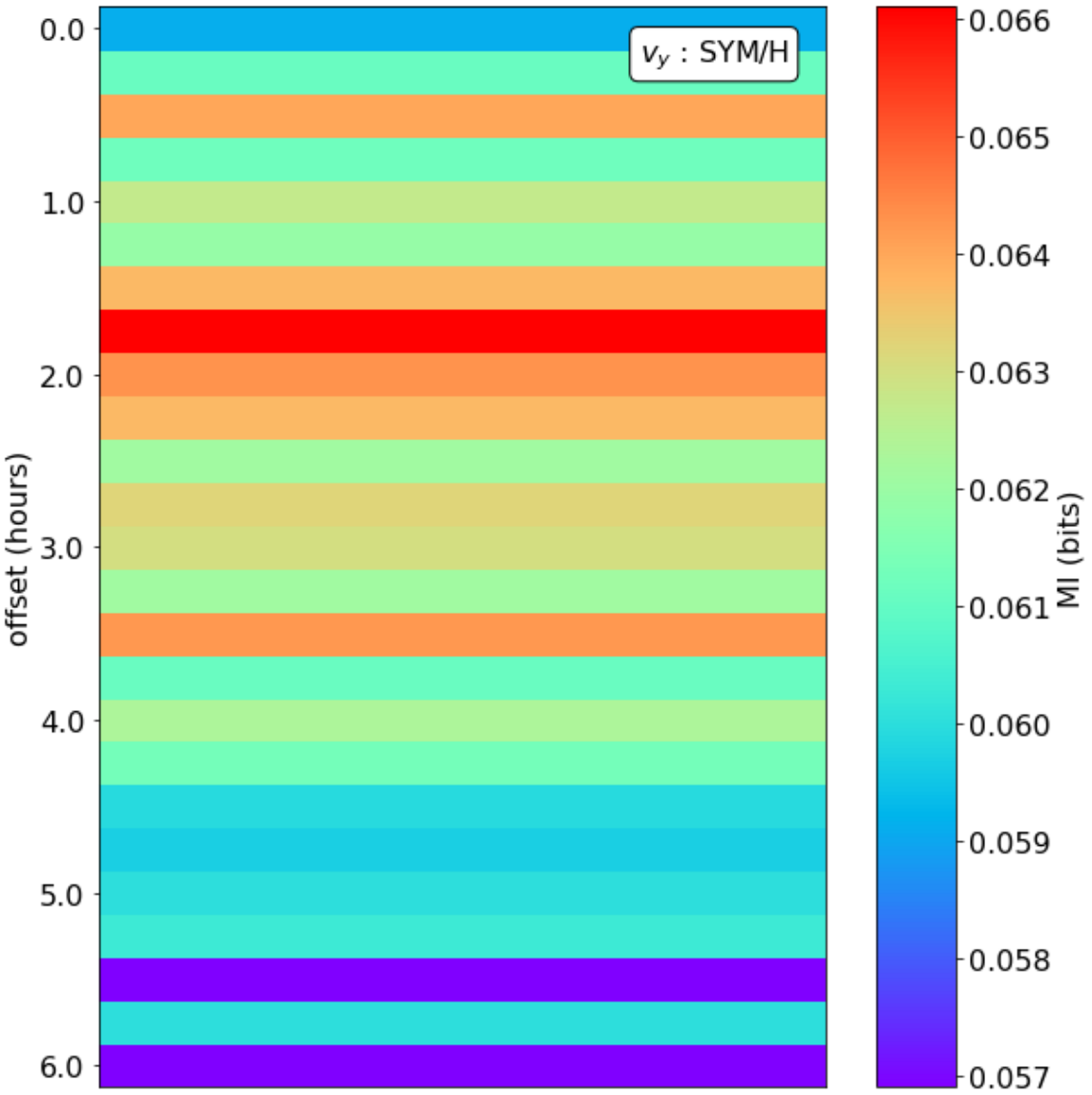

Figure C.20: As Figure C.11 for v_y of the solar wind

Appendix D

Coupling Functions

D.1 Coupling Function vs AL Results Values

	B_Z		ϵ		Φ_D		E_{KL}	
Time (Hours)	MI	±	MI	±	MI	±	MI	±
0	0.1758	0.0004	0.2551	0.0004	0.2683	0.0007	0.2661	0.0004
0.25	0.1833	0.0006	0.3156	0.0007	0.3426	0.0008	0.3265	0.0006
0.5	0.1931	0.0005	0.35	0.0005	0.3943	0.001	0.3624	0.0006
0.75	0.1968	0.0004	0.3614	0.0007	0.4118	0.0009	0.3723	0.0005
1	0.1883	0.0004	0.3569	0.0006	0.4054	0.001	0.3653	0.0006
1.25	0.1746	0.0004	0.3389	0.0007	0.382	0.0008	0.3448	0.0005
1.5	0.1611	0.0004	0.3121	0.0007	0.3448	0.0008	0.3156	0.0005
1.75	0.1487	0.0004	0.2784	0.0005	0.3042	0.0008	0.2822	0.0004
2	0.1407	0.0005	0.2461	0.0005	0.2635	0.0007	0.2493	0.0004
2.25	0.1337	0.0006	0.2158	0.0004	0.2271	0.0008	0.2195	0.0004
2.5	0.1265	0.0004	0.1904	0.0004	0.1967	0.0006	0.195	0.0005
2.75	0.121	0.0004	0.1698	0.0003	0.173	0.0005	0.1734	0.0003
3	0.1149	0.0005	0.154	0.0004	0.1543	0.0006	0.1587	0.0004
3.25	0.1095	0.0004	0.1422	0.0003	0.1405	0.0004	0.1466	0.0004
3.5	0.1065	0.0005	0.1348	0.0006	0.1317	0.0008	0.1384	0.0005
3.75	0.1033	0.0004	0.1281	0.0005	0.1243	0.0004	0.1317	0.0003
4	0.101	0.0005	0.123	0.0005	0.1182	0.0004	0.1277	0.0009
4.25	0.0993	0.0009	0.1192	0.0003	0.1142	0.0009	0.1235	0.0004
4.5	0.0975	0.0006	0.1162	0.0005	0.1098	0.0005	0.1201	0.0003
4.75	0.0946	0.0003	0.1127	0.0003	0.1058	0.0005	0.117	0.0004
5	0.0931	0.0004	0.11	0.0003	0.1029	0.0006	0.114	0.0003
5.25	0.0917	0.0006	0.1074	0.0003	0.0998	0.0004	0.1115	0.0004
5.5	0.0908	0.0006	0.1045	0.0003	0.0969	0.0004	0.1088	0.0004
5.75	0.0898	0.0005	0.1023	0.0003	0.0947	0.0005	0.1061	0.0003
6	0.0882	0.0004	0.1004	0.0005	0.0913	0.0005	0.1042	0.0003

Table D.1: MI information results for the AL geomagnetic index against IMF parameter, B_z, and coupling functions: Akasofu, ϵ, dayside reconnection, Φ_D, Kan and Lee Electric Field, E_{KL} as described in subsection 3.3.2.

D.2 Coupling Function vs AL Results Figures

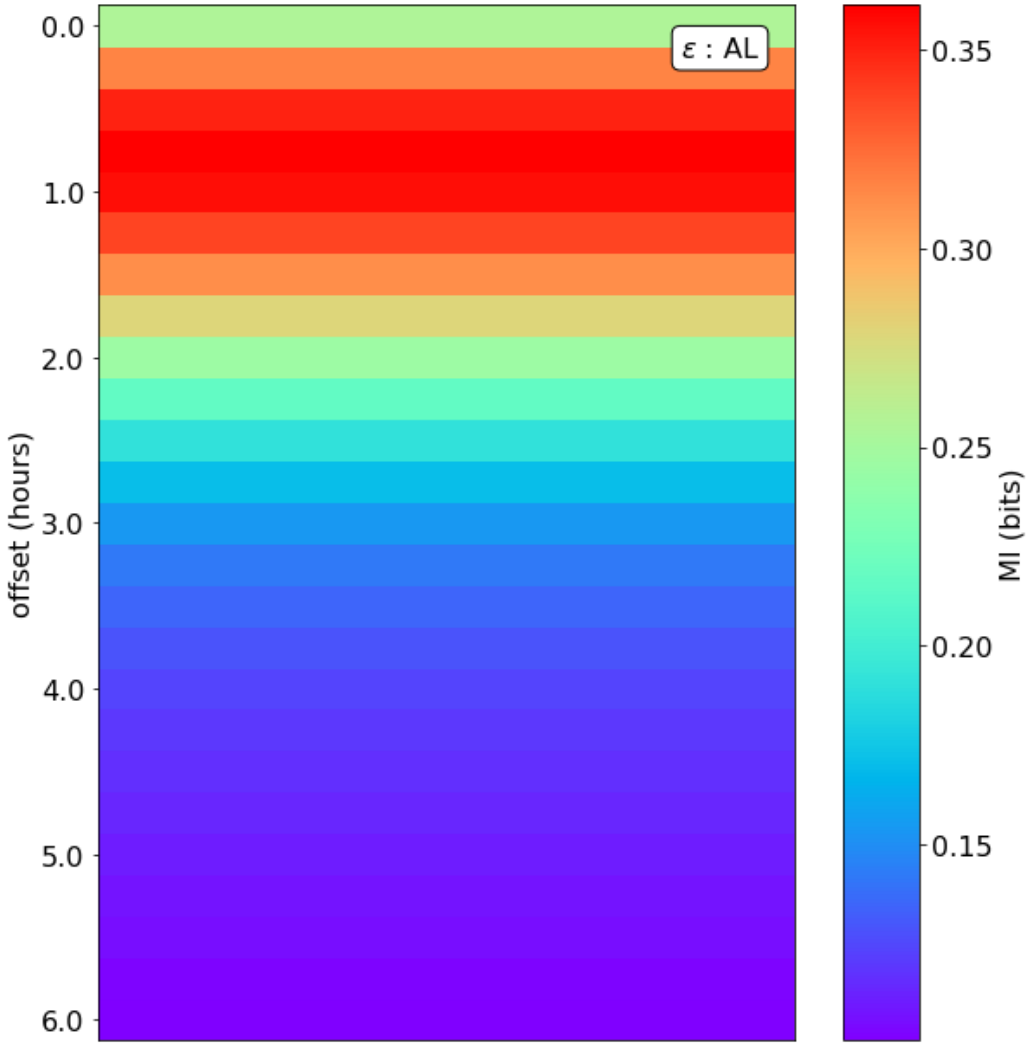

Figure D.1: Mutual information results for ϵ, when compared to the geomagnetic index, AL. The y-axis represents the time offset, in hours, between ϵ and the AL index data set's timestamps, as described in section 6.4.

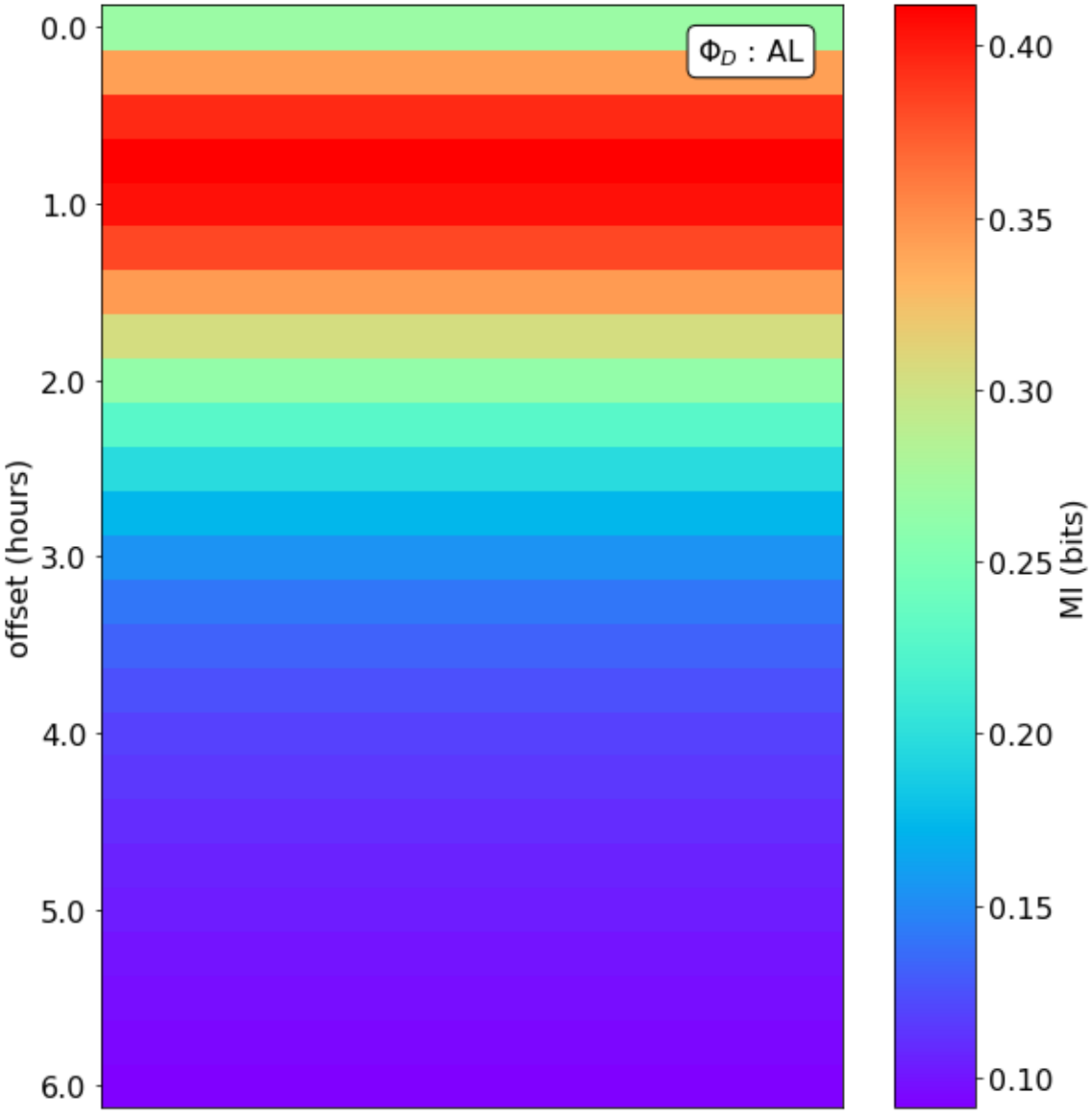

Figure D.2: As Figure D.1 for Φ_D

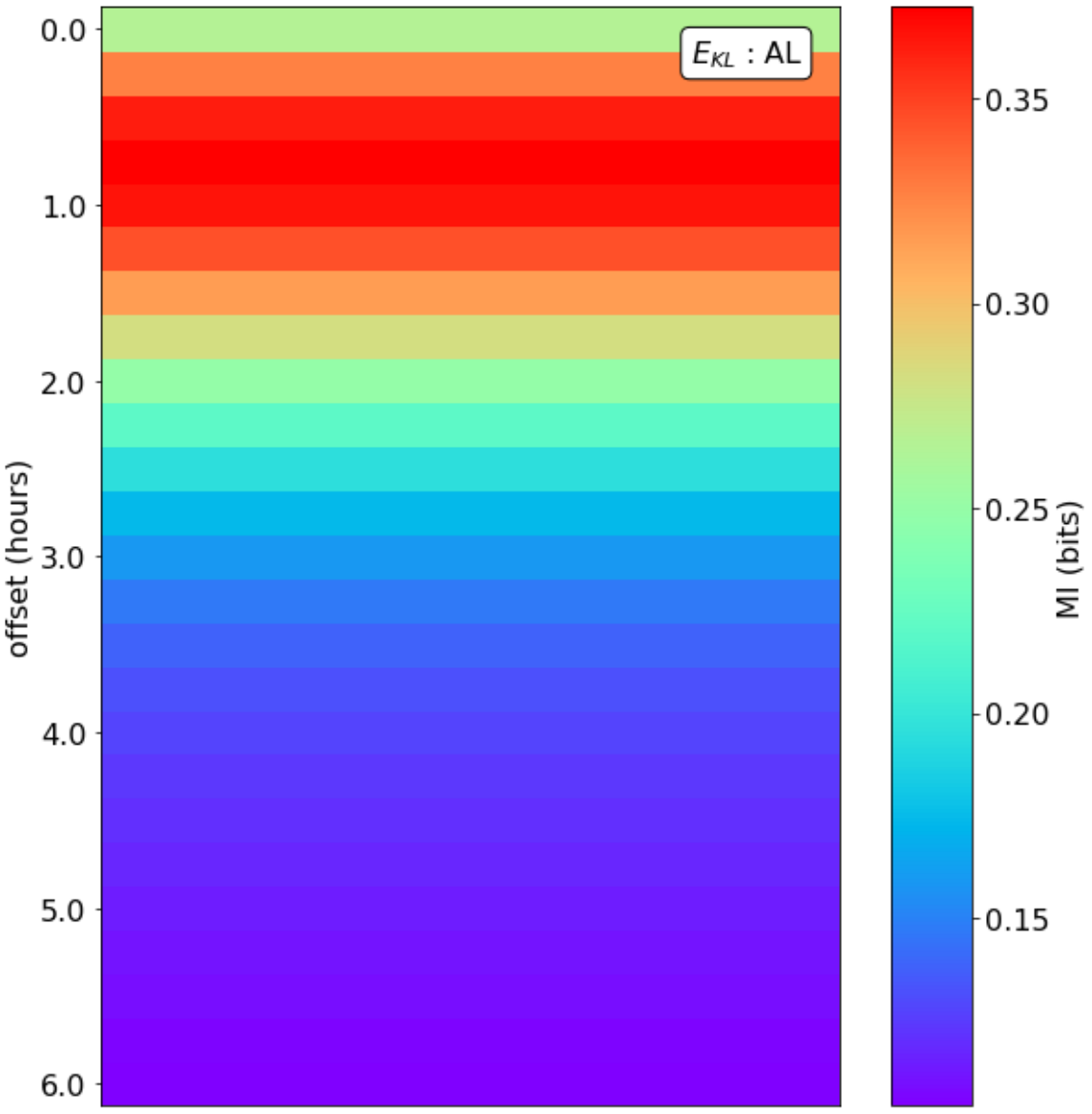

Figure D.3: As Figure D.1 for E_{KL}

D.3 Coupling Function vs SYM/H Results Values

	B_Z		ϵ		Φ_D		E_{KL}	
Time (Hours)	MI	±	MI	±	MI	±	MI	±
0	0.0981	0.0008	0.1385	0.0003	0.127	0.0005	0.1344	0.0004
0.25	0.1144	0.0004	0.15	0.0003	0.1413	0.0013	0.1474	0.0005
0.5	0.126	0.0004	0.1665	0.0006	0.1607	0.0006	0.1641	0.0003
0.75	0.1292	0.0008	0.1808	0.0005	0.1774	0.0005	0.1789	0.0004
1	0.1277	0.0004	0.188	0.0003	0.187	0.0006	0.1873	0.0005
1.25	0.1243	0.0005	0.1919	0.0003	0.1913	0.0005	0.1922	0.0005
1.5	0.1212	0.0008	0.1938	0.0004	0.1921	0.0005	0.1941	0.0004
1.75	0.1208	0.0008	0.1928	0.0004	0.1916	0.0007	0.1933	0.0007
2	0.1183	0.0004	0.1921	0.0005	0.1882	0.0009	0.1922	0.0005
2.25	0.1162	0.0004	0.1889	0.0003	0.1856	0.0006	0.1921	0.0009
2.5	0.1132	0.0004	0.1863	0.0003	0.1808	0.0005	0.1875	0.0004
2.75	0.1116	0.0004	0.1833	0.0003	0.1771	0.0005	0.1848	0.0004
3	0.1094	0.0008	0.1805	0.0004	0.1728	0.0004	0.1821	0.0003
3.25	0.1061	0.0003	0.178	0.0004	0.1691	0.0005	0.1799	0.0004
3.5	0.1058	0.0005	0.1762	0.0004	0.166	0.0005	0.1784	0.0004
3.75	0.1029	0.0003	0.1742	0.0008	0.1643	0.0005	0.1771	0.0004
4	0.1013	0.0005	0.1734	0.0006	0.1633	0.0006	0.1749	0.0009
4.25	0.1011	0.0004	0.1735	0.0005	0.1608	0.0005	0.1759	0.0003
4.5	0.0997	0.0008	0.1731	0.0004	0.1601	0.0005	0.1754	0.0003
4.75	0.0979	0.0004	0.1731	0.0005	0.1595	0.0005	0.1757	0.0004
5	0.0966	0.0008	0.1728	0.0003	0.1595	0.0005	0.1764	0.0005
5.25	0.0957	0.0003	0.1729	0.0004	0.159	0.0006	0.1772	0.0004
5.5	0.0944	0.0004	0.1725	0.0004	0.1592	0.0006	0.1775	0.0004
5.75	0.094	0.0004	0.1728	0.0003	0.1591	0.0005	0.1782	0.0004
6	0.0918	0.0008	0.1733	0.0004	0.1596	0.0008	0.1782	0.0004

Table D.2: MI information results for the SYM/H geomagnetic index against IMF parameter, B_z, and coupling functions: Akasofu, ϵ, dayside reconnection, Φ_D, and Kan and Lee Electric Field, E_{KL} as described in subsection 3.3.2.

D.4 Coupling Function vs SYM/H Results Figures

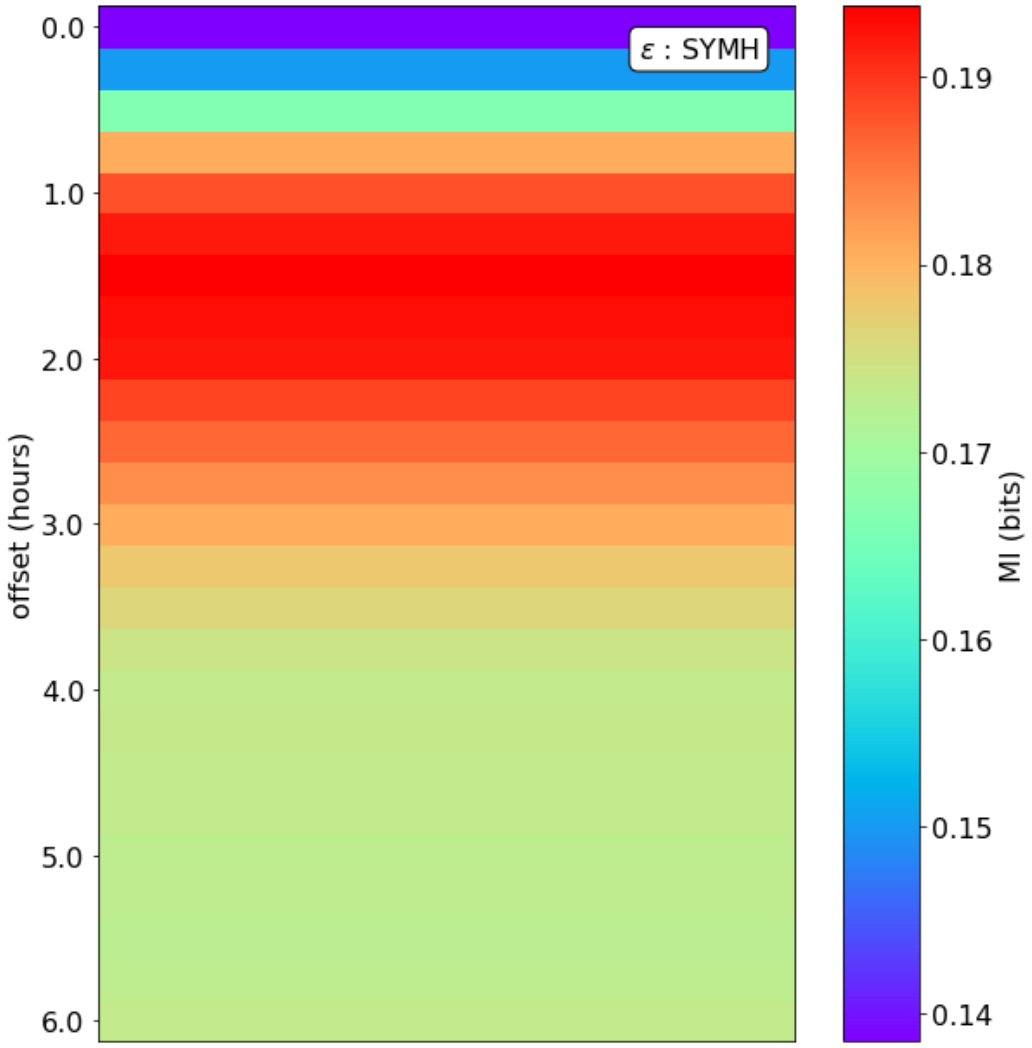

Figure D.4: Mutual information results for ϵ, when compared to the geomagnetic index, SYM/H. The y-axis represents the time offset, in hours, between ϵ and the SYM/H index data set's timestamps, as described in section 6.4.

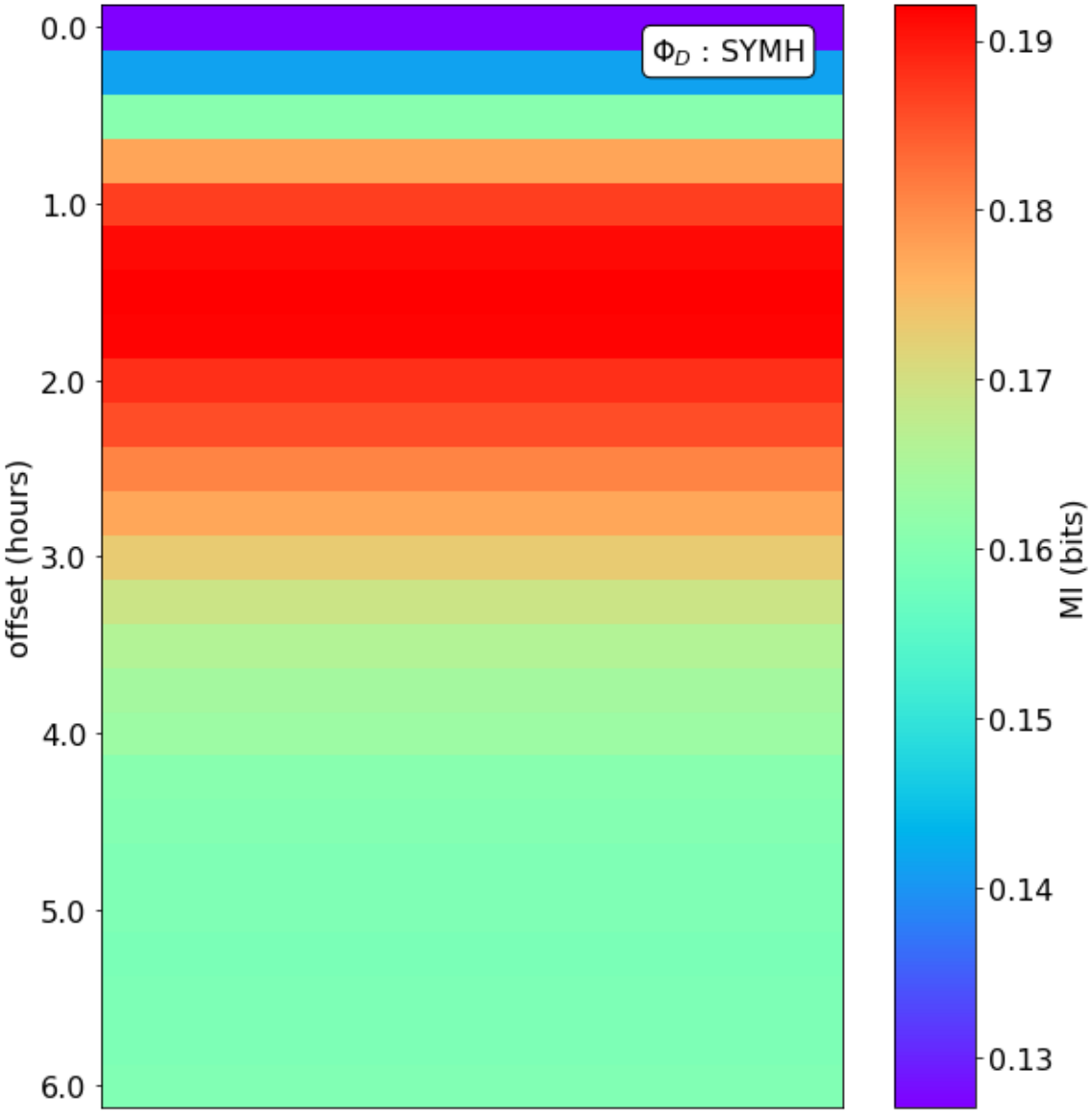

Figure D.5: As Figure D.4 for Φ_D

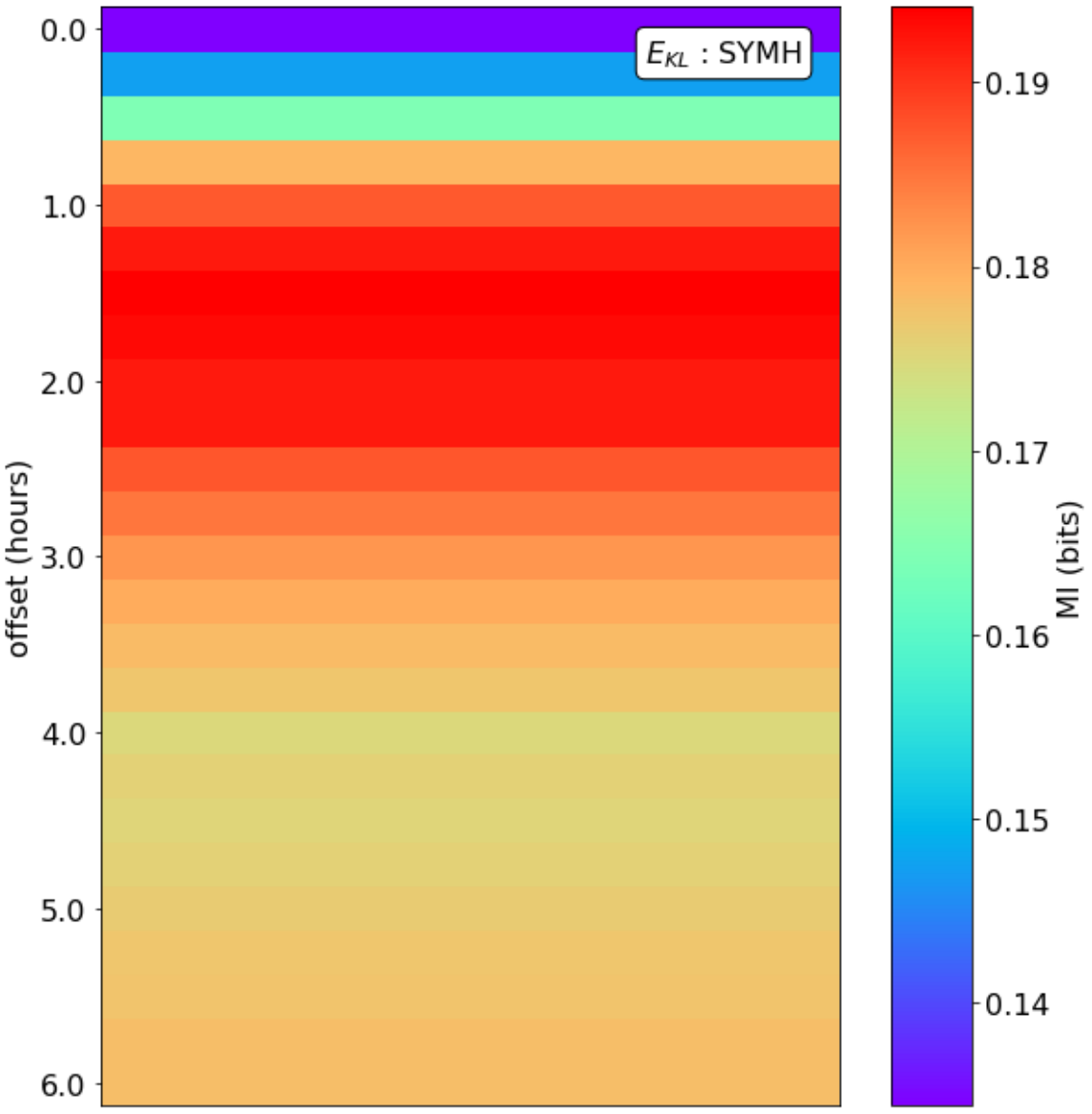

Figure D.6: As Figure D.4 for E_{KL}

Appendix E

Saturn Kilometric Radiation and the Solar Wind

E.1 SKR Results

	B_y		ρ		p_{dyn}	
Time (Hours)	MI	±	MI	±	MI	±
-72	0.1461	0.0054	0.045	0.0046	0.0356	0.0037
-69	0.0885	0.0014	0.0498	0.0037	0.0345	0.0027
-66	0.0888	0.0013	0.0432	0.0024	0.0375	0.0029
-63	0.0929	0.0015	0.0422	0.0034	0.0375	0.0032
-60	0.1264	0.0032	0.0495	0.0032	0.0358	0.0023
-57	0.1441	0.0061	0.057	0.0044	0.0424	0.0032
-54	0.1224	0.0028	0.0626	0.0045	0.0331	0.0031
-51	0.1356	0.0036	0.056	0.005	0.0367	0.0022
-48	0.1221	0.0026	0.0495	0.0047	0.0364	0.0023
-45	0.1355	0.0037	0.0454	0.0046	0.0325	0.0047
-42	0.1386	0.0041	0.0513	0.0035	0.0436	0.0047
-39	0.119	0.0024	0.0609	0.0046	0.0313	0.0033
-36	0.1399	0.0057	0.0564	0.0052	0.0319	0.0034
-33	0.1048	0.0019	0.0564	0.005	0.0352	0.0047
-30	0.1289	0.003	0.0583	0.0048	0.0387	0.0029
-27	0.1448	0.006	0.0464	0.0045	0.0374	0.0031
-24	0.1494	0.0056	0.0489	0.0045	0.0368	0.0029
-21	0.0969	0.0015	0.046	0.0024	0.0328	0.0036
-18	0.1193	0.0025	0.0539	0.0049	0.0367	0.0034
-15	0.1284	0.0032	0.0502	0.0033	0.0385	0.0028
-12	0.1131	0.0024	0.0527	0.0025	0.0407	0.0022
-9	0.1483	0.0053	0.0458	0.0048	0.0447	0.0031
-6	0.131	0.0031	0.0467	0.0048	0.0411	0.0033
-3	0.1326	0.004	0.0491	0.0028	0.0364	0.0034
0	0.1328	0.0039	0.0456	0.0035	0.0387	0.0025
3	0.1229	0.0029	0.0501	0.0028	0.0332	0.0019

6	0.1288	0.0031	0.0529	0.0037	0.0383	0.0029
9	0.1292	0.0031	0.0567	0.005	0.0357	0.0047
12	0.1273	0.0032	0.0583	0.0048	0.0339	0.0026
15	0.1218	0.0028	0.0537	0.0046	0.0404	0.0028
18	0.1122	0.002	0.0557	0.0052	0.0393	0.0024
21	0.1446	0.005	0.0467	0.0048	0.0373	0.0029
24	0.1227	0.0028	0.0599	0.0046	0.0349	0.0025
27	0.1122	0.002	0.0512	0.0033	0.0382	0.0026
30	0.1523	0.0056	0.0489	0.0032	0.0366	0.0029
33	0.1234	0.003	0.0511	0.0047	0.0408	0.0025
36	0.1176	0.0024	0.0529	0.0051	0.0385	0.0023
39	0.1329	0.0036	0.0584	0.0048	0.0378	0.0033
42	0.1502	0.006	0.047	0.0046	0.0343	0.0033
45	0.1229	0.0024	0.0584	0.005	0.0416	0.0036
48	0.092	0.0013	0.0494	0.005	0.0381	0.0027
51	0.1482	0.0057	0.0532	0.0049	0.0413	0.0047
54	0.1057	0.0019	0.0525	0.0026	0.0403	0.0046
57	0.1203	0.0024	0.0487	0.0026	0.0415	0.0029
60	0.0967	0.0014	0.0482	0.0024	0.0384	0.0026
63	0.0972	0.0015	0.0666	0.0049	0.0408	0.0025
66	0.1286	0.0031	0.0484	0.0029	0.0369	0.0025
69	0.1308	0.004	0.0529	0.0046	0.0346	0.003
72	0.1288	0.0032	0.0473	0.0031	0.0403	0.0027

Table E.1: MI information results for SKR, LH 10 - 1,000 kHz and propagated solar wind parameters B_y, ρ, and p_{dyn}.

	v_x		v_y		T	
Time (Hours)	MI	±	MI	±	MI	±
-72	0.1089	0.0037	0.0764	0.005	0.0509	0.0011
-69	0.108	0.0055	0.0769	0.005	0.0819	0.0026
-66	0.1077	0.0049	0.0775	0.0052	0.0733	0.0023
-63	0.1077	0.0055	0.0638	0.0021	0.0511	0.001
-60	0.1012	0.003	0.0696	0.0028	0.0511	0.0011
-57	0.0974	0.0027	0.0703	0.0027	0.0553	0.0013
-54	0.1085	0.0053	0.0711	0.0034	0.0553	0.0012
-51	0.1018	0.0027	0.0793	0.005	0.0957	0.0051
-48	0.1093	0.0059	0.0811	0.0054	0.0508	0.0011
-45	0.0974	0.0021	0.0798	0.0052	0.0506	0.001
-42	0.0986	0.0025	0.0704	0.0028	0.0554	0.0012
-39	0.1105	0.0036	0.0701	0.0032	0.0947	0.005
-36	0.1036	0.003	0.0643	0.0022	0.062	0.0016
-33	0.1119	0.0053	0.0796	0.0047	0.0508	0.0011
-30	0.1042	0.0029	0.0701	0.0038	0.0509	0.0011
-27	0.111	0.0054	0.0594	0.0018	0.051	0.0011
-24	0.0993	0.0024	0.0635	0.0022	0.0622	0.0015
-21	0.1108	0.0059	0.0589	0.002	0.0687	0.0018
-18	0.1107	0.0056	0.0711	0.0034	0.0887	0.0032
-15	0.1113	0.0057	0.0684	0.0024	0.0518	0.001
-12	0.1112	0.005	0.0826	0.0053	0.0826	0.0028
-9	0.0793	0.0014	0.0706	0.0028	0.0517	0.001
-6	0.1114	0.0058	0.072	0.0035	0.0517	0.0011
-3	0.1101	0.0038	0.084	0.0053	0.0517	0.0011
0	0.1099	0.0037	0.0714	0.0034	0.0517	0.0011
3	0.1129	0.0053	0.0844	0.0053	0.0519	0.001

6	0.1038	0.0034	0.0836	0.0052	0.052	0.0011
9	0.0776	0.0014	0.0826	0.0047	0.0519	0.0011
12	0.1114	0.0056	0.0701	0.0032	0.0521	0.0011
15	0.1046	0.003	0.0843	0.0048	0.0561	0.0013
18	0.1098	0.0055	0.0872	0.0055	0.0521	0.0011
21	0.1039	0.003	0.0681	0.0025	0.0558	0.0012
24	0.1102	0.0051	0.085	0.0053	0.052	0.0011
27	0.11	0.0053	0.0679	0.0026	0.0564	0.0013
30	0.1108	0.0059	0.0709	0.0035	0.0565	0.0011
33	0.1114	0.006	0.0645	0.0021	0.0523	0.0009
36	0.1108	0.0057	0.0651	0.0022	0.0524	0.001
39	0.1039	0.003	0.0858	0.0052	0.0527	0.001
42	0.0988	0.0026	0.0699	0.0023	0.0526	0.0012
45	0.1043	0.0032	0.0722	0.0028	0.0525	0.001
48	0.1119	0.0056	0.0838	0.0051	0.057	0.0012
51	0.099	0.0026	0.0718	0.0034	0.057	0.0012
54	0.0965	0.0025	0.0543	0.0016	0.093	0.0053
57	0.0983	0.0025	0.0713	0.0026	0.0562	0.0013
60	0.0976	0.0025	0.0851	0.0054	0.0857	0.0035
63	0.1029	0.0031	0.0656	0.002	0.0666	0.0019
66	0.1026	0.003	0.0729	0.0029	0.0524	0.0011
69	0.1073	0.0036	0.066	0.002	0.0563	0.0014
72	0.1104	0.0053	0.0728	0.0033	0.0519	0.0011

Table E.2: MI information results for SKR, LH 10 - 1,000 kHz and propagated solar wind parameters v_x, v_y, and T.

	B_y		ρ		p_{dyn}	
Time (Hours)	MI	±	MI	±	MI	±
-72	0.1118	0.0058	0.0302	0.0034	0.03	0.0021
-69	0.0885	0.0027	0.0322	0.0031	0.0318	0.0025
-66	0.1072	0.0054	0.0337	0.0023	0.0318	0.0027
-63	0.1042	0.0061	0.0287	0.0046	0.0352	0.0036
-60	0.103	0.0064	0.0339	0.0026	0.0319	0.0024
-57	0.0835	0.0023	0.0318	0.0021	0.0308	0.0029
-54	0.0875	0.0026	0.0323	0.0024	0.0327	0.0028
-51	0.1115	0.0061	0.0373	0.0038	0.0296	0.0026
-48	0.1073	0.0059	0.0313	0.0035	0.0315	0.0024
-45	0.1027	0.0062	0.0354	0.0034	0.0289	0.0029
-42	0.0989	0.0065	0.0395	0.0049	0.0343	0.0022
-39	0.0947	0.004	0.0337	0.0021	0.0347	0.0025
-36	0.0965	0.004	0.0258	0.0051	0.0278	0.0025
-33	0.0714	0.0015	0.0336	0.0029	0.0337	0.0022
-30	0.0995	0.0043	0.0315	0.0023	0.0298	0.003
-27	0.1135	0.0057	0.0404	0.004	0.0335	0.0028
-24	0.1124	0.0063	0.0313	0.0025	0.041	0.0049
-21	0.0914	0.003	0.0355	0.0031	0.0318	0.0023
-18	0.1089	0.0061	0.0344	0.0027	0.0333	0.0025
-15	0.106	0.006	0.0312	0.0023	0.0293	0.0025
-12	0.114	0.0067	0.0315	0.0029	0.0317	0.0015
-9	0.0802	0.0019	0.027	0.0026	0.0354	0.0037
-6	0.0955	0.0037	0.033	0.0027	0.0372	0.0029
-3	0.1046	0.0063	0.0335	0.0026	0.0347	0.0031
0	0.0958	0.0043	0.0331	0.0035	0.0315	0.0031
3	0.0972	0.0044	0.0352	0.005	0.0261	0.0032

6	0.1007	0.0061	0.0368	0.0037	0.0288	0.0025
9	0.103	0.0063	0.0305	0.0019	0.0342	0.0045
12	0.0744	0.0013	0.0377	0.0026	0.0332	0.0025
15	0.1095	0.0061	0.0348	0.0037	0.0315	0.0029
18	0.096	0.0035	0.0387	0.0035	0.035	0.0023
21	0.0989	0.0044	0.0366	0.0032	0.0343	0.0022
24	0.0983	0.0043	0.0341	0.0022	0.0367	0.0028
27	0.1139	0.006	0.0359	0.0026	0.0387	0.0039
30	0.1024	0.0067	0.0362	0.003	0.0314	0.0032
33	0.1	0.0059	0.0336	0.0027	0.0371	0.0031
36	0.1103	0.0059	0.0415	0.0046	0.0339	0.0023
39	0.0976	0.0046	0.0317	0.0022	0.0334	0.0018
42	0.1063	0.0062	0.034	0.0027	0.035	0.0039
45	0.1031	0.0064	0.038	0.0048	0.0372	0.0024
48	0.0965	0.0034	0.0351	0.0022	0.0323	0.0021
51	0.106	0.0061	0.0334	0.0036	0.0317	0.0024
54	0.109	0.006	0.0327	0.0027	0.0326	0.0029
57	0.0986	0.0044	0.0386	0.0024	0.0353	0.0026
60	0.1047	0.0059	0.0426	0.0049	0.0318	0.0051
63	0.1011	0.0057	0.0293	0.0022	0.0315	0.0026
66	0.1062	0.0063	0.0353	0.002	0.0381	0.0048
69	0.1008	0.0062	0.0348	0.003	0.0373	0.0037
72	0.102	0.0063	0.0339	0.0025	0.0321	0.0026

Table E.3: MI information results for SKR, LH 100 - 400 kHz and propagated solar wind parameters B_y, ρ, and p_{dyn}.

	v_x		v_y		T	
Time (Hours)	MI	±	MI	±	MI	
-72	0.0937	0.006	0.0471	0.0029	0.0588	0.0037
-69	0.095	0.0062	0.0475	0.003	0.0686	0.0049
-66	0.0796	0.0041	0.05	0.0039	0.0301	0.0011
-63	0.0924	0.0054	0.0471	0.003	0.0302	0.0012
-60	0.0921	0.0065	0.05	0.0035	0.0302	0.001
-57	0.0802	0.0045	0.0516	0.0036	0.0481	0.0022
-54	0.0795	0.0032	0.0367	0.0019	0.0341	0.0012
-51	0.0915	0.0058	0.0473	0.0026	0.0664	0.0055
-48	0.0796	0.0041	0.0485	0.0029	0.0484	0.0021
-45	0.08	0.0041	0.0391	0.0025	0.0664	0.0058
-42	0.0942	0.0056	0.0389	0.0023	0.0445	0.0017
-39	0.0925	0.0063	0.0475	0.0032	0.0536	0.003
-36	0.0928	0.0057	0.0556	0.0057	0.0586	0.0035
-33	0.08	0.0042	0.0504	0.0036	0.0674	0.0051
-30	0.0803	0.0038	0.0431	0.0027	0.0591	0.0037
-27	0.0947	0.0059	0.047	0.0029	0.059	0.0041
-24	0.0793	0.0039	0.0393	0.0025	0.0304	0.0012
-21	0.0944	0.006	0.0475	0.003	0.0679	0.0053
-18	0.0777	0.0029	0.0367	0.002	0.0489	0.0022
-15	0.0794	0.0034	0.0509	0.0034	0.0582	0.0035
-12	0.0801	0.0039	0.0507	0.0034	0.0544	0.0029
-9	0.0809	0.0041	0.0508	0.0036	0.0384	0.0016
-6	0.0953	0.0064	0.0494	0.0034	0.0434	0.0017
-3	0.0946	0.0056	0.0458	0.003	0.0331	0.0013
0	0.0807	0.0036	0.0453	0.0028	0.043	0.0019
3	0.0949	0.0056	0.0577	0.0054	0.0304	0.0011

6	0.0949	0.0057	0.0504	0.0036	0.0308	0.0012
9	0.0951	0.0059	0.047	0.0027	0.0305	0.0011
12	0.0972	0.0059	0.0498	0.0035	0.0429	0.0018
15	0.0963	0.0063	0.0504	0.0038	0.0576	0.0035
18	0.0962	0.0056	0.0453	0.0031	0.0701	0.0053
21	0.0821	0.0034	0.0485	0.0033	0.0581	0.0035
24	0.0962	0.0064	0.0444	0.0033	0.053	0.0029
27	0.0752	0.0027	0.0446	0.0029	0.0297	0.0011
30	0.0826	0.0039	0.038	0.0023	0.0562	0.0034
33	0.0953	0.0064	0.0477	0.0037	0.0697	0.0056
36	0.0951	0.0059	0.0585	0.0058	0.0573	0.0034
39	0.0959	0.0057	0.0437	0.0029	0.0536	0.0028
42	0.0955	0.0056	0.0426	0.0031	0.0295	0.0011
45	0.096	0.0061	0.047	0.0036	0.0503	0.0023
48	0.0825	0.004	0.0432	0.003	0.0675	0.0051
51	0.0827	0.0042	0.0376	0.0023	0.0501	0.0026
54	0.0951	0.0056	0.0448	0.003	0.0696	0.0049
57	0.0663	0.0018	0.0495	0.0036	0.0667	0.005
60	0.0808	0.0032	0.0374	0.0025	0.0587	0.0033
63	0.0808	0.0034	0.0518	0.0035	0.0698	0.0056
66	0.0802	0.0033	0.0519	0.0037	0.0432	0.0019
69	0.081	0.004	0.0456	0.0032	0.0428	0.0019
72	0.0814	0.0041	0.0587	0.0051	0.0551	0.0031

Table E.4: MI information results for SKR, LH 100 - 400 kHz and propagated solar wind parameters v_x, v_y, and T.

	B_y		ρ		p_{dyn}	
Time (Hours)	MI	±	MI	±	MI	
-72	0.0799	0.0017	0.0516	0.0047	0.0314	0.003
-69	0.0674	0.0012	0.0583	0.0049	0.037	0.0026
-66	0.0988	0.0027	0.0491	0.0026	0.0338	0.0024
-63	0.0675	0.0011	0.053	0.0042	0.0329	0.0015
-60	0.0717	0.0014	0.0445	0.003	0.0315	0.0017
-57	0.0668	0.0012	0.0427	0.0045	0.0324	0.0032
-54	0.1041	0.0036	0.0449	0.0026	0.0319	0.0021
-51	0.0666	0.0011	0.0478	0.0046	0.0302	0.0022
-48	0.1116	0.0049	0.0461	0.0031	0.0309	0.0022
-45	0.0975	0.0029	0.0438	0.0032	0.0343	0.003
-42	0.067	0.0011	0.0444	0.0024	0.0329	0.0021
-39	0.1054	0.0047	0.0477	0.0025	0.0261	0.0025
-36	0.0667	0.0012	0.0517	0.0045	0.0325	0.0025
-33	0.1081	0.0049	0.0549	0.0049	0.032	0.002
-30	0.0667	0.0012	0.0462	0.0032	0.0392	0.0031
-27	0.0956	0.0026	0.057	0.0046	0.0342	0.0023
-24	0.0783	0.0017	0.0486	0.0027	0.03	0.0022
-21	0.0924	0.0026	0.0523	0.0047	0.0303	0.0021
-18	0.0664	0.0012	0.0443	0.0023	0.0389	0.0026
-15	0.1026	0.0032	0.0532	0.0051	0.0311	0.0021
-12	0.0662	0.0011	0.0464	0.0038	0.0333	0.0024
-9	0.094	0.0031	0.0522	0.0045	0.031	0.0026
-6	0.0657	0.0012	0.0545	0.0028	0.0319	0.0021
-3	0.0773	0.0016	0.0515	0.0043	0.0323	0.003
0	0.0652	0.0012	0.0465	0.0026	0.0298	0.0021
3	0.0694	0.0013	0.0628	0.004	0.032	0.0025

6	0.0659	0.0012	0.0454	0.0033	0.0264	0.0024
9	0.0831	0.0018	0.0414	0.0026	0.0331	0.0031
12	0.0949	0.0026	0.0496	0.0042	0.0303	0.0018
15	0.1026	0.0036	0.0453	0.0026	0.0325	0.0024
18	0.0645	0.0012	0.0524	0.0045	0.031	0.0044
21	0.0959	0.003	0.0452	0.0047	0.0335	0.003
24	0.0998	0.0036	0.049	0.0044	0.0365	0.0031
27	0.0769	0.0017	0.0463	0.0045	0.0336	0.0024
30	0.0774	0.0017	0.0438	0.0034	0.0263	0.003
33	0.1141	0.005	0.0466	0.0045	0.0297	0.002
36	0.0656	0.0012	0.0442	0.0024	0.029	0.002
39	0.0659	0.0012	0.0433	0.0031	0.0312	0.0026
42	0.0656	0.0012	0.0426	0.0027	0.0304	0.0031
45	0.0954	0.0031	0.0431	0.0027	0.0344	0.003
48	0.1032	0.0054	0.0459	0.0031	0.0267	0.0025
51	0.0663	0.0013	0.0495	0.0044	0.0259	0.0019
54	0.1031	0.0032	0.0394	0.0032	0.0322	0.0022
57	0.0712	0.0013	0.0427	0.002	0.0282	0.0029
60	0.1064	0.0052	0.0472	0.0049	0.0323	0.0031
63	0.1093	0.005	0.0415	0.0051	0.0287	0.0032
66	0.1053	0.0053	0.0498	0.0043	0.0332	0.0024
69	0.0719	0.0014	0.045	0.0044	0.0321	0.0024
72	0.0672	0.0012	0.0427	0.0031	0.0297	0.003

Table E.5: MI information results for SKR, RH 10 - 1,000 kHz and propagated solar wind parameters B_y, ρ, and p_{dyn}.

	v_x		v_y		T	
Time (Hours)	MI	±	MI	±	MI	
-72	0.0439	0.001	0.0382	0.001	0.0452	0.001
-69	0.0713	0.0032	0.0348	0.001	0.0628	0.002
-66	0.0468	0.0013	0.0346	0.0009	0.0671	0.0026
-63	0.0706	0.0032	0.0349	0.0009	0.0663	0.0028
-60	0.0699	0.0054	0.0349	0.0009	0.0476	0.0012
-57	0.0465	0.0013	0.0494	0.002	0.0445	0.0011
-54	0.052	0.0015	0.0491	0.0022	0.0444	0.0011
-51	0.0709	0.0034	0.035	0.001	0.0771	0.0051
-48	0.0655	0.0024	0.0386	0.0011	0.0641	0.0022
-45	0.0701	0.0049	0.0755	0.0044	0.0723	0.003
-42	0.0699	0.0053	0.0723	0.0044	0.0713	0.0035
-39	0.0691	0.0045	0.0386	0.0011	0.0652	0.0021
-36	0.052	0.0014	0.0348	0.001	0.0723	0.0035
-33	0.0699	0.0045	0.038	0.001	0.0727	0.0032
-30	0.0694	0.0046	0.0494	0.0022	0.0647	0.0023
-27	0.0679	0.0027	0.0574	0.003	0.0447	0.001
-24	0.0672	0.0027	0.0381	0.0012	0.0803	0.0047
-21	0.0518	0.0014	0.0379	0.0011	0.0801	0.0047
-18	0.0692	0.0046	0.0348	0.0009	0.065	0.0022
-15	0.0696	0.0033	0.0379	0.0011	0.062	0.002
-12	0.0612	0.0021	0.0344	0.0009	0.073	0.0032
-9	0.0607	0.0021	0.0342	0.001	0.0474	0.0013
-6	0.0691	0.0049	0.0346	0.0011	0.0733	0.0032
-3	0.0682	0.0049	0.0724	0.0046	0.0797	0.0052
0	0.0426	0.001	0.0703	0.0041	0.074	0.0034
3	0.0685	0.0047	0.0383	0.0011	0.0627	0.002

6	0.0674	0.003	0.0559	0.0031	0.0815	0.0046
9	0.0626	0.0022	0.0384	0.0011	0.0745	0.0032
12	0.0559	0.0018	0.0347	0.001	0.0479	0.0011
15	0.0429	0.0011	0.0415	0.0014	0.0665	0.0025
18	0.0627	0.0022	0.0491	0.0021	0.0455	0.0011
21	0.0514	0.0015	0.0709	0.0045	0.0457	0.001
24	0.0626	0.0023	0.0379	0.001	0.074	0.0032
27	0.0683	0.0044	0.0566	0.0028	0.0747	0.0035
30	0.0669	0.003	0.0348	0.001	0.0466	0.0012
33	0.0668	0.0035	0.0351	0.001	0.0829	0.0054
36	0.0502	0.0014	0.0586	0.0033	0.0845	0.005
39	0.0674	0.0054	0.0354	0.0009	0.0463	0.0011
42	0.0646	0.0027	0.0748	0.0045	0.084	0.0051
45	0.0546	0.0018	0.0387	0.0011	0.0465	0.0011
48	0.0418	0.0011	0.0707	0.0051	0.0833	0.0052
51	0.062	0.0023	0.0586	0.003	0.0492	0.0013
54	0.0649	0.0026	0.0726	0.0045	0.0826	0.005
57	0.0553	0.0018	0.0354	0.0009	0.0715	0.0033
60	0.0663	0.0046	0.0578	0.003	0.083	0.0052
63	0.0665	0.0046	0.0352	0.0009	0.0673	0.0026
66	0.067	0.0044	0.0735	0.0044	0.0818	0.0049
69	0.0678	0.0049	0.0593	0.0031	0.0501	0.0013
72	0.043	0.001	0.0588	0.0033	0.0739	0.0032

Table E.6: MI information results for SKR, RH 10 - 1,000 kHz and propagated solar wind parameters v_x, v_y, and T.

	B_y		ρ		p_{dyn}	
Time (Hours)	MI	±	MI	±	MI	
-72	0.0679	0.0034	0.0312	0.0025	0.0239	0.0016
-69	0.069	0.0034	0.0308	0.0021	0.0193	0.0028
-66	0.0652	0.0028	0.0345	0.0027	0.0247	0.002
-63	0.0779	0.0055	0.0298	0.0021	0.0255	0.0018
-60	0.0727	0.0048	0.0293	0.0022	0.0222	0.0016
-57	0.0686	0.0035	0.0327	0.0022	0.0276	0.0032
-54	0.0775	0.005	0.0313	0.0021	0.0237	0.0021
-51	0.0732	0.005	0.0314	0.0018	0.0241	0.0018
-48	0.0599	0.0024	0.0294	0.0033	0.0213	0.0024
-45	0.0741	0.0056	0.0295	0.0028	0.0242	0.0026
-42	0.0754	0.0053	0.0267	0.0016	0.0189	0.0023
-39	0.0659	0.0028	0.0312	0.0024	0.0244	0.0023
-36	0.0636	0.0037	0.032	0.0025	0.0248	0.0023
-33	0.0785	0.0049	0.0331	0.0047	0.0188	0.0031
-30	0.0729	0.0053	0.0373	0.0033	0.0238	0.0021
-27	0.0757	0.0052	0.0309	0.0023	0.022	0.002
-24	0.0762	0.0055	0.0323	0.0027	0.023	0.0021
-21	0.0529	0.002	0.0346	0.0029	0.0229	0.0028
-18	0.0568	0.0023	0.0292	0.0031	0.0244	0.0019
-15	0.0732	0.0055	0.0314	0.0027	0.0234	0.0027
-12	0.045	0.0013	0.0339	0.0025	0.0303	0.0027
-9	0.0748	0.005	0.0363	0.0034	0.0219	0.0026
-6	0.0441	0.0011	0.0301	0.0028	0.0188	0.0032
-3	0.0666	0.0035	0.0285	0.0044	0.0212	0.002
0	0.0723	0.0051	0.0308	0.0032	0.0269	0.0024
3	0.0435	0.0011	0.0402	0.0046	0.0226	0.0022

6	0.0527	0.0017	0.0255	0.0032	0.0222	0.0026
9	0.0452	0.0014	0.0256	0.0024	0.0244	0.0025
12	0.0526	0.0018	0.0326	0.0026	0.0255	0.0047
15	0.068	0.0038	0.0276	0.0018	0.0261	0.0017
18	0.0716	0.0049	0.0321	0.003	0.0204	0.0012
21	0.0664	0.0036	0.0267	0.002	0.0236	0.0046
24	0.0747	0.0054	0.0251	0.0024	0.02	0.0043
27	0.0488	0.0017	0.0295	0.0041	0.0196	0.0027
30	0.0759	0.0052	0.0287	0.0024	0.0257	0.0022
33	0.0832	0.0055	0.0303	0.003	0.0228	0.0022
36	0.0762	0.0052	0.0292	0.0026	0.0229	0.0024
39	0.0462	0.0014	0.0276	0.0019	0.0195	0.0022
42	0.067	0.0035	0.0265	0.0021	0.0234	0.002
45	0.0811	0.0054	0.0319	0.0025	0.0203	0.0022
48	0.0796	0.0052	0.0269	0.0026	0.0218	0.0014
51	0.075	0.0048	0.0289	0.0022	0.0222	0.0019
54	0.0655	0.0033	0.0283	0.0021	0.0196	0.0023
57	0.0802	0.0055	0.0292	0.0023	0.0133	0.0023
60	0.0808	0.0051	0.0293	0.0032	0.022	0.0023
63	0.0461	0.0014	0.0296	0.0033	0.021	0.002
66	0.0781	0.005	0.0292	0.0024	0.0217	0.0023
69	0.0836	0.005	0.0305	0.0032	0.0212	0.0022
72	0.0671	0.003	0.0317	0.0034	0.0247	0.0023

Table E.7: MI information results for SKR, RH 100 - 400 kHz and propagated solar wind parameters B_y, ρ, and p_{dyn}.

	v_x		v_y		T	
Time (Hours)	MI	±	MI	±	MI	
-72	0.0464	0.0023	0.0513	0.0044	0.0609	0.0047
-69	0.0462	0.0025	0.0357	0.0022	0.043	0.0022
-66	0.0445	0.0019	0.037	0.0022	0.0424	0.0024
-63	0.0507	0.0027	0.0522	0.0046	0.0485	0.0034
-60	0.0453	0.0021	0.0426	0.0031	0.0421	0.0022
-57	0.0543	0.0046	0.0524	0.0047	0.0487	0.0034
-54	0.0518	0.0032	0.0317	0.0016	0.0473	0.0031
-51	0.0556	0.0047	0.0412	0.0029	0.0604	0.0049
-48	0.0498	0.0026	0.0389	0.0023	0.0387	0.0023
-45	0.034	0.0012	0.0538	0.0051	0.0563	0.0045
-42	0.0452	0.0024	0.0406	0.003	0.0348	0.0017
-39	0.0517	0.0034	0.0384	0.0026	0.0477	0.003
-36	0.0569	0.0047	0.0505	0.0046	0.046	0.0024
-33	0.0512	0.0031	0.0521	0.0046	0.0347	0.0018
-30	0.0517	0.0035	0.0354	0.0021	0.047	0.0032
-27	0.0502	0.003	0.0373	0.0025	0.0479	0.0034
-24	0.051	0.0031	0.0543	0.0046	0.0386	0.0021
-21	0.0514	0.0032	0.0353	0.0021	0.0461	0.0026
-18	0.0494	0.0026	0.0421	0.0033	0.0605	0.0049
-15	0.0509	0.0034	0.0547	0.0043	0.0382	0.0023
-12	0.0544	0.0051	0.0357	0.0022	0.0621	0.0047
-9	0.0506	0.0032	0.0349	0.0023	0.0594	0.0048
-6	0.0496	0.0025	0.0551	0.0042	0.0489	0.0035
-3	0.0502	0.0032	0.0371	0.0027	0.0415	0.0022
0	0.0422	0.002	0.0248	0.0013	0.0619	0.0048
3	0.0491	0.0034	0.042	0.0031	0.0512	0.0035

6	0.0538	0.0051	0.0376	0.0025	0.0506	0.0036
9	0.0487	0.0029	0.0421	0.0026	0.0497	0.0031
12	0.0544	0.0053	0.0413	0.0032	0.0593	0.0049
15	0.0493	0.0031	0.0296	0.0017	0.0509	0.0033
18	0.0547	0.0048	0.0376	0.0024	0.0348	0.0017
21	0.0499	0.0031	0.0376	0.0024	0.0313	0.0012
24	0.0496	0.0026	0.0245	0.0014	0.0622	0.0045
27	0.0504	0.0033	0.0384	0.0025	0.0464	0.0025
30	0.0501	0.0038	0.0572	0.0048	0.0498	0.0031
33	0.0436	0.0021	0.0346	0.0018	0.0599	0.0043
36	0.0554	0.0046	0.0561	0.0049	0.0513	0.0035
39	0.0484	0.0033	0.0244	0.0013	0.0598	0.0051
42	0.0463	0.0023	0.0569	0.0046	0.0579	0.0044
45	0.0562	0.0053	0.0374	0.0023	0.058	0.0049
48	0.0318	0.001	0.056	0.0045	0.0585	0.0047
51	0.0479	0.0033	0.043	0.0031	0.0581	0.005
54	0.0547	0.0053	0.0347	0.002	0.0469	0.0027
57	0.054	0.0051	0.0556	0.0046	0.0413	0.0023
60	0.0473	0.0032	0.0384	0.0026	0.0352	0.0018
63	0.0473	0.0033	0.0283	0.0017	0.0584	0.0046
66	0.0472	0.0033	0.0381	0.0026	0.0587	0.0048
69	0.0476	0.0033	0.0338	0.0021	0.0593	0.005
72	0.0544	0.0045	0.043	0.0031	0.0498	0.0032

Table E.8: MI information results for SKR, RH 100 - 400 kHz and propagated solar wind parameters v_x, v_y, and T.

E.2 SKR Figures

E.2.1 LH 10 - 1,000 kHz

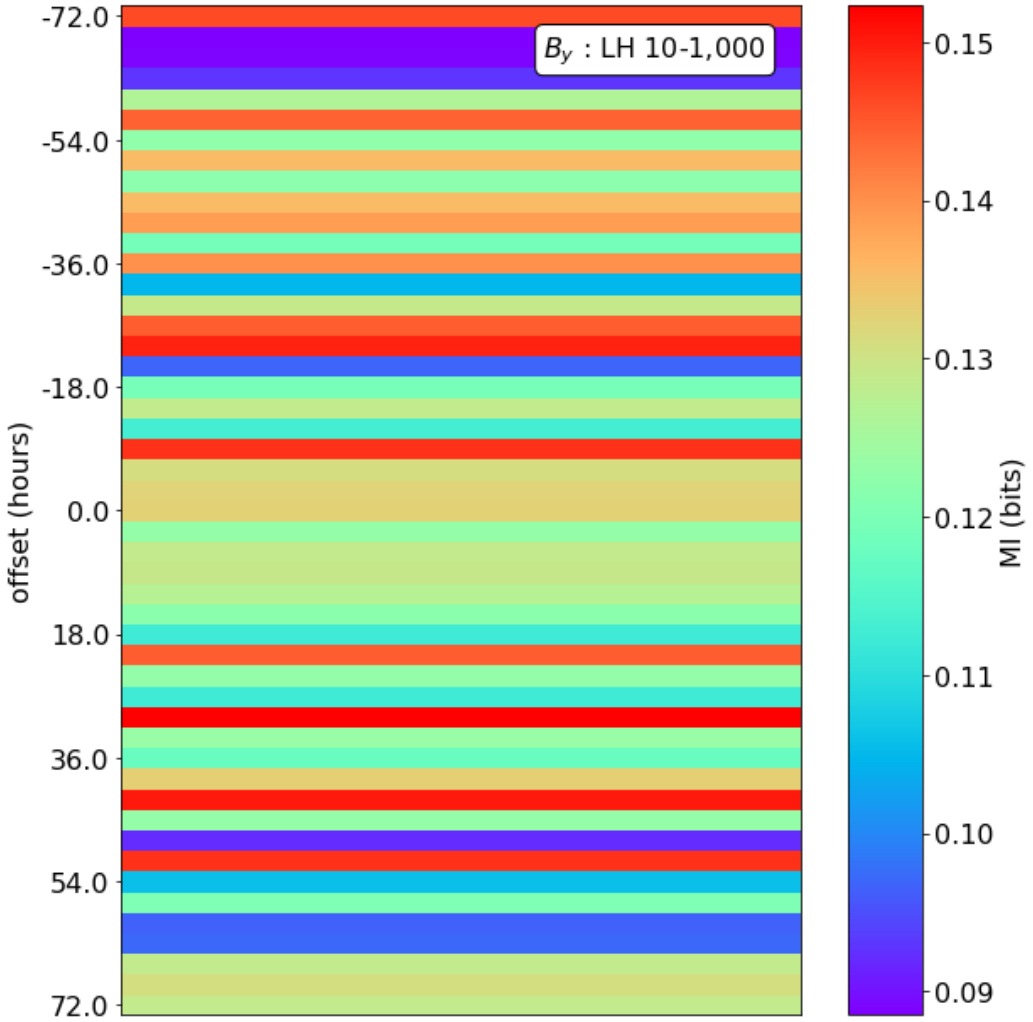

Figure E.1: Mutual information results for SKR, LH 10 - 1,000 kHz data when compared to propagated B_y of the solar wind. The y-axis represents the time offset, in hours, between the SKR and propagated solar wind variable data's timestamps, as described in section 6.4.

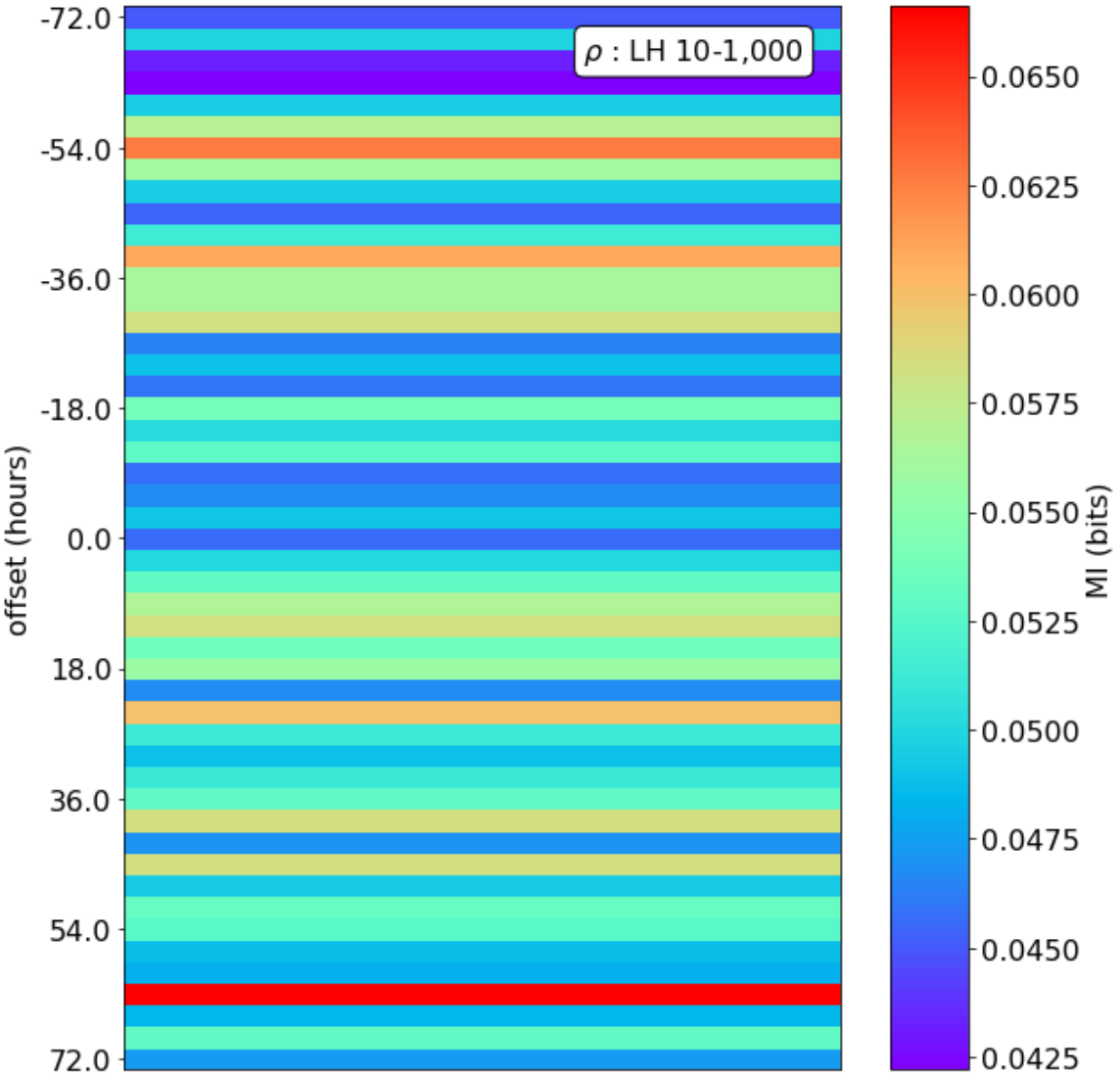

Figure E.2: As Figure E.1 for ρ

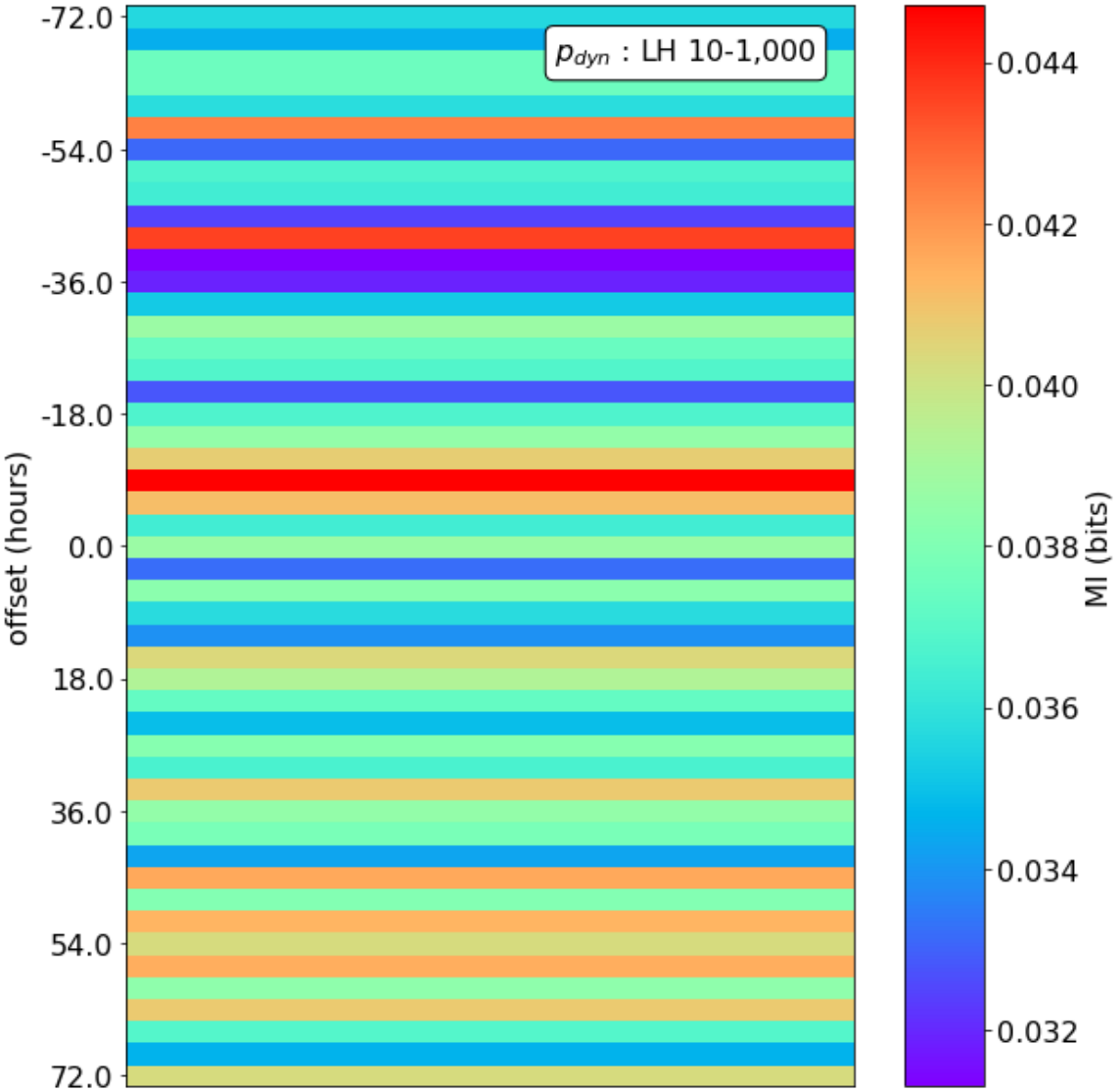

Figure E.3: As Figure E.1 for p_{dyn}

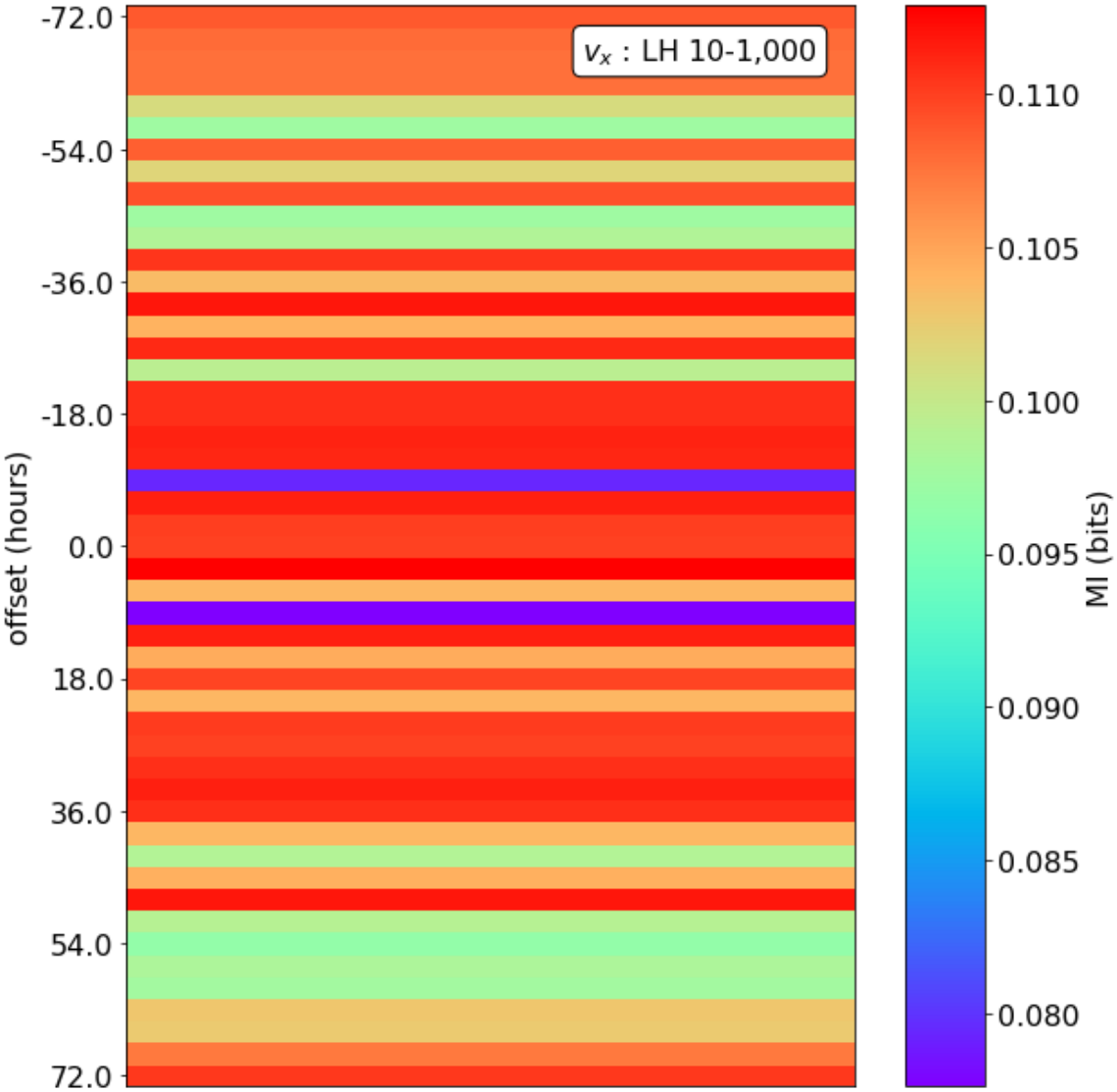

Figure E.4: As Figure E.1 for v_x

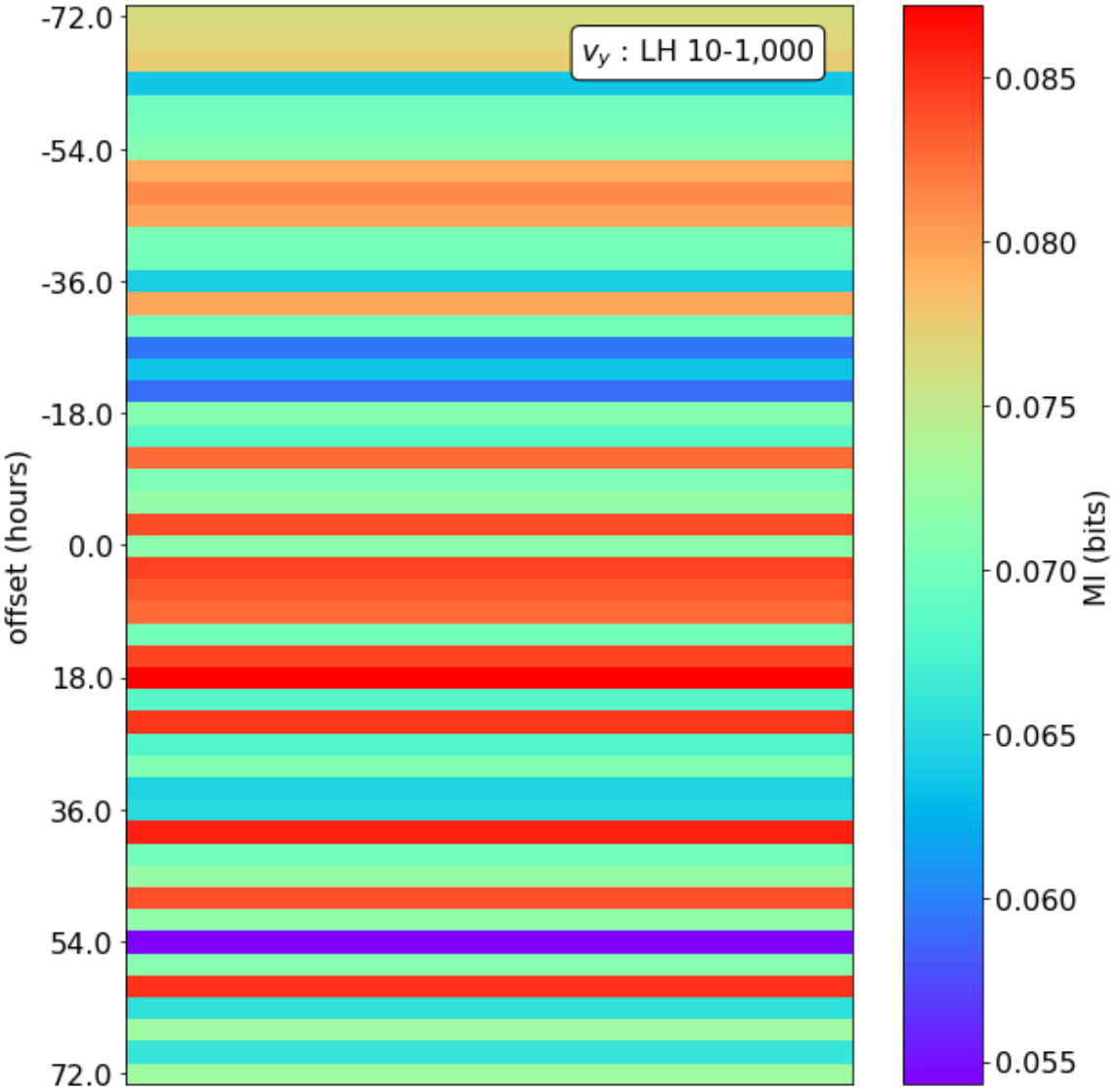

Figure E.5: As Figure E.1 for v_y

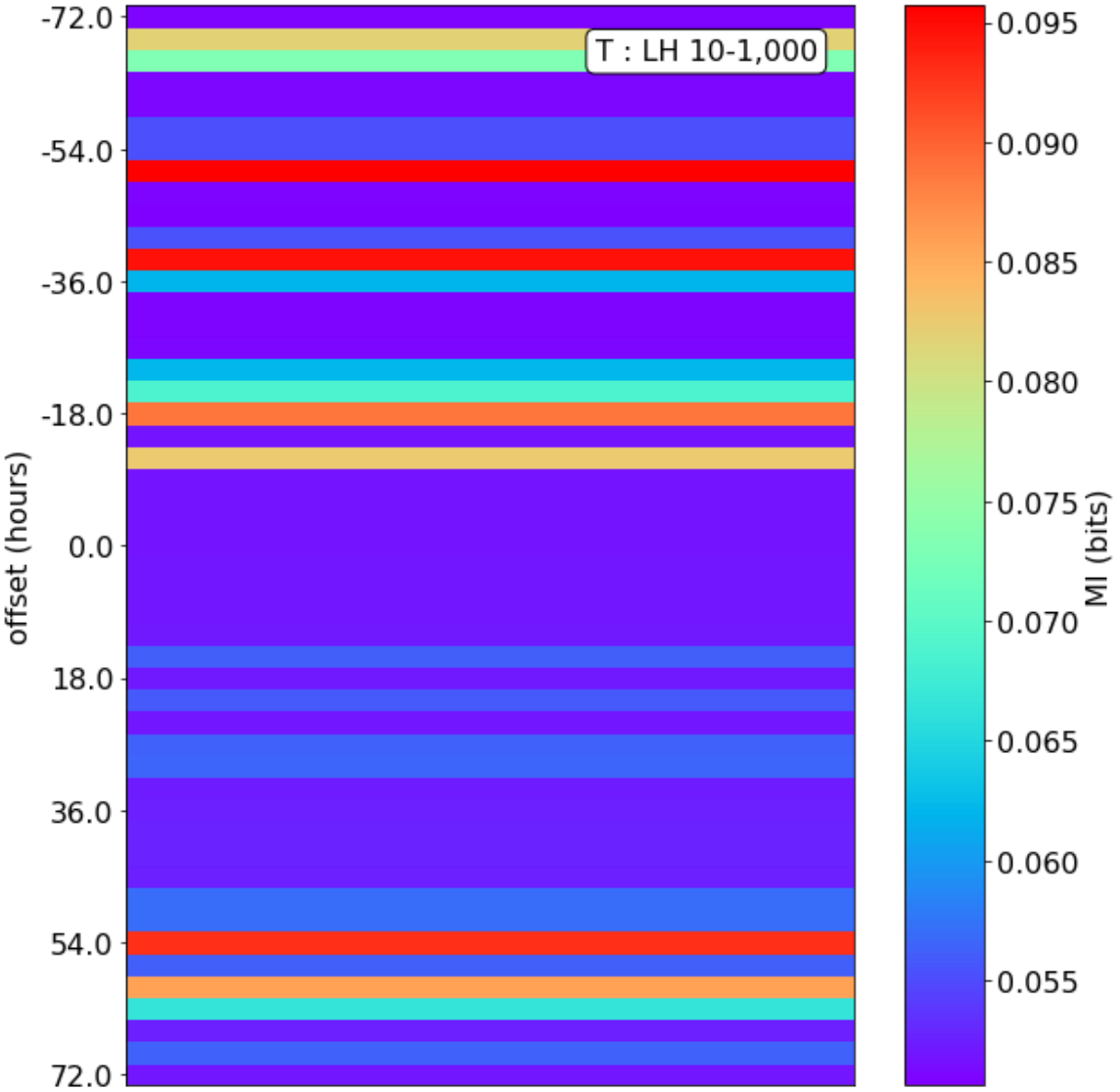

Figure E.6: As Figure E.1 for T

E.2.2 LH 100 - 400 kHz

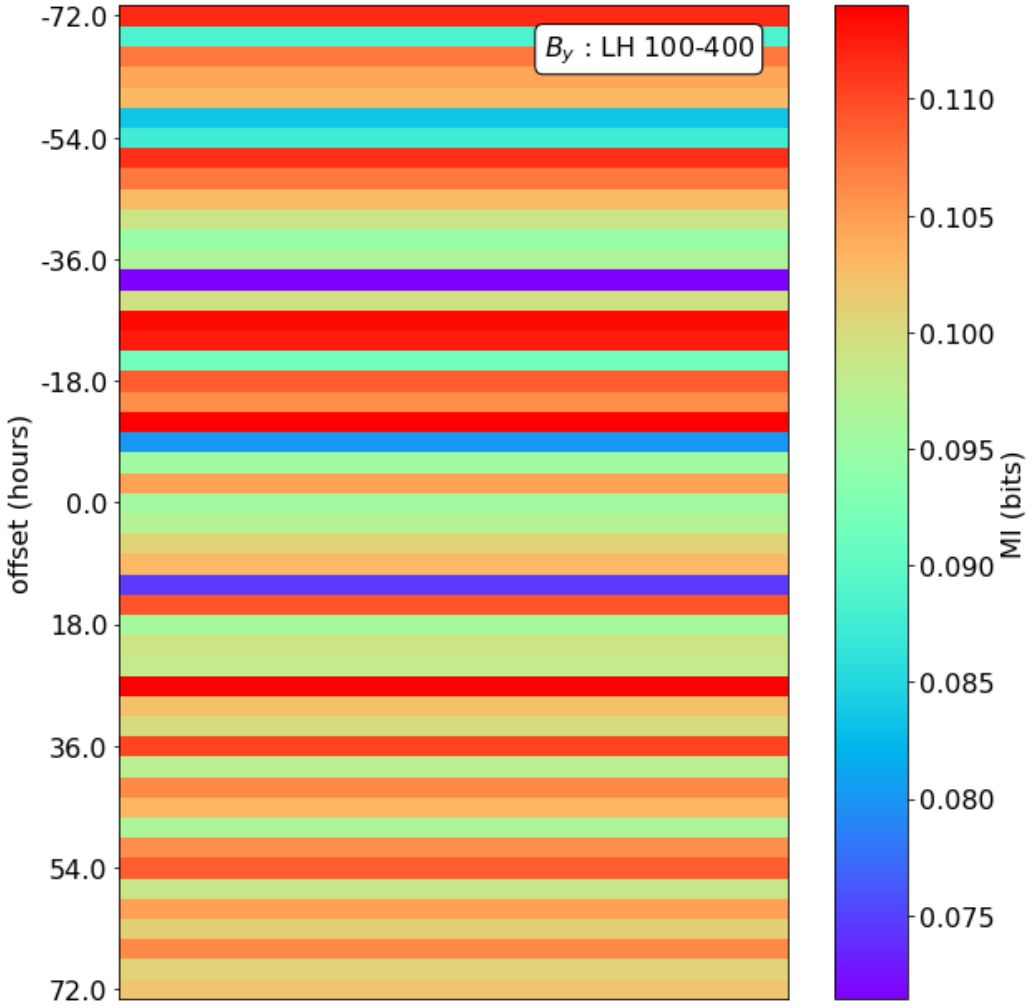

Figure E.7: Mutual information results for SKR, LH 100 - 400 kHz data when compared to propagated B_y of the solar wind. The y-axis represents the time offset, in hours, between the SKR and propagated solar wind variable data's timestamps, as described in section 6.4.

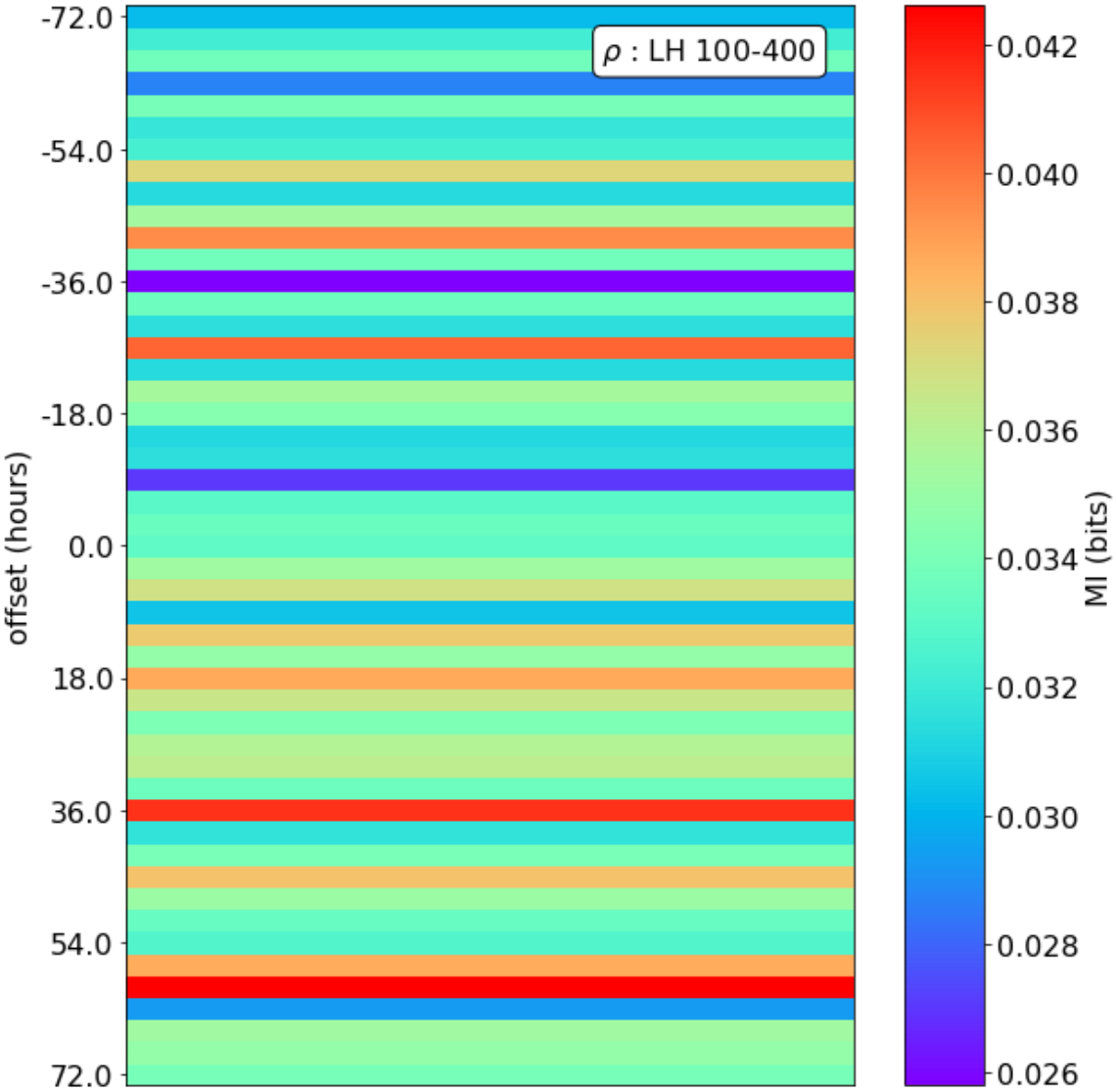

Figure E.8: As Figure E.7 for ρ

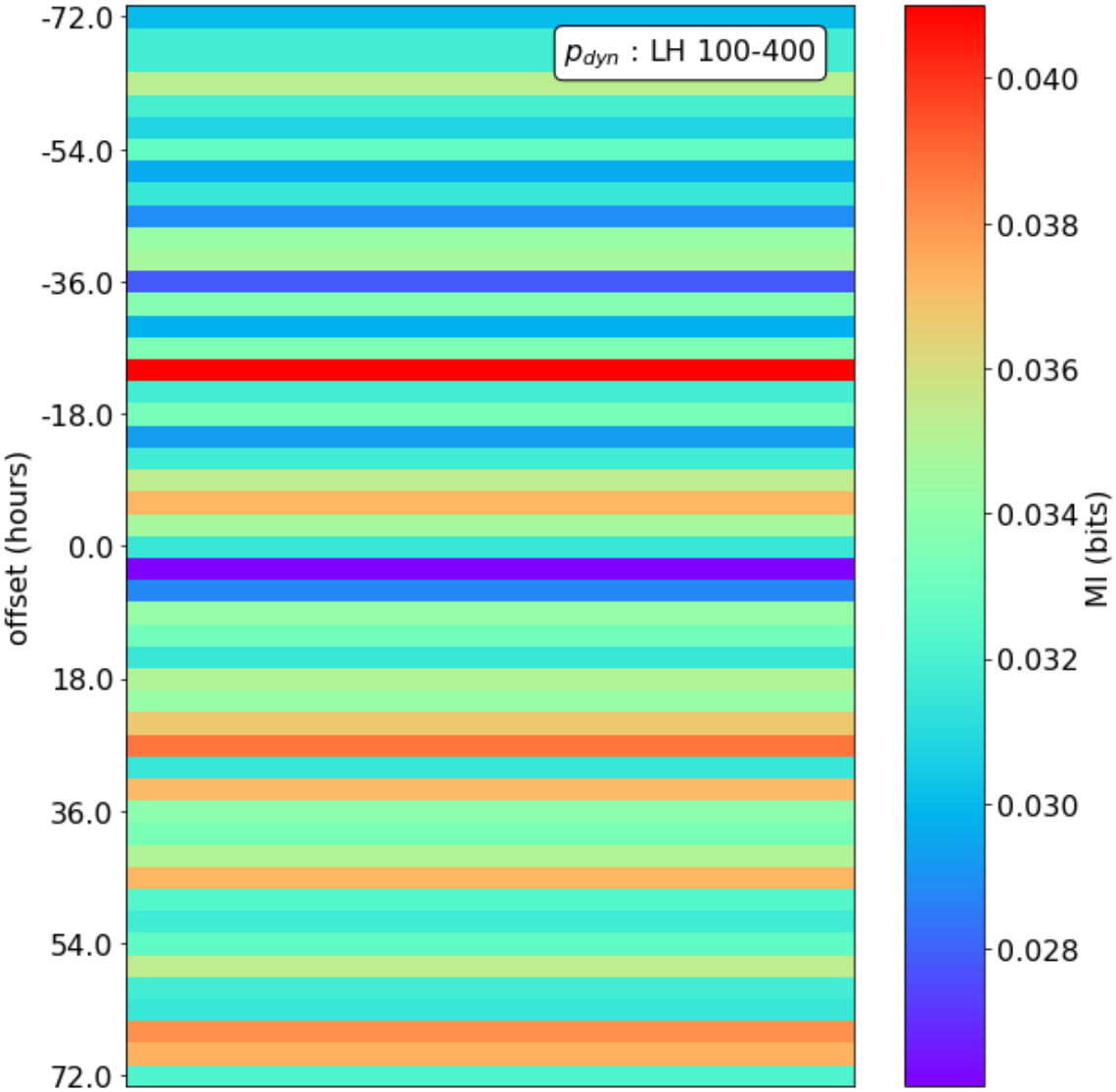

Figure E.9: As Figure E.7 for p_{dyn}

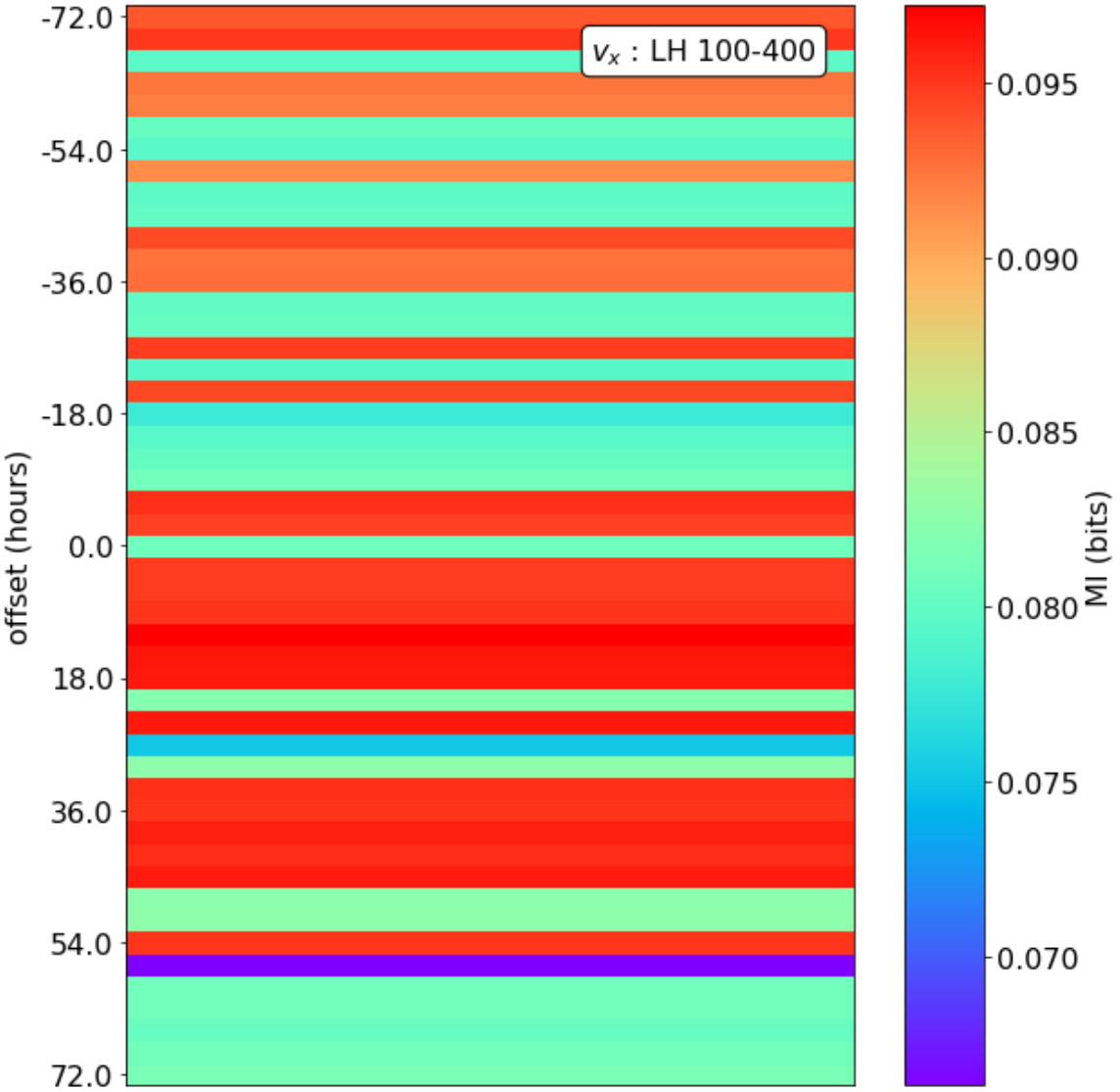

Figure E.10: As Figure E.7 for v_x

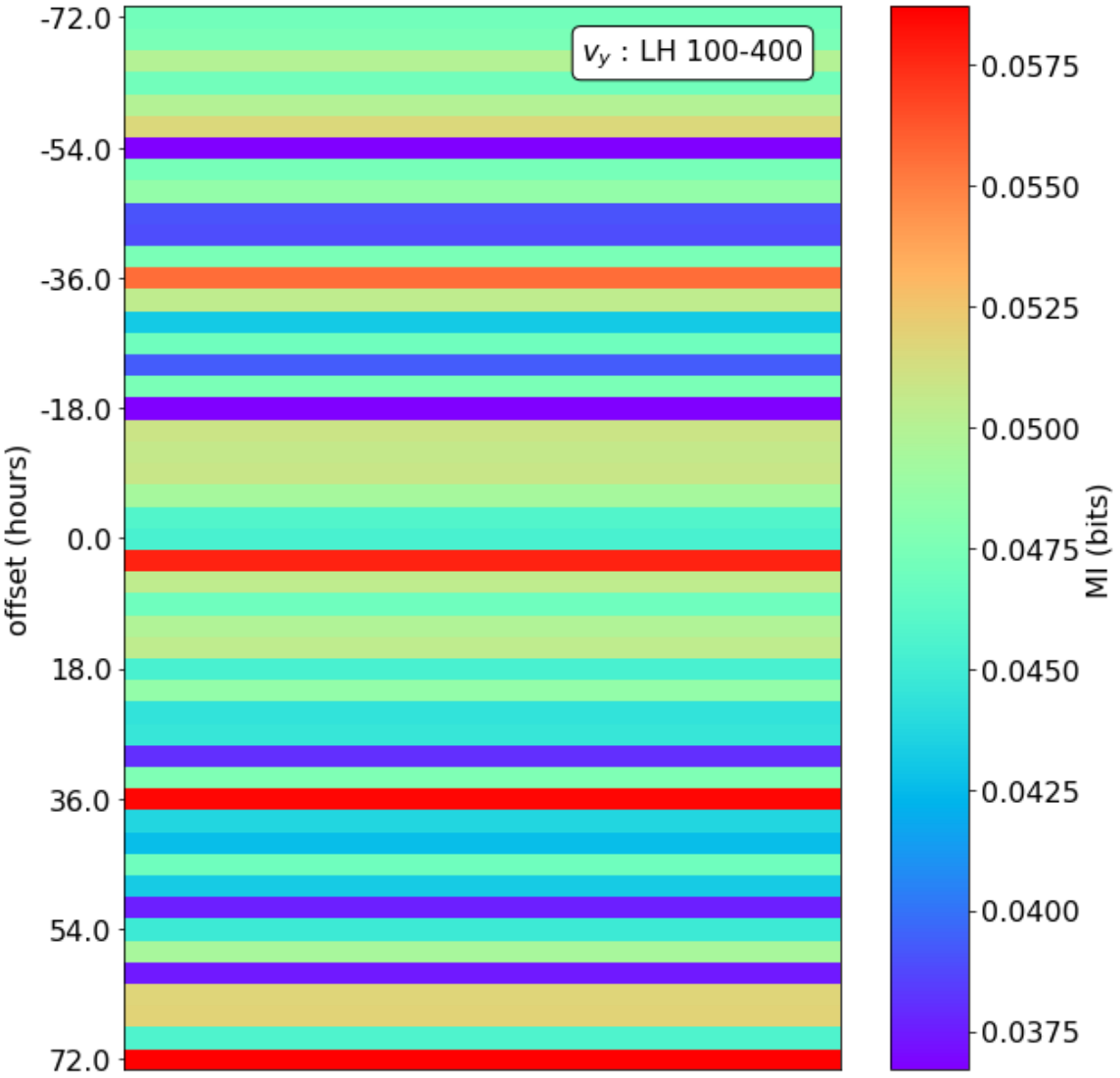

Figure E.11: As Figure E.7 for v_y

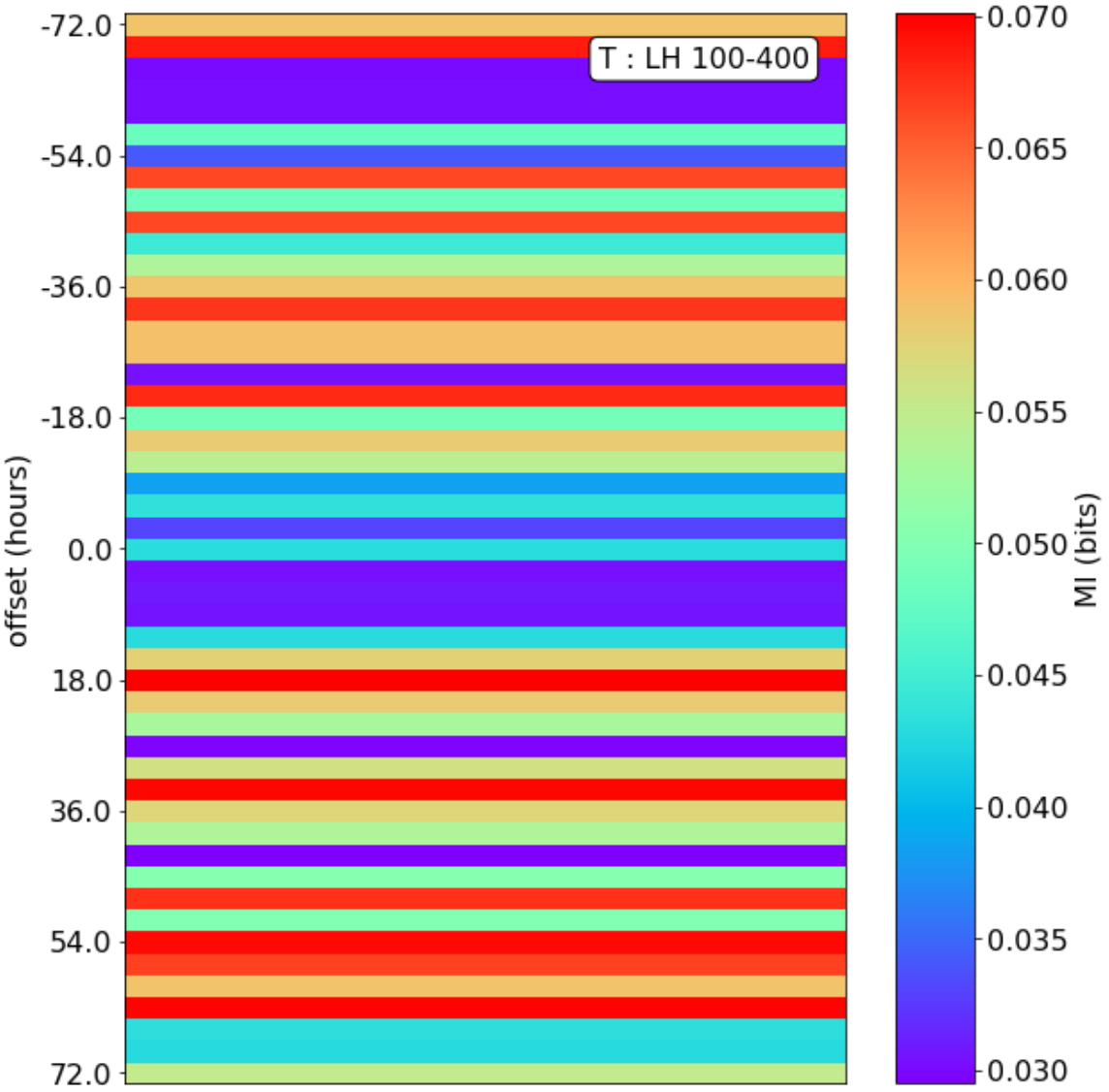

Figure E.12: As Figure E.7 for T

E.2.3 RH 10 - 1,000 kHz

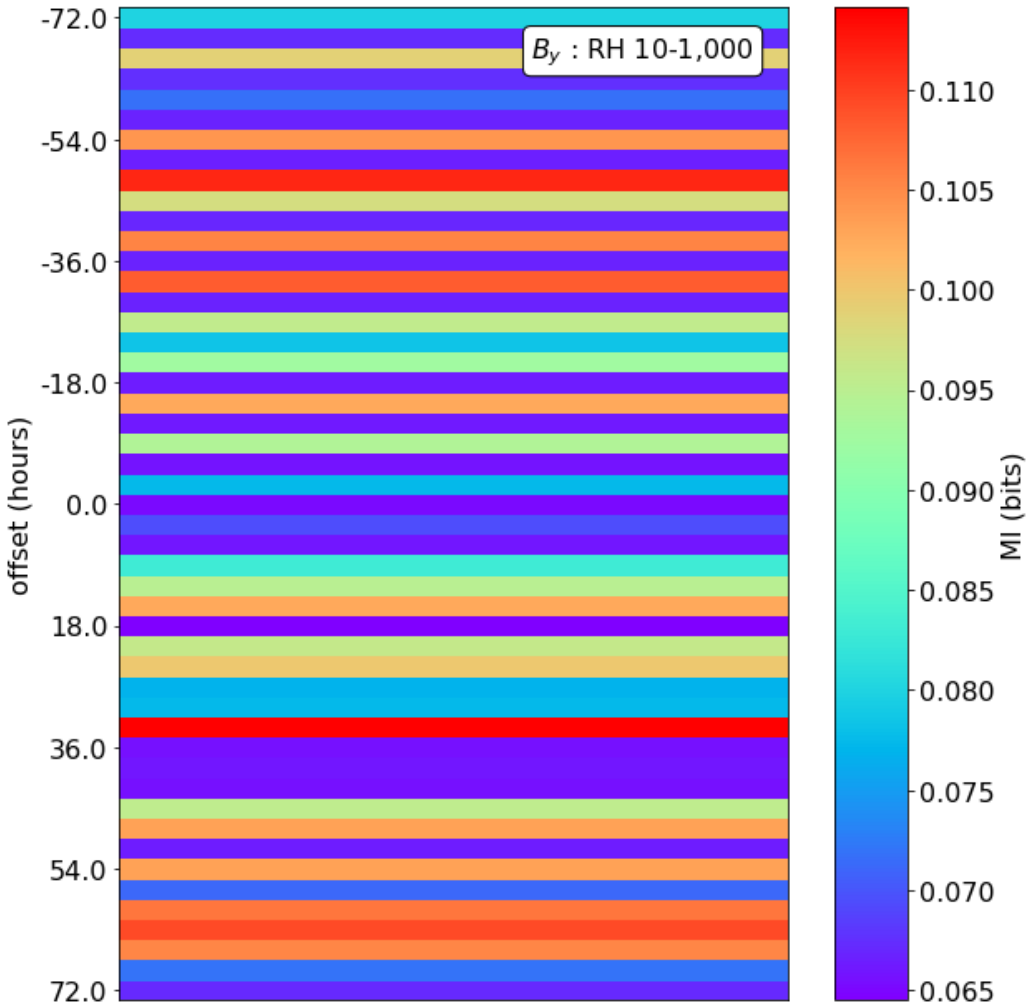

Figure E.13: Mutual information results for SKR, RH 10 - 1,000 kHz data when compared to propagated B_y of the solar wind. The y-axis represents the time offset, in hours, between the SKR and propagated solar wind variable data's timestamps, as described in section 6.4.

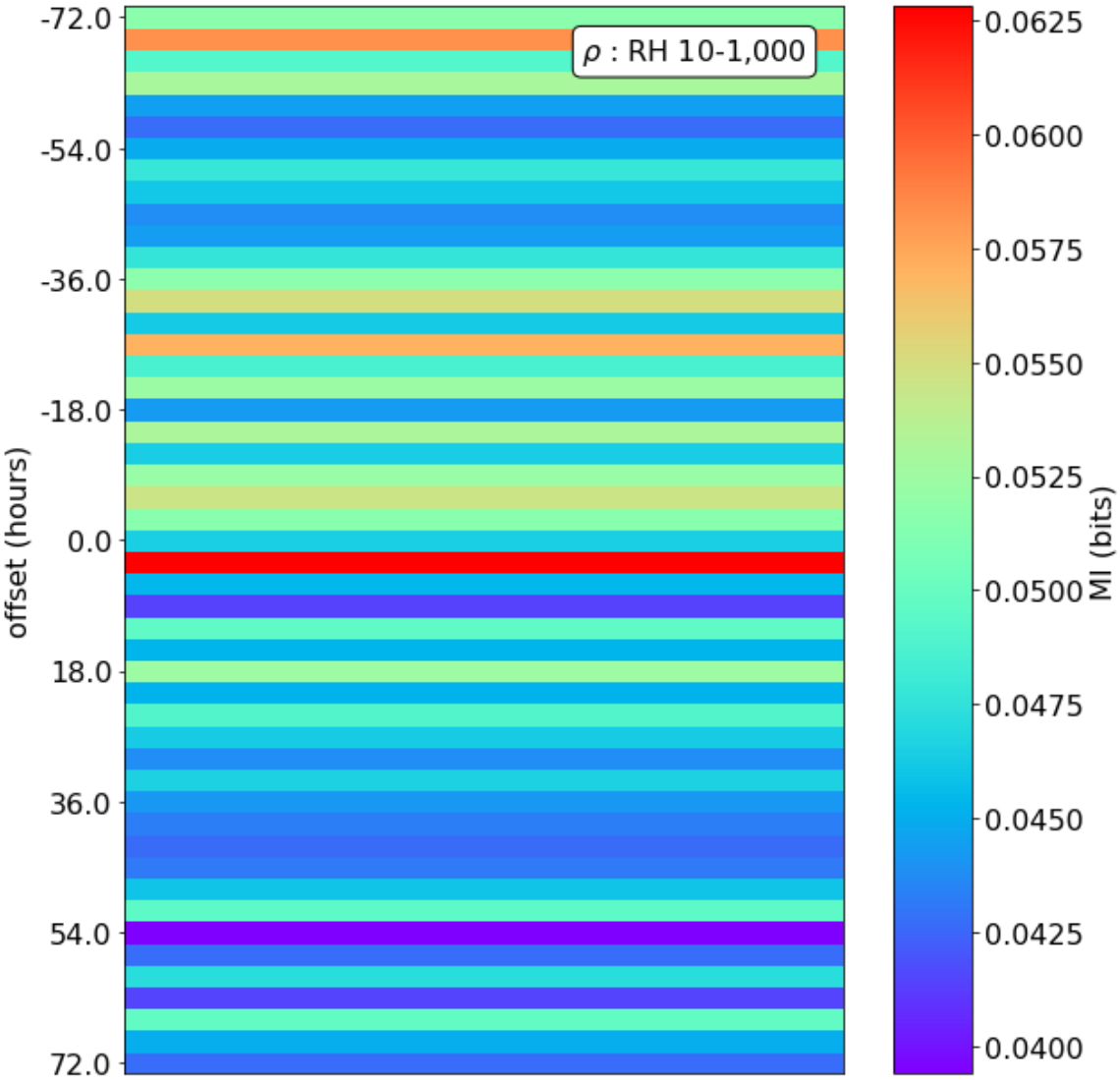

Figure E.14: As Figure E.13 for ρ

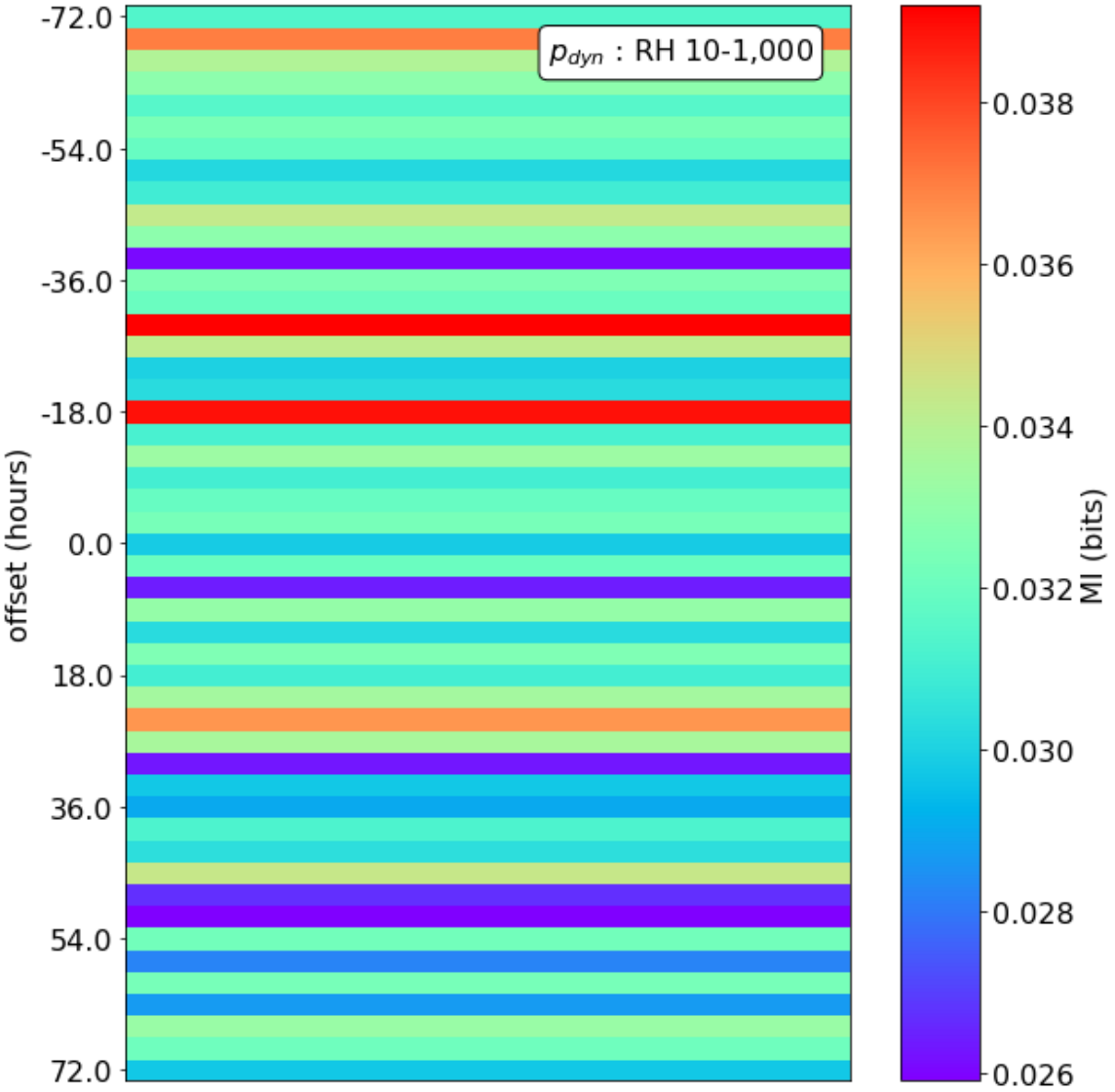

Figure E.15: As Figure E.13 for p_{dyn}

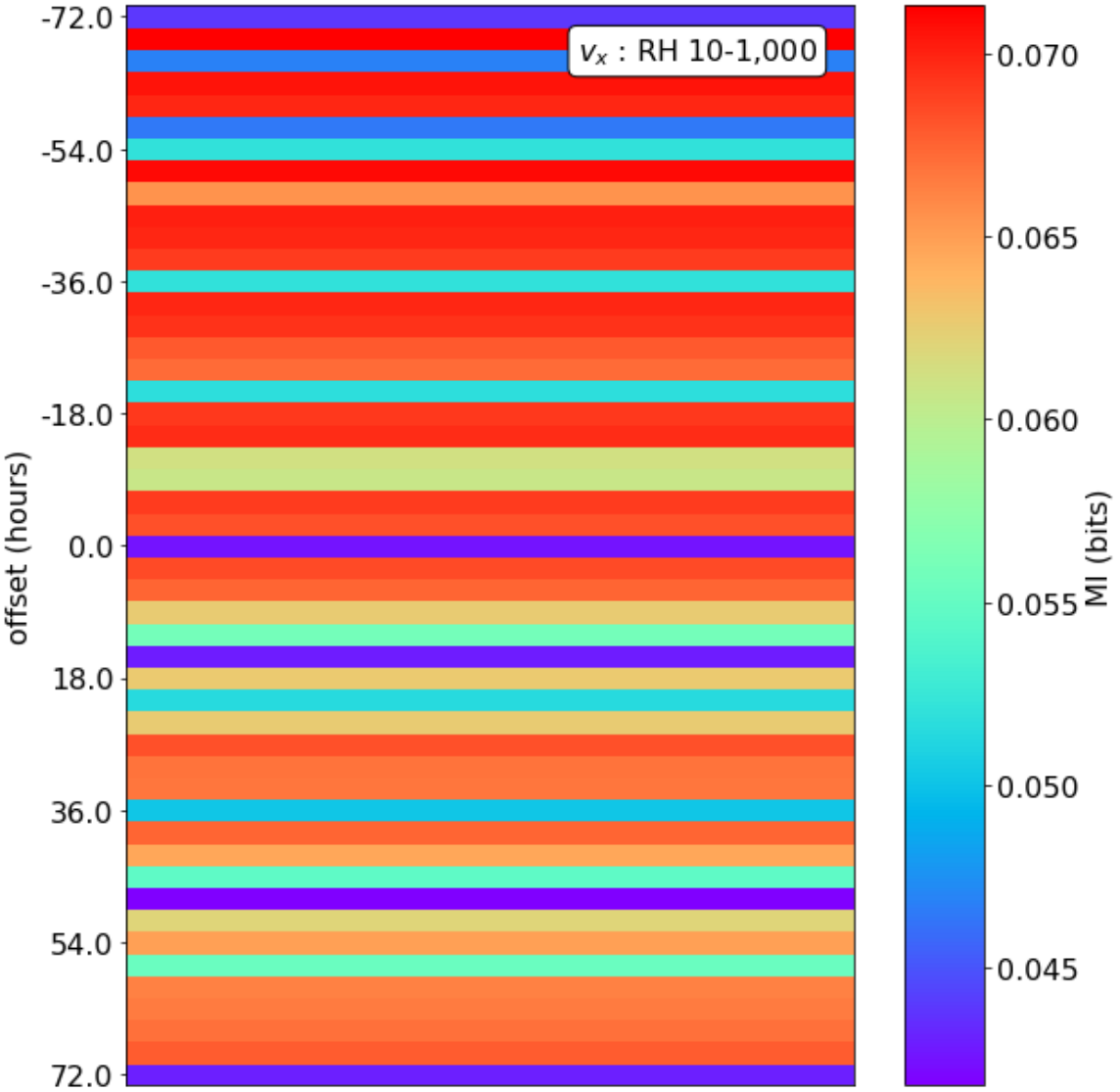

Figure E.16: As Figure E.13 for v_x

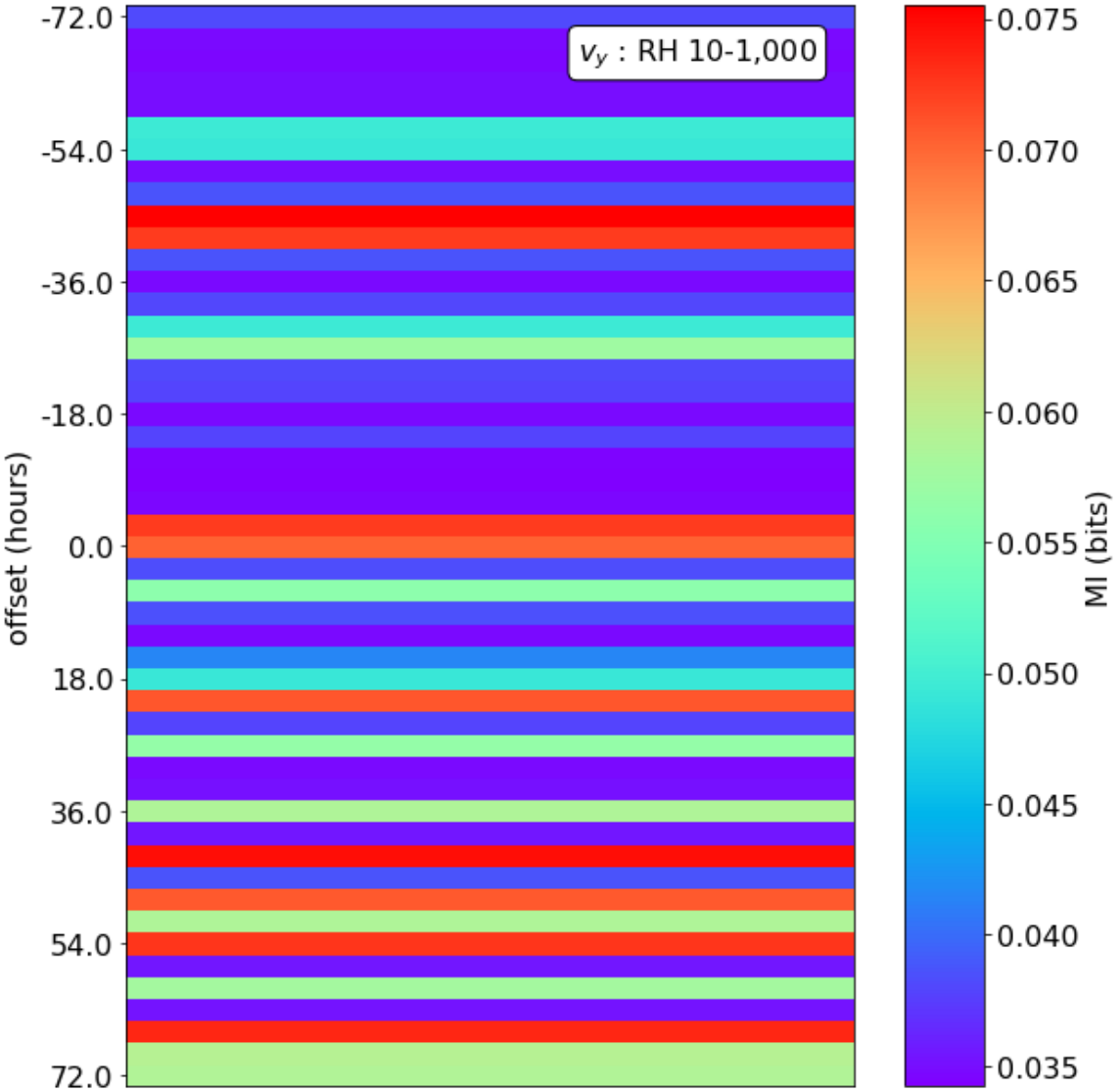

Figure E.17: As Figure E.13 for v_y

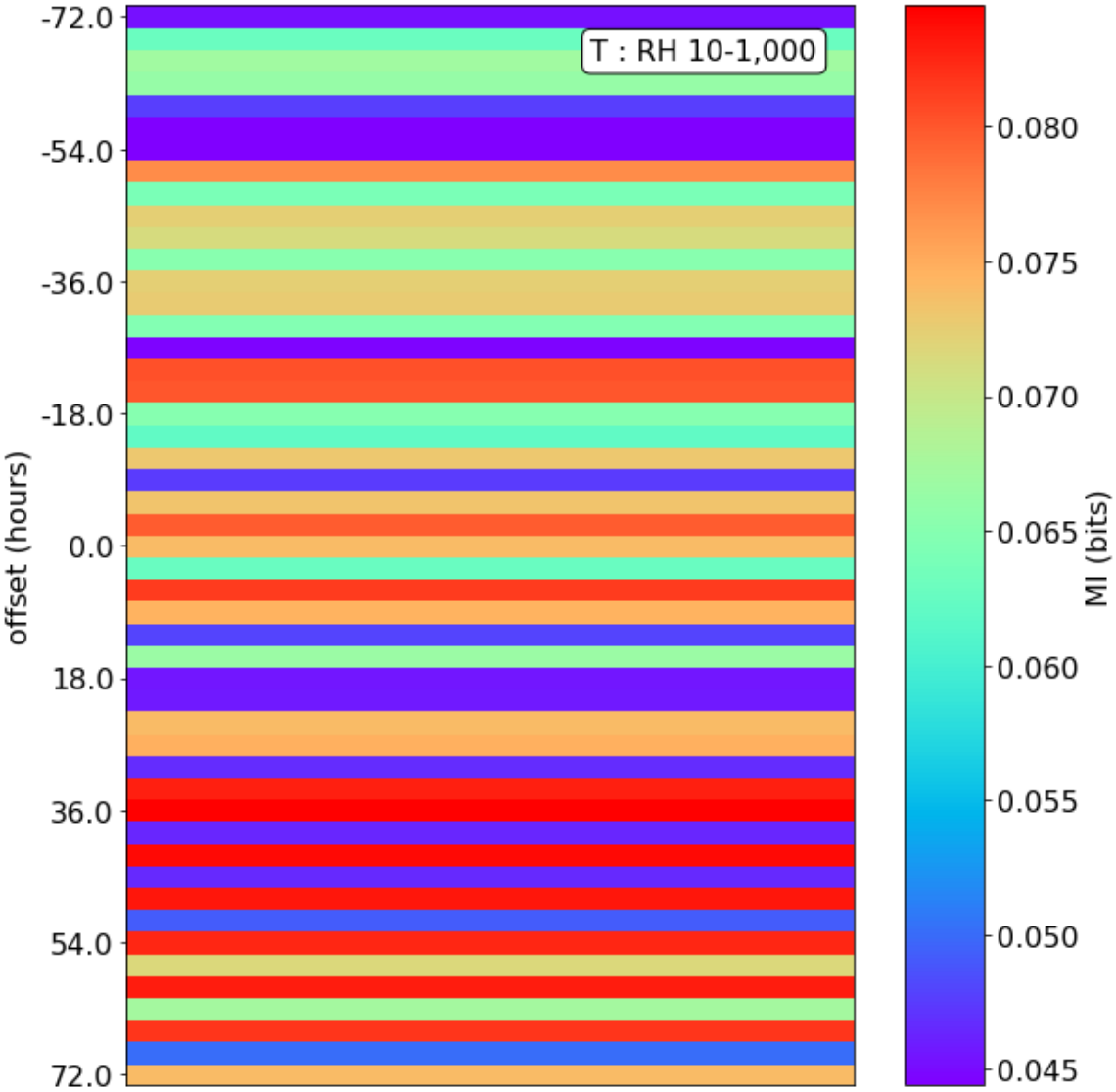

Figure E.18: As Figure E.13 for T

E.2.4 RH 100 - 400 kHz

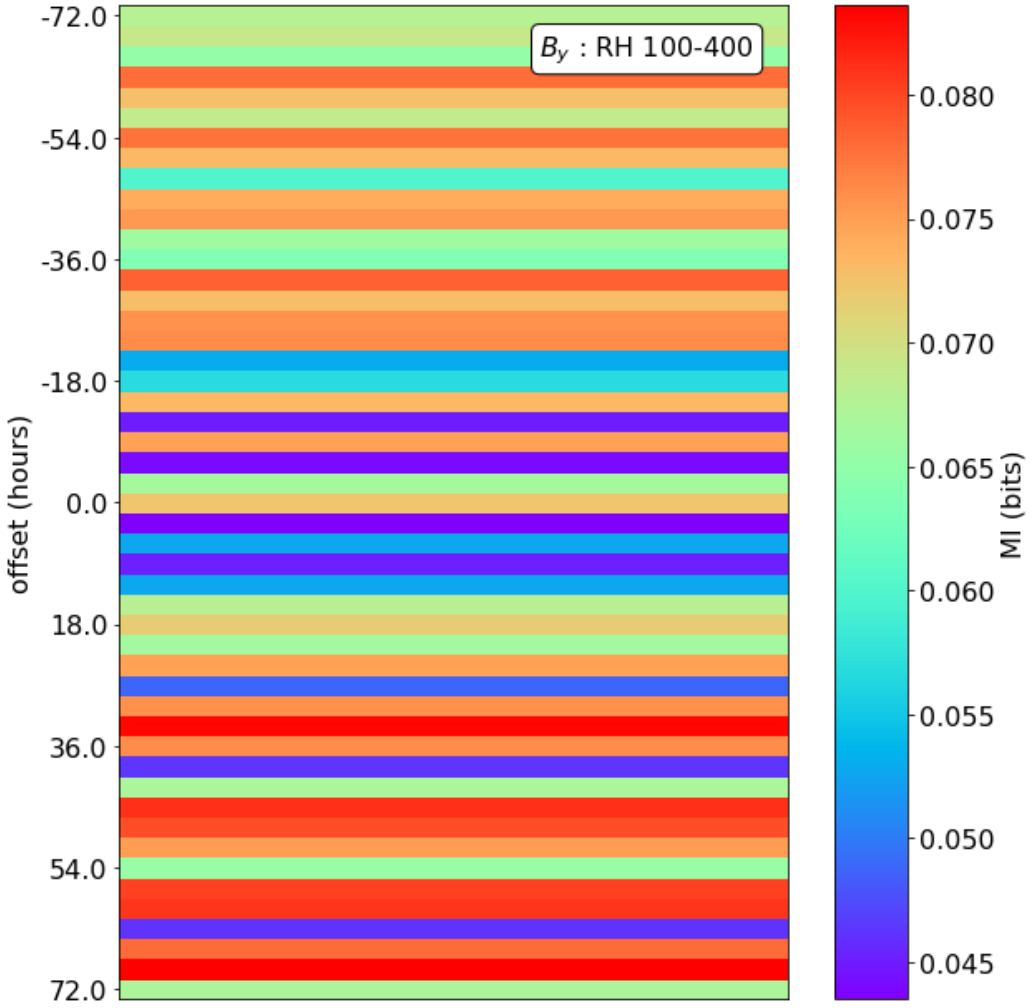

Figure E.19: Mutual information results for SKR, RH 100 - 400 kHz data when compared to propagated B_y of the solar wind. The y-axis represents the time offset, in hours, between the SKR and propagated solar wind variable data's timestamps, as described in section 6.4.

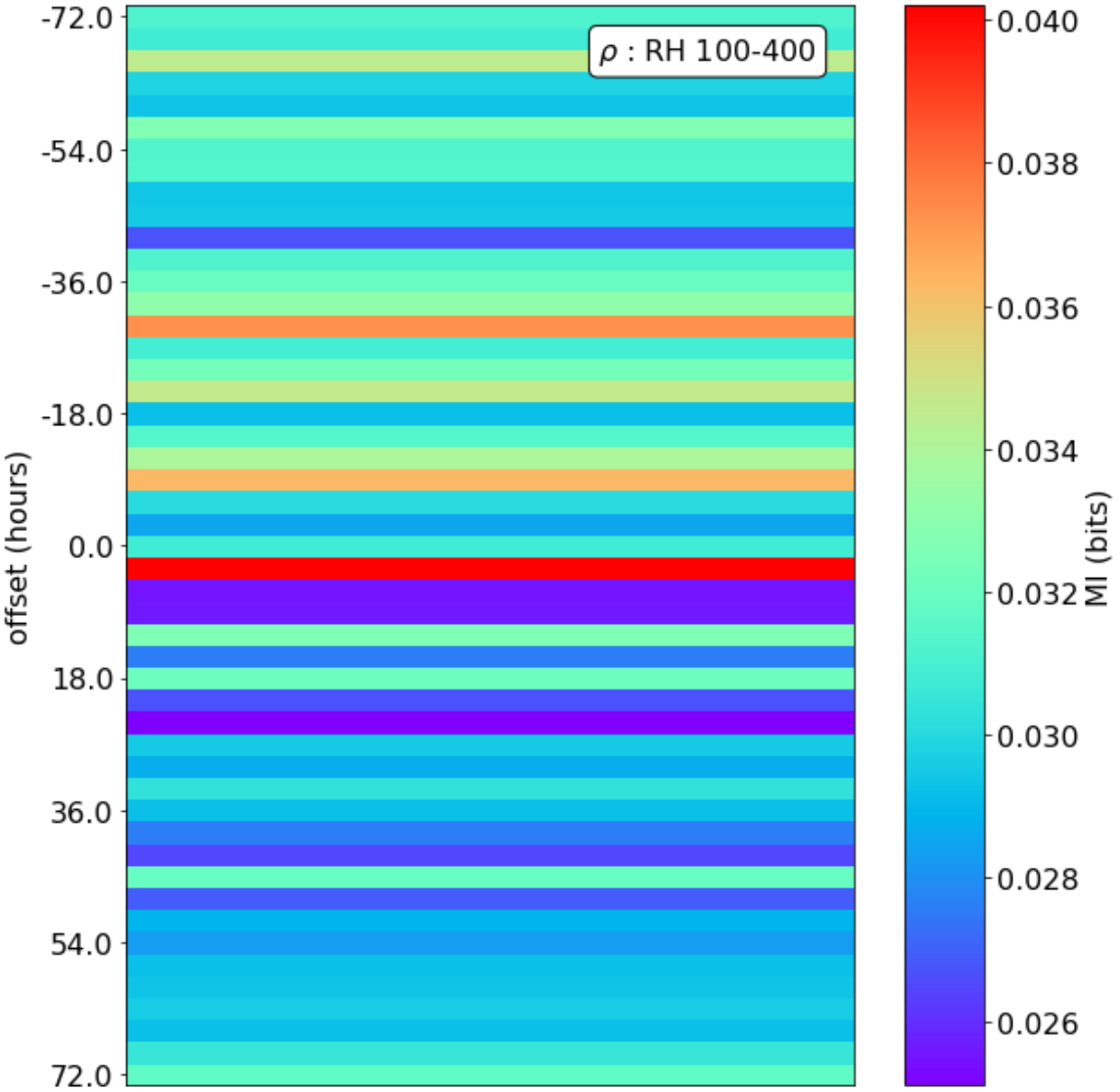

Figure E.20: As Figure E.19 for ρ

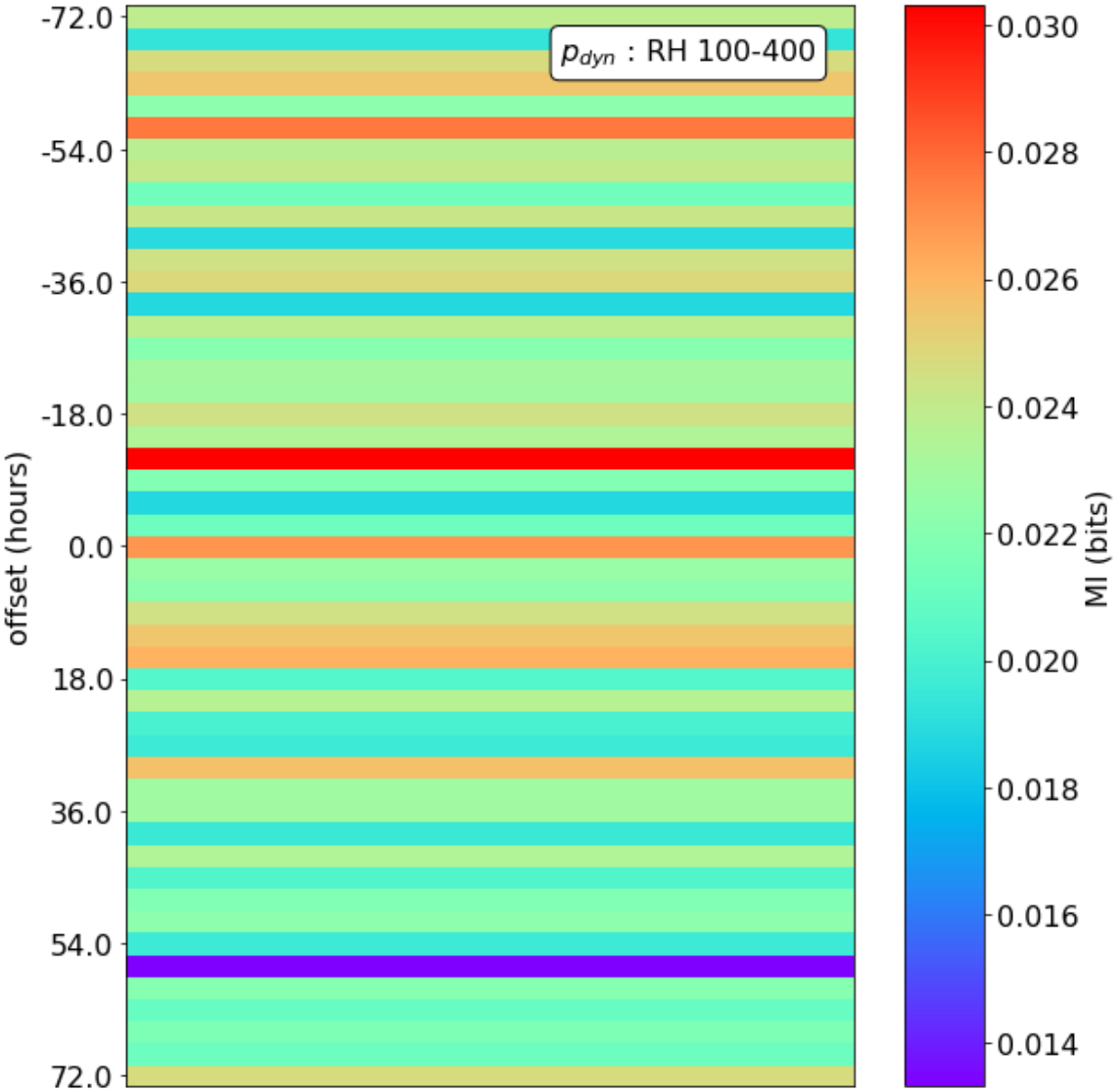

Figure E.21: As Figure E.19 for p_{dyn}

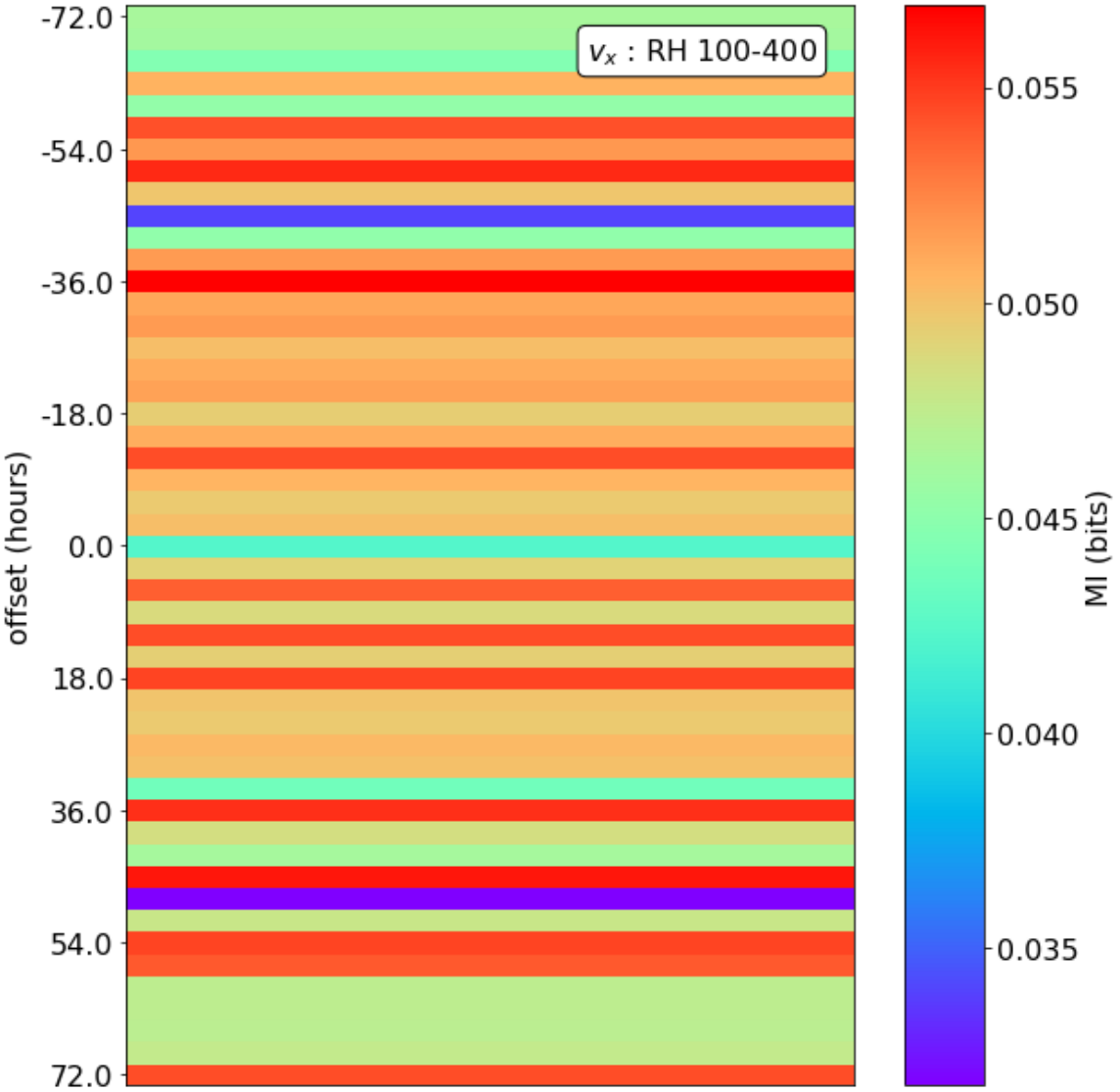

Figure E.22: As Figure E.19 for v_x

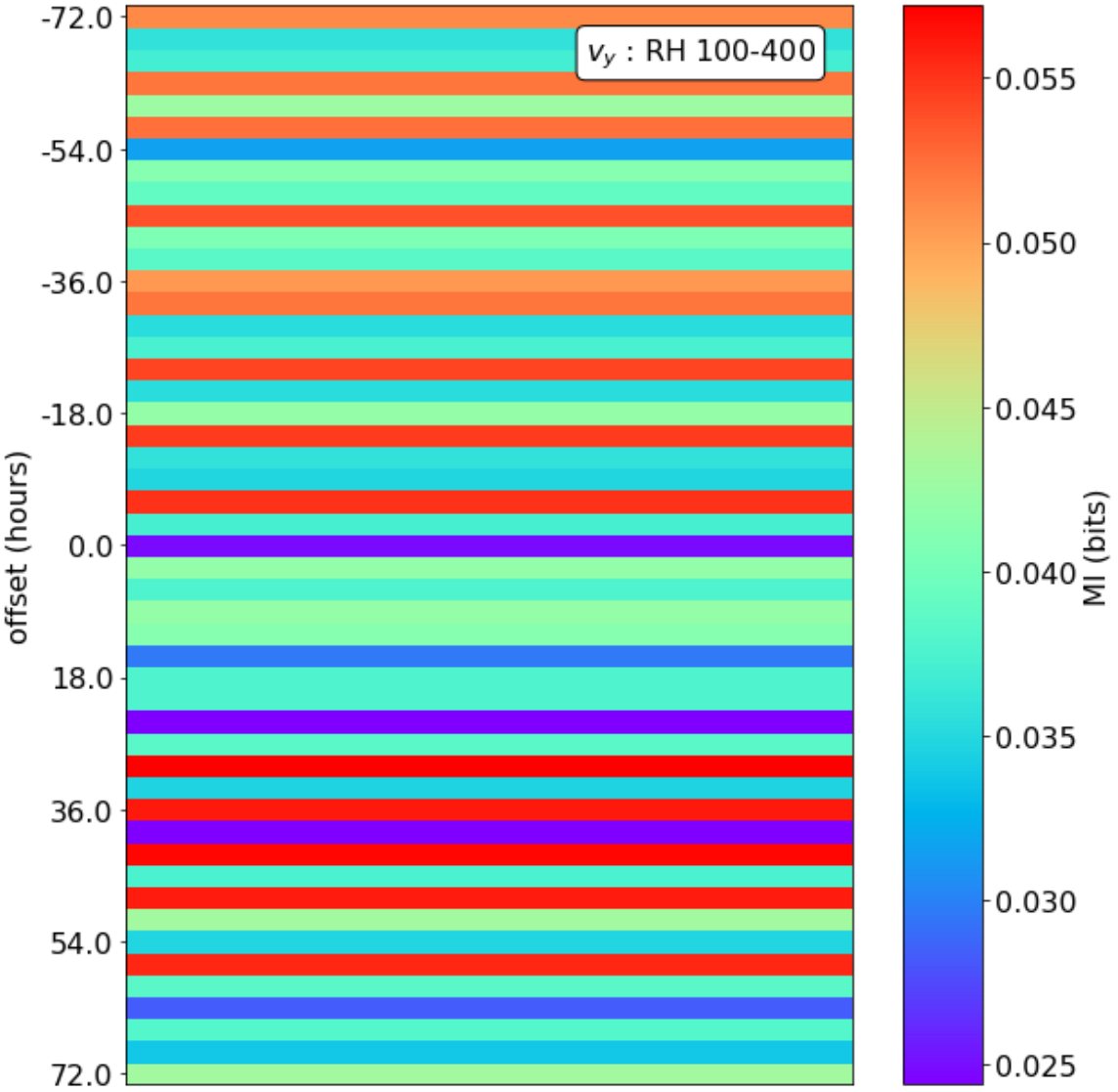

Figure E.23: As Figure E.19 for v_y

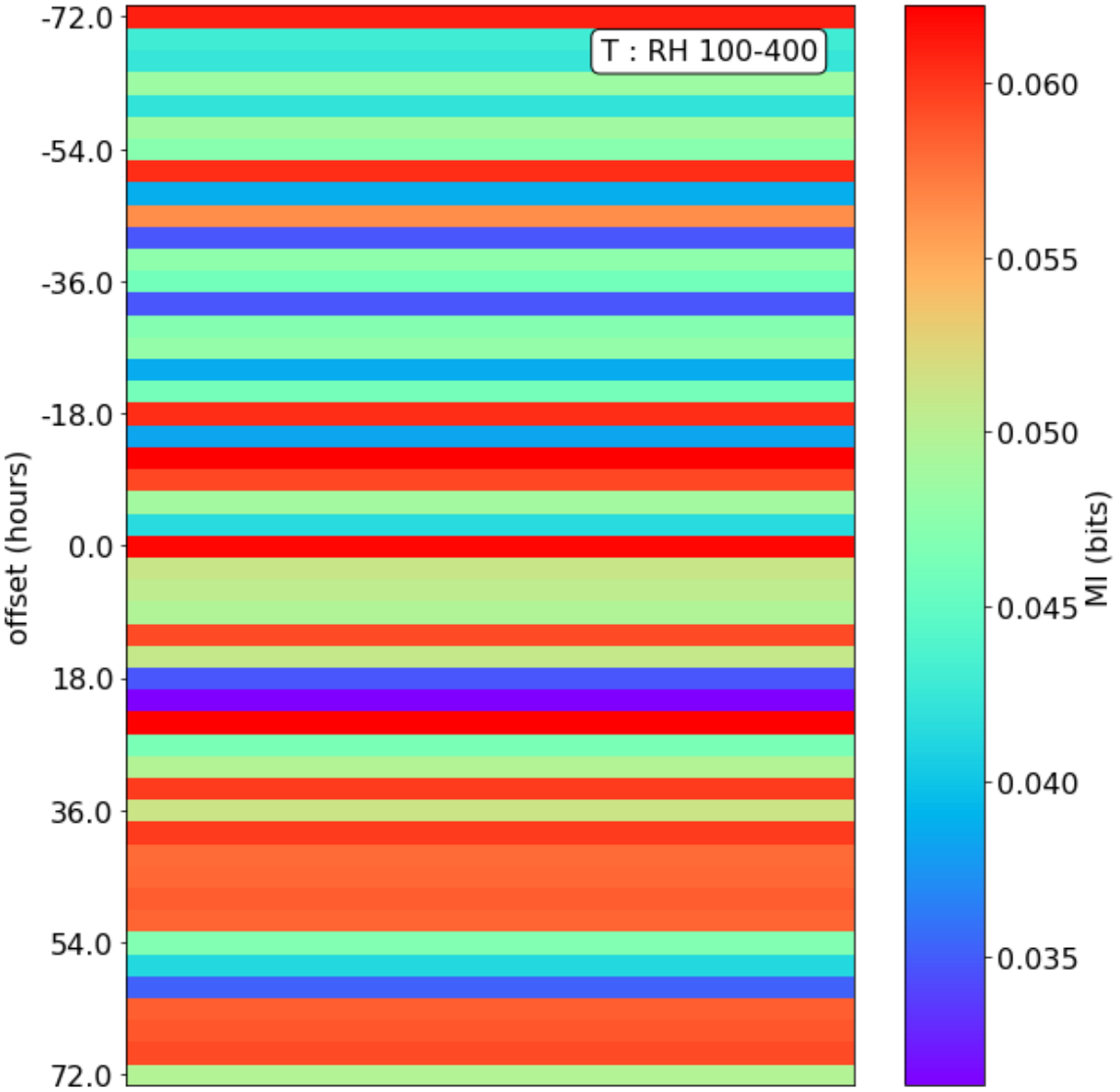

Figure E.24: As Figure E.19 for T

References

ACT-JST (2005). *ACT-JST database, Development of Space Simulation Net-Laboratory System, Principal Investigator: Ryoji, Matsumoto (Chiba Univ.)* URL: https://www.astro.phys.s.chiba-u.ac.jp/netlab/pub/index.html (visited on 10/01/2023).

Alberti, Tommaso et al. (2017). "Timescale separation in the solar wind-magnetosphere coupling during St. Patrick's Day storms in 2013 and 2015". In: *Journal of Geophysical Research: Space Physics* 122.4, pp. 4266–4283.

Axford, W Ian and Colin O Hines (1961). "A unifying theory of high-latitude geophysical phenomena and geomagnetic storms". In: *Canadian Journal of Physics* 39.10, pp. 1433–1464.

Badman, Sarah V et al. (2008). "Relationship between solar wind corotating interaction regions and the phasing and intensity of Saturn kilometric radiation bursts". In: *Annales Geophysicae*. Vol. 26. 12. Copernicus Publications Göttingen, Germany, pp. 3641–3651.

Baines, Kevin H et al. (2018). *Saturn in the 21st Century*. Vol. 20. Cambridge University Press.

Bargatze, LF, DN Baker, et al. (1985). "Magnetospheric impulse response for many levels of geomagnetic activity". In: *Journal of Geophysical Research: Space Physics* 90.A7, pp. 6387–6394.

Bargatze, LF, T Ogino, et al. (1999). "Solar wind magnetic field control of magnetospheric response delay and expansion phase onset timing". In: *Journal of Geophysical Research: Space Physics* 104.A7, pp. 14583–14599.

Baumjohann, Wolfgang and Rudolf A Treumann (2012). *Basic space plasma physics*. World Scientific.

Bayes, Thomas (1763). "LII. An essay towards solving a problem in the doctrine of chances. By the late Rev. Mr. Bayes, FRS communicated by Mr. Price, in a letter to John Canton, AMFR S". In: *Philosophical transactions of the Royal Society of London* 53, pp. 370–418.

Bertsekas, Dimitri P and John N Tsitsiklis (2002). "Introduction to Probability (Athena Scientific, Belmont, MA)". In: *EKLER Ek A: Sıralı Istatistik Ek B: Integrallerin Sayısal Hesabı Ek B* 1.

Bhaskar, Ankush and Geeta Vichare (2019). "Forecasting of SYMH and ASYH indices for geomagnetic storms of solar cycle 24 including St. Patrick's day, 2015 storm using NARX neural network". In: *Journal of Space Weather and Space Climate* 9, A12.

Blanchard, Gerard T and Robert L McPherron (1995). "Analysis of the linear response function relating AL to VBs for individual substorms". In: *Journal of Geophysical Research: Space Physics* 100.A10, pp. 19155–19165.

Cai, Lei et al. (2009). "Prediction of SYM-H index by NARX neural network from IMF and solar wind data". In: *Science in China Series E: Technological Sciences* 52, pp. 2877–2885.

CDPP (2005). *AMDA database*. URL: http://amda.irap.omp.eu/index.html (visited on 11/30/2022).

Clarke, John T et al. (2009). "Response of Jupiter's and Saturn's auroral activity to the solar wind". In: *Journal of Geophysical Research: Space Physics* 114.A5.

Clauer, C Robert et al. (1981). "Solar wind control of auroral zone geomagnetic activity". In: *Geophysical Research Letters* 8.8, pp. 915–918.

Cover, Thomas M and Joy A Thomas (1991). "Information theory and the stock market". In: *Elements of Information Theory. Wiley Inc., New York*, pp. 543–556.

Cowley, SWH et al. (2005). "Reconnection in a rotation-dominated magnetosphere and its relation to Saturn's auroral dynamics". In: *Journal of Geophysical Research: Space Physics* 110.A2.

Davis, T Neil and Masahisa Sugiura (1966). "Auroral electrojet activity index AE and its universal time variations". In: *Journal of Geophysical Research* 71.3, pp. 785–801.

Desch, MD (1982). "Evidence for solar wind control of Saturn radio emission". In: *Journal of Geophysical Research: Space Physics* 87.A6, pp. 4549–4554.

Desch, MD and HO Rucker (1983). "The relationship between Saturn kilometric radiation and the solar wind". In: *Journal of Geophysical Research: Space Physics* 88.A11, pp. 8999–9006.

Dungey, James W (1961). "Interplanetary magnetic field and the auroral zones". In: *Physical Review Letters* 6.2, p. 47.

Eriksson, Stefan et al. (2000). "The cross-polar potential drop and its correlation to the solar wind". In: *Journal of Geophysical Research: Space Physics* 105.A8, pp. 18639–18653.

EUROfusion (2023). *Cyclotron motion*. URL: https://euro-fusion.org/glossary/cyclotron-frequency/ (visited on 11/19/2023).

Galopeau, Patrick, Philippe Zarka, and Dominique Le Quéau (1989). "Theoretical model of Saturn's kilometric radiation spectrum". In: *Journal of Geophysical Research: Space Physics* 94.A7, pp. 8739–8755.

Gonzalez, WD et al. (1994). "What is a geomagnetic storm?" In: *Journal of Geophysical Research: Space Physics* 99.A4, pp. 5771–5792.

Gurnett, DA, WS Kurth, et al. (2004). "The Cassini radio and plasma wave investigation". In: *Space Science Reviews* 114, pp. 395–463.

Gurnett, DA, AM Persoon, et al. (2007). "The variable rotation period of the inner region of Saturn's plasma disk". In: *science* 316.5823, pp. 442–445.

Hartley, Ralph VL (1928). "Transmission of information 1". In: *Bell System technical journal* 7.3, pp. 535–563.

Hathaway, David H (2015). "The solar cycle". In: *Living reviews in solar physics* 12, pp. 1–87.

Holmes, Caroline M and Ilya Nemenman (2019). "Estimation of mutual information for real-valued data with error bars and controlled bias". In: *Physical Review E* 100.2, p. 022404.

Iyemori, Toshihiko (1990). "Storm-time magnetospheric currents inferred from mid-latitude geomagnetic field variations". In: *Journal of geomagnetism and geoelectricity* 42.11, pp. 1249–1265.

Jackman, Caitriona M et al. (2010). "In situ observations of the effect of a solar wind compression on Saturn's magnetotail". In: *Journal of Geophysical Research: Space Physics* 115.A10.

Kaiser, ML and MD Desch (1982). "Saturnian kilometric radiation: Source locations". In: *Journal of Geophysical Research: Space Physics* 87.A6, pp. 4555–4559.

Kan, JR and LC Lee (1979). "Energy coupling function and solar wind-magnetosphere dynamo". In: *Geophysical Research Letters* 6.7, pp. 577–580.

Khinchin, Aleksandr Yakovlevich (1956). "On the basic theorems of information theory". In: *Uspekhi matematicheskikh nauk* 11.1, pp. 17–75.

— (1957). "Mathematical Foundations of Information Theory". In.

Kimura, Tomoki et al. (2013). "Long-term modulations of Saturn's auroral radio emissions by the solar wind and seasonal variations controlled by the solar ultraviolet flux". In: *Journal of Geophysical Research: Space Physics* 118.11, pp. 7019–7035.

Kozachenko, LF and Nikolai N Leonenko (1987). "Sample estimate of the entropy of a random vector". In: *Problemy Peredachi Informatsii* 23.2, pp. 9–16.

Kraskov, Alexander, Harald Stögbauer, and Peter Grassberger (2004). "Estimating mutual information". In: *Physical review E* 69.6, p. 066138.

Krimigis, SM et al. (2004). "Magnetosphere imaging instrument (MIMI) on the Cassini mission to Saturn/Titan". In: *The Cassini-Huygens Mission: Orbiter In Situ Investigations Volume 2*, pp. 233–329.

Kuijpers, Jan, Harald U Frey, and Lyndsay Fletcher (2016). "Electric current circuits in astrophysics". In: *Multi-scale Structure Formation and Dynamics in Cosmic Plasmas*, pp. 3–57.

Kurth, William S et al. (2005). "An Earth-like correspondence between Saturn's auroral features and radio emission". In: *Nature* 433.7027, pp. 722–725.

Lamy, L, P Zarka, et al. (2008). "Saturn kilometric radiation: Average and statistical properties". In: *Journal of Geophysical Research: Space Physics* 113.A7.

Lamy, Laurent, R Prangé, et al. (2017). "The aurorae of Uranus past equinox". In: *Journal of Geophysical Research: Space Physics* 122.4, pp. 3997–4008.

Lepping, RP et al. (1995). "The WIND magnetic field investigation". In: *Space Science Reviews* 71, pp. 207–229.

Li, Xinlin, Kap Soo Oh, and M Temerin (2007). "Prediction of the AL index using solar wind parameters". In: *Journal of Geophysical Research: Space Physics* 112.A6.

Lockwood, Mike and Kathryn A McWilliams (2021). "On optimum solar wind-magnetosphere coupling functions for transpolar voltage and planetary geomagnetic activity". In: *Journal of Geophysical Research: Space Physics* 126.12, e2021JA029946.

Luo, Bingxian et al. (2013). "Prediction of the AU, AL, and AE indices using solar wind parameters". In: *Journal of Geophysical Research: Space Physics* 118.12, pp. 7683–7694.

MacKay, David JC (2003). *Information theory, inference and learning algorithms*. Cambridge university press.

Manu, V et al. (2022). "Association of the Main Phase of the Geomagnetic Storms in Solar Cycles 23 and 24 With Corresponding Solar Wind-IMF Parameters". In: *Journal of Geophysical Research: Space Physics* 127.10, e2022JA030747.

March, TK, SC Chapman, and RO Dendy (2005). "Mutual information between geomagnetic indices and the solar wind as seen by WIND: Implications for propagation time estimates". In: *Geophysical research letters* 32.4.

McComas, DJ et al. (2008). "Weaker solar wind from the polar coronal holes and the whole Sun". In: *Geophysical Research Letters* 35.18.

Milan, SE, JS Gosling, and Benoit Hubert (2012). "Relationship between interplanetary parameters and the magnetopause reconnection rate quantified from observations of the expanding polar cap". In: *Journal of Geophysical Research: Space Physics* 117.A3.

Milan, Stephen E, J Hutchinson, et al. (2009). "Influences on the radius of the auroral oval". In: *Annales Geophysicae*. Vol. 27. 7. Copernicus Publications Göttingen, Germany, pp. 2913–2924.

Moser, Stefan M and Po-Ning Chen (2012). *A student's guide to coding and information theory*. Cambridge University Press.

Mutel, RL et al. (2010). "CMI growth rates for Saturnian kilometric radiation". In: *Geophysical research letters* 37.19.

Nakamura, Yuki et al. (2019). "Seasonal variation of north–south asymmetry in the intensity of Saturn Kilometric Radiation from 2004 to 2017". In: *Planetary and Space Science* 178, p. 104711.

Newell, PT et al. (2007). "A nearly universal solar wind-magnetosphere coupling function inferred from 10 magnetospheric state variables". In: *Journal of Geophysical Research: Space Physics* 112.A1.

Nishida, A (1994). *The GEOTAIL mission*.

Palmerio, Erika et al. (2021). "Magnetic structure and propagation of two interacting CMEs from the Sun to Saturn". In: *Journal of Geophysical Research: Space Physics* 126.11, e2021JA029770.

Papitashvili, Natalia E. and Joseph H. King (2020). *"OMNI 1-min Data", High resolution (1-min, 5-min) OMNI: Solar wind magnetic field and plasma data at Earth's Bow Shock Nose (BSN), also geomagnetic activity indices and 5-min energetic proton fluxes, NASA Space Physics Data Facility.* URL: https://doi.org/10.48322/45bb-8792 (visited on 11/30/2022).

Parker, Eugene N (1958). "Dynamics of the interplanetary gas and magnetic fields." In: *Astrophysical Journal, vol. 128, p. 664* 128, p. 664.

Perreault, Paul and SI Akasofu (1978). "A study of geomagnetic storms". In: *Geophysical Journal International* 54.3, pp. 547–573.

Perreault, Paul David (1974). *On the relationship between interplanetary magnetic fields and magnetospheric storms and substorms.* University of Alaska Fairbanks.

Petrukovich, AA and AA Rusanov (2005). "AL index dependence on the solar wind input revisited". In: *Advances in Space Research* 36.12, pp. 2440–2444.

Poudel, Prashant et al. (2019). "Variation of solar wind parameters along with the understanding of energy dynamics within the magnetospheric system during geomagnetic disturbances". In: *Earth and Space Science* 6.2, pp. 276–293.

Provan, Gabrielle et al. (2015). "Planetary period oscillations in Saturn's magnetosphere: Examining the relationship between abrupt changes in behavior and solar wind-induced magnetospheric compressions and expansions". In: *Journal of Geophysical Research: Space Physics* 120.11, pp. 9524–9544.

Rucker, Helmut O et al. (2008). "Saturn kilometric radiation as a monitor for the solar wind?" In: *Advances in Space Research* 42.1, pp. 40–47.

Russell, Christopher T (1971). "Geophysical coordinate transformations". In: *Cosmic electrodynamics* 2.2, pp. 184–196.

Russell, Christopher T, Janet G Luhmann, and Robert J Strangeway (2016). *Space physics: An introduction*. Cambridge University Press.

Russell, CT (2000). "The polar cusp". In: *Advances in Space Research* 25.7-8, pp. 1413–1424.

Shannon, Claude Elwood (1948). "A mathematical theory of communication". In: *The Bell system technical journal* 27.3, pp. 379–423.

Siciliano, F et al. (2021). "Forecasting SYM-H index: A comparison between long short-term memory and convolutional neural networks". In: *Space Weather* 19.2, e2020SW002589.

Siddiqi, Asif A (2018). *Beyond Earth: A chronicle of deep space exploration, 1958-2016*. Vol. 4041. National Aeronautis & Space Administration.

Smith, Charles W, Jacques L'Heureux, et al. (1998). "The ACE magnetic fields experiment". In: *The advanced composition explorer mission*, pp. 613–632.

Smith, Paul H, RA Hoffman, and TA Fritz (1976). "Ring current proton decay by charge exchange". In: *Journal of Geophysical Research* 81.16, pp. 2701–2708.

Stögbauer, Harald et al. (2004). "Least-dependent-component analysis based on mutual information". In: *Physical Review E* 70.6, p. 066123.

Stone, Edward C, AM Frandsen, et al. (1998). "The advanced composition explorer". In: *Space Science Reviews* 86, pp. 1–22.

Stone, James M and Michael L Norman (1992a). "ZEUS-2D: a radiation magnetohydrodynamics code for astrophysical flows in two space dimensions. I-The hydrodynamic algorithms and tests." In: *Astrophysical Journal Supplement Series (ISSN 0067-0049), vol. 80, no. 2, June 1992, p. 753-790. Research supported by University of Illinois.* 80, pp. 753–790.

— (1992b). "ZEUS-2D: a radiation magnetohydrodynamics code for astrophysical flows in two space dimensions. II. The magnetohydrodynamic algorithms and tests". In: *The Astrophysical Journal Supplement Series* 80, p. 791.

Stumpo, Mirko et al. (2020). "Measuring information coupling between the solar wind and the magnetosphere–ionosphere system". In: *Entropy* 22.3, p. 276.

Tao, Chihiro (2005). *ACT-JST project "Development of space simulation and network laboratory system"*. URL: http://www.astro.phys.s.chiba-u.ac.jp/netlab/pub/index.html (visited on 12/01/2022).

Tao, Chihiro et al. (2005). "Magnetic field variations in the Jovian magnetotail induced by solar wind dynamic pressure enhancements". In: *Journal of Geophysical Research: Space Physics* 110.A11.

Taubenschuss, U et al. (2006). "Linear prediction studies for the solar wind and Saturn kilometric radiation". In: *Annales Geophysicae*. Vol. 24. 11. Copernicus Publications Göttingen, Germany, pp. 3139–3150.

Thomsen, MF, CM Jackman, and L Lamy (2019). "Solar wind dynamic pressure upstream from Saturn: Estimation from magnetosheath properties and comparison with SKR". In: *Journal of Geophysical Research: Space Physics* 124.10, pp. 7799–7819.

Tibshirani, Robert J and Bradley Efron (1993). "An introduction to the bootstrap". In: *Monographs on statistics and applied probability* 57.1.

Vasyliunas, Vytenis M (1983). "Plasma distribution and flow". In: *Physics of the Jovian magnetosphere* 1, pp. 395–453.

Wanliss, James A and Kristin M Showalter (2006). "High-resolution global storm index: Dst versus SYM-H". In: *Journal of Geophysical Research: Space Physics* 111.A2.

Warwick, JW, DR Evans, et al. (1982). "Planetary radio astronomy observations from Voyager 2 near Saturn". In: *Science* 215.4532, pp. 582–587.

Warwick, JW, JB Pearce, et al. (1981). "Planetary radio astronomy observations from Voyager 1 near Saturn". In: *Science* 212.4491, pp. 239–243.

WDC for Geomagnetism, Kyoto (2005). *World Data Center for Geomagnetism, Kyoto*. URL: https://wdc.kugi.kyoto-u.ac.jp/index.html (visited on 12/01/2022).

Wilson III, Lynn B et al. (2021). *A quarter century of wind spacecraft discoveries*.

Wintoft, Peter (2005). "Study of the solar wind coupling to the time difference horizontal geomagnetic field". In: *Annales Geophysicae*. Vol. 23. 5. Copernicus Publications Göttingen, Germany, pp. 1949–1957.

Wu, CS and LC Lee (1979). "A theory of the terrestrial kilometric radiation". In: *Astrophysical Journal, Part 1, vol. 230, June 1, 1979, p. 621-626.* 230, pp. 621–626.

Zarka, Philippe (1998). "Auroral radio emissions at the outer planets: Observations and theories". In: *Journal of Geophysical Research: Planets* 103.E9, pp. 20159–20194.

Zarka, Philippe et al. (2007). "Modulation of Saturn's radio clock by solar wind speed". In: *Nature* 450.7167, pp. 265–267.

Zhang, LQ et al. (2019). "Statistical properties of the IMF clock angle in the solar wind with northward and southward interplanetary magnetic field based on ACE observation from 1998 to 2009: Dependence on the temporal scale of the solar wind". In: *Advances in Space Research* 63.10, pp. 3077–3087.

Zieger, Bertalan and Kenneth C Hansen (2008). "Statistical validation of a solar wind propagation model from 1 to 10 AU". In: *Journal of Geophysical Research: Space Physics* 113.A8.